UNIVERSITY OF CALIFORNIA SAN DIEGO

Advances in Representing Atmospheric Circulation and Structure for Carbon Cycle Studies

A Dissertation submitted in partial satisfaction of the requirements
for the degree Doctor of Philosophy

in

Earth Sciences

by

Yuming Jin

Committee in charge:

Professor Ralph F. Keeling, Chair
Professor Ian Eisenman
Professor Nicholas Lutsko
Professor Armin Schwartzman
Professor Jeffrey Severinghaus

2023

The Dissertation of Yuming Jin is approved, and it is acceptable in quality and form for publication on microfilm and electronically.

University of California San Diego

2023

EPIGRAPH

而世之奇伟、瑰怪，非常之观，常在于险远，而人之所罕至焉，故非有志者不能至也。

The marvels and wonders of the world, those extraordinary spectacles, often lie in places perilous and remote, where few dare to venture. Therefore, only those with unwavering determination can ever reach them.

- Wang, Anshi, *A Journey to Baochan Mountain*, A.C. 1054

TABLE OF CONTENTS

DISSERTATION APPROVAL PAGE ..... **iii**

EPIGRAPH ..... **iv**

TABLE OF CONTENTS ..... **v**

LIST OF FIGURES ..... **ix**

LIST OF TABLES ..... **xiv**

ACKNOWLEDEMENT ..... **xvi**

VITA ..... **xviii**

ABSTRACT OF THE DISSERTATION ..... **xix**

INTRODUCTION **1**

Chapter 1 A mass-weighted isentropic coordinate for mapping chemical tracers and computing atmospheric inventories **9**

Abstract 9

1.1 Introduction 9

1.2 Methods 12
1.2.1 Meteorological reanalysis products 12
1.2.2 Equivalent potential temperature (θ_e) and dry air mass (M) of the atmospheric fields 12
1.2.3 Determination of $M_{\theta e}$ 14

1.3 Characteristics of $M_{\theta e}$ 15
1.3.1 Spatial and temporal distribution of $M_{\theta e}$ 15
1.3.2 θ_e-$M_{\theta e}$ relationship 21
1.3.3 Relationship to diabatic heating and mass fluxes 22

1.4 Applications of $M_{\theta e}$ as an atmospheric coordinate 27
1.4.1 Mapping Northern Hemisphere CO_2 30
1.4.2 Computing the hemispheric mass-weighted average CO_2 mole fraction 34

1.5 Discussion and summary 42

1.6 Code availability 45

1.7 Data availability 45

1.8 Appendix A: Temporal variation of Mθe 46

1.9 Supplement 51
1.9.1 Contribution of each heating term to the overall time variation of $M_{\theta e}$ 51

1.10 Acknowledgements 56
References 57

Chapter 2 Seasonal Tropospheric Distribution and Air-sea Fluxes of Atmospheric Potential Oxygen from Global Airborne Observations 65

Abstract 65
Plain Language Summary 65
2.1 Introduction 66
2.2 Materials and Methods 68
2.2.1 Definition of APO and air-sea APO fluxes 68
2.2.2 Airborne campaigns and airborne APO measurements 69
2.2.3 Filtering and detrending of APO airborne observations 73
2.2.4 Air-sea APO flux products 76
2.2.5 Atmospheric simulations 77
2.2.6 Calculation of $M_{\theta e}$ and $M_{\theta e}$-weighted average APO 77
2.3 Seasonal atmospheric APO distributions 79
2.4 Seasonal cycles of tropospheric APO inventories 83
2.4.1 Method 83
2.4.2 Results and discussion of APO inventories 85
2.5 Seasonal cycles of hemispheric air-sea APO fluxes 88
2.5.1 Method 88
2.5.2 Results and discussion of air-sea APO fluxes 91
2.6 Comparisons to other APO flux estimates 96
2.6.1 Comparison to GKT 96
2.6.2 Comparison to Jena APO inversion 97
2.6.3 Comparison to CESM 97
2.7 Summary and outlook 98
2.8 Appendix A: Box model 100
2.9 Data Availability Statement 102
2.10 Supplement 103
2.10.1 Possible Sampling Biases in APO Inventories 103
2.10.2 Uncertainties in the seasonal cycle of troposphere APO inventory 104
2.10.3 Uncertainties in the seasonal cycle of air-sea APO flux 106
S4 Deriving annual ocean uptake of anthropogenic CO_2 from annual ocean APO uptake 108
2.11 Acknowledgments 118
Reference 119

Chapter 3 Improved Atmospheric Constraints on Southern Ocean CO_2 Exchange 134

Abstract 134

Significance Statement 134
3.1 Introduction 135
3.2 Results and Discussions 137
3.2.1 Box-model Architecture and Evaluation 137
3.2.2 Diabatic Mixing Rate Evaluation 141
3.2.3 Airborne-based air-sea CO_2 fluxes 143
3.3 Overview and outlook 149
3.4 Materials and methods 150
3.4.1 Airborne campaigns and airborne CO2 observations 150
3.4.2 Mass-indexed moist isentropic coordinate ($M_{\theta e}$) 151
3.4.3 Box model architecture and diabatic mixing rates 151
3.4.4 Validation of box-model approach 155
3.4.5 Airborne estimates of air-sea CO_2 fluxes 156
3.5 Acknowledgement 158
3.6 Reference 159
3.7 Supporting Information Appendix 169
3.7.1: Bias due to sparse airborne spatial coverage 169
3.7.2: Uncertainty 170
3.7.2.1: Uncertainty of AO2 CO_2 measurement 171
3.7.3 Thermal-driven CO_2 flux cycle 174
3.7.4: Airborne campaigns 175
3.7.5: Calculation of $M_{\theta e}$ for each airborne observation 176
3.7.6: Atmospheric CO_2 inversion products, empirical surface ocean pCO_2 products, global biogeochemistry models, and prior airborne estimate 177
3.7.7: Discussion of diabatic mixing rates 179
3.7.8 Reference of Supporting Information 197

Chapter 4 Impact of Changing Winds on the Mauna Loa CO_2 Seasonal Cycle in Relation to the Pacific Decadal Oscillation 203

Abstract 203
Plain Language Summary 203
4.1 Introduction 204
4.2 Data and Methods 207
4.2.1 CO_2 observation and its seasonal cycle amplitude 207
4.2.2 Modeled MLO CO_2 seasonal cycle 208
4.2.3 Climate data 209
4.2.4 Backward trajectories 210
4.3 Results 210
4.3.1 Observed and modeled seasonal cycle amplitude at MLO 210

4.3.2 Correlation between MLO CO_2 seasonal cycle amplitude and climate indices 213
4.3.3 Correlation between components of amplitude variability and PDSI or PDO 216
4.3.4 Large-scale wind-patterns associated with PDO variability 217
4.4 Discussion 220
4.4.1 The impact of varying winds on the SCA trend 220
4.4.2 The impact of varying winds on the variability of MLO SCA 224
4.5 Summary and conclusion 226
4.6 Data Availability Statement 227
4.7 Supplement 228
4.7.1 Empirical orthogonal function (EOF) analysis of winds 228
4.7.2 Vector projection method 229
4.7.3 North edge of the Hadley cell 230
4.8 Acknowledgments 235
Reference 236
Chapter 5 Concluding Remark 248

LIST OF FIGURES

Figure 1.1: Schematic of the conceptual basis to calculate $M_{\theta e}$. 15

Figure 1.2: Snapshot of the distribution of (a) zonal average θ_e surfaces on 1 January 2009 (solid lines) and 1 July 2009 (dashed lines), (b) zonal average $M_{\theta e}$ surfaces on 1 January 2009 (solid lines) and 1 July 2009 (dashed lines). 16

Figure 1.3: $M_{\theta e}$ surfaces as Jan-2009 average (solid lines) and July-2009 average (dashed lines) for (a) 180°E (mostly over the Pacific Ocean), and (b) 100°E (mostly over the Eurasia land in the Northern Hemisphere).. 18

Figure 1.4: Time series of meridional displacement of selected zonal average θ_e (K) surfaces over a year at (a) 500 mbar, (b) 700 mbar and (c) 925 mbar. Meridional displacement of selected zonal average $M_{\theta e}$ (10^{16} kg) surfaces over a year at (d) 500 mbar, (e) 700 mbar and (f) 925 mbar.. 19

Figure 1.5: Snapshots (1 January 2009 and 1 July 2009) of the mass distribution of different $M_{\theta e}$ bins from three pressure bins (surface to 800 mbar, 800 mbar to 500 mbar, and 500 mbar to tropopause)..... 20

Figure 1.6: Variability of $M_{\theta e}$ of given θ_e surfaces (i.e., θ_e-$M_{\theta e}$ look-up table) over a year with daily resolution in the Northern and Southern Hemisphere..... 22

Figure 1.7: (a) Temporal variation of $M_{\theta e}$ in the Northern Hemisphere at θ_e = 300 K computed by integrating air mass (blue line) and estimated from the sum of five heating terms (Table 1.1) in MERRA-2 (black line). (b) The heating variables decomposed into five contributions as indicated (see Table 1.1). 26

Figure 1.8: (a) HIPPO and ATom horizontal flight tracks coloured by campaigns. (b) Latitude and pressure cross-section of detrended CO_2 of each airborne campaign transect..... 29

Figure 1.9: Seasonal cycles of airborne Northern Hemisphere CO_2 data sorted by (a) $M_{\theta e}$-pressure bins and (b) latitude-pressure bins. $M_{\theta e}$ bins (10^{16} kg) and latitude bins are shown on the top of each panel. 30

Figure 1.10: CO_2 seasonal cycles of multiple surface stations (2009-2018) compared to seasonal cycles of airborne observations averaged over corresponding $M_{\theta e}$ bin. 33

Figure 1.11: (a) Detrended CO_2 measurements from HIPPO-1 Southbound (from 12 January 2009 to 17 January 2009) plotted as a function of $M_{\theta e}$ in the Northern Hemisphere. (b) Integral of the data in (a), rescaled from ppm to Pg, integrating from $M_{\theta e}$ = 0 to a given $M_{\theta e}$ value. 35

Figure 1.12: Comparison between the CO_2 seasonal cycle of Northern Hemisphere tropospheric average computed from airborne observation and the $M_{\theta e}$ integration method (black points and line) and the mean cycle at MLO measured by Scripps CO_2 Program from 2009 to 2018 (red line). 36

Figure 1.13: Comparison between the Northern Hemisphere average CO_2 from full integration of the simulated atmospheric fields from the Jena CO_2 Inversion (cutoff at PVU = 2) and from two methods that use the same simulated data subsampled with HIPPO/ATom coverage: (1) the $M_{\theta e}$ integration method (blue) and (2) simple integration by sin(latitude)-pressure (red). 40

Figure 1.14: Illustration of terms defined in Table A1. Shaded area denotes the region R(θ, t) with θ' lower than θ, which is the area of mass integration to yield M_θ. 48

Figure 1.15: (a) Temporal variation of $M_{\theta e}$ in the Northern Hemisphere at θ_e = 300 K computed by integrating air mass (blue line) and estimated from the sum of five heating terms (Table 1.1) in MERRA-2 (black line). (b) The heating variables decomposed into five contributions as indicated (see Table 1). 52

Figure 1.16: Similar to Figure 1.15, but for the year 2011. 53

Figure 1.17: Similar to Figure 1.15, but for the year 2009. 54

Figure 1.18: Similar to Figure 1.17, but on the 310 K θ_e surface. 55

Figure 2.1: (a) HIPPO and ATom flight tracks colored by campaigns. (b) Latitude and pressure cross-sections of ΔAPO for each airborne campaign transect.. 75

Figure 2.2: (a) Seasonal cycles of detrended airborne APO (ΔAPO). (b) Schematic of the contours of zonal and annual average Mθe in the Latitude-Pressure coordinate. (c) Seasonal amplitude (shading) and phase (upward zero-crossing Julian date) of the fitted APO seasonal cycles in Figure 2.2a. 82

Figure 2.3: Seasonal anomaly of tropospheric APO inventory (Tmol) or concentration (per meg) in the Northern (a) and Southern (b) Hemisphere. 87

Figure 2.4: (a) Climatological monthly seasonal APO exchange time scale (τ) between the Northern and the Southern troposphere. (b) and (c) Troposphere-stratosphere APO exchange rate (Tmol day^{-1}) in the Northern Hemisphere (STE_N) and Southern Hemisphere (STE_S), respectively. 94

Figure 2.5: Seasonality of area-integrated daily air-sea APO fluxes in the Northern (a) and Southern (b) Hemisphere. We show our estimate of the flux cycle as black curves. 95

Figure 2.6: Schematic of the box model. 100

Figure 2.7: Difference between airborne observation of Ar/N2-corrected APO (ΔAPO) and ΔAPO*, computed as ΔAPO-ΔAPO*. 109

Figure 2.8: APO inventory seasonal cycle (annual mean subtracted) of selected M_θ bins..... 109

Figure 2.9: Seasonal cycles of airborne Northern Hemisphere APO data sorted by (a) $M_{\theta e}$-pressure bins and (b) latitude-pressure bins. $M_{\theta e}$ bins (10^{16} kg) and latitude bins are shown on the top of each panel. 110

Figure 2.10: Quantification of biases in estimates of hemispheric average troposphere seasonal APO anomaly due to the limited temporal and spatial coverage of HIPPO and ATom airborne campaigns, and the $M_{\theta e}$ integration method, based on simulated atmospheric data using fluxes from the Jena APO inversion and TM3 in (a) and (b), or based on ACTM in (c) and (d). 111

Figure 2.11: Comparison between simulated air-sea APO fluxes (from Jena inversion) and box model reconstructed flux. This reconstruction follows Eq. 2.21-25, with the knowledge of model tropospheric APO inventory and parameter $\tau(t)$ and STE computed from TM3 model in (a) and from ACTM model in (b). 112

Figure 2.12: Seasonal cycles of air-sea APO fluxes ($FAPO(ocn)$, same as the black line in Figure 2.5a and b), with additional components that sum to yield $FAPO(ocn)$, as detailed in Eqs. 2.15, 2.16, and 2.19. 113

Figure 2.13: Comparing simulated air-sea APO fluxes from the hemispheric scale (Equator to 90°, solid line) and equatorial region (Equator to 20°, dashed line) in each hemisphere. 114

Figure 3.1: (a) Schematic of the box model. Boundaries of the box model are selected $M_{\theta e}$ surfaces at 15, 30, 45, and 60 $M_{\theta e}$ values (10^{16} kg), which are shown as zonal and 2009-2018 averages. (b) Selected near-surface $M_{\theta e}$ contours as 2009-2018 averages. 139

Figure 3.2: Diabatic mixing rates of the 30 (10^{16} kg) $M_{\theta e}$ surface. 140

Figure 3.3: (a) Monthly reconstructed air-sea CO_2 fluxes (solid gray) for the 0-30 (10^{16} kg) $M_{\theta e}$ band (south of ~ 43°S near the Earth surface) based on CarbonTracker 2019b. (b) Similar to (a), but showing the flux and other components as climatological monthly averages (2009 to 2018).. 141

Figure 3.4: Exploring the correlation between Jan. and Feb. ATM-based mixing rates at each $M_{\theta e}$ surface and simulated atmospheric CO_2 gradients across the corresponding $M_{\theta e}$ surface of four transport models (3-D CO_2 inversion products).. 142

Figure 3.5: (a)-(d) Seasonal cycle of air-sea CO_2 fluxes. In (e)-(h), we compare our estimates with four 3-D CO_2 inversion products, and two neural network interpolated surface ocean pCO_2 products. In (i)-(l), we compare our estimates with thermally-driven air-sea CO_2 flux cycles.. 144

Figure 3.6: HIPPO, ORCAS and ATom horizonal flight tracks, colored by campaigns or sub-campaigns.. 180

Figure 3.7: Similar to Fig. 3.1b, but showing $M_{\theta e}$ surface contours for each season (by color, averaged from 2009 to 2018 based on MERRA-2 reanalysis) of three $M_{\theta e}$ surfaces (10^{16} kg). 181

Figure 3.8: Diabatic mixing rates of the (a) 15 (10^{16} kg), (b) 30 (10^{16} kg), and (c) 45 (10^{16} kg) $M_{\theta e}$ surface. 181

Figure 3.9: (a) – (d) Monthly reconstructed air-sea CO_2 fluxes (solid black) of the 0-15 (10^{16} kg) $M_{\theta e}$ band (~ south of 51°S near the Earth surface, detailed in Fig. 3.1b and SI Appendix, Fig.

3.6). (e) – (h) Similar to (a) – (d), but showing the flux and each component as a climatological monthly average (2009 to 2018). 182

Figure 3.10: Similar to Figure 3.7, but showing reconstruction of surface CO_2 flux for the $M_{\theta e}$ band of 15 to 30 (10^{16} kg). 183

Figure 3.11: Similar to Figure 3.7, but showing reconstruction of surface CO_2 flux for the $M_{\theta e}$ band of 30 to 45 (10^{16} kg). 184

Figure 3.12: Similar to Fig. 3.4a-c but exploring the correlation between April to November averaged ATM-based mixing rates for three $M_{\theta e}$ surfaces and simulated atmospheric CO_2 gradients across the corresponding $M_{\theta e}$ surfaces of four transport models (inversion products). 185

Figure 3.13: Seasonal cycles (2009 to 2018 average) of biosphere and anthropogenic CO_2 fluxes estimated by the atmospheric inversion products for three approximate latitude bands (calculated based on surface $M_{\theta e}$ range). 186

Figure 3.14: Similar to Fig. 3.5e-h, but comparing our airborne-based estimates (black) with ocean biogeochemistry models that are used in Global Carbon Project 2020 (20, 21). 186

Figure 3.15: Similar to Fig. 3.5a–d but showing the fitted flux cycles calculated using the mean of four ATM-based mixing rates and 2 MSE-based mixing rates. 187

Figure 3.16: Similar to Fig. 3.5a–d but showing the fitted flux cycles calculated using each set of diabatic mixing rate (i.e., 4 ATM-based and 2 MST-based). 187

Figure 3.17: Identifying bias in our estimates of CO_2 concentration for each $M_{\theta e}$ box due to limited spatial coverage of the airborne CO_2 measurements. 188

Figure 3.18: Histogram of CO_2 differences, averaged over each flight, between the AO2 instrument and other instruments (for method see *SI Appendix,* Text 3.7.2.1). 189

Figure 3.19: Identifying bias in CO_2 flux estimates for each $M_{\theta e}$ box and each airborne campaign or sub-campaign due to limited temporal coverage (interannual variability), based on estimated flux from MIROC-ACTM. 190

Figure 3.20: Detrended airborne CO_2 observations (ΔCO_2) expressed on the $M_{\theta e}$ coordinate. . 191

Figure 4.1: (a) Observed MLO SCA and modeled MLO SCA from Jena-WF. The Jena-WF simulation is scaled down by 5% since it systematically overestimates the SCA. (b) Anomalies (reference year 1959) of MLO SCA components simulated by Jena-W and Jena F. Each simulation is scaled down by 5%. 212

Figure 4.2: Correlations between MLO SCA (observation), and various climate indices: annual average PDO, annual average U-PDO, annual growing season (May to October) average land temperature, and Palmer Drought Severity Index (PDSI) over the Eastern Eurasia ($LandT_{EU}$, $PDSI_{EU}$) and Northern America ($LandT_{NA}$, $PDSI_{NA}$).. 215

Figure 4.3: Correlations between (a) annual average PDO or (b) between $PDSI_{NA}$ and various decompositions of the MLO SCA variations: modeled MLO SCA from ACTM-W, Jena-W, and Jena-F. 217

Figure 4.4: (a) Spatial pattern of the first EOF of 700 mbar monthly average wind (NCEP/NCAR) from 1959 to 2020 within the domain of 10°N to 40°N and 120°E to 100°W. (b) Temporal pattern of U (solid blue, U-PDO) and V (dashed blue) winds of the first EOF, and PDO (solid black). 219

Figure 4.5: Seasonally-varying fraction of MLO 10-day back-trajectories that originate from Eurasia (red) versus North America (blue), sorted by PDO range. 219

Figure 4.6: (a) Example of a map of climate variables for a positive PDO year (1997). (b) Example of a map of climate variables for a negative PDO year (2008). 220

Figure 4.7: Similar to Figure 4.3 but exploring the correlations between annual average U-PDO and various decompositions of the MLO SCA variations: modeled MLO SCA from ACTM-W, Jena-W, and Jena-F. 231

Figure 4.8: HYSPLIT back trajectories of different seasons and PDO phases. (a) DJF of positive PDO years (PDO index $\geqslant$ 1), (b) DJF of positive PDO years (PDO index $\leqslant$ -1), (c) JJA positive PDO years (PDO index $\geqslant$ 1), and (d) JJA of positive PDO years (PDO index $\leqslant$ -1)..... 232

Figure 4.9: Simulated MLO CO_2 seasonal amplitude using fluxes from each tagged region (map in (a)) of Jena CarboScope CO_2 Inversion (version ID: s57Xoc_v2020) transported by TM3 model. We show simulations driven by both varying winds and fluxes in (b) and simulations driven by either varying winds or varying fluxes in (c)..... 233

Figure 4.10: Correlation between annual average PDO and land temperature (detrended) within the time slice from (a) 1960 to 1979, (b) 1980 to 1999, and (c) 2000 to 2019. Correlation between annual average PDO and PDSI (detrended) within the time slice from (d) 1960 to 1979, (e) 1980 to 1999, and (f) 2000 to 2019. 234

Figure 4.11: Anomaly of the annual average latitude of the Hadley cell north edge from 1959 to 2019 computed based on NCEP reanalysis. 234

Figure 4.12: Similar to Figure 4.3 but exploring the correlations between observed MLO SCA and annual average ENSO index. 235

LIST OF TABLES

Table 1.1: Correspondence of heating variables between our derivation (Eq. 1.9) and MERRA-2. 24

Table 1.2: Fractional contribution of the individual heating terms in Figure 1.7b to their sum for θ_e = 300K.. 27

Table 1.3: RMSE, seasonal amplitude and day of year of the downward zero-crossing of each simulation based on the Jena CO_2 Inversion..... 38

Table 1.4: Definition of variables. 47

Table 1.5: Number of data points of each airborne campaign transect for each simulation..... 56

Table 2.1: Statistics of the seasonal cycle of tropospheric APO inventory (Figure 2.3) from two-harmonic fits (annual mean removed) for each hemisphere computed from airborne observations with correction for sparse spatial and temporal coverage..... 87

Table 2.2: Statistical indices of the seasonal cycle of air-sea APO fluxes from two-harmonic fits for each hemisphere computed from airborne observations, Jena inversion, GKT, and CESM.. 96

Table 2.3: Summary of longitude, latitude, and time range of each airborne campaign transect. Each airborne campaign transect is consisted of campaign name, leg name, and correspondent hemisphere. 115

Table 2.4: A list of stations used in the Jena APO Inversion s99XS_v2022..... 116

Table 2.5: A list of stations used in calculating global mean APO time series (based on the latitudinal weights from Hamme & Keeling, 2008). 116

Table 2.6: Airborne observation of APO inventory seasonal anomalies in the Northern Hemisphere, including overall uncertainty of each estimate. 117

Table 2.7: Similar to Table 2.6, but showing the seasonal anomalies of APO inventory in the Southern Hemisphere..... 118

Table 3.1: RMSE (PgC yr^{-1}) of reconstructed monthly surface CO_2 fluxes compared to the original fluxes. 191

Table 3.2: Summary of research flight number latitude coverage, and duration of each airborne mission in the Southern Hemisphere. 192

Table 3.3: Atmospheric inversion products. 192

Table 3.4: Airborne-based air-sea CO_2 fluxes estimated for each campaign and $M_{\theta e}$ band..... 193

Table 3.5: Atmospheric CO_2 gradients across $M_{\theta e}$ bands observed by each airborne campaign. 194

Table 3.6: Bias of averaged CO_2 concentration due to limited spatial coverage (detailed in *SI Appendix,* Text 3.7.1).. 195

Table 3.7: $AR10-\sec$ coefficient (unitless) and 1σ uncertainty (ppm) of random error $\epsilon(t)$ estimated from the autoregressive model for each pair of in situ instruments (detailed in SI Appendix, Text 3.7.2.1). 196

Table 3.8: 1σ Interannual variability (IAV, PgC yr^{-1}) of air-sea CO_2 flux for each $M_{\theta e}$ band and each airborne campaign or sub-campaign, as suggested by the MIROC-ACTM model..... 197

Table 4.1: Observed and simulated (Jena-WF, Jena-W, and ACTM-W) long-term SCA trends in ppm $decade^{-1}$ at selected stations (methods see Section 4.2.1).. 213

ACKNOWLEDEMENT

The sands of time slip through my fingers all too quickly.

I have immensely enjoyed the past five years at Scripps, and I extend my heartfelt gratitude to everyone who has offered their support throughout my Ph.D. journey. Dr. Ralph Keeling has been an exceptional advisor, consistently offering invaluable guidance and support while also granting me the freedom to pursue my own interests. I have greatly benefited from even brief conversations with Ralph, during which a wealth of ideas often emerges spontaneously. I owe a sincere thank you to Dr. Eric Morgan for his patient mentorship when I first arrived at Scripps, as well as for the generous sharing of his profound insights along my Ph.D. journey. Dr. Britton Stephens, a senior scientist at NCAR, has served as my mentor in all but name. Britt has consistently provided effective mentorship, unwavering support, and has generously shared his extensive knowledge in both carbon cycle science and tracer measurements.

My Ph.D. research builds upon the integration of atmospheric CO_2 and O_2 measurements, coupled with various models. I wish to extend my gratitude to all scientists and engineers from the Scripps CO_2 and O_2 program, who contributed to these pivotal measurements. I also deeply appreciate the collective efforts of the entire HIPPO, ORCAS, and ATom airborne campaign science teams, including the dedicated pilots and crew of the NSF/NCAR GV and NASA DC-8. My thanks also go to the NCAR and NASA project managers, field support staff, and logistics experts who made these campaigns possible. Special thanks to Dr. Prabir Patra, Dr. Christian Rödenbeck, and Dr. Matthew Long for their invaluable contributions to insightful discussions on the modeling aspects of my research.

I would also like to express my profound gratitude to my thesis committee members, both present and former members of the Keeling lab, as well as my collaborators and co-authors, for

their invaluable guidance in shaping my career as a scientist. And most importantly, my deepest and most heartfelt gratitude goes to my parents, who have provided me with their selfless love and steadfast encouragement, serving as my unwavering foundation throughout my life.

Chapter 1, in full, is a reprint of the material as it appears in Jin, Y., Keeling, R. F., Morgan, E. J., Ray, E., Parazoo, N. C., & Stephens, B. B, 2021. A mass-weighted isentropic coordinate for mapping chemical tracers and computing atmospheric inventories. Atmospheric Chemistry and Physics, 21(1), 217-238. https://doi.org/10.5194/acp-21-217-2021. The dissertation author was the primary investigator and author of this paper.

Chapter 2, in full, is a reprint of the material as it appears in Jin. Y., Stephens, B. B, Keeling, R. F., Morgan, E. J., Rödenbeck, C., Patra, P., Long, M. C.: Seasonal Tropospheric Distribution and Air-sea Fluxes of Atmospheric Potential Oxygen from Global Airborne Observations, Global Biogeochemical Cycles, 37, e2023GB007827. https://doi.org/10.1029/2023GB007827. The dissertation author was the primary investigator and author of this paper.

Chapter 3, in full, has been submitted for publication of the material as it may appear in Jin, Y., Keeling, R. F., Long, M. C., Stephens, B. B., Patra, P., Rödenbeck, C., Morgan, E. J.: Improved Atmospheric Constraint of the Southern Ocean CO_2 Exchange, PNAS. The dissertation author was the primary investigator and author of this paper.

Chapter 4, in full, is a reprint of the material as it appears in Jin, Y., Keeling, R. F., Rödenbeck, C., Patra, P. K., Piper, S. C., & Schwartzman, A., 2022. Impact of changing winds on the Mauna Loa CO2 seasonal cycle in relation to the Pacific decadal oscillation. *Journal of Geophysical Research: Atmospheres*, *127*(13), e2021JD035892. https://doi.org/10.1029/2021JD035892. The dissertation author was the primary investigator and author of this paper.

VITA

2018 Bachelor of Science in Environmental Sciences, Donghua University, China

2023 Doctor of Philosophy in Earth Sciences, University of California San Diego, USA

ABSTRACT OF THE DISSERTATION

Advances in Representing Atmospheric Circulation and Structure for Carbon Cycle Studies

by

Yuming Jin

Doctor of Philosophy in Earth Sciences

University of California San Diego, 2023

Professor Ralph F. Keeling, Chair

This thesis advances the understanding of the global carbon cycle and atmospheric tracer transport by optimizing the use of CO_2 and O_2 measurements from global airborne campaigns and surface stations. The first three chapters provide toolboxes that leverage the use of airborne data in many aspects. Chapter 1 introduces a novel transformed isentropic coordinate system, $M_{\theta e}$, initially designed to organize airborne data, correct for meteorological variability, and calculate atmospheric inventories of trace gases. This system is versatile and has enabled the development of several toolboxes and models to assess large-scale atmospheric tracer transport and surface

tracer flux rates. In Chapter 2, I present the first comprehensive application of $M_{\theta e}$ coordinate, focusing on estimating atmospheric potential oxygen (APO ~ O_2 + 1.1 CO_2) and its seasonal air-sea fluxes, contributing valuable insights into oceanic carbon cycles, and benchmarking existing observation-based and modeled APO flux estimations. In chapter 3, I tackle the challenge of uncertainties in atmospheric transport models (ATMs), by developing two evaluative constraints based on atmospheric CO_2 gradients across $M_{\theta e}$ and parameterized diabatic mixing rates (tracer transport timescales across $M_{\theta e}$). These constraints lead to a more intuitive evaluation of ATMs, and more accurate descriptions of large-scale tracer transport, particularly over the extratropical Southern Ocean (SO). I also applied the diabatic mixing rates derived from reanalyses to improve seasonal air-sea CO_2 flux estimations across different latitudes over the SO. In Chapter 4, I explore the role of large-scale CO_2 transport in interpreting long-term CO_2 variability at low-latitude stations like Mauna Loa (MLO). It identifies circulation changes as key contributors to variations in CO_2 seasonal cycle amplitude at MLO and establishes correlations with climate modes like the Pacific Decadal Oscillation. The implications are significant for ecosystem studies, suggesting that using observed CO_2 at low-latitude to constrain large-scale ecosystem changes requires a correct representation of large-scale CO_2 transport.

Collectively, this thesis represents a multifaceted approach to promote our understanding of the global carbon cycle and atmospheric tracer transport, by leveraging new data types and developing novel analytical tools. The findings support technical advancement in atmospheric science and have broad implications for carbon-climate feedback, climate variability, and global biogeochemical cycles.

INTRODUCTION

Long-term observations of atmospheric CO_2 and O_2 are critical for assessing the exchange rates of these trace gases across multiple reservoirs, such as ecosystems, oceans, and the atmosphere. These exchange rates are crucial indicators for understanding carbon-climate feedback, changes in global climate and biogeochemistry under internal natural variability and externally forced variability (e.g., human activities). At surface stations (e.g., Mauna Loa, MLO), both CO_2 and O_2 observations reveal several essential patterns:

1. Long-term Trends: The increasing atmospheric CO_2 and decreasing O_2 are primarily attributed to anthropogenic factors, most notably the burning of fossil fuels. The increase in CO_2 is partly offset (~45%) by the uptake from the land biosphere and ocean, while the decrease in O_2 is partly offset (~15%) by the net O_2 release from the land biosphere due to photosynthesis, and from the ocean due to ocean heat flux.

2. Seasonal Cycles: Both CO_2 and O_2 show seasonal variations that are closely related to land ecosystem photosynthesis and respiration, and the interaction of ocean thermal, biological, and ventilation changes. At the mid- to high-latitude stations in the Northern Hemisphere, the amplitude of the CO_2 seasonal cycle (SCA) has increased since the 1960s, which indicates enhanced growing season ecosystem productivity, probably due to rising CO_2 (i.e., CO_2 fertilization effect) and land temperature (Graven et al., 2013; Keeling et al., 1996).

3. Interannual to Decadal Variability: The fluctuations of annual mean CO_2 and O_2 at surface stations are influenced by a variety of factors, including natural climate variability (e.g., ENSO, PDO, etc.) and volcanic eruptions. These natural events contribute to variability in global temperature, precipitation, and ocean and atmospheric circulation, which effectively alter the

corresponding surface fluxes from the land ecosystem and ocean, and the large-scale transport of tracer gas to the station.

Using atmospheric observations at stations to quantify the exchange rates and understand the global carbon cycle requires the correct representation of atmospheric tracer transport, which is conventionally achieved by atmospheric transport models (ATMs). This approach, which is referred to as atmospheric inversions (e.g., Rödenbeck et al., 2018), requires accurate simulation of advection, convection, and boundary height parameterizations in ATMs (Schuh et al., 2019). The approach also requires filtering observations to avoid signals related to local emissions and meteorology conditions which may not be resolved in the ATM.

Over the past decade, global airborne campaigns (e.g., HIPPO and ATom) have provided CO_2 and O_2 observations with substantial spatial coverage from pole to pole, from surface to above tropopause, and with seasonal coverage (Prather et al., 2018; Wofsy, 2017). These airborne data, on the one hand, provide additional information on the global carbon cycle from the free troposphere that is not sensitive to local conditions (e.g., Graven et al., 2013). On the other hand, the spatial gradients of airborne observations also provide constraints on simulated tracer transport in the troposphere (e.g., Stephens et al., 2007).

In this thesis, I develop a series of tools for making the best use of airborne data, which includes a transformed coordinate system, and includes box models based on the coordinate to invert airborne data. I explore several aspects of using airborne CO_2 and O_2 data to promote our understanding of the global carbon cycle and large-scale atmospheric tracer transport.

Airborne data have been used to study the spatial and temporal distribution of CO_2 and O_2, for example, the regular seasonal cycles and gradients with pressure and latitudes (Conway & Tans, 1999; Ehhalt, 1978; Ishidoya et al., 2022; Randerson et al., 1997; Rasmussen & Khalil, 1981;

Tohjima et al., 2012). However, patterns inferred from individual airborne campaigns are potentially distorted by synoptic weather disturbances, especially at middle to high latitudes (Parazoo et al., 2008; Wang et al., 2007). One approach to correcting synoptic distortion is to use transformed coordinates that consider atmospheric dynamics and transport barriers. For example, the isentropic coordinate (θ) has been widely applied to evaluate the distribution of CO_2 in the troposphere (Miyazaki et al., 2008; Parazoo et al., 2011, 2012) taking advantage of two characteristics: (1) θ and the tracer tend to be similarly displaced while air parcels moving with synoptic disturbances (Keppel-Aleks et al., 2011); (2) vertical mixing tends to be rapid on θ surfaces, so θ and tracer contours are often nearly parallel (Barnes et al., 2016). However, θ varies greatly with latitude and altitude over seasons due to changes in heating and cooling with solar insolation, which complicates the interpretation of θ–tracer relationships on seasonal timescales.

Chapter 1 introduces a transformed isentropic coordinate $M_{\theta e}$, which is defined as the dry air mass under a given equivalent potential temperature surface (θ_e) within a hemisphere. The $M_{\theta e}$ coordinate is similar to θ_e on the synoptic scale, but has a more stable relationship to latitude and altitude over seasons (i.e., small seasonal displacement). The $M_{\theta e}$ coordinate was originally conceived as a means to organize airborne data while correcting for variability due to meteorology conditions, and to calculate the atmospheric inventory of trace gases, taking advantage of the coordinate having airmass as the unit. These early applications are presented in Chapters 1 and 2. Chapter 1 also explore fundamental meteorological questions of what processes control the temporal variation in the θ_e-$M_{\theta e}$ relation. During this work, it become evident that the $M_{\theta e}$ coordinate had further applications, including deriving atmospheric diabatic mixing rates (i.e., mixing across isentropes), which are crucial metrics to validate ATMs, and building $M_{\theta e}$-aligned

box models to derive surface tracer flux rate from airborne observations. These two applications are described in Chapter 3.

Chapter 2 explores the application of the $M_{\theta e}$ coordinate to study the troposphere atmospheric potential oxygen (APO ~ O_2 + CO_2) and the seasonal air-sea fluxes on the hemispheric scale. APO is a tracer for air-sea O_2 flux with little sensitivity to the terrestrial exchange of O_2 and CO_2. Precise quantification of seasonal air-sea APO flux cycles helps us to better understand the upper-ocean biological activities, thermally-induced solubility changes, and ocean ventilation, which effectively add complementary information about the ocean carbon cycle. Observation-based APO flux estimates are available using surface station data from the Scripps O_2 program network, and Japanese station and shipboard measurements over the Western Pacific through an inversion approach (Rödenbeck et al., 2008). Flux estimates are also available using surface ocean dissolved O_2 measurements that are interpolated by weighing ocean heat flux anomalies (Garcia & Keeling, 2001). Chapter 2 presents the first estimates of the hemispheric scale seasonal flux using free troposphere airborne data of HIPPO and ATom campaigns. The seasonal APO flux estimates identify clear hemispheric asymmetries, pointing to different physical and biological processes that drive the surface ocean dissolved oxygen changes between two hemispheres, including the formation of subsurface oxygen maximum zone in the Northern Hemisphere, faster oxygen equilibration time in the north, etc. The airborne-based flux estimates benchmark modeled O_2 outgassing products, highlighting the limitations in the atmospheric inversion approach arising from not enough spatial coverage of surface stations and biases in large-scale atmospheric transport simulated by ATMs.

Chapter 3 extends the applications of the $M_{\theta e}$ coordinate in two novel contexts: estimating seasonal air-sea CO_2 flux over three coarse latitudinal bands in the Southern Ocean (SO), and

constraining atmospheric tracer transport over the extratropical SO using airborne CO_2 data from the HIPPO, ORCAS, and ATom campaigns. This research builds on earlier work of Long et al. (2021), who employed the same airborne data sets to estimate the seasonal cycle of SO CO_2 flux in one band (90°S to 45°S) by relying on atmospheric CO_2 gradients across potential temperature (θ) as emergent constraints on the underlying air-sea flux. Long et al. derive the flux-gradient relation using flux from multiple CO_2 inversion products or observation-based products, and gradients from ATMs which forward transport corresponding flux.

Chapter 3 improves upon Long et al. in several respects. I conduct a systematic analysis of uncertainty in ATMs, arguing that the simulated gradient-flux relationship could be skewed by the specific choice of ATM, given that this flux-gradient relation varies across different models. I discovered that, in ATMs, the timescale of CO_2 transport across $M_{\theta e}$ (or θ_e) serves as the pivotal factor influencing large-scale CO_2 redistribution. This insight led me to formulate two evaluative constraints for ATMs. One constraint is based on observed and simulated atmospheric CO_2 gradients across $M_{\theta e}$ surfaces. The other constraint is based on parameterized diabatic mixing rates (mixing rates across $M_{\theta e}$) derived from ATMs, and from moist static energy (MSE) budgets of reanalyses. These two types of mixing rates are derived from a $M_{\theta e}$-aligned box model. Two constraints converge in showing that ATMs overestimate the diabatic mixing rates over the mid- to high-latitudes of the SO, and suggest that the mixing rates derived from reanalyses are more realistic. The $M_{\theta e}$-aligned box model could further be applied to derive seasonal SO CO_2 flux over three latitude bands rather than one band in Long et al. (2021), while CO_2 exchange between boxes is constrained by mixing rates derived from reanalyses. My flux estimate scales down the summer-time CO_2 uptake over the high-latitudes SO as in Long et al. (2021). The derived flux shows clear changes in the seasonal cycles over latitudes, suggesting a clear meridional change in biological

production/mixing processes and temperature-related solubility changes that drive seasonal changes in dissolved inorganic carbon (DIC).

Understanding the large-scale CO_2 transport is also important in interpreting CO_2 variabilities on a station level, for example, at MLO. A prominent feature of long-term CO_2 changes is an increase in the CO_2 seasonal cycle amplitude (SCA), which has a larger relative increase at higher latitudes at both surface stations and along airborne transects (Forkel et al., 2016; Graven et al., 2013). At MLO (19.5°N), a ~15% increase has been observed from 1959 to the early 2010s, while at northern high-latitude station Barrow (BRW, 71.3°N), the increase of the same time period is ~35% (Graven et al., 2013). These long-term amplitude trends are superimposed on considerable interannual to decadal variability (Keeling et al., 1996), which are driven by enhanced growing-season ecosystem productivity over the northern temperate and boreal forest (Graven et al., 2013; Lin et al., 2020), but modulated by variations in atmospheric circulation.

In Chapter 4, I examined the relative contribution of circulation changes to the MLO CO_2 SCA on the decadal scale and over the long term. I find a third of the observed MLO SCA increasing trend is offset by circulation changes. On the decadal scale, I find that the MLO SCA change is highly correlated with PDO-related wind patterns, which effectively modulate the sensitivity of MLO to the ecosystem CO_2 flux from the Eurasia boreal forest. The results highlight the significant role of changing circulation on the variability and SCA trend at MLO as well as other low-latitude stations. The implications of these findings are far-reaching, emphasizing the need for nuanced interpretation when using observed SCA variability and trend to constrain large-scale ecosystem changes, such as the enhanced magnitude of CO_2 fertilization effect (Wenzel et al., 2016) and North America drought (Buermann et al., 2007).

Reference

Barnes, E. A., Parazoo, N., Orbe, C., & Denning, A. S. (2016). Isentropic transport and the seasonal cycle amplitude of CO_2. *Journal of Geophysical Research: Atmospheres*, *121*(13), 8106–8124. https://doi.org/https://doi.org/10.1002/2016JD025109

Buermann, W., Lintner, B. R., Koven, C. D., Angert, A., Pinzon, J. E., Tucker, C. J., & Fung, I. Y. (2007). The changing carbon cycle at Mauna Loa Observatory. *Proceedings of the National Academy of Sciences*, *104*(11), 4249–4254. https://doi.org/https://doi.org/10.1073/pnas.0611224104

Conway, T. J., & Tans, P. P. (1999). Development of the CO_2 latitude gradient in recent decades. *Global Biogeochemical Cycles*, *13*(4), 821–826. https://doi.org/https://doi.org/10.1029/1999GB900045

Ehhalt, D. H. (1978). The CH_4 concentration over the ocean and its possible variation with latitude. *Tellus*, *30*(2), 169–176. https://doi.org/https://doi.org/10.3402/tellusa.v30i2.10329

Forkel, M., Carvalhais, N., Rödenbeck, C., Keeling, R., Heimann, M., Thonicke, K., et al. (2016). Enhanced seasonal CO_2 exchange caused by amplified plant productivity in northern ecosystems. *Science*, *351*(6274), 696–699. https://doi.org/10.1126/science.aac4971

Garcia, E., & Keeling, F. (2001). On the global oxygen anomaly and air-sea flux. *Journal of Geophysical Research*, *106*(C12), 31155–31166. https://doi.org/10.1029/1999JC000200

Graven, H. D., Keeling, R. F., Piper, S. C., Patra, P. K., Stephens, B. B., Wofsy, S. C., et al. (2013). Enhanced seasonal exchange of CO2 by northern ecosystems since 1960. *Science*, *341*(6150), 1085–1089. https://doi.org/https://doi.org/10.1126/science.1239207

Ishidoya, S., Tsuboi, K., Niwa, Y., Matsueda, H., Murayama, S., Ishijima, K., & Saito, K. (2022). Spatiotemporal variations of the $\delta(O_2/N_2)$, CO_2 and δ(APO) in the troposphere over the western North Pacific. *Atmospheric Chemistry and Physics*, *22*(10), 6953–6970. https://doi.org/10.5194/acp-22-6953-2022

Keeling, C. D., Chin, J. F. S., & Whorf, T. P. (1996). Increased activity of northern vegetation inferred from atmospheric CO_2 measurements. *Nature*, *382*, 146–149. https://doi.org/10.1038/382146a0

Keppel-Aleks, G., Wennberg, P. O., & Schneider, T. (2011). Sources of variations in total column carbon dioxide. *Atmospheric Chemistry and Physics*, *11*, 3581–3593. https://doi.org/https://doi.org/10.5194/acp-11-3581-2011

Lin, X., Rogers, B. M., Sweeney, C., Chevallier, F., Arshinov, M., & Dlugokencky, E. (2020). Siberian and temperate ecosystems shape Northern Hemisphere atmospheric CO_2 seasonal amplification. *Proceedings of the National Academy of Sciences*, *117*(35), 21079–21087. https://doi.org/10.1073/pnas.1914135117

Long, M. C., Stephens, B. B., McKain, K., Sweeney, C., Keeling, R. F., Kort, E. A., et al. (2021). Strong Southern Ocean carbon uptake evident in airborne observations. *Science*, *374*(6572), 1275–1280. https://doi.org/10.1126/science.abi4355

Miyazaki, K., Patra, P. K., Takigawa, M., Iwasaki, T., & Nakazawa, T. (2008). Global-scale transport of carbon dioxide in the troposphere. *Journal of Geophysical Research: Atmospheres*, *113*(D15), D15301. https://doi.org/https://doi.org/10.1029/2007JD009557

Parazoo, N. C., Denning, A. S., Kawa, S. R., Corbin, K. D., Lokupitiya, R. S., & Baker, I. T. (2008). Mechanisms for synoptic variations of atmospheric CO_2 in North America, South America and Europe. *Atmospheric Chemistry and Physics*, *8*, 7239–7254. https://doi.org/https://doi.org/10.5194/acp-8-7239-2008

Parazoo, N. C., Denning, A. S., Berry, J. A., Wolf, A., Randall, D. A., Kawa, S. R., et al. (2011). Moist synoptic transport of CO_2 along the mid-latitude storm track. *Geophysical Research Letters*, *38*, L09804. https://doi.org/https://doi.org/10.1029/2011GL047238

Parazoo, N. C., Denning, A. S., Kawa, S. R., Pawson, S., & Lokupitiya, R. (2012). CO_2 flux estimation errors associated with moist atmospheric processes. *Atmospheric Chemistry and Physics*, *12*, 6405–6416. https://doi.org/https://doi.org/10.5194/acp-12-6405-2012

Prather, M. J., Flynn, C. M., Fiore, A., Correa, G., Strode, S. A., Steenrod, S. D., et al. (2018). *ATom: Simulated Data Stream for Modeling ATom-like Measurements*. ORNL Distributed Active Archive Center. https://doi.org/10.3334/ORNLDAAC/1597

Randerson, J. T., Matthew, T. V., Conway, J., Fung, I. Y., & Field, B. (1997). The contribution of terrestrial sources and sinks to trends in the seasonal cycle of atmospheric carbon dioxide. *Global Biogeochemical Cycles*, *11*(4), 535–560. https://doi.org/https://doi.org/10.1029/97GB02268

Rasmussen, R. A., & Khalil, R. A. K. (1981). Atmospheric Methane (CH_4): Trends and Seasonal Cycles. *Journal of Geophysical Research*, *86*(C10), 9826–9832. https://doi.org/https://doi.org/10.1029/JC086iC10p09826

Rödenbeck, C., Le Quéré, C., Heimann, M., & Keeling, R. F. (2008). Interannual variability in oceanic biogeochemical processes inferred by inversion of atmospheric O_2/N_2 and CO_2 data. *Tellus B: Chemical and Physical Meteorology*, *60*(5), 685–705. https://doi.org/10.1111/j.1600-0889.2008.00375.x

Rödenbeck, C., Zaehle, S., Keeling, R., & Heimann, M. (2018). How does the terrestrial carbon exchange respond to interannual climatic variations? A quantification based on atmospheric CO_2 data. *Biogeosciences*, *15*, 2481–2498. https://doi.org/10.5194/bg-2018-34

Schuh, A. E., Jacobson, A. R., Basu, S., Weir, B., Baker, D., Bowman, K., et al. (2019). Quantifying the Impact of Atmospheric Transport Uncertainty on CO_2 Surface Flux Estimates. *Global Biogeochemical Cycles*, *33*(4), 484–500. https://doi.org/10.1029/2018GB006086

Stephens, B. B., Gurney, K. R., Tans, P. P., Sweeney, C., Peters, W., Bruhwiler, L., et al. (2007). Weak Northern and Strong Tropical Land Carbon Uptake from Vertical Profiles of Atmospheric CO_2. *Science*, *316*(5832), 1732–1735. https://doi.org/10.1126/science.1137004

Tohjima, Y., Minejima, C., Mukai, H., MacHida, T., Yamagishi, H., & Nojiri, Y. (2012). Analysis of seasonality and annual mean distribution of atmospheric potential oxygen (APO) in the Pacific region. *Global Biogeochemical Cycles*, *26*, GB4008. https://doi.org/10.1029/2011GB004110

Wang, J. W., Denning, A. S., Lu, L., Baker, I. T., Corbin, K. D., & Davis, K. J. (2007). Observations and simulations of synoptic, regional, and local variations in atmospheric CO2. *Journal of Geophysical Research Atmospheres*, *112*(D4). https://doi.org/https://doi.org/10.1029/2006JD007410

Wenzel, S., Cox, P. M., Eyring, V., & Friedlingstein, P. (2016). Projected land photosynthesis constrained by changes in the seasonal cycle of atmospheric CO_2. *Nature*, *538*, 499–501. https://doi.org/10.1038/nature19772

Wofsy, S. C. HIPPO Merged 10-Second Meteorology, Atmospheric Chemistry, and Aerosol Data. Version 1.0. UCAR/NCAR - Earth Observing Laboratory. https://doi.org/10.3334/CDIAC/HIPPO_010. (2017).

Chapter 1 A mass-weighted isentropic coordinate for mapping chemical tracers and computing atmospheric inventories

Abstract

We introduce a transformed isentropic coordinate $M_{\theta e}$, defined as the dry air mass under a given equivalent potential temperature surface (θ_e) within a hemisphere. Like θ_e, the coordinate $M_{\theta e}$ follows the synoptic distortions of the atmosphere, but unlike θ_e, has a nearly fixed relationship with latitude and altitude over the seasonal cycle. Calculation of $M_{\theta e}$ is straightforward from meteorological fields. Using observations from the recent HIPPO and ATom airborne campaigns, we map the CO_2 seasonal cycle as a function of pressure and $M_{\theta e}$, where $M_{\theta e}$ is thereby effectively used as an alternative to latitude. We show that the CO_2 seasonal cycles are more constant as a function of pressure using $M_{\theta e}$ as the horizontal coordinate compared to latitude. Furthermore, short-term variability of CO_2 relative to the mean seasonal cycle is also smaller when the data are organized by $M_{\theta e}$ and pressure than when organized by latitude and pressure. We also present a method using $M_{\theta e}$ to compute mass-weighted averages of CO_2 on a hemispheric scale. Using this method with the same airborne data and applying corrections for limited coverage, we resolve the average CO_2 seasonal cycle in the Northern Hemisphere (mass weighted tropospheric climatological average for 2009-2018), yielding an amplitude of 7.8 ± 0.14 ppm and a downward zero-crossing at Julian day 173 ± 6.1 (i.e., late June). $M_{\theta e}$ may be similarly useful for mapping the distribution and computing inventories of any long-lived chemical tracer.

1.1 Introduction

The spatial and temporal distribution of long-lived chemical tracers like CO_2, CH_4, and O_2/N_2 typically includes regular seasonal cycles and gradients with latitude and pressure (Conway and Tans, 1999; Ehhalt, 1978; Randerson et al., 1997; Rasmussen and Khalil, 1981; Tohjima et

al., 2012). These patterns are evident in climatological averages but are potentially distorted on short time scales by synoptic weather disturbances, especially at middle to high latitudes (i.e. poleward of 30° N/S) (Parazoo et al., 2008; Wang et al., 2007). With a temporally-dense dataset such as from satellite remote sensing or tower in-situ measurements, climatological averages can be created by averaging over this variability. For temporally sparse datasets such as from airborne campaigns, it may be necessary to correct for synoptic distortion.

A common approach to correct synoptic distortion is to use transformed coordinates rather than geographic coordinates (i.e., pressure-latitude), to take into account atmospheric dynamics and transport barriers. Such coordinate transformation has been used, for example, to reduce dynamically induced variability in the stratosphere using equivalent latitude rather than latitude as horizontal coordinate (Butchart and Remsberg, 1986), to diagnose tropopause profile using tropopause-based rather than surface-based vertical coordinate (Birner et al., 2002), to study transport regime in the Arctic using a horizontal coordinate based on Polar Dome (Bozem et al., 2019), and to study UTLS (Upper Troposphere Lower Stratosphere) tracer data by using tropopause-based, jet-based, and equivalent latitude coordinates (Irina et al., 2019). In the troposphere, a transformed coordinate, isentropic coordinate (θ) has been widely applied to evaluate the distribution of tracer data (Miyazaki et al., 2008; Parazoo et al., 2011, 2012). As air parcels move with synoptic disturbances, θ and the tracer tend to be similarly displaced so that the θ-tracer relationship is relatively conserved (Keppel-Aleks et al., 2011). Furthermore, vertical mixing tends to be rapid on θ surfaces, so θ and tracer contours are often nearly parallel (Barnes et al., 2016). However, θ varies greatly with latitude and altitude over seasons due to changes in heating and cooling with solar insolation, which complicates the interpretation of θ-tracer relationships on seasonal time scales.

During analysis of airborne data from the HIAPER Pole-to-Pole Observations (HIPPO) (Wofsy, 2011) and the Atmospheric Tomography Mission (ATom) (Prather et al., 2018) airborne campaigns, we have found it useful to transform potential temperature into a mass-based unit, M_θ, which we define as the total mass of dry air under a given isentropic surface in the hemisphere. In contrast to θ, which has large seasonal variation, M_θ has a more stable relationship to latitude and altitude, while varying in parallel with θ on synoptic scales. Also, for a tracer which is well-mixed on θ, a plot of this tracer versus M_θ can be directly integrated to yield the atmospheric inventory of the tracer, because M_θ directly corresponds to the mass of air. We note that a similar concept to $M_{\theta e}$ has been introduced in the stratosphere by Linz et al. (2016), in which $M(\theta)$ is defined as the mass above the θ surface, to study the relationship between age of air and diabatic circulation of the stratosphere.

Several choices need to be made in the definition of M_θ, including defining boundary conditions (e.g. in altitude and latitude) for mass integration and whether to use potential temperature θ or equivalent potential temperature θ_e. Here, for boundaries, we use the dynamical tropopause (based on potential vorticity unit, PVU) and the Equator, thus integrating the dry air mass of the troposphere in each hemisphere. We also focus on M_θ defined using equivalent potential temperature (θ_e) to conserve moist static energy in the presence of latent heating during vertical motion, which improves alignment between mass transport and mixing especially within storm tracks in mid-latitudes (Parazoo et al., 2011; Pauluis et al., 2008, 2010). We call this tracer $M_{\theta e}$.

In this paper we describe the method for calculating $M_{\theta e}$ and discuss its variability on synoptic to seasonal scales. We also discuss the time variation of the θ_e-$M_{\theta e}$ relationship within each hemisphere and explore the stability of $M_{\theta e}$ and θ_e-$M_{\theta e}$ relationship using different reanalysis

products. To illustrate the application of $M_{\theta e}$, we map CO_2 data from two recent airborne campaigns (HIPPO and ATom) on $M_{\theta e}$. Further, we show how $M_{\theta e}$ can be used to accurately compute the average CO_2 concentration over the entire troposphere of the Northern Hemisphere using measurements from the same airborne campaigns. We examine the accuracy of this method and propose an appropriate way to sample the atmosphere with aircraft to compute the average of a chemical tracer within a large zonal domain.

1.2 Methods

1.2.1 Meteorological reanalysis products

The calculation of $M_{\theta e}$ requires the distribution of dry air mass and θ_e. For these quantities, we alternately use three reanalysis products: ERA-Interim (Dee et al., 2011), NCEP2 (Kanamitsu et al., 2002), and Modern-Era Retrospective analysis for Research and Applications Version 2 (MERRA-2) (Gelaro et al., 2017). All products have 2.5° horizontal resolution. NCEP2 has daily resolution and we average 6-hourly ERA-Interim fields and 3-hourly MERRA-2 fields to yield daily fields. ERA-Interim has 32 vertical levels from 1000 mbar to 1 mbar, with approximately 20 to 27 levels in the troposphere. NCEP2 has 17 vertical levels from 1000 mbar to 10 mbar, with approximately 8 to 12 levels in the troposphere. MERRA-2 has 42 vertical levels from 985 mbar to 0.01 mbar, with approximately 21 to 25 levels in the troposphere.

1.2.2 Equivalent potential temperature (θ_e) and dry air mass (M) of the atmospheric fields

We compute θ_e (K) using the following expression:

$$\theta_e = \left(T + \frac{L_v(T)}{C_{pd}} \cdot w\right) \cdot \left(\frac{P_0}{P}\right)^{\frac{R_d}{C_{pd}}} \quad (1.1)$$

from Stull (2012). T(K) is the temperature of air, w (kg water vapor per kg air mass) is the water vapor mixing ratio, R_d (287.04, J kg^{-1} K^{-1}) is the gas constant for air, C_{pd} (1005.7 J kg^{-1} K^{-1}) is the specific heat of dry air at constant pressure, P_0 (1013.25, mbar) is the reference pressure

at the surface, and $L_v(T)$ is the latent heat of evaporation at temperature T. $L_v(T)$ is defined as 2406 kJ kg^{-1} at 40 °C, and 2501 kJ kg^{-1} at 0 °C and scales linearly with temperature.

Following Bolton (1980), we compute water vapor mixing ratio (w) from relative humidity (RH, kg kg^{-1}) provided by the reanalysis products and the formula for saturation mixing ratio of water vapor ($P_{s,v}$, mbar) modified by Wexler (1976).

$$P_{s,v} = 0.06122 \cdot e^{\frac{17.67 \cdot T}{T+243.5}} \tag{1.2}$$

$$w = RH \cdot 0.622 \cdot \frac{P_{s,v}}{P - P_{s,v}} \tag{1.3}$$

We compute the total air mass of each grid cell x at time t, $M_x(t)$, shown in Eq. 4, from the product of pressure range and surface area, and divided by a latitude and height dependent gravity constant provided by Arora et al. (2011). The surface area is computed by using latitude (Φ), longitude (λ), radius of the earth (R, 6371 km). The total air mass of each grid cell is computed from

$$M_x = \frac{\Delta P}{g} \cdot |\Delta \sin(\Phi) \cdot \Delta \lambda| \cdot R^2 \tag{1.4}$$

where Δ represents the difference between two boundaries of each grid cell.

The gravity constant (g, kg m^{-2}) is computed following Arora et al. (2011) as:

$$g(\Phi, h) = g_0 \cdot (1 + 0.0053 \cdot \sin^2(\Phi) - 0.000006 \cdot \sin^2(2 \cdot \Phi)) - 0.000003086 \cdot h \tag{1.5}$$

where the reference gravity constant (g_0) is assumed to be 9.78046 m s^{-2}, and the height (h) in unit of m is computed from

$$P = P_0 \cdot e^{-\frac{h}{H}} \tag{1.6}$$

where H is the scale height of the atmosphere and assumed to be 8400 m.

The dry air mass is then computed by subtracting the water mass, computed from relative humidity, saturation water vapor mass mixing ratio, and total air mass of the grid cell (Eq. 3). Since

this study focuses on tracer distributions in the troposphere, we compute $M_{\theta e}$ with an upper boundary at the dynamical tropopause defined as the 2 PVU (potential vorticity units, 10^{-6} K kg^{-1} m^2 s^{-1}) surface.

ERA-Interim and NCEP2 include hypothetical levels below the true land/sea surface, for example, the 850 hPa level over the Himalayan, which we exclude in the calculation of $M_{\theta e}$.

1.2.3 Determination of $M_{\theta e}$

We show a schematic of the conceptual basis for the calculation of $M_{\theta e}$ in Figure 1.1. To compute $M_{\theta e}$, we sort all tropospheric grid cells in the hemisphere by increasing θ_e, and sum the dry air mass over grid cells following

$$M_{\theta_e}(\theta_e, t) = \sum M_x(t)|_{\theta_{e_x} < \theta_e} \quad (1.7)$$

where $M_x(t)$ is the dry air mass of each grid cell x at time t, and θ_{e_x} is the equivalent potential temperature of the grid cell. The sum is over all grid cells with θ_{e_x} less than θ_e.

This calculation yields a unique value of $M_{\theta e}$ for each value of θ_e. We refer to the relationship between θ_e and $M_{\theta e}$ as the "θ_e-$M_{\theta e}$ look-up table", which we generate at daily resolution. We provide this look-up table for each hemisphere computed from ERA-Interim from 1980 to 2018 with daily resolution and from the lowest to the highest θ_e surface in the troposphere with 1 K interval (see data availability).

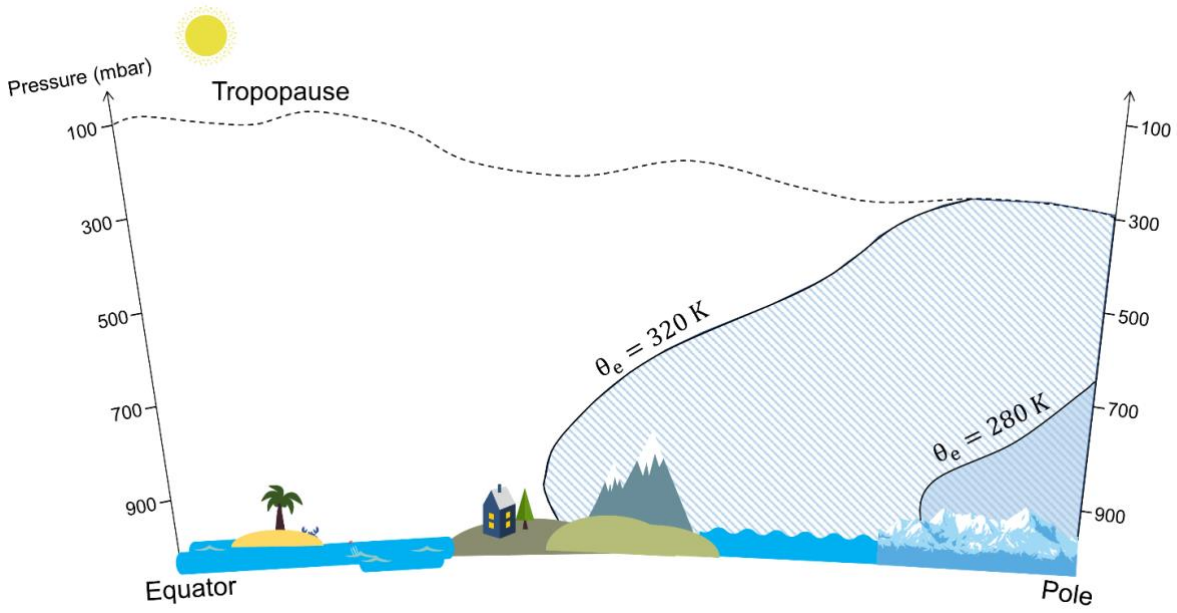

Figure 1.1: Schematic of the conceptual basis to calculate $M_{\theta e}$. $M_{\theta e}$ of a given θ_e surface is computed by summing all dry air mass with a low equivalent potential temperature in the troposphere of the hemisphere. This calculation yields a unique θ_e-$M_{\theta e}$ relation at a given time point.

1.3 Characteristics of $M_{\theta e}$

1.3.1 Spatial and temporal distribution of $M_{\theta e}$

Figure 1.2 shows snapshots of the distribution of zonal average θ_e and $M_{\theta e}$ with latitude and pressure at two arbitrary time slices (1 January 2009, 1 July 2009). $M_{\theta e}$ is not continuous across the Equator because it is defined separately in each hemisphere. By definition, each $M_{\theta e}$ surface is exactly aligned with a corresponding θ_e surface, and $M_{\theta e}$ surfaces have the same characteristics as θ_e surfaces, which decrease with latitude and generally increase with altitude. Whereas, the zonal average θ_e surfaces vary by up to 20 degrees in latitude over seasons, the meridional displacement of zonal average $M_{\theta e}$ is much smaller, with less than 5 degrees in latitude poleward of 30°N/S, as expected, because the zonal average displacement of atmospheric mass over seasons is small. This small seasonal displacement is closely associated with the seasonality of vertical sloping of θ_e surfaces (Figure 1.2). As the mass under each $M_{\theta e}$ surface is always constant, the change in tilt must cause the meridional displacement. In the summer, the tilt is

steeper (due to increased deep convection) so $M_{\theta e}$ surfaces move poleward in the lower troposphere but move equatorward in the upper troposphere.

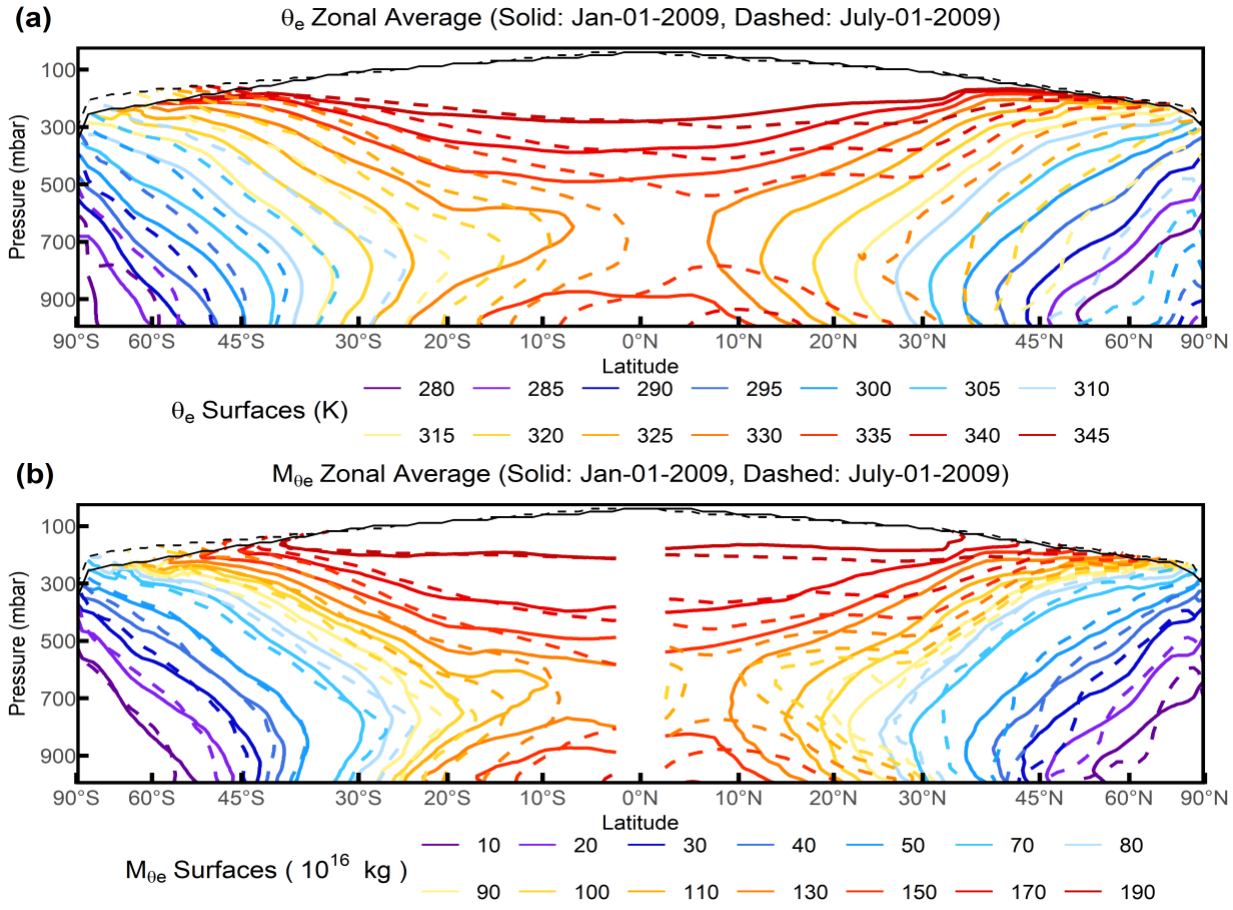

Figure 1.2: Snapshot of the distribution of (a) zonal average θ_e surfaces on 1 January 2009 (solid lines) and 1 July 2009 (dashed lines), (b) zonal average $M_{\theta e}$ surfaces on 1 January 2009 (solid lines) and 1 July 2009 (dashed lines). The zonal average tropopause is also shown here for 1 January 2009 (solid black line) and 1 July 2009 (dashed black line). θ_e, $M_{\theta e}$ and tropopause are computed from ERA-Interim.

$M_{\theta e}$ surfaces at given meridians (Figure 1.3) in the Northern Hemisphere show clear zonal asymmetry, with larger and more complex displacements compared to the zonal averages, associated with differential heating by land and ocean, and orographic stationary Rossby waves (Hoskins and Karoly, 1981; Wills and Schneider, 2018). For example, over the Northern Hemisphere ocean at 180°E (Figure 1.3a) and from the summer to winter, $M_{\theta e}$ surfaces move

poleward in the mid- to high latitude (e.g. poleward of 45°N), but move equatorward in the mid- to low latitude lower troposphere (e.g. equatorward of 45°N, 900 – 700 mbar), with the magnitude smaller than 10 degrees latitude in both. In comparison, over the Northern Hemisphere land at 100°E (Figure 1.3b) and from the summer to winter, $M_{\theta e}$ surfaces moves equatorward by up to 30 degrees latitude, except high latitude middle troposphere (e.g. poleward of 70°N, ~ 500 mbar), where the flat $M_{\theta e}$ surfaces lead to slightly poleward displacements. In the Southern Hemisphere, in contrast, the summer to winter displacements of the 180°E and 100°E sections are similar to the zonal average.

At lower latitudes, the zonal averages of $M_{\theta e}$ and θ_e both exhibit strong secondary maxima near the surface associated with the Hadley circulation (Equatorward of 30° N/S) and in the summer, driven by high water vapor. From the contours in Figure 1.2, this surface branch of high $M_{\theta e}$ and θ_e appears disconnected from the upper tropospheric branch. In fact, these two branches are connected through air columns undergoing deep convection, which are not resolved in the zonal means shown in Figure 1.2, but are resolved in some meridians (e.g. Figure 1.3a). We also note that, over the land at 100°E (Figure 1.3b), the two disconnected $M_{\theta e}$ and θ_e branches in the Northern Hemisphere summer are displaced poleward compared to the zonal average, consistent with a northward shift of intertropical convergence zone (ITCZ) over southern Asia. The existence of these two branches may limit some applications of $M_{\theta e}$, as discussed in Section 4.

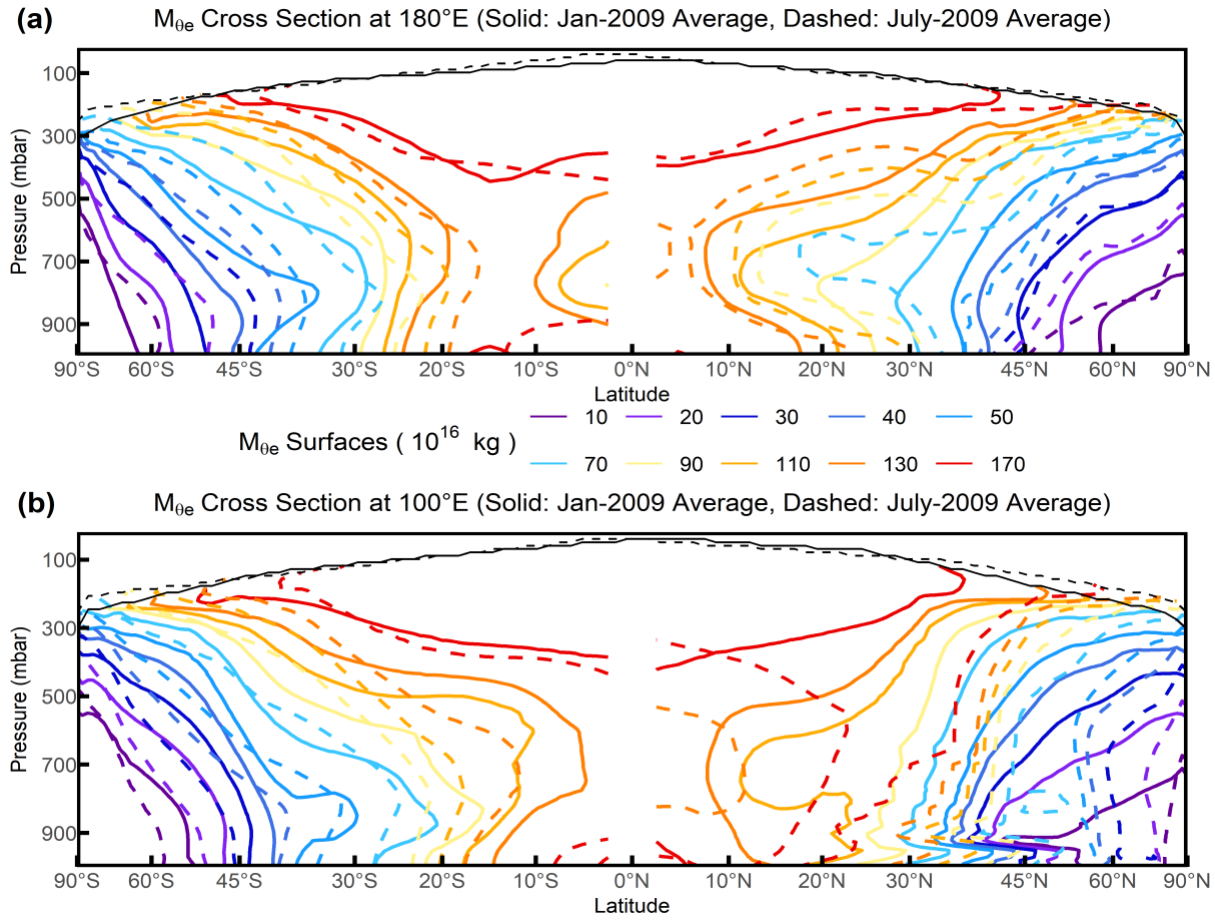

Figure 1.3: $M_{\theta e}$ surfaces as Jan-2009 average (solid lines) and July-2009 average (dashed lines) for (a) 180°E (mostly over the Pacific Ocean), and (b) 100°E (mostly over the Eurasia land in the Northern Hemisphere). $M_{\theta e}$ and tropopause are computed from ERA-Interim.

Figure 1.4 shows the zonal average meridional displacement of θ_e and $M_{\theta e}$ with daily resolution. In summer, $M_{\theta e}$ surfaces displace poleward in the lower troposphere but equatorward in the upper troposphere. The displacements in the lower troposphere (925 mbar) are greater in the Northern Hemisphere, where the $M_{\theta e}$ = 140 (10^{16} kg) surface, for example, displaces poleward by 10 degrees in latitude between winter and summer (Figure 1.4b). Beside the seasonal variability, Figure 1.4 also shows evident synoptic-scale variability.

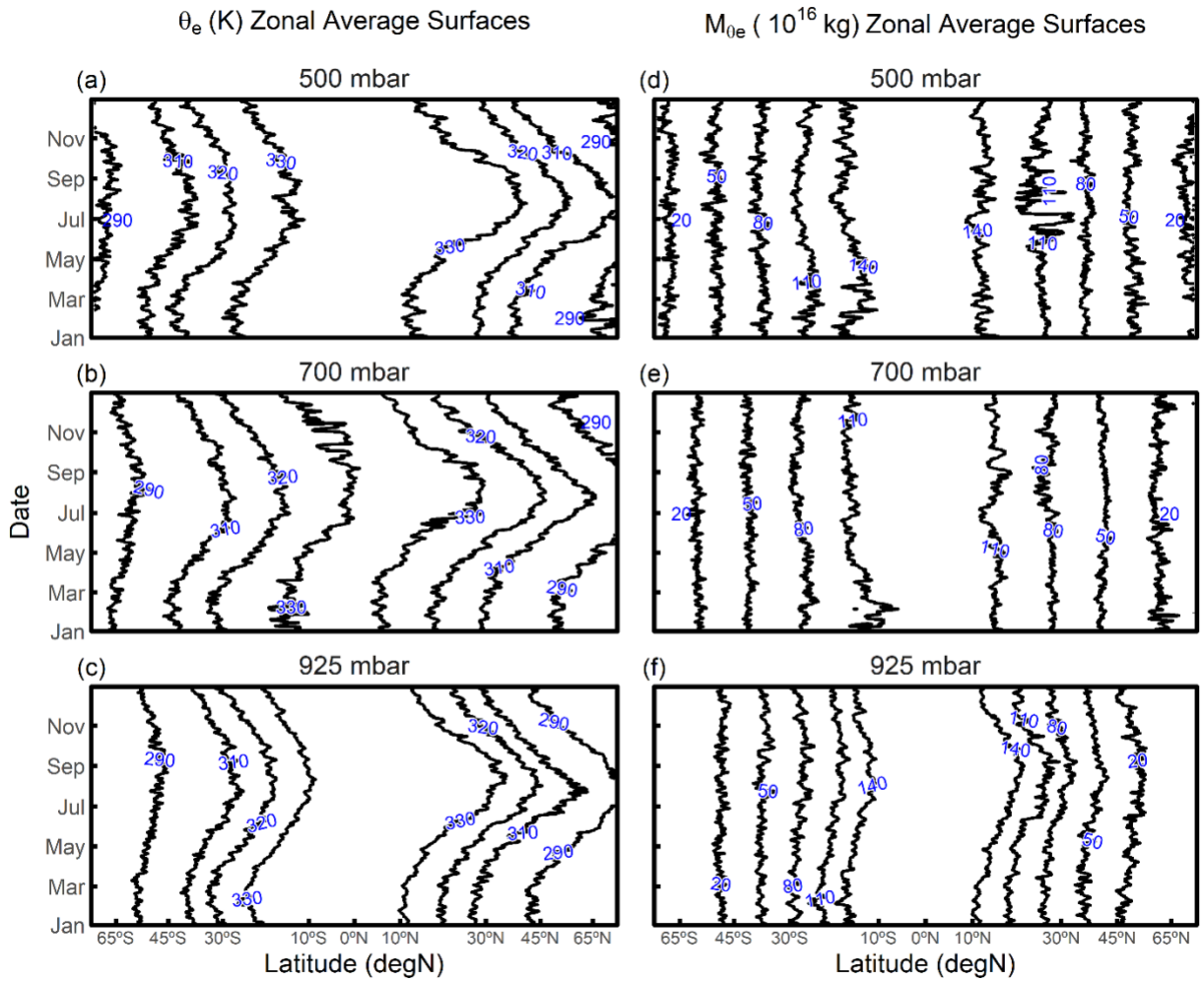

Figure 1.4: Time series of meridional displacement of selected zonal average θ_e (K) surfaces over a year at (a) 500 mbar, (b) 700 mbar and (c) 925 mbar. Meridional displacement of selected zonal average $M_{\theta e}$ (10^{16} kg) surfaces over a year at (d) 500 mbar, (e) 700 mbar and (f) 925 mbar. The value of each surface is labelled. θ_e and $M_{\theta e}$ are computed from ERA-Interim. Results shown are for year 2009.

Since the tilting of θ_e surfaces has an impact on the seasonal displacement of $M_{\theta e}$ surfaces, the contribution of different pressure levels to the mass of a given $M_{\theta e}$ bin must also vary with season. In Figure 1.5, we show these contributions as two daily snapshots on 1 January 2009 and 1 July 2009. Low $M_{\theta e}$ bins consist of air masses mostly below 500 mbar near the Pole. As $M_{\theta e}$ increases, the contribution from the upper troposphere gradually increases while the contribution from the surface to 800 mbar decreases to its minimum at around 100 to 120 (10^{16} kg). The

contribution from the surface to 800 mbar increases as $M_{\theta e}$ increases above 120 (10^{16} kg). The mass fraction shows only small variations with season, with the lower troposphere (Surface to 800 mbar) contributing slightly less in the low $M_{\theta e}$ bands and slightly more in the high $M_{\theta e}$ bands in the summer, which is closely related to the seasonal tilting of corresponding θ_e surfaces.

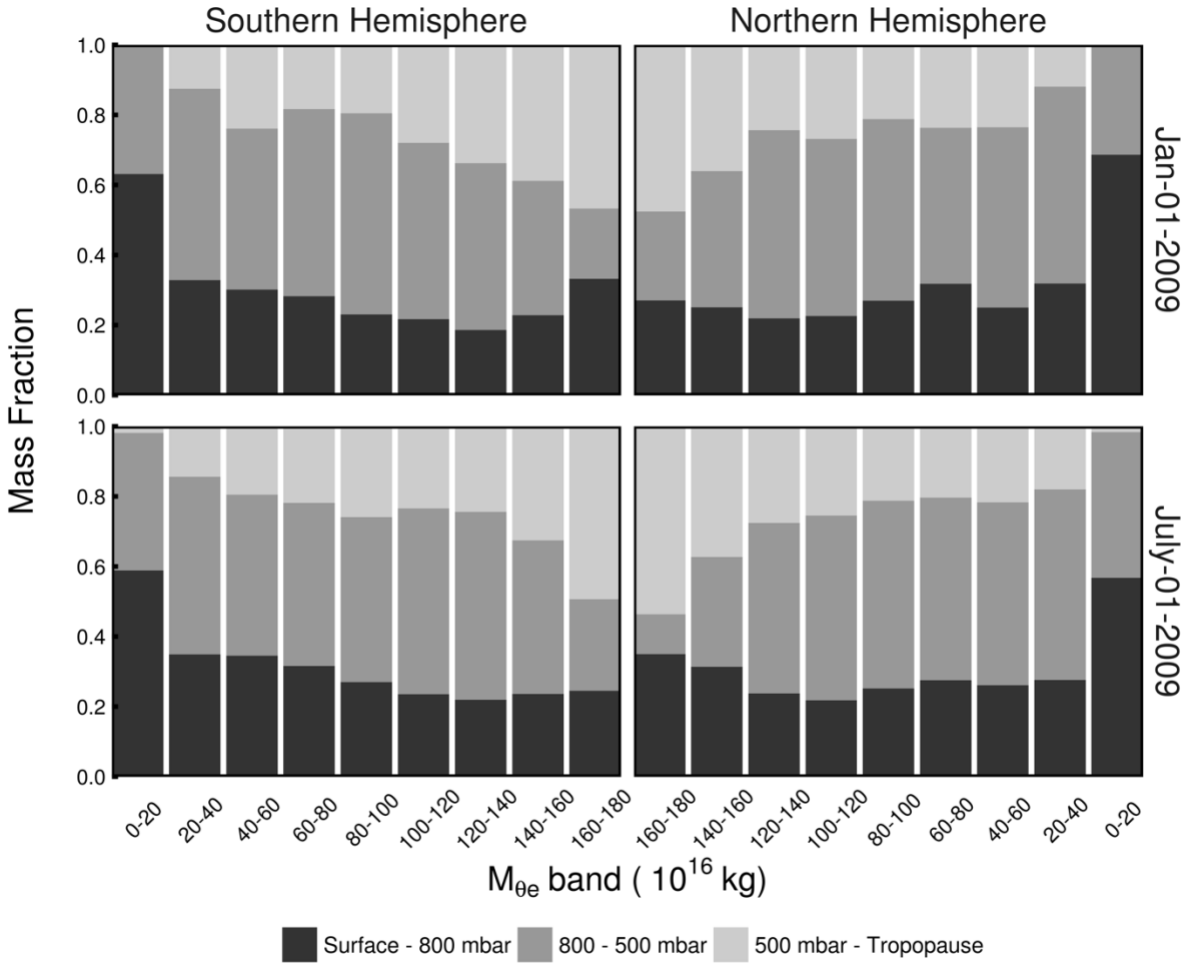

Figure 1.5: Snapshots (1 January 2009 and 1 July 2009) of the mass distribution of different $M_{\theta e}$ bins from three pressure bins (surface to 800 mbar, 800 mbar to 500 mbar, and 500 mbar to tropopause). $M_{\theta e}$ is computed from ERA-Interim. Low $M_{\theta e}$ bins are seen to have larger contributions from the air near the surface, and high $M_{\theta e}$ bins have larger contributions from air aloft. Comparing the top and the bottom panels shows that the seasonal differences in pressure contributions are small except for the highest $M_{\theta e}$ bins (160-180, 10^{16} kg) and the lowest $M_{\theta e}$ bin in the northern hemisphere (0-20, 10^{16} kg).

1.3.2 θ_e-$M_{\theta e}$ relationship

Figure 1.6 compares the temporal variation of $M_{\theta e}$ of several given θ_e surfaces (i.e., θ_e-$M_{\theta e}$ look-up table) computed from different reanalysis products for 2009. The deviations are indistinguishable between ERA-Interim and MERRA-2, except near θ_e = 340 K, where MERRA-2 is systematically lower than ERA-Interim by 1.5 to 6.5 (10^{16} kg). NCEP2 shows slightly larger deviations from ERA-Interim, but less than 8.5 (10^{16} kg). The products are highly consistent in seasonal variability, and they also show agreement on synoptic time scales. The small difference between products is expected because of different resolutions and methods (Mooney et al., 2011). We expect these differences would be negligible for most applications of $M_{\theta e}$.

Figure 1.6 shows that, in both hemispheres, $M_{\theta e}$ reaches its minimum in summer and maximum in winter for a given θ_e surface, with the largest seasonality at the lowest θ_e (or $M_{\theta e}$) values. The seasonality decreases as θ_e increases, following the reduction in the seasonality of shortwave absorption at lower latitudes (Li and Leighton, 1993). The seasonality is smaller in the Southern Hemisphere, consistent with the larger ocean area and hence greater heat capacity and transport (Fasullo and Trenberth, 2008; Foltz and McPhaden, 2006). Figure 1.6 also shows that $M_{\theta e}$ has significant synoptic-scale variability but smaller than the seasonal variability. Synoptic variability is typically larger in winter than summer, as discussed below.

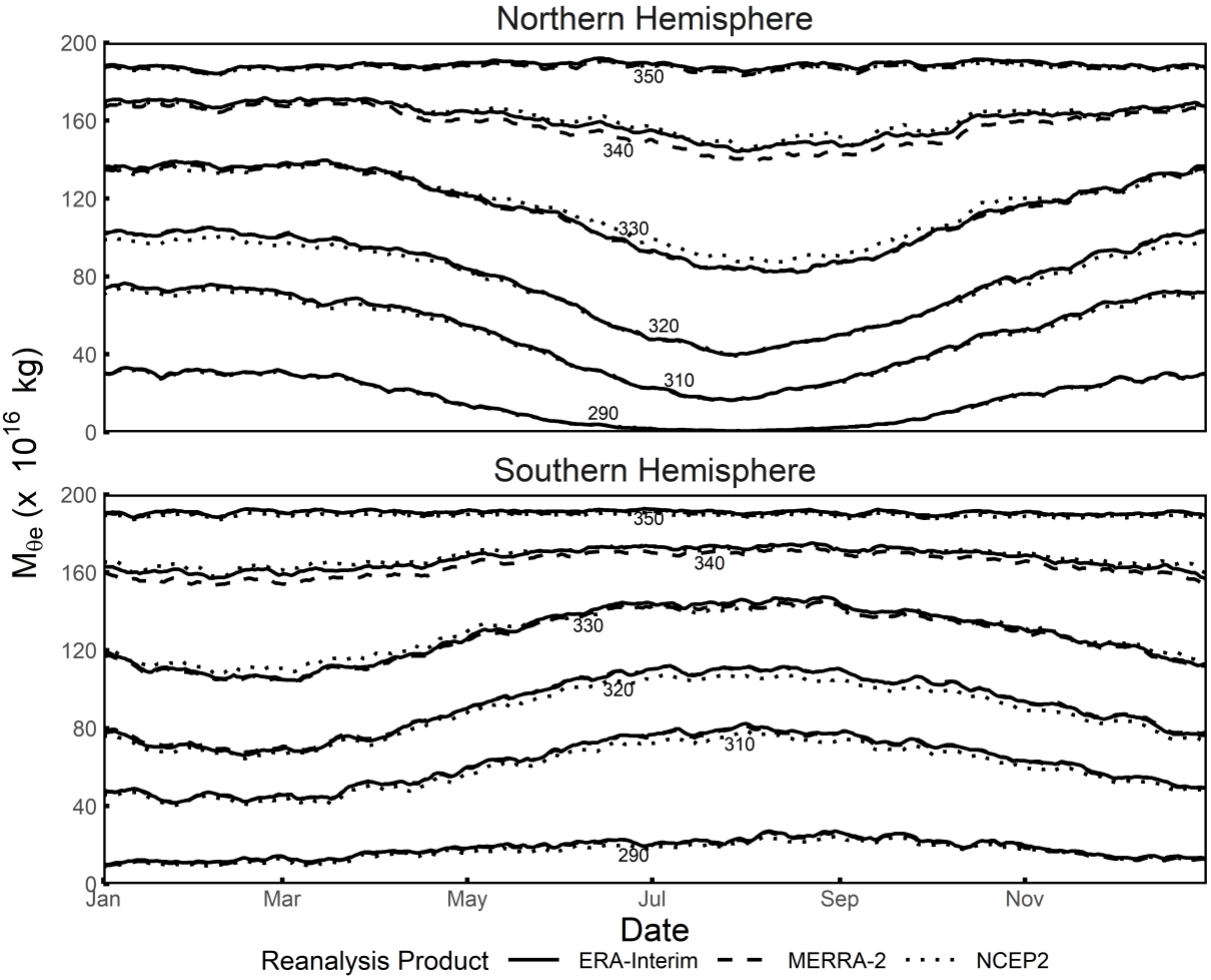

Figure 1.6: Variability of $M_{\theta e}$ of given θ_e surfaces (i.e., θ_e-$M_{\theta e}$ look-up table) over a year with daily resolution in the Northern and Southern Hemisphere. Data from ERA-Interim is shown as a solid line, MERRA-2 is shown as a dashed line and NCEP2 is shown as a dotted line. Results shown are for year 2009.

1.3.3 Relationship to diabatic heating and mass fluxes

A key step of the application of $M_{\theta e}$ for interpreting tracer data is the generation of the look-up table that relates θ_e and $M_{\theta e}$. In this section, we address a tangential question of what controls the temporal variation of the look-up table, which is not necessary for the application but may be of fundamental meteorological interest.

As shown in Appendix A, the temporal variation of the lookup table, $\dot{M}_{\theta_e} = \frac{\partial}{\partial t} M_{\theta_e}(\theta_e, t)$, can be related to underlying mass and heat fluxes according to

$$\dot{M_{\theta_e}} = -\frac{1}{C_{pd}}\frac{\partial Q_{dia}(\theta_e, t)}{\partial \theta_e} + m_T(\theta_e, t) + m_E(\theta_e, t) \quad (1.8)$$

where $\frac{\partial Q_{dia}(\theta_e,t)}{\partial \theta_e}$ (J s^{-1} K^{-1}) is the effective diabatic heating, integrated over the full θ_e surface per unit width in θ_e, $m_T(\theta_e, t)$ (kg s^{-1}) is the net mass flux across the tropopause and $m_E(\theta_e, t)$ (kg s^{-1}) is the net mass flux across the Equator, including all air with equivalent potential temperature less than θ_e. Q_{dia} has contributions from internal heating without ice formation (Q'_{int}), heating from ice formation (Q_{ice}), sensible heating from the surface (Q_{sen}), surface evaporation (Q_{evap}), turbulent diffusion of heat (Q_{diff}), and turbulent transport of water vapor (Q_{H_2O}) following

$$\begin{aligned} Q_{dia}(\theta_e, t) = Q'_{int}(\theta_e, t) + Q_{ice}(\theta_e, t) + Q_{sen}(\theta_e, t) \\ + Q_{evap}(\theta_e, t) + Q_{diff}(\theta_e, t) + Q_{H_2O}(\theta_e, t) \end{aligned} \quad (1.9)$$

The terms Q_{evap} and Q_{H_2O} are expressed as heating rates by multiplying the underlying water fluxes by $L_v(T)/C_{pd}$. In order to quantify the dominant processes contributing to temporal variation of $M_{\theta e}$, the terms in Eqs. 1.8 and 1.9 must be linked to diagnostic variables available in the reanalysis or model products. Although there was no perfect match with any of the three reanalysis products, MERRA-2 provides temperature tendencies for individual processes, which can be converted to heating rates per Eq. 9 following

$$\frac{\partial Q_i(\theta_e, t)}{\partial \theta_e} = \frac{C_{pd}}{\Delta \theta_e} \sum_x \left(\frac{dT}{dt}\right)_{x,i} M_x \quad (1.10)$$

where i refers a specific process (Q'_{int}, Q_{ice}, etc.), $\left(\frac{dT}{dt}\right)_x$ (K s^{-1}) is the temperature tendency of grid cell x, M_x (kg) is the mass of grid cell x, and $\Delta\theta_e$ is the width of the θ_e surface.

There are 5 heating terms provided in the MERRA-2 product, which we can approximately relate to terms in Eq. 9, as shown in Table 1.1. The first three terms (Q_{rad}, Q_{dyn}, and Q_{ana}) can be summed to yield Q'_{int}, the forth (Q_{trb}) is equal to the sum of Q_{diff} and Q_{sen}, and the fifth (Q_{mst})

approximates the sum of Q_{ice} and Q_{evap}. MERRA-2 does not provide terms corresponding to Q_{H_2O} or Q_{evap} but Q_{mst} represents heating due to moist processes, which includes Q_{ice} plus water vapor evaporation and condensation within the atmosphere. This water vapor evaporation and condensation should be approximately equal to Q_{evap} with small time lag when integrated over a θ_e surface because mixing is preferentially along θ_e surfaces and water vapor released into a θ_e surface by surface evaporation will tend to transport and precipitate from the same θ_e surface within a short time period (Bailey et al., 2019). Thus, the MERRA-2 term for heating by moist processes (Q_{mst}) should approximate $Q_{ice} + Q_{evap}$.

Table 1.1: Correspondence of heating variables between our derivation (Eq. 1.9) and MERRA-2.

Diabatic heating terms in our derivation (Eq. 1.9)	Diabatic heating terms in MERRA-2, $\frac{\partial Q_i(\theta_e,t)}{\partial \theta_e}$
Q'_{int}	1. Radiative heating (i.e., sum of shortwave and longwave radiative heating, Q_{rad}) + 2. Absorption of kinetic energy that breaking the eddies (Q_{dyn}) + 3. The analysis tendency introduced during the corrector segment of the Incremental Analysis Update (IAU) cycle (Q_{ana})
$Q_{diff} + Q_{sen}$	4. Turbulent heat flux including surface sensible heating (Q_{trb})
$Q_{evap} + Q_{ice}$	5. Moist processes including all latent heating due to condensation and evaporation as well as the mixing by convective parameterization (Q_{mst})
Q_{H_2O}	Not available

Figure 1.7a compares the temporal variation of $\dot{M}_{\theta_e}$ computed by integrating dry air mass (i.e., θ_e-$M_{\theta e}$ look-up table) with $M_{\theta e}$ computed from the sum of the diabatic heating terms from MERRA-2 (via Eq. 8 to Eq. 10). The comparison focuses on the θ_e = 300 K surface, which does not intersect with the Equator or tropopause, so that the two mass flux terms (m_T, m_E) vanish. These two methods have a high correlation at 0.71. We do not expect perfect agreement because $\dot{M}_{\theta_e}$ computed by the sum of heating neglects turbulent water vapor transport (Q_{H_2O}), and only approximates Q_{evap} as discussed above. This relatively good agreement nevertheless demonstrates that the formulation based on MERRA-2 heating terms includes the dominant processes that drive temporal variations in the look-up table. Figure 1.7a shows poorer agreement from late August to October, which we also find in other years (Figure 1.15 and 1.16) and on lower (e.g., θ_e = 290K, Figure 1.17) but not higher surfaces (e.g., θ_e = 310K, Figure 1.18), where the two methods agree better. The poor agreement may reflect a partial breakdown of the assumption that Q_{mst} approximates the sum of Q_{ice} and Q_{evap}, but further analysis is beyond the scope of this study.

Figure 1.7b further breaks down the sum of the heating terms in Eq. 8 and 10 from MERRA-2 into individual components. Each term clearly displays variability on synoptic to seasonal scales. To quantify the contribution of different terms on the different time scales, we separate each term into a seasonal and synoptic component, where the seasonal component is derived by a two-harmonic fit with constant offset and the synoptic component is the residual. We estimate the fractional contribution of each heating term on seasonal and synoptic time scales separately in Table 1.2, using the method in Supplementary 1.9.1. On the seasonal time scale, the variance is dominated by radiative heating and cooling of the atmosphere and moist processes (including both ice formation and extra water vapor from surface evaporation) together, with

prominent counteraction between each other. On the synoptic time scale, dissipation of kinetic energy of turbulence dominates the variance.

Similar analyses on different θ_e surfaces and in different years (Figure 1.15 to 1.18) all show that combination of radiative heating and moist processes dominates the temporal variation of $M_{\theta e}$ on the seasonal time scale, while dissipation of kinetic energy of turbulence dominates on the synoptic time scale.

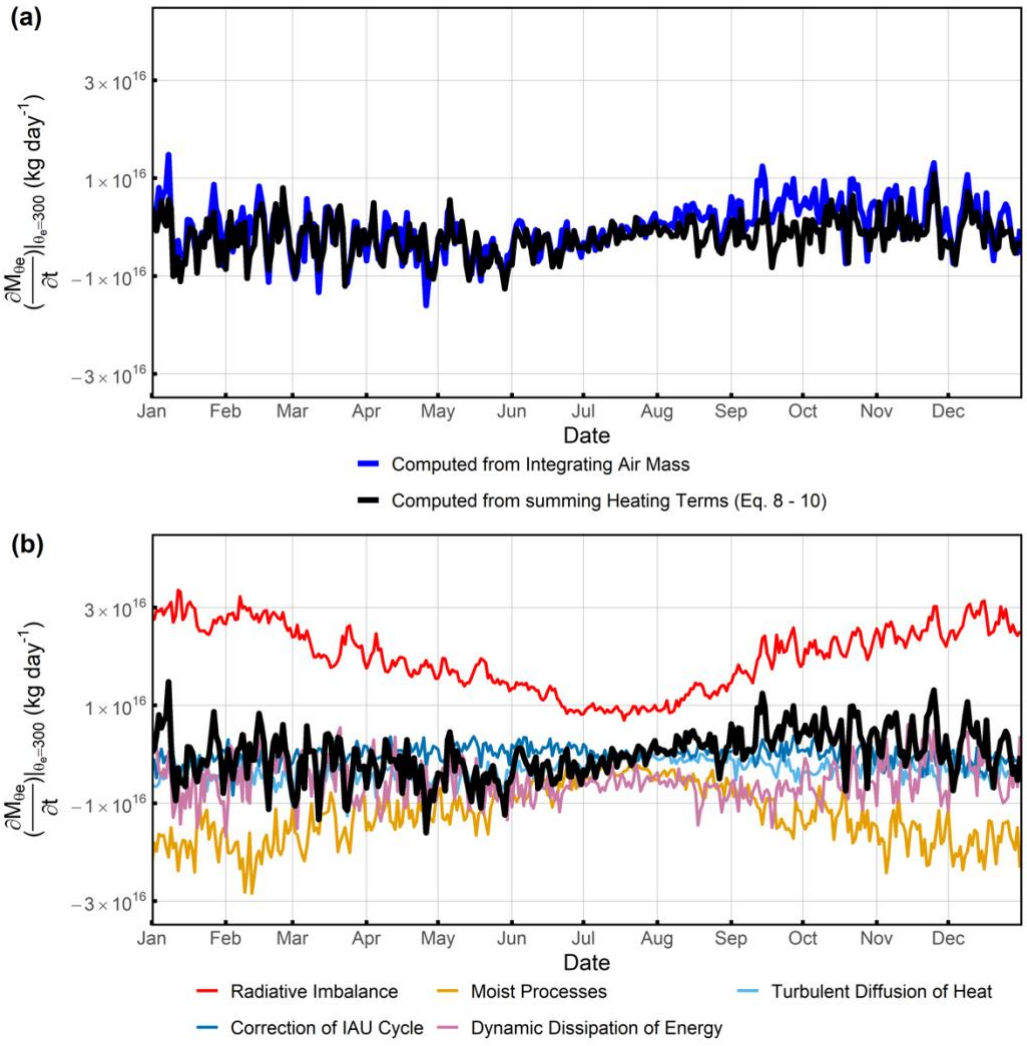

Figure 1.7: (a) Temporal variation of $M_{\theta e}$ in the Northern Hemisphere at θ_e = 300 K computed by integrating air mass (blue line) and estimated from the sum of five heating terms (Table 1.1) in MERRA-2 (black line). (b) The heating variables decomposed into five contributions as indicated (see Table 1.1). Results shown are for year 2009.

Table 1.2: Fractional contribution of the individual heating terms in Figure 1.7b to their sum for θ_e = 300K. The analysis is done separately on synoptic and seasonal components. The seasonal component is based on a 2-harmonic fit and the synoptic component is defined as the residual. The fractional contributions sum to 1, while a positive contribution means in phase and negative contribution means anti-phase. A contribution in absolute value that is bigger than 1 illustrates that the variability of the heating term is larger than the variability of the sum on the corresponding time scale.

Heating terms	Seasonal component	Synoptic component
Q_{rad}	2.25	0.03
Q_{mst}	-1.39	0.07
Q_{dyn}	0.24	0.72
Q_{dyn}	0.21	0.11
Q_{ana}	-0.31	0.07
Sum	1	1

1.4 Applications of $M_{\theta e}$ as an atmospheric coordinate

To illustrate the potential application of $M_{\theta e}$ for interpreting sparse data, we focus on the seasonal cycle of CO_2 in the Northern Hemisphere as resolved by two series of global airborne campaigns, HIPPO and ATom. HIPPO consisted of five campaigns between 2009 and 2011 and ATom consisted of four campaigns between 2016 and 2018. Each campaign covered from ~ 150 m to ~ 14000 m and from nearly Pole to Pole, along both northbound and southbound transects. On HIPPO, both transects were over the Pacific Ocean, while on ATom, southbound transects were over the Pacific Ocean and northbound transects were over the Atlantic Ocean. The flight tracks are shown in Figure 1.8a. We aggregate data from each campaign into northbound and southbound transects within each hemisphere, but only use data from the Northern Hemisphere. We only consider tropospheric observations by excluding measurements from the stratosphere, which is defined by observed water vapor less than 50 ppm and either O_3 greater than 150 ppb or detrended N_2O to the reference year of 2009 less than 319 ppb. Water vapor and O_3 were measured by the NOAA UCATS (UAS Chromatograph for Atmospheric Trace Species, Hurst) instrument and were interpolated to 10-sec resolution. N_2O was measured by the Harvard QCLS (Quantum Cascade Laser System, Santoni et al., 2014) instrument. Furthermore, we exclude all near-surface

observations within ~ 100 seconds of take-offs, within ~ 600 seconds of landings, and missed approaches, which usually show high CO_2 variability due to strong local influences. In-situ measurements of CO_2 were made by 3 different instruments on both HIPPO and Atom. Of these, we use the CO_2 measurements made by the NCAR Airborne Oxygen Instrument (AO2) with a 2.5 seconds measurement interval (Stephens et al., 2020), for consistency with planned future applications to APO (atmospheric potential oxygen) computed from AO2. The differences between instruments are small for our application (Santoni et al., 2014). The data used in this study are averaged to 10-sec resolution and we show the detrended CO_2 values along each airborne campaign transect for the Northern Hemisphere in Figure 1.8b. Since we focus on the seasonal cycle of CO_2, all airborne observations are detrended by subtracting an interannual trend fitted to CO_2 measured at the Mauna Loa Observatory (MLO) by the Scripps CO_2 Program. This trend is computed by a stiff cubic spline function plus 4-harmonic terms with linear gain to the MLO record. $M_{\theta e}$ is computed from ERA-Interim in this section.

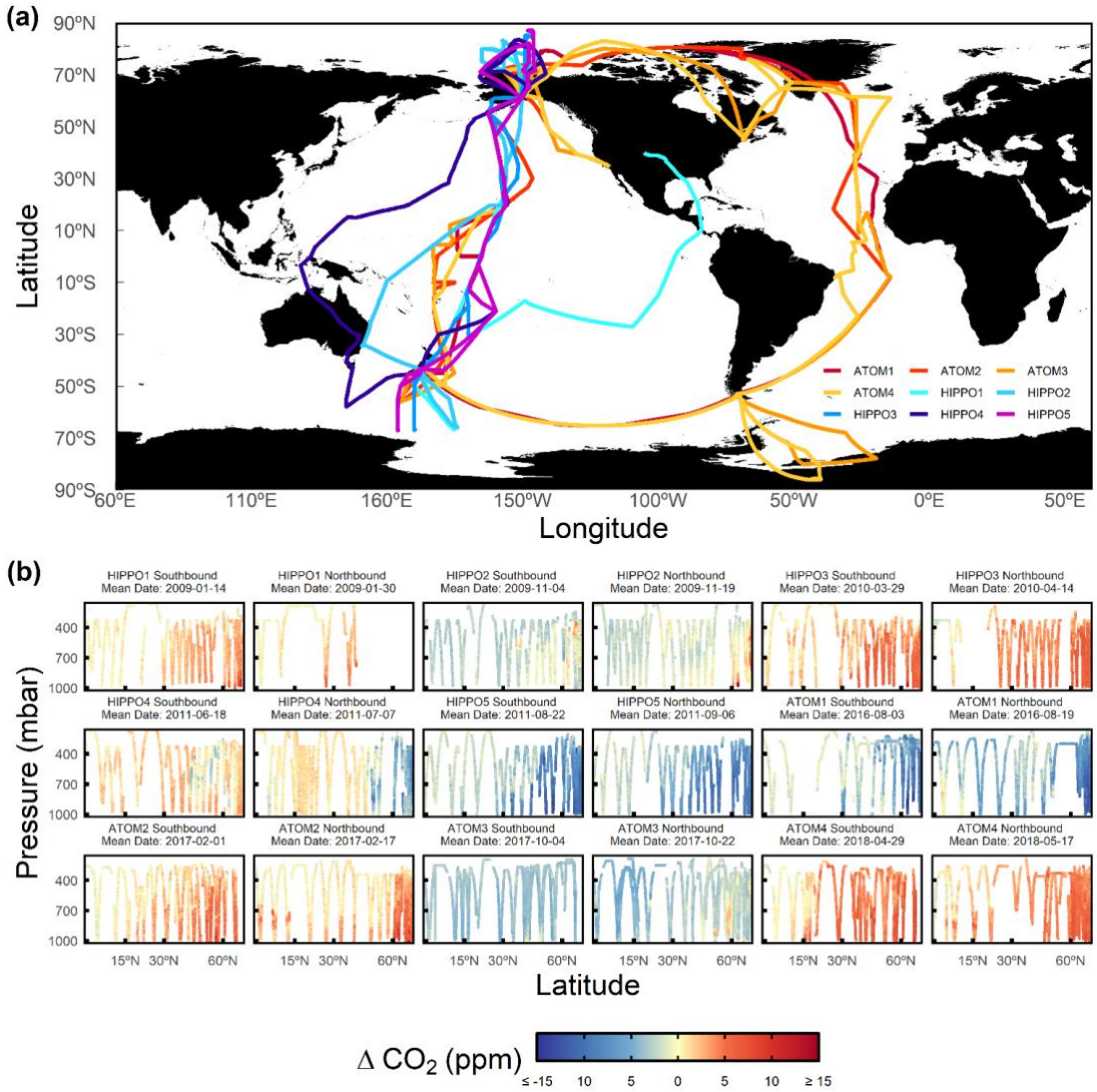

Figure 1.8: (a) HIPPO and ATom horizontal flight tracks coloured by campaigns. (b) Latitude and pressure cross-section of detrended CO_2 of each airborne campaign transect. CO_2 is detrended by subtracting MLO stiff cubic spline trend, which is computed by a stiff cubic spline function plus 4-harmonic functions with linear gain to MLO record.

1.4.1 Mapping Northern Hemisphere CO_2

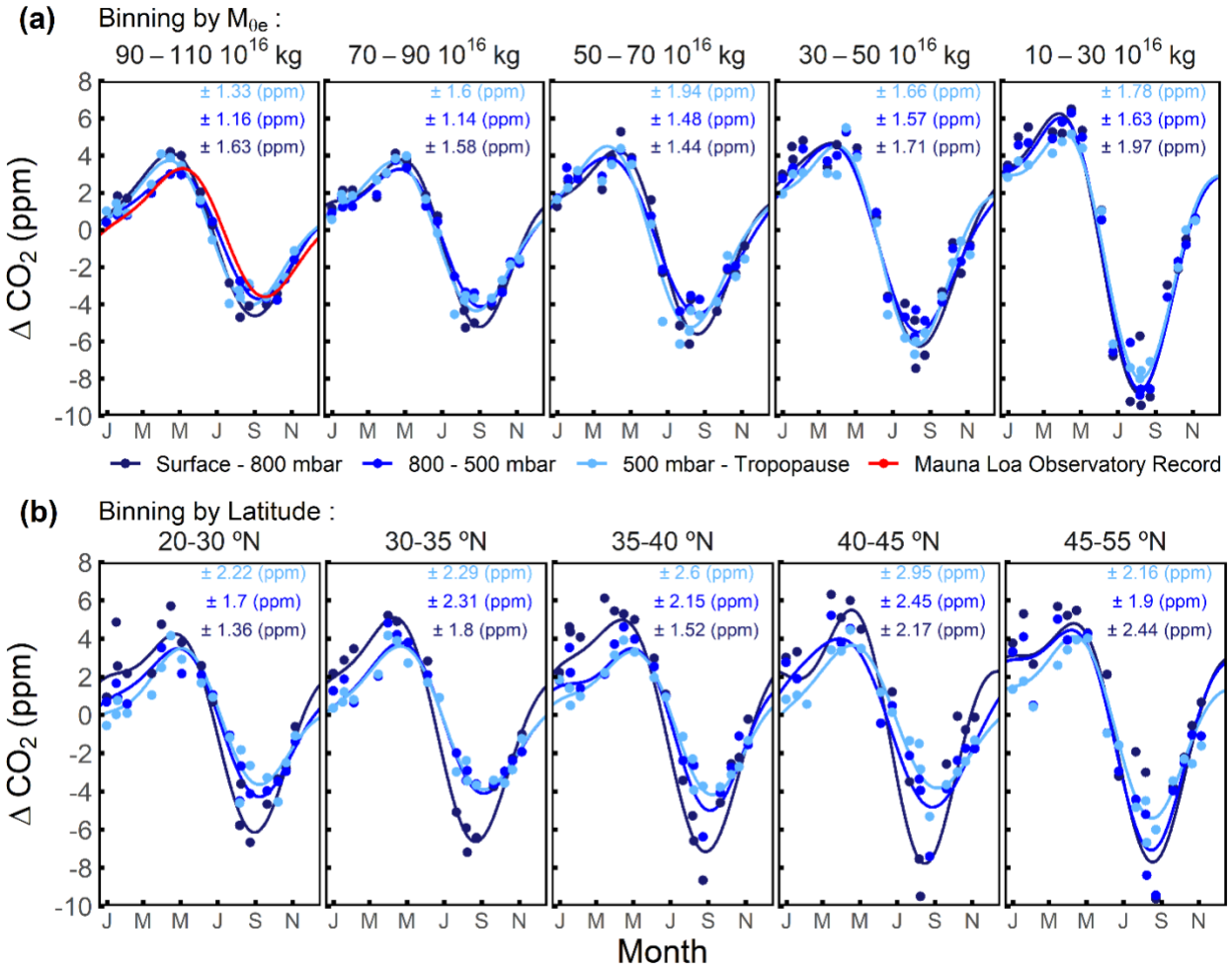

Figure 1.9: Seasonal cycles of airborne Northern Hemisphere CO_2 data sorted by (a) $M_{\theta e}$-pressure bins and (b) latitude-pressure bins. $M_{\theta e}$ bins (10^{16} kg) and latitude bins are shown on the top of each panel. Pressure bins are coloured. The latitude bounds are chosen to approximate the meridional coverage of each corresponding $M_{\theta e}$ bin in the lower troposphere. The seasonal cycle at MLO from 2009 to 2018 is shown on the 90–110 $M_{\theta e}$ bin panel, which spans the $M_{\theta e}$ of the station. Airborne observations are first grouped into $M_{\theta e}$-pressure or latitude-pressure bins, and then averaged for each airborne campaign transect, shown as points. We filter out the points averaged from less than 20 10-sec observations. The seasonal cycle of airborne data and MLO (2009-2018) are computed by a 2-harmonic fit to the detrended time series. The 1σ variability about the seasonal cycle fits for each $M_{\theta e}$-pressure or latitude-pressure bin are labelled on top of each panel. These 1σ values are based on the distribution of all binned observations (not shown), rather than the distribution of average CO_2 of each bin and airborne campaign transect (shown).

A conventional method to display seasonal variations in CO_2 from airborne data is to plot time series of the data at a given location or latitude and different pressure levels (Graven et al.,

2013; Sweeney et al., 2015). In Figure 1.9, we compare this method using HIPPO and ATom airborne data, binning and averaging the data from each airborne campaign transect by pressure and latitude bins, with our new method, binning the data by pressure and $M_{\theta e}$. For each latitude bin, we choose a corresponding $M_{\theta e}$ bin which has approximately the same meridional coverage in the lower troposphere. We remind the reader that $M_{\theta e}$ decreases poleward, while also generally increasing with altitude (Figures 1.2 to 1.4).

As shown in Figure 1.9, the transect average of detrended CO_2 (shown as points) from both binning methods resolve well-defined seasonal cycles (based on 2-harmonic fit) in all bins, with higher amplitudes near the surface (low pressure) and at high latitude (low $M_{\theta e}$). However, binning by $M_{\theta e}$ leads to much smaller variations of the mean seasonal cycle (shown as solid curves) with pressure, as expected, because moist isentropes are preferential surfaces of mixing. Also, within individual pressure bins, the short-term variability relative to the mean cycles based on the distribution of all detrended observations (not shown as points but denoted as 1σ values in Figure 1.9) is smaller when binning by $M_{\theta e}$ (F-test, $p < 0.01$), except in the lower troposphere of the highest $M_{\theta e}$ bin (90-110 10^{16} kg). The smaller short-term variability is expected because $M_{\theta e}$ tracks the synoptic variability of the atmosphere. When binning by latitude, the smallest short-term variability is found at the lowest bin (surface-800 mbar) and the largest short-term variability is found in the highest bin (500 mbar-tropopause), except the highest latitude bin (45°N-55°N). When binning by $M_{\theta e}$, in contrast, the short-term variability in the middle pressure bin is always smaller than the higher and lower pressure bins (F-test, $p < 0.01$), except for the 50 to 70 $M_{\theta e}$ bin, where the difference between the lowest and middle pressure bins is not significant (based on 1σ levels). The lower variability in the mid troposphere may reflect the suppression of variability from synoptic disturbances, leaving a clearer signal of the influence of surface fluxes of CO_2 and

stratosphere-troposphere exchanges. We compare the variance of detrended airborne observations within each $M_{\theta e}$-pressure bin with its fitted value. The fitted seasonal cycle of each bin explains 63.2% to 90.5% of the variability for different bins, with higher fractions in the middle troposphere.

Figure 1.9 also shows the CO_2 seasonal cycle at MLO, which falls within a single $M_{\theta e}$-pressure bin (90-110 10^{16} kg, 500-800 mbar) at all seasons. Although the airborne data in this bin span a wide range of latitudes (~10°N-75°N), the seasonal cycle averaged over this bin is very similar to the cycle at MLO (airborne cycle leads by ~10 days with 1.0% lower amplitude). This small difference is within the 1σ uncertainty of our estimation from airborne observation, and some difference is expected, since we choose a $M_{\theta e}$-pressure bin wider than the seasonal variation of $M_{\theta e}$ and pressure at MLO.

It is also of interest to examine how CO_2 data from surface stations fit into the framework based on $M_{\theta e}$. Figure 1.10 compares the CO_2 seasonal cycle of five NOAA surface stations (Dlugokencky et al., 2019) with the cycle from the airborne observations binned into selected $M_{\theta e}$ bins. These surface stations are chosen to be representative of different $M_{\theta e}$ ranges. For the comparison, we chose $M_{\theta e}$ bins that span the seasonal maximum and minimum $M_{\theta e}$ value of the station. These bins are narrower than the bins used in Figure 1.9, in order to sharply focus on the latitude of the station. To maximize sampling coverage, we bin the airborne data only by $M_{\theta e}$ without pressure sub-bins. For mid- and high latitude surface stations (right three panels), the seasonal amplitude of station CO_2 and corresponding airborne CO_2 are close (within 4-5%), while airborne cycles lag by 2-3 weeks. The lag presumably represents the slow mixing from the mid-latitude surface to the high latitude mid-troposphere (Jacob, 1999). In contrast, for low latitude stations (left two panels) which generally sample trade winds, the seasonal cycles differ

significantly, indicating that the air sampled at these stations is not rapidly mixed along surfaces of constant $M_{\theta e}$ or θ_e with air aloft. As mentioned above (Section 3.1), surfaces of high $M_{\theta e}$ within the Hadley circulation have two branches, one near the surface and one aloft. A timescale of several months for transport from the lower to the upper branch can be estimated from the known overturning flows based on air mass flux streamfunctions (Dima and Wallace, 2003). This delay, plus strong mixing and diabatic effects (Miyazaki et al., 2008), ensures that the lower and upper branches are not well connected on seasonal time scales. Our results nevertheless demonstrate that the $M_{\theta e}$ framework combining airborne and surface data could help understand details of atmospheric transport both along and across θ_e surfaces.

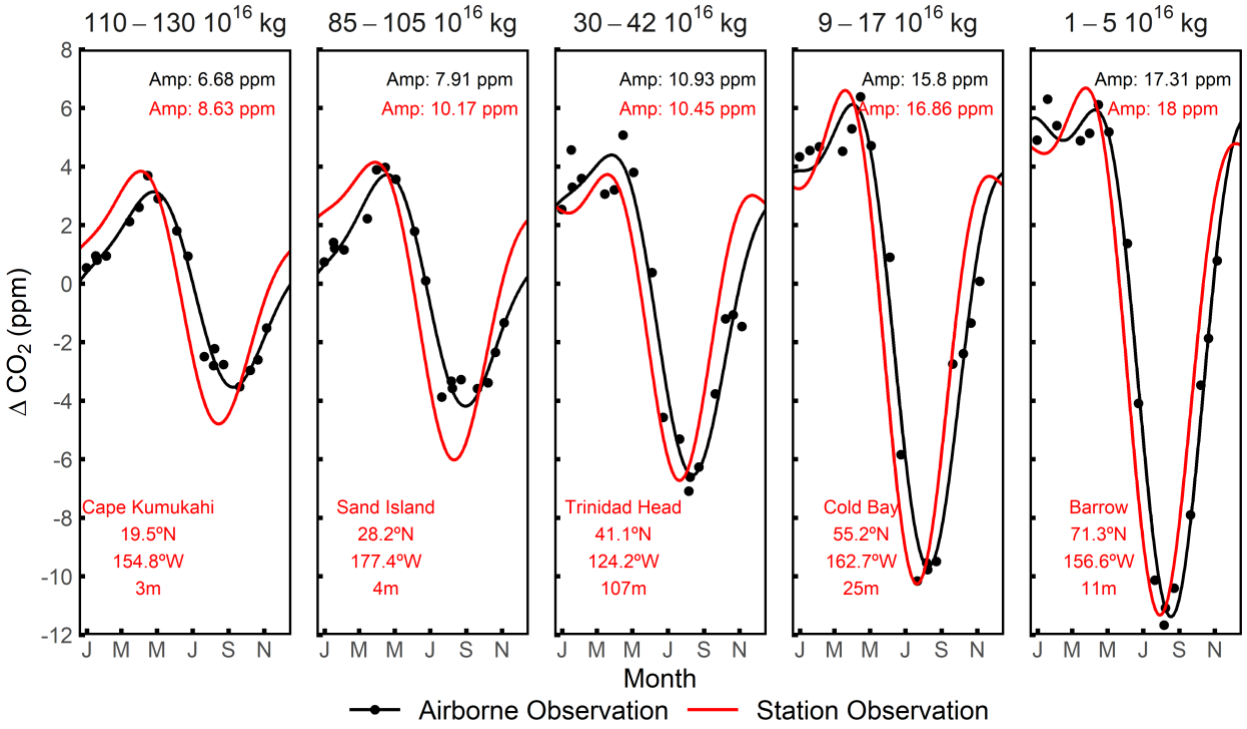

Figure 1.10: CO_2 seasonal cycles of multiple surface stations (2009-2018) compared to seasonal cycles of airborne observations averaged over corresponding $M_{\theta e}$ bin. The choice of $M_{\theta e}$ bin is to approximate the range of $M_{\theta e}$ at each corresponding surface station and is shown on the top of each panel. Daily $M_{\theta e}$ of the station is computed from ERA-Interim, based on its location. We detrend station and airborne observations by subtracting the MLO stiff cubic spline trend. We compute an average detrended CO_2 for each airborne campaign transect and each $M_{\theta e}$ bin, shown as black points. The seasonal cycles are computed from a 2-harmonic fit, with the seasonal amplitude (Amp.) shown on the upper right of each panel.

1.4.2 Computing the hemispheric mass-weighted average CO_2 mole fraction

We next illustrate the use of $M_{\theta e}$ for computing the mass-weighted average of a long-lived chemical tracer by performing this exercise for CO_2 in the Northern Hemisphere. We calculate the Northern Hemisphere tropospheric mass-weighted average CO_2 from each airborne transect using a method that assumes that CO_2 is uniformly mixed on θ_e surfaces throughout the hemisphere (Barnes et al., 2016; Parazoo et al., 2011, 2012). We exclude airborne observation from HIPPO-1 Northbound due to the lack of data north of 40°N. We use the θ_e-$M_{\theta e}$ lookup table of the corresponding date to assign a value of $M_{\theta e}$ to each observation based on its θ_e. The observations for each transect are then sorted by $M_{\theta e}$. The hemispheric average CO_2 is calculated by trapezoidal integration of CO_2 as a function of $M_{\theta e}$ and divided by the total dry air mass as computed from the corresponding range of $M_{\theta e}$.

To illustrate the $M_{\theta e}$ integration method, we choose HIPPO-1 Southbound and show CO_2 measurements and ΔCO_2 atmospheric inventory (Pg) as a function of $M_{\theta e}$ in Figure 1.11. The Northern Hemisphere tropospheric average detrended ΔCO_2 is computed by integrating the area under the curve (subtracting negative contributions) and dividing by the maximum value of $M_{\theta e}$ within the hemisphere (here 195.13×10^{16} kg). This yields a mass-weighted average detrended ΔCO_2 of 1.13 ppm for the full troposphere of the Northern Hemisphere. The trapezoidal integration has a high accuracy because the data are dense over $M_{\theta e}$. The ΔCO_2 atmospheric inventory is dominated by the domain $M_{\theta e} < 120 \times 10^{16}$ kg (mid- to high latitude), which has a large CO_2 seasonal cycle driven by temperate and boreal ecosystem, with less than 4.1% contributed by the additional ~38.8% of the air mass outside this domain in the low latitude or upper troposphere (Fig. 11b), where ΔCO_2 differs less from the subtracted baseline.

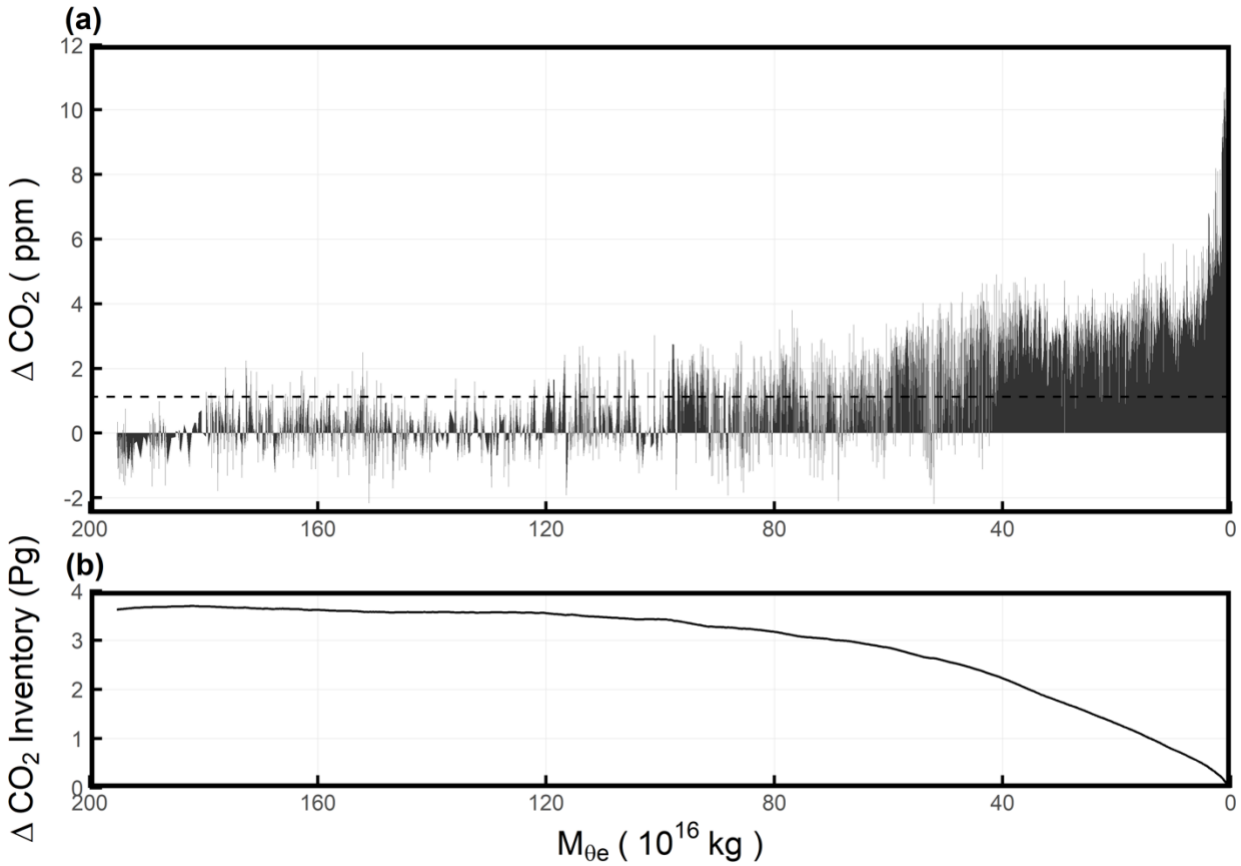

Figure 1.11: (a) Detrended CO_2 measurements from HIPPO-1 Southbound (from 12 January 2009 to 17 January 2009) plotted as a function of $M_{\theta e}$ in the Northern Hemisphere. The data are detrended by subtracting the MLO stiff cubic spline trend. Individual points are connected by straight line segments and the area under the resulting curve is shaded. We note that the area under the curve has units of ppm × kg, and dividing this by the total dry air mass (i.e., the range of $M_{\theta e}$ of the integral) gives ppm unit because the mass of dry air is proportional to the moles of dry air. The Northern Hemisphere average of 1.13 ppm is indicated by the dashed line. (b) Integral of the data in (a), rescaled from ppm to Pg, integrating from $M_{\theta e} = 0$ to a given $M_{\theta e}$ value.

We compute a Northern Hemisphere mass-weighted average detrended ΔCO_2 for each airborne campaign transect and fit the time series to a 2-harmonic fit to estimate the seasonal cycle (Figure 1.12). We find that the cycle has a seasonal amplitude of 7.9 ppm and a downward zero-crossing at Julian day 179, where the latter is defined as the date when the detrended seasonal cycle changes from positive to negative.

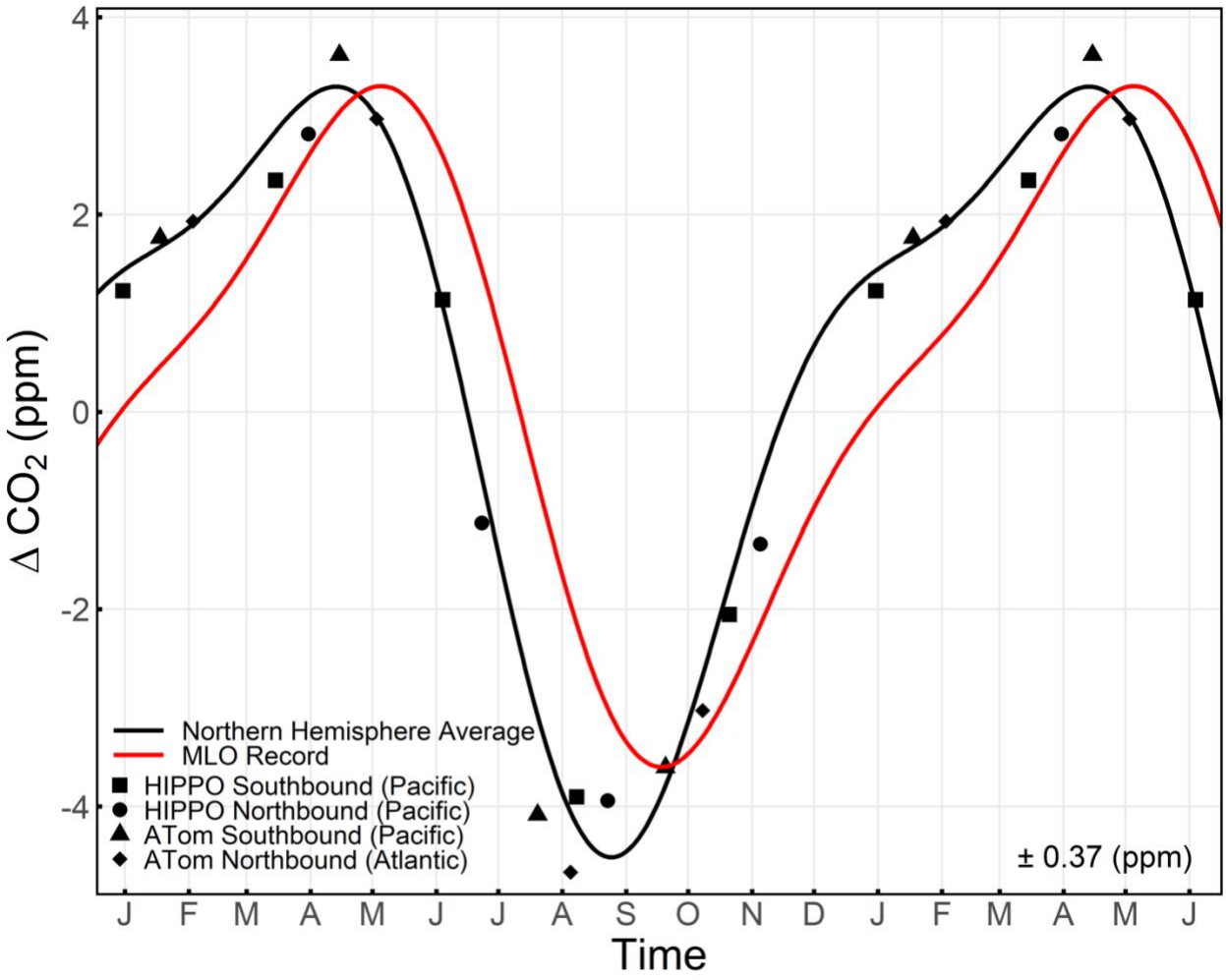

Figure 1.12: Comparison between the CO_2 seasonal cycle of Northern Hemisphere tropospheric average computed from airborne observation and the $M_{\theta e}$ integration method (black points and line) and the mean cycle at MLO measured by Scripps CO_2 Program from 2009 to 2018 (red line). Both are detrended by subtracting a stiff cubic spline trend at MLO. We then compute a mass-weighted average detrended CO_2 for each airborne campaign transect, shown as black points, with campaigns and transects be presented in different shapes. The seasonal cycle of both are computed by a 2-harmonic fit to the detrended time series. The 1$\boldsymbol{\sigma}$ variability of the detrended average CO_2 values about the fit line is shown on the lower right. The first half year is repeated for clarity.

To address the error in our estimation of Northern Hemisphere mass-weighted average CO_2 seasonal cycle from HIPPO and Atom airborne observation, we consider two main sources: (1) irreproducibility in the CO_2 measurements and (2) limited coverage in space and time. For the first contribution, we compute the difference between mass-weighted average CO_2 from AO2 and mean mass-weighted average CO_2 from Harvard QCLS, Harvard OMS, and NOAA Picarro for each

airborne campaign transect, while masking values that are missing in any of these datasets. We compute the standard deviation of these differences (± 0.15 ppm) for mass-weighted average CO_2 of each airborne campaign transect as the 1σ level of uncertainty. We further compute the uncertainties for the seasonal amplitude of ± 0.11 ppm and for the downward zero-crossing of ± 0.83 days, which are calculated from 1000 iterations of the 2-harmonic fit, allowing for random Gaussian uncertainty (σ = ± 0.15 ppm) for each transect.

For the contribution to the error in the amplitude and phase from limited special and temporal coverage, we use simulated CO_2 data from the Jena CO_2 Inversion Run ID: s04oc v4.3 (Rödenbeck et al., 2003). This model includes full atmospheric fields from 2009 to 2018, which we detrend using the cubic spline fit to the observed MLO trend. From these detrended fields, we compute the climatological cycle of the Northern Hemisphere average by integrating over all tropospheric grid cells (cutoff at PVU = 2) to produce a daily time series of the hemispheric mean, which we take as the model "truth". We fit a 2-harmonic function to this "true" time series to compute a "true" climatological cycle over the 2009-2018 period (Table 1.3), which is our target for validation. We then subsample the Jena CO_2 Inversion along the HIPPO and ATom flight tracks and process the data similarly to the observations, using the $M_{\theta e}$ integration method and a 2-harmonic fit. The comparison shows that the $M_{\theta e}$ integration method yields an amplitude which is 1% too large and yields a downward zero-crossing date which is 6 days too late. We view these offsets as systematic biases, which we correct from the observed amplitude and phase reported above. The uncertainties in these biases are hard to quantify, but we take ±100 % as a conservative estimate. We thus allow an additional random error of ± 0.08 ppm in amplitude and ± 6.0 days in downward zero crossing for uncertainty in the bias. Combining the random and systematic error contributions leads to a corrected Northern Hemisphere tropospheric average CO_2 seasonal cycle

amplitude of 7.8 ± 0.14 ppm and downward zero-crossing of 173 ± 6.1 days. This corrected cycle is an estimate of the climatological average from 2009 to 2018.

Table 1.3: RMSE, seasonal amplitude and day of year of the downward zero-crossing of each simulation based on the Jena CO_2 Inversion. The true value (daily average CO_2) is computed by integrating over all tropospheric grid cells of the Jena CO_2 Inversion, while troposphere is defined by PVU < 2 from ERA-Interim. Seasonal amplitude and downward zero-crossing of true average and each simulation is computed from 2-harmonic fit to the detrended value, which is detrended by subtracting the MLO cubic stiff spline. Subsample with randomly retaining a certain fraction of data are conducted by randomly subsampling for 1000 times, thus, the seasonal amplitude and day of year of the downward zero-crossing is computed as the mean ± standard deviation of the 1000 iterations.

Method	RMSE (ppm)[1]	Seasonal Amplitude (ppm)	Downward Zero-Crossing (day)
True Value (Cut off at PVU = 2)	/	7.58	175.1
Evaluation of $M_{\theta e}$ Integration Method			
Full Airborne Coverage	0.30	7.65	181.1
Subsample: Equator to 30°N	1.26	5.74	197.8
Subsample: Poleward of 30°N	0.82	9.47	179.0
Subsample: Surface – 600 mbar	0.57	7.77	185.1
Subsample: 600 mbar – Tropopause	0.38	7.28	180.7
Subsample: Pacific Only	0.33	7.33	181.6
Subsample: Randomly retain 10%	0.38	7.64 ± 0.116	182.4 ± 0.82
Subsample: Randomly retain 5%	0.40	7.65 ± 0.163	182.3 ± 1.08
Subsample: Randomly retain 1%	0.56	7.72 ± 0.366	182.2 ± 2.24
Subsample: MEDUSA Coverage	0.48	7.52	181.7
Evaluation of Latitude-Pressure Weighted Average Method			
Full Airborne Coverage	0.68	9.16	182.2

[1] Each simulation yields 17 data points of different date over the seasonal cycle from 17 airborne campaign transects. RMSE of each simulation is computed with respect to the true value.

The error due to limited spatial and temporal coverage can be divided into three components: limited seasonal coverage (17 transects over the climatological year), limited

interannual coverage (sampling particular years instead of all years), and limited spatial coverage (under-sampling the full hemisphere). We quantify the combined biases due to both limited seasonal and interannual coverage by comparing the two-harmonic fit of the full "true" daily time series of the hemispheric mean to a two-harmonic fit of that data subsampled on the actual mean sampling dates of the 17 flight tracks. We isolate the bias associated with limited seasonal coverage by repeating this calculation, replacing the "true" daily time series with the daily climatological cycle. The bias associated with limited spatial coverage is quantified as the residual. Combining these results, we estimate that the limited seasonal, interannual, and spatial coverage, account for biases in the downward zero-crossing of 1.1, 1.4, and 3.5 days respectively, all in the same direction (too late). The seasonal amplitude bias due to individual components are all small (< 0.5%).

It is of interest to compare our estimate of the Northern Hemisphere average cycle with the cycle at Mauna Loa, which is also broadly representative of the hemisphere. Our comparison in Figure 1.12 shows small but significant differences in both amplitude and phase, with the MLO amplitude being ~ 11.5% smaller than the hemispheric average and lagging in phase by ~ 1 month. There are also differences in the shape of the cycle, with the MLO cycle rising more slowly from October to February, but more quickly from February to May. These features at least partly reflects variations in the transport of air masses to the station (Harris et al., 1992; Harris and Kahl, 1990).

In Figure 1.13, we compare the $M_{\theta e}$ integration method with an alternate latitude-pressure weighted average method, with no correction for synoptic variability. For this method, we bin flight track subsampled Jena CO_2 Inversion data into sin(latitude)-pressure bins with 0.01 and 25 mbar as intervals respectively, while all bins without data are filtered. We further compute a weighted average CO_2 for each airborne campaign transect. The root-mean-square errors (RMSE)

to the true average of the $M_{\theta e}$ integration method are ± 0.32 and ± 0.27 ppm for HIPPO and ATom campaigns, respectively, which are smaller than the RMSE of the simple latitude-pressure weighted average method at ± 0.82 and ± 0.53 ppm.

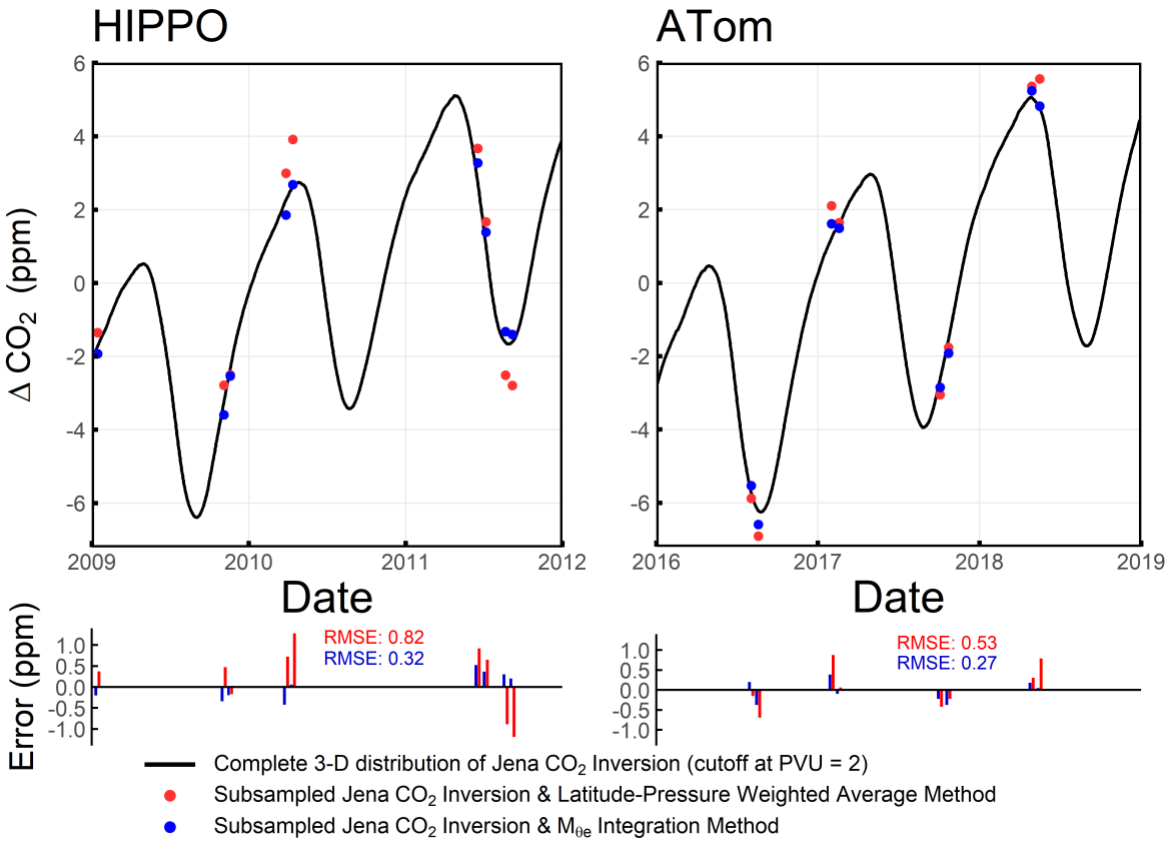

Figure 1.13: Comparison between the Northern Hemisphere average CO_2 from full integration of the simulated atmospheric fields from the Jena CO_2 Inversion (cutoff at PVU = 2) and from two methods that use the same simulated data subsampled with HIPPO/ATom coverage: (1) the $M_{\theta e}$ integration method (blue) and (2) simple integration by sin(latitude)-pressure (red). We divide the comparison into HIPPO (left) and ATom (right) temporal coverage. The lower panel shows the Error for individual tracks using alternate subsampling methods.

We also evaluate the biases in the hemispheric average seasonal cycles computed with the simple latitude-pressure weighted average method. As summarized in Table 1.3, the latitude-pressure weighted average method yields a larger error in seasonal amplitude ($M_{\theta e}$ method 1.0 % too large, latitude-pressure method 20.8% too large), while both methods show similar phasing error (6 to 7 days late). The larger error associated with the latitude-pressure weighted average

method is consistent with strong influence of synoptic variability. This synoptic variability could potentially be corrected using model simulations of the 3-dimensional CO_2 fields (Bent, 2014). The $M_{\theta e}$ integration method appears advantageous because it accounts for synoptic variability, and easily yields a hemispheric average by directly integrating over $M_{\theta e}$.

The relative success of the $M_{\theta e}$ integration method in yielding accurate hemispheric averages using HIPPO and ATom data is attributable partly to the extensive data coverage. To explore the coverage requirement for reliably resolving hemispheric averages, we also test the integration method when applied to simulated data with lower coverage. We start with the same coverage as for ATom and HIPPO but select only subsets of the points in four groups: poleward of 30°N, Equator to 30°N, surface to 600 mbar, and 600 mbar to tropopause. We also examine whether we can only utilize observation along the Pacific transect by excluding measurements along the Atlantic transects (ATom northbound). We further explore the impact of reduced sampling density by subsampling the Jena CO_2 Inversion based on the spatial coverage of the Medusa sampler, which is an airborne flask sampler that collected 32 cryogenically dried air samples per flight during HIPPO and ATom (Stephens et al., 2020). We further randomly retain 10%, 5%, and 1% of the full flight track subsampled data, repeating each ratio with 1000 iterations. We compute the detrended average CO_2 from these nine simulations by the $M_{\theta e}$ integration method and then compute the RMSE relative to the detrended true hemispheric average, together with the seasonal magnitude and day of year of the downward zero-crossing, as summarized in Table 1.3. HIPPO-1 Northbound is excluded in all these simulations. The number of data points of each simulation and number of observations of the original HIPPO and ATom data sets are summarized in Table 1.5. These results show that limiting sampling to either equatorward or poleward of 30°N yields significant error (24.3% smaller and 24.9% larger seasonal amplitude, respectively).

Additionally, there is a ~ 25-day lag in phase if sampling is limited to equatorward of 30°N. However, restricting sampling to be exclusively above or below 600 mbar, or only along the Pacific transect does not lead to significant errors. Randomly reducing the sampling by 10- to 100-fold or only keeping Medusa spatial coverage also have minimal impact. This suggests that, to compute the average CO_2 of a given region, it may be sufficient to have low sampling density provided that the measurements adequately cover the full range in θ_e (or $M_{\theta e}$).

1.5 Discussion and summary

We have presented a transformed isentropic coordinate, $M_{\theta e}$, which is the total dry air mass under a given θ_e surface in the troposphere of the hemisphere. $M_{\theta e}$ can be computed from meteorological fields by integrating dry air mass under a specific θ_e surface, and different reanalysis products show a high consistency. The θ_e-$M_{\theta e}$ relationship varies seasonally due to seasonal heating/cooling of the atmosphere via radiative heating and moist processes. The seasonality in the relationship is greater at low θ_e compared to high θ_e, and is greater in the Northern than the Southern Hemisphere. The θ_e-$M_{\theta e}$ relationship also shows synoptic-scale variability, which is mainly driven by the dissipation of kinetic energy of turbulence. $M_{\theta e}$ surfaces show much less seasonal displacement with latitude and altitude than surfaces of constant θ_e, while being parallel and exhibiting essentially identical synoptic scale variability. As a coordinate for mapping tracer distributions, $M_{\theta e}$ shares with θ_e the advantages of following displacements due to synoptic disturbances and aligning with surfaces of rapid mixing. $M_{\theta e}$ has the additional advantage of being approximately fixed in space seasonally, which allows mapping to be done on seasonal time scales, and having units of mass, which provides a close connection with atmospheric inventories.

As a coordinate, $M_{\theta e}$ is probably better viewed as an alternative to latitude, due to its nearly fixed relationship with latitude over season, rather than as an alternative to altitude (or pressure), as typically done for potential temperature (Miyazaki et al., 2008; Miyazaki and Iwasaki, 2005;

Parazoo et al., 2011; Tung, 1982; Yang et al., 2016). Even though the contours of constant $M_{\theta e}$ extend over a wide range of latitudes (from low latitudes at the Earth surface to high latitudes aloft), a close association with latitude is provided by the point of contact with Earth's surface. Also, $M_{\theta e}$ is nearly always monotonic with latitude (increasing equatorward) while it is not necessarily monotonic with altitude in the lower troposphere (Figure 1.2 and 1.3).

As a first application, we have illustrated using $M_{\theta e}$ to map the seasonal variation of CO_2 in the Northern Hemisphere, with data from the HIPPO and ATom airborne campaigns. This application shows that $M_{\theta e}$ has several advantages as a coordinate compared to using latitude: (1) variations in CO_2 with pressure are smaller at fixed $M_{\theta e}$ than at fixed latitude, and (2) the scatter about the mean CO_2 seasonal cycle is smaller when sorting data into pressure/$M_{\theta e}$ bins than into pressure/latitude bins. We have also shown that, at middle and high latitudes, the CO_2 seasonal cycles that are resolved in the airborne data (binned by $M_{\theta e}$ but not pressure) are very similar to the cycles observed at surface stations at the appropriate latitude, with a phase lag of ~ 2 to 3 weeks. At lower latitudes, CO_2 cycles in the airborne data (binned similarly by $M_{\theta e}$) are less consistent with surface data, as expected due to slow transport and diabatic processes within the Hadley Circulation. For characterizing the patterns of variability in airborne CO_2 data, we expect the advantages of $M_{\theta e}$ over latitude will be greatest for sparse datasets, allowing data to be binned more coarsely with pressure or elevation while still resolving features of large-scale variability, such as seasonal cycles or gradients with latitude.

As a second application, we use $M_{\theta e}$ to compute the Northern Hemisphere tropospheric average CO_2 from the HIPPO and ATom airborne campaigns by integrating CO_2 over $M_{\theta e}$ surfaces. With a small correction for systematic biases induced by limited hemispheric coverage of the HIPPO and ATom flight tracks, we report a seasonal amplitude of 7.8 ± 0.14 ppm and a downward

zero-crossing at Julian day 173 ± 6.1. This hemispheric average cycle may prove valuable as a target for validation of models of surface CO_2 exchange.

Our analysis also clarifies that computing hemispheric averages with the $M_{\theta e}$ integration method depends on adequate spatial coverage. The coverage provided by the HIPPO and ATom campaigns appears more than adequate for computing the average seasonal cycle of CO_2 in the Northern Hemisphere, and the errors for this application remain small if the coverage is limited to either above or below 600 mbar, or reduced to retain only 1% of the measurements. Most critical is maintaining coverage in latitude, or $M_{\theta e}$ surfaces. The $M_{\theta e}$ integration method of computing hemispheric averages assumes that the tracer is uniformly distributed and instantly mixed on θ_e ($M_{\theta e}$) surfaces. We have shown that systematic gradients in CO_2 are resolved with pressure at fixed $M_{\theta e}$, which reflects the finite rates of dispersion on θ_e surfaces. Further improvements to the integration method seem possible by integrating separately over different pressure levels, taking account of the different mass fraction in different pressure bins (e.g. Figure 1.5). The need is especially relevant for high $M_{\theta e}$ bins which are less completely mixed, and which tend to intersect the Equator or have separate surface branches. For these $M_{\theta e}$ bins, it would be more appropriate to integrate over M_θ in the upper and lower atmosphere separately. This complication is of minor importance for computing the mass-weighted average CO_2 cycle, because the cycle of CO_2 is small in these air masses.

The definition of $M_{\theta e}$ requires horizontal and vertical boundaries for the integration of dry air mass. We use the dynamic tropopause (based on PVU) and the Equator as boundaries, which is appropriate for integrating tropospheric inventories in a hemisphere. Other boundaries may be more appropriate for other applications. For example, $M_{\theta e}$ could be computed from the lowest θ_e surface in the Southern Hemisphere with a latitude cutoff at 30°S, to apply to airborne observations

only over the Southern Ocean. On the other hand, the boundary choice only influences $M_{\theta e}$ surfaces that actually intercept the boundaries, making the choice less important at high latitude in the lower troposphere (lowest $M_{\theta e}$ surfaces). Some tropospheric applications may also benefit by integrating over dry potential temperature (θ) rather than θ_e.

Based on our promising results for CO_2, we expect that $M_{\theta e}$ may be usefully applied as a coordinate for mapping and computing atmospheric inventories of many tracers, such as O_2/N_2, N_2O, CH_4, and the isotopes of CO_2, whose residence time is long compared to the time scale for mixing along isentropes. $M_{\theta e}$ may also prove useful in the design phase of airborne campaigns to ensure strategic coverage. Our results show that, to study the seasonal cycle of a tracer on a hemispheric scale, it is critical to have well-distributed sampling in $M_{\theta e}$.

1.6 Code availability

We provide R code to generate θ_e-$M_{\theta e}$ look-up tables from ERA-Interim meteorological fields at https://github.com/yumingjin0521/Mtheta.

1.7 Data availability

All HIPPO 10-sec merge data are available from: https://doi.org/10.3334/CDIAC/HIPPO_010 (Wofsy et al., 2017b). Besides, all HIPPO Medusa merge data are available from: http://dx.doi.org/10.3334/CDIAC/hippo_014 (Wofsy et al., 2017a). All ATom 10-sec and Medusa merges data are available from: https://doi.org/10.3334/ORNLDAAC/1581 (Wofsy et al., 2018).

CO_2 data from Mauna Loa Observatory are available from the Scripps CO_2 Program at: https://scrippsco2.ucsd.edu. Other surface station CO_2 data, including Trinidad Head, Cold Bay, Barrow, Cape Kumukahi, Sand Island are provided by NOAA/ESRL GMD flask sampling network (http://www.cmdl.noaa.gov/ccgg/trends) and downloaded from Observation Package (ObsPack) at http://dx.doi.org/10.25925/20190812 (Dlugokencky et al., 2019).

The Jena CO_2 Inversion are available at the project website: http://www.bgc-jena.mpg.de/CarboScope/s/main.html. Run ID: s04oc v4.3 was used in this study.

ERA-Interim is available at: https://www.ecmwf.int/en/forecasts/datasets/reanalysis-datasets/era-interim. NCEP2 is available at: https://psl.noaa.gov/data/gridded/data.ncep.reanalysis2.html. MERRA-2 is available at the NASA Goddard Earth Sciences (GES) Data and Information Services Center (DISC) at: https://disc.gsfc.nasa.gov/datasets?keywords=%22MERRA-2%22&page=1&source=Models%2FAnalyses%20MERRA-2.

θ_e-$M_{\theta e}$ look-up tables with daily resolution and 1 K intervals in θ_e from 1980 to 2018 computed from ERA-Interim are available at https://github.com/yumingjin0521/Mtheta.

1.8 Appendix A: Temporal variation of Mθe

Following Walin's derivation for cross-isothermal volume flow in the ocean (Walin, 1982), we show how $\dot{M}_{\theta_e} = \frac{\partial}{\partial t} M_{\theta_e}(\theta_e, t)$ can be related to energy and mass fluxes. We start by deriving the relationship for M_θ (based on potential temperature θ) but later generalize to apply to $M_{\theta e}$.

All definitions are summarized in Table 1.4, and Figure 14 is the schematic diagram of mass and energy flux.

Table 1.4: Definition of variables.

Variable	Definition	Unit
$\theta'(r,t)$	Potential temperature at location r and time t.	K
θ	Potential temperature of the chosen isentropic surface.	K
$R(\theta,t)$	A region in which $\theta'(r,t) < \theta$ shown as shaded area in Figure A1.	
$A_T(\theta,t)$	Area at the tropopause where $\theta'(r,t) < \theta$.	m^2
$A_E(\theta,t)$	Area at the Equator where $\theta'(r,t) < \theta$.	m^2
$A_I(\theta,t)$	Area where $\theta'(r,t) = \theta$.	m^2
$A_S(\theta,t)$	Area at the Earth surface where $\theta'(r,t) < \theta$.	m^2
$M_\theta(\theta,t)$	Dry air mass of $R(\theta,t)$.	kg
$F_T(\theta,t)$	Mass flux through $A_T(\theta,t)$. Positive value denotes flux into region $R(\theta,t)$.	kg s^{-1}
$F_E(\theta,t)$	Mass flux through $A_E(\theta,t)$. Positive value denotes flux into region $R(\theta,t)$.	kg s^{-1}
$F_I(\theta,t)$	Mass flux through $A_I(\theta,t)$. Positive value denotes flux into region $R(\theta,t)$.	kg s^{-1}
$Q_T(\theta,t)$	Heat flux through $A_T(\theta,t)$. Positive value denotes flux into region $R(\theta,t)$.	J s^{-1}
$Q_E(\theta,t)$	Heat flux through $A_E(\theta,t)$. Positive value denotes flux into region $R(\theta,t)$.	J s^{-1}
$Q_I(\theta,t)$	Heat flux through $A_I(\theta,t)$. Positive value denotes flux into region $R(\theta,t)$.	J s^{-1}
$Q_s(\theta,t)$	Surface sensible heat flux to the region $R(\theta,t)$. Positive value denotes flux into the atmosphere.	J s^{-1}
$Q_{int}(\theta,t)$	Internal heating and cooling within region $R(\theta,t)$. Positive value denotes absorbing heat.	J s^{-1}
$\frac{\partial Q_s(\theta,t)}{\partial\theta}$	Surface sensible heat flux to the θ surface. Positive value denotes flux into the atmosphere (i.e., θ surface).	J s^{-1} K^{-1}
$\frac{\partial Q_{int}(\theta,t)}{\partial\theta}$	Internal heating and cooling on the θ surface. Positive value denotes absorbing heat.	J s^{-1} K^{-1}
$\frac{\partial Q_{diff}(\theta,t)}{\partial\theta}$	Turbulent diffusive heat fluxes into the θ surface. Positive value denotes heat flux into the θ surface	J s^{-1} K^{-1}

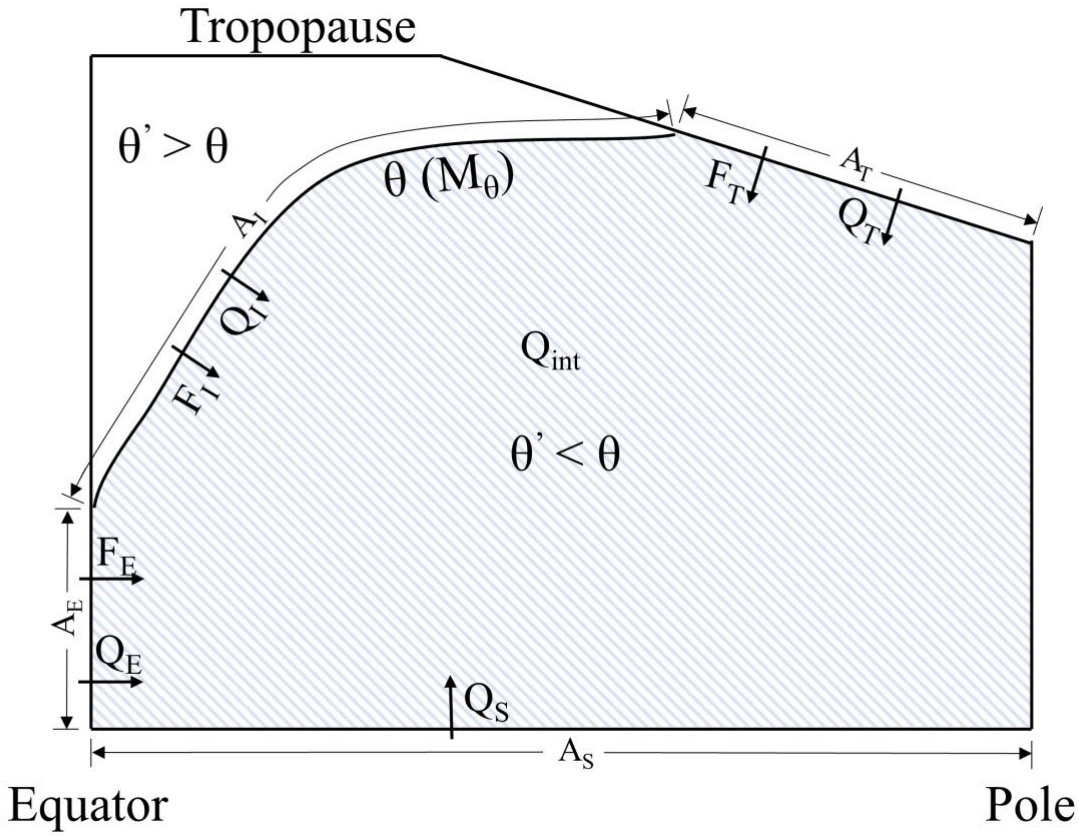

Figure 1.14: Illustration of terms defined in Table A1. Shaded area denotes the region R(θ, t) with θ′ lower than θ, which is the area of mass integration to yield M_θ. The curve denotes a given θ or M_θ surface.

All mass and heat fluxes are counted positive as into region R(θ, t). The heat fluxes through tropopause, Equator and surface of region R(θ, t) can be divided into an advective (F(θ, t)) and a turbulent (D(θ, t)) component. Integrating over the tropopause and equatorial boundary, we have:

$$Q_T(\theta,t) = C_{pd}\int_{-\infty}^{\theta}\frac{\partial F_T(\theta',t)}{\partial\theta'}\theta' d\theta' + \int_{-\infty}^{\theta}\frac{\partial D_T(\theta',t)}{\partial\theta'}d\theta' \quad (1.11)$$

$$Q_E(\theta,t) = C_{pd}\int_{-\infty}^{\theta}\frac{\partial F_E(\theta',t)}{\partial\theta'}\theta' d\theta' + \int_{-\infty}^{\theta}\frac{\partial D_E(\theta',t)}{\partial\theta'}d\theta' \quad (1.12)$$

$$Q_I(\theta,t) = C_{pd}\cdot F_I(\theta,t)\cdot\theta + D_I(\theta,t) \quad (1.13)$$

where C_{pd} is the heat capacity of dry air in units of J kg^{-1} K^{-1}.

Based on the continuity of mass and energy for region R(θ, t), we obtain

$$\frac{\partial}{\partial t}M_\theta(\theta,t) = F_T(\theta,t) + F_E(\theta,t) + F_I(\theta,t)$$

$$= \int_{-\infty}^{\theta} \frac{\partial F_T(\theta',t)}{\partial \theta'} d\theta' + \int_{-\infty}^{\theta} \frac{\partial F_E(\theta',t)}{\partial \theta'} d\theta' + F_I(\theta,t) \tag{1.14}$$

$$C_{pd}\frac{\partial}{\partial t}\int_{-\infty}^{\theta} \frac{\partial M_\theta(\theta',t)}{\partial \theta'}\theta' d\theta' = Q_T(\theta,t) + Q_E(\theta,t) + Q_I(\theta,t) + \int_{-\infty}^{\theta} \frac{\partial Q_s(\theta',t)}{\partial \theta'} d\theta' + \int_{-\infty}^{\theta} \frac{\partial Q_{int}(\theta',t)}{\partial \theta'} d\theta' \tag{1.15}$$

Substituting Eq. 1.11 to Eq. 1.13 into Eq. 1.15 and differentiating with respect to θ yields

$$C_{pd}\theta\frac{\partial}{\partial t}\frac{\partial M_\theta(\theta,t)}{\partial \theta} = C_{pd}\theta\left(\frac{\partial F_T(\theta,t)}{\partial \theta} + \frac{\partial F_E(\theta,t)}{\partial \theta} + \frac{\partial F_I(\theta,t)}{\partial \theta}\right) + C_{pd}F_I(\theta,t) + \frac{\partial Q_{diff}(\theta,t)}{\partial \theta} + \frac{\partial Q_s(\theta,t)}{\partial \theta} + \frac{\partial Q_{int}(\theta,t)}{\partial \theta} \tag{1.16}$$

where,

$$Q_{diff}(\theta,t) = \int_{-\infty}^{\theta} \frac{\partial D_T(\theta',t)}{\partial \theta'} d\theta' + \int_{-\infty}^{\theta} \frac{\partial D_E(\theta',t)}{\partial \theta'} d\theta' + D_I(\theta,t) \tag{1.17}$$

Differentiating Eq. 1.14 with respect to θ, and multiplying $C_{pd} \cdot \theta$ yields

$$C_{pd}\theta\frac{\partial}{\partial t}\frac{\partial M_\theta(\theta,t)}{\partial \theta} = C_{pd}\theta\left(\frac{\partial F_T(\theta,t)}{\partial \theta} + \frac{\partial F_E(\theta,t)}{\partial \theta} + \frac{\partial F_I(\theta,t)}{\partial \theta}\right) \tag{1.18}$$

Subtracting Eq. 1.18 from Eq. 1.16, we obtain

$$C_{pd}F_I(\theta,t) = -\frac{\partial Q_{diff}(\theta,t)}{\partial \theta} - \frac{\partial Q_s(\theta,t)}{\partial \theta} - \frac{\partial Q_{int}(\theta,t)}{\partial \theta} \tag{1.19}$$

Eq. 1.19 divided by C_{pd} plus Eq. 1.14 yields

$$\frac{\partial}{\partial t}M_\theta(\theta,t) = -\frac{1}{C_{pd}}\left(\frac{\partial Q_{diff}(\theta,t)}{\partial \theta} + \frac{\partial Q_s(\theta,t)}{\partial \theta} + \frac{\partial Q_{int}(\theta,t)}{\partial \theta}\right) + \int_{-\infty}^{\theta} \frac{\partial F_T(\theta',t)}{\partial \theta'} d\theta' + \int_{-\infty}^{\theta} \frac{\partial F_E(\theta',t)}{\partial \theta'} d\theta' \tag{1.20}$$

Eq. 1.20 illustrates the temporal variation of M_θ, where Q_{int} includes radiative heating (i.e. sum of shortwave and longwave heating), dissipation of kinetic energy of turbulence, and latent heat release due to evaporation and condensation.

To modify Eq. 1.20 to apply to $M_{\theta e}$ rather than M_θ, it is necessary to replace all θ with θ_e, and additionally account for the following:

1. Condensation and evaporation is conserved on the θ_e surfaces, but the gaining and losing of water vapor through surface evaporation and water vapor transport contributes to θ_e. This contribution can be computed as the product of latent heat of evaporation and the extra water vapor content. Thus, the surface contribution (Q_S) needs to include both sensible heating of the atmosphere (Q_{sen}) and the water vapor flux from the surface into the atmosphere (Q_{evap}). Similarly, the diffusion term within the atmosphere (Q_{diff}) needs to include both heat and water vapor (Q_{H_2O}).

2. Internal heating (Q_{int}) needs to exclude latent heat releasing due to evaporation and condensation of liquid water, which cancel in θ_e, but it still needs to include heating from ice formation, which does not cancel in θ_e. We subtract this ice component from the rest of the internal heating, yielding two terms Q'_{int} and Q_{ice}, with $Q_{int} = Q'_{int} + Q_{ice}$.

Therefore, we can write the temporal variation of $M_{\theta e}$ as

$$\frac{\partial}{\partial t} M_{\theta e}(\theta_e, t) = \int_{-\infty}^{\theta_e} \frac{\partial F_T(\theta'_e, t)}{\partial \theta'_e} d\theta'_e + \int_{-\infty}^{\theta_e} \frac{\partial F_E(\theta'_e, t)}{\partial \theta'_e} d\theta'_e - \frac{1}{C_{pd}} \left(\begin{array}{c} \frac{\partial Q_{diff}(\theta_e, t)}{\partial \theta_e} + \frac{\partial Q_{sen}(\theta_e, t)}{\partial \theta_e} + \frac{\partial Q_{evap}(\theta_e, t)}{\partial \theta_e} + \\ \frac{\partial Q'_{int}(\theta_e, t)}{\partial \theta_e} + \frac{\partial Q_{ice}(\theta_e, t)}{\partial \theta_e} + \frac{\partial Q_{H_2O}(\theta_e, t)}{\partial \theta_e} \end{array} \right) \quad (1.21)$$

1.9 Supplement

1.9.1 Contribution of each heating term to the overall time variation of $M_{\theta e}$

The fractional contributions from different heating terms to the temporal variation of $M_{\theta e}$ on seasonal and synoptic scales are computed by using a vector projection method (Graven et al., 2013). In this method, each heating term ($\frac{\partial}{\partial t} M^{i}_{\theta_e}(\theta_e, t)$) is projected onto the sum of all the heating terms ($\frac{\partial}{\partial t} M_{\theta_e}(\theta_e, t)$) via:

$$x_i = \frac{\sum_t \left[\frac{\partial}{\partial t} M^{i}_{\theta_e}(\theta_e, t) \cdot \frac{\partial}{\partial t} M_{\theta_e}(\theta_e, t)\right]}{\sum_t \left[\frac{\partial}{\partial t} M_{\theta_e}(\theta_e, t) \cdot \frac{\partial}{\partial t} M_{\theta_e}(\theta_e, t)\right]} \tag{1.22}$$

with

$$\frac{\partial}{\partial t} M_{\theta_e}(\theta_e, t) = \sum_i \frac{\partial}{\partial t} M^{i}_{\theta_e}(\theta_e, t) \tag{1.23}$$

where the sum is over all time steps, and the mean of each $\frac{\partial}{\partial t} M^{i}_{\theta_e}(\theta_e, t)$ has been pre-subtracted (i.e., $\sum_t \frac{\partial}{\partial t} M^{i}_{\theta_e}(\theta_e, t) = 0$). The sum over x_i equals 1, but individual x_i can be either positive or negative and the absolute value can be either larger or smaller than 1.

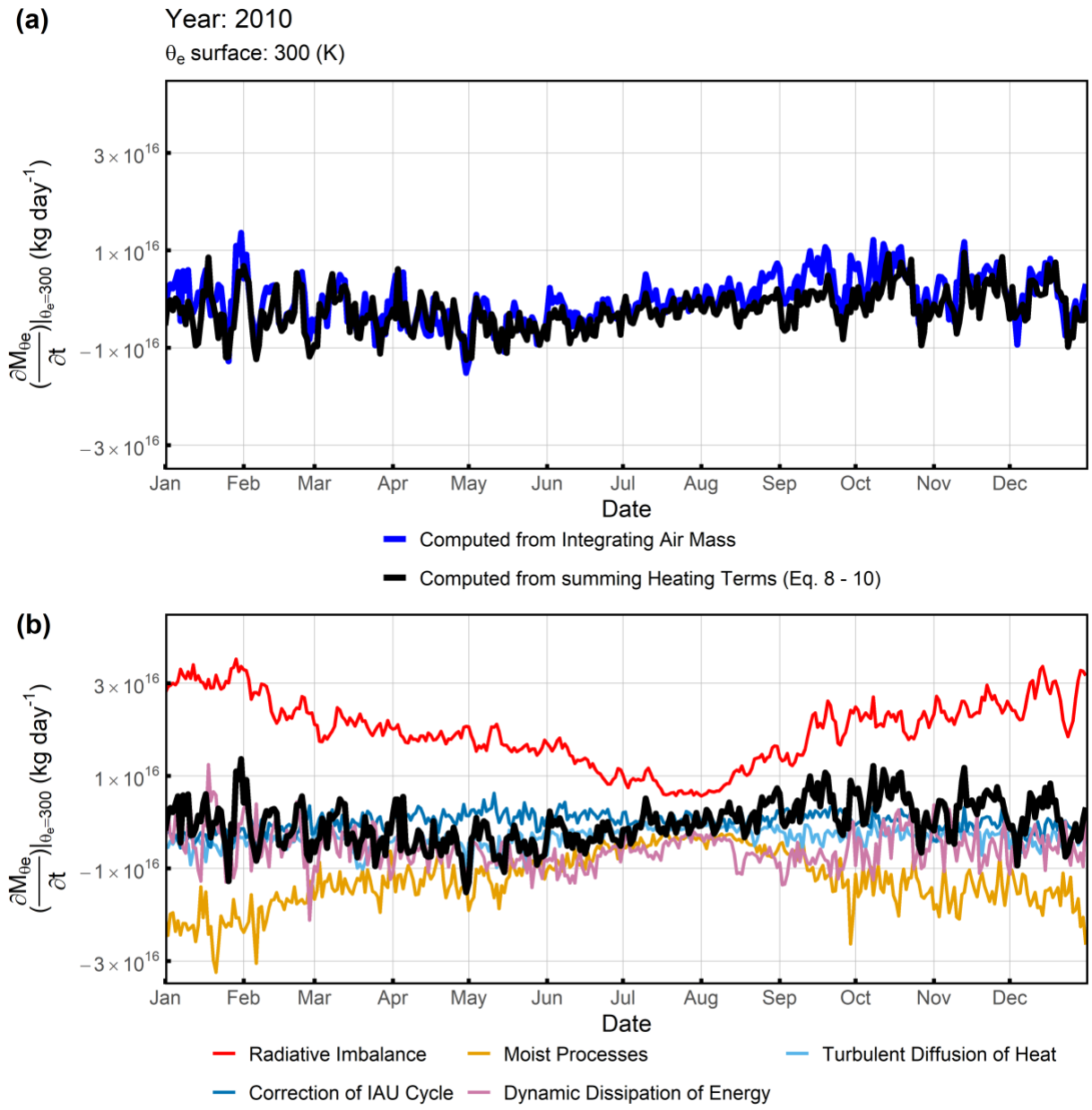

Figure 1.15: (a) Temporal variation of $M_{\theta e}$ in the Northern Hemisphere at θ_e = 300 K computed by integrating air mass (blue line) and estimated from the sum of five heating terms (Table 1.1) in MERRA-2 (black line). (b) The heating variables decomposed into five contributions as indicated (see Table 1). Results shown are for the year 2010.

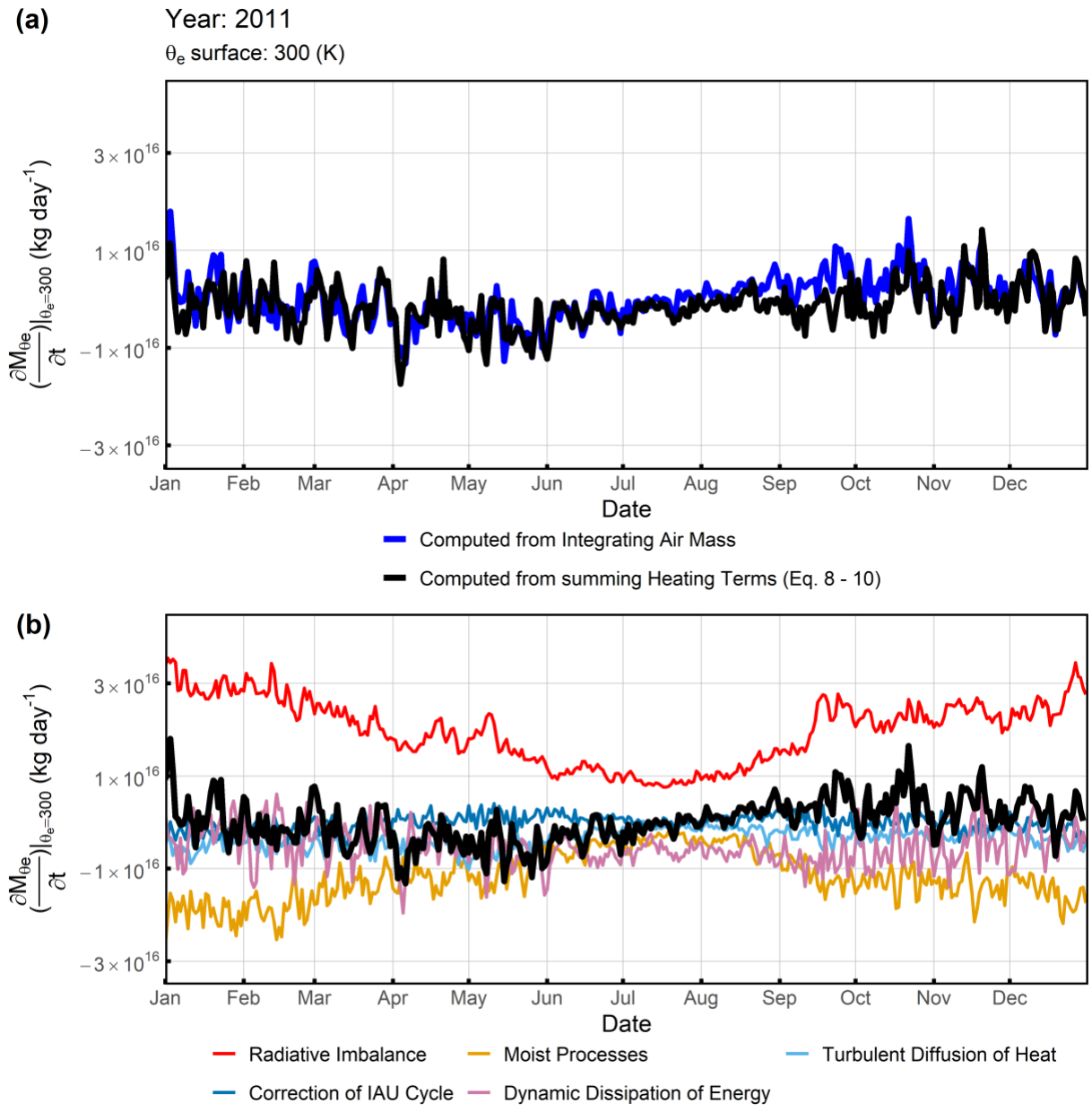

Figure 1.16: Similar to Figure 1.15, but for the year 2011.

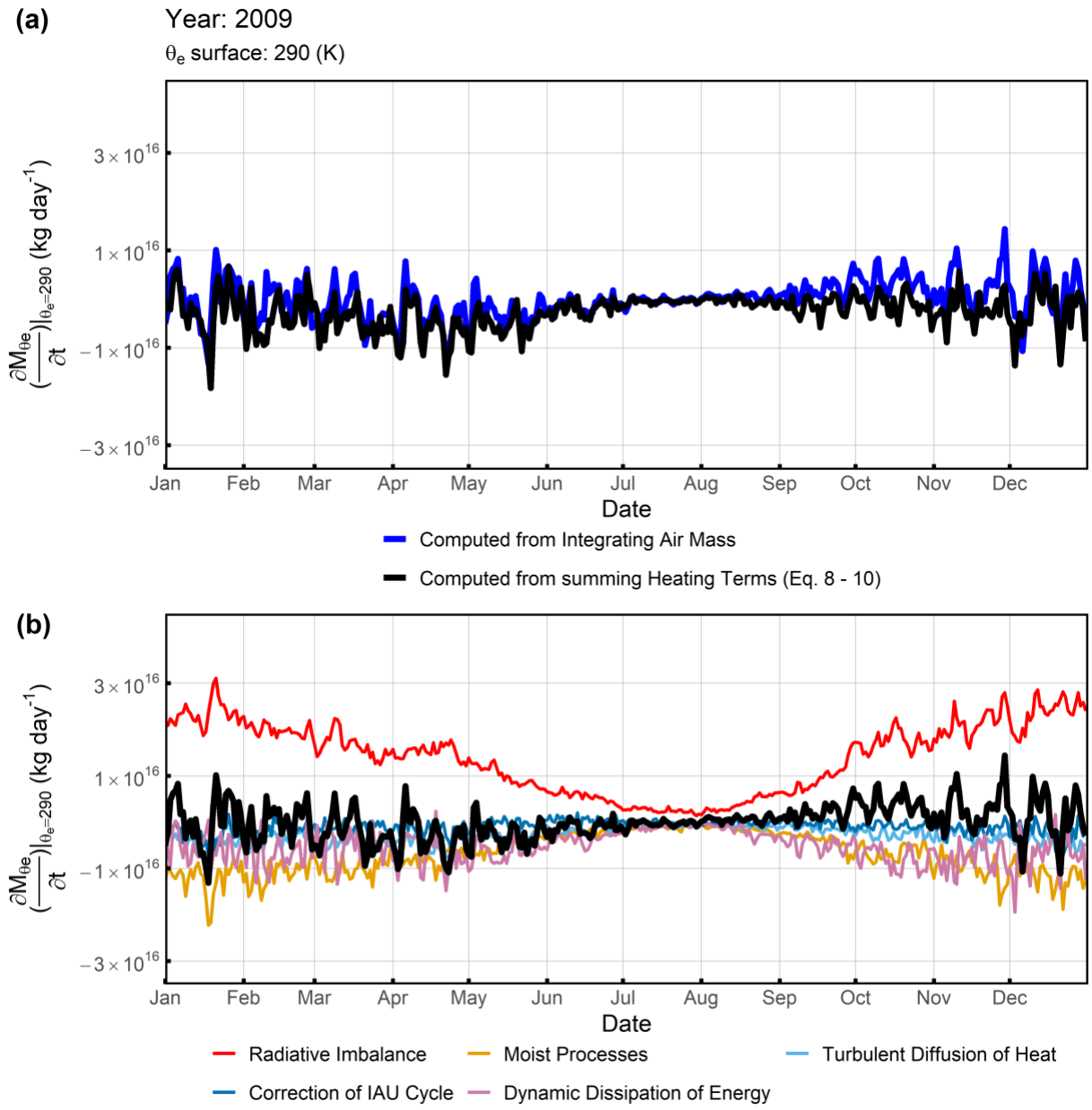

Figure 1.17: Similar to Figure 1.15, but for the year 2009.

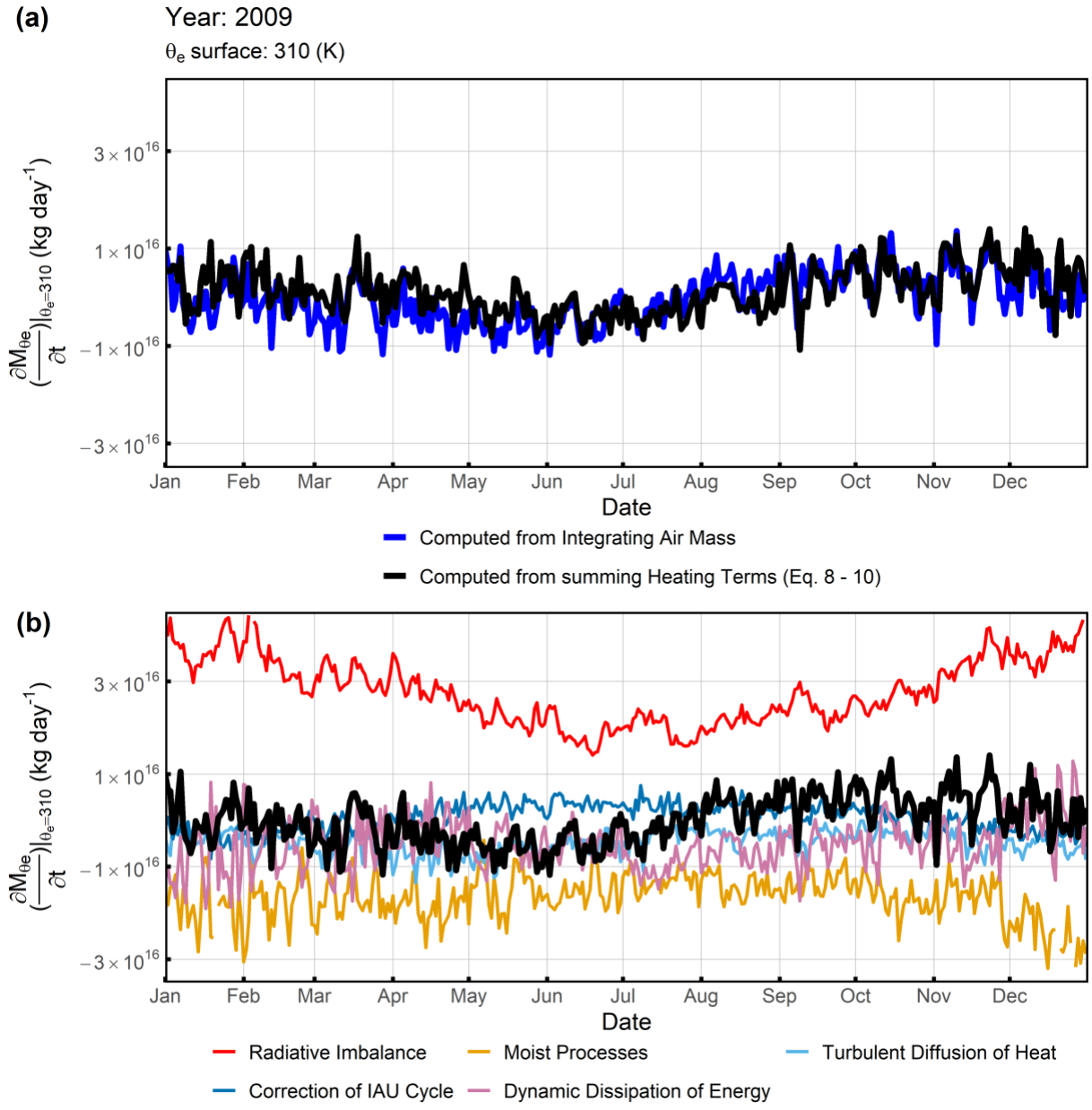

Figure 1.18: Similar to Figure 1.17, but on the 310 K θ_e surface.

Table 1.5: Number of data points of each airborne campaign transect for each simulation

Airborne Transect	Original	Equator to 30 °N	Poleward of 30 °N	Surface – 600 mbar	600 mbar – Trop.	Pacific Only	Medusa Coverage	Random 10 %	Random 5 %	Random 1 %
HIPPO1 SB	4837	1454	3383	1794	3043	4837	76	484	242	48
HIPPO2 SB	4665	1510	3155	1945	2720	4665	82	451	233	45
HIPPO2 NB	5508	2428	3080	2159	3349	5508	93	543	275	54
HIPPO3 SB	4439	1371	3068	2038	2401	4439	88	427	222	43
HIPPO3 NB	4086	1135	2951	1790	2296	4086	84	399	204	40
HIPPO4 SB	5491	1602	3889	2340	3151	5491	81	534	275	53
HIPPO4 NB	6411	3134	3277	3142	3269	6411	124	626	321	63
HIPPO5 SB	5538	1678	3860	2569	2969	5538	78	548	277	55
HIPPO5 NB	4715	1705	3010	2066	2649	4715	86	392	236	39
ATom1 SB	9832	2333	7499	3186	6646	9832	83	455	492	46
ATom1 NB	10685	3186	7499	3665	7020	0	59	893	534	89
ATom2 SB	11372	3909	7463	4057	7315	11372	84	1109	569	111
ATom2 NB	10741	3284	7457	3792	6949	0	91	1042	537	104
ATom3 SB	15143	3751	11392	4817	10326	15143	87	1460	757	146
ATom3 NB	14039	4173	9866	4764	9275	0	92	1362	702	136
ATom4 SB	13554	3683	9871	5249	8305	13554	84	1327	678	132
ATom4 NB	11995	3626	8369	4130	7865	0	89	1187	600	119

1.10 Acknowledgements

The original $M_{\theta e}$ concept arose out of discussions during the ORCAS field campaign that included Ralph Keeling, Colm Sweeney, Eric Kort, Matthew Long, and Martin Hoecker-Martinez. We would like to acknowledge the efforts of the full HIPPO and ATom science teams and the pilots and crew of the NCAR/NSF GV and NASA DC-8, the NCAR and NASA project managers, field support staff, and logistics experts. In this work, we have used the HIPPO and ATom 10-sec merge files, supported by the National Center for Atmospheric Research (NCAR). NCAR is sponsored by the National Science Foundation under Cooperative Agreement No. 1852977. The HIPPO program was supported by NSF grants ATM-0628575, ATM-0628519 and ATM-0628388 to Harvard University, University of California San Diego, NCAR, and the University of Colorado/CIRES. The ATom program was supported by the NASA grant NNX15AJ23G. Medusa and AO2 measurements on ATom were supported NSF grants AGS-1547797 and AGS-1623748 to University of California San Diego and NCAR. YJ and EJM are also supported under AGS-

1623748. We thank the Harvard QCLS, Harvard OMS, NOAA UCATS and NOAA Picarro teams for sharing measurements. We thank NOAA ESRL GML for providing surface station CO_2 data measured at Trinidad Head, Cold Bay, Barrow, Cape Kumukahi, and Sand Island. We thank Christian Rödenbeck for sharing Jena CO_2 Inversion run. We thank the two anonymous reviewers for their valuable comments and efforts.

Any opinions, findings, and conclusions or recommendations expressed in this material are those of the authors and do not necessarily reflect the views of the National Science Foundation.

Chapter 1, in full, is a reprint of the material as it appears in Jin, Y., Keeling, R. F., Morgan, E. J., Ray, E., Parazoo, N. C., & Stephens, B. B, 2021. A mass-weighted isentropic coordinate for mapping chemical tracers and computing atmospheric inventories. Atmospheric Chemistry and Physics, 21(1), 217-238. https://doi.org/10.5194/acp-21-217-2021. The dissertation author was the primary investigator and author of this paper.

References

Arora, K., Cazenave, A., Engdahl, E. R., Kind, R., Manglik, A., Roy, S., Sain, K. and Uyeda, S.: Encyclopedia of solid earth geophysics, Springer Science & Business Media, 2011.

Bailey, A., Singh, H. K. A. and Nusbaumer, J.: Evaluating a Moist Isentropic Framework for Poleward Moisture Transport: Implications for Water Isotopes Over Antarctica, Geophys. Res. Lett., 46(13), 7819–7827, https://doi.org/10.1029/2019GL082965, 2019.

Barnes, E. A., Parazoo, N., Orbe, C. and Denning, A. S.: Isentropic transport and the seasonal cycle amplitude of CO_2, J. Geophys. Res. Atmos., 121(13), 8106–8124, https://doi.org/10.1002/2016JD025109, 2016.

Bent, J. D.: Airborne oxygen measurements over the Southern Ocean as an integrated constraint of seasonal biogeochemical processes, University of California, San Diego, 2014.

Birner, T., Do, A. and Schumann, U.: How sharp is the tropopause at midlatitudes?, Geophys. Res.

Lett., 29(14), 1–4, https://doi.org/10.1029/2002GL015142, 2002.

Bolton, D.: The computation of equivalent potential temperature, Mon. Weather Rev., 108(7), 1046–1053, https://doi.org/10.1175/1520-0493(1980)108<1046:TCOEPT>2.0.CO;2, 1980.

Bozem, H., Hoor, P., Kunkel, D., Köllner, F., Schneider, J., Herber, A., Schulz, H., Leaitch, W. R., Aliabadi, A. A., Willis, M. D. and Burkart, J.: Characterization of transport regimes and the polar dome during Arctic spring and summer using in situ aircraft measurements, Atmos. Chem. Phys., 19, 15049–15071, https://doi.org/10.5194/acp-19-15049-2019, 2019.

Butchart, N. and Remsberg, E. E.: The area of the stratospheric polar vortex as a diagnostic for tracer transport on an isentropic surface, J. Atmos. Sci., 43(13), 1319–1339, https://doi.org/10.1175/1520-0469(1986)043<1319:TAOTSP>2.0.CO;2, 1986.

Conway, T. J. and Tans, P. P.: Development of the CO_2 latitude gradient in recent decades, Global Biogeochem. Cycles, 13(4), 821–826, https://doi.org/10.1029/1999GB900045, 1999.

Dee, D. P., Uppala, S. M., Simmons, A. J., Berrisford, P., Poli, P., Kobayashi, S., Andrae, U., Balmaseda, M. A., Balsamo, G., Bauer, P., Bechtold, P., Beljaars, A. C. M., van de Berg, L., Bidlot, J., Bormann, N., Delsol, C., Dragani, R., Fuentes, M., Geer, A. J., Haimberger, L., Healy, S. B., Hersbach, H., Hólm, E. V., Isaksen, L., Kållberg, P., Köhler, M., Matricardi, M., Mcnally, A. P., Monge-Sanz, B. M., Morcrette, J. J., Park, B. K., Peubey, C., de Rosnay, P., Tavolato, C., Thépaut, J. N. and Vitart, F.: The ERA-Interim reanalysis: Configuration and performance of the data assimilation system, Q. J. R. Meteorol. Soc., 137(656), 553–597, https://doi.org/10.1002/qj.828, 2011.

Dima, I. M. and Wallace, J. M.: On the Seasonality of the Hadley Cell, J. Atmos. Sci., 60(12), 1522–1527, https://doi.org/10.1175/1520-0469(2003)060<1522:OTSOTH>2.0.CO;2, 2003.

Dlugokencky, E. J., Mund, J. W., Crotwell, A. M., Crotwell, M. J. and Thoning, K. W.:

Atmospheric Carbon Dioxide Dry Air Mole Fractions from the NOAA ESRL Carbon Cycle Cooperative Global Air Sampling Network, 1968-2018, Version: 2019-07, https://doi.org/10.15138/wkgj-f215., 2019.

Ehhalt, D. H.: The CH_4 concentration over the ocean and its possible variation with latitude, Tellus, 30(2), 169–176, https://doi.org/10.3402/tellusa.v30i2.10329, 1978.

Fasullo, J. T. and Trenberth, K. E.: The annual cycle of the energy budget. Part I: Global mean and land-ocean exchanges, J. Clim., 21(10), 2297–2312, https://doi.org/10.1175/2007JCLI1935.1, 2008.

Foltz, G. R. and McPhaden, M. J.: The role of oceanic heat advection in the evolution of tropical North and South Atlantic SST anomalies, J. Clim., 19(23), 6122–6138, https://doi.org/10.1175/JCLI3961.1, 2006.

Gelaro, R., McCarty, W., Suárez, M. J., Todling, R., Molod, A., Takacs, L., Randles, C. A., Darmenov, A., Bosilovich, M. G., Reichle, R., Wargan, K., Coy, L., Cullather, R., Draper, C., Akella, S., Buchard, V., Conaty, A., da Silva, A. M., Gu, W., Kim, G. K., Koster, R., Lucchesi, R., Merkova, D., Nielsen, J. E., Partyka, G., Pawson, S., Putman, W., Rienecker, M., Schubert, S. D., Sienkiewicz, M. and Zhao, B.: The Modern-Era Retrospective Analysis for Research and Applications, Version 2 (MERRA-2), J. Clim., 30(14), 5419–5454, https://doi.org/10.1175/JCLI-D-16-0758.1, 2017.

Graven, H. D., Keeling, R. F., Piper, S. C., Patra, P. K., Stephens, B. B., Wofsy, S. C., Welp, L. R., Sweeney, C., Tans., P. P., Kelley, J. J., Daube, B. C., Kort, E. A., Santoni, G. W. and Bent, J. D.: Enhanced seasonal exchange of CO_2 by northern ecosystems since 1960, Science, 341(6150), 1085–1089, https://doi.org/10.1126/science.1239207, 2013.

Harris, J. M. and Kahl, J. D.: A descriptive atmospheric transport climatology for the Mauna Loa

Observatory, using clustered trajectories, J. Geophys. Res. Atmos., 95(D9), 13651–13667, https://doi.org/10.1029/jd095id09p13651, 1990.

Harris, J. M., Tans, P. P., Dlugokencky, E. J., Masarie, K. A., Lang, P. M., Whittlestone, S. and Steele, L. P.: Variations in atmospheric methane at Mauna Loa Observatory related to long-range transport, J. Geophys. Res. Atmos., 97(D5), 6003–6010, https://doi.org/10.1029/92JD00158, 1992.

Hoskins, B. J. and Karoly, D. J.: The Steady Linear Response of a Spherical Atmosphere to Thermal and Orographic Forcing, J. Atmos. Sci., 38(6), 1179–1196, https://doi.org/10.1175/1520-0469(1981)038<1179:TSLROA>2.0.CO;2, 1981.

Hurst, D.: Global Monitoring Division (GMD), Earth System Research Laboratory, NOAA. 2011. UCATS 2-Channel Gas Chromatograph (GC). Version 1.0. UCAR/NCAR - Earth Observing Laboratory. https://data.eol.ucar.edu/dataset/112.021., n.d.

Irina, P., Hoor, P., Millán, L., Jordan, A., Kunkel, D., Leblanc, T., Manney, G. and Damadeo, R.: An Overview of OCTAV-UTLS (Observed Composition Trends and Variability in the UTLS), a SPARC Activity, Geophys. Res. Abstr., 21, 2019.

Jacob, D. J.: Introduction to atmospheric chemistry, Princeton University Press, 1999.

Kanamitsu, M., Ebisuzaki, W., Woollen, J., Yang, S.-K., Hnilo, J. J., Fiorino, M. and Potter, G. L.: NCEP-DOE AMIP-II Renalalysys (R-2), Bull. Am. Meteorol. Soc., 83(11), 1631–1643, https://doi.org/10.1175/BAMS-83-11, 2002.

Keppel-Aleks, G., Wennberg, P. O. and Schneider, T.: Sources of variations in total column carbon dioxide, Atmos. Chem. Phys., 11, 3581–3593, https://doi.org/10.5194/acp-11-3581-2011, 2011.

Li, Z. and Leighton, H. G.: Global climatologies of solar radiation budgets at the surface and in

the atmosphere from 5 years of ERBE data, J. Geophys. Res. Atmos., 98(D3), 4919–4930, https://doi.org/10.1029/93jd00003, 1993.

Linz, M., Plumb, R. A., GerBer, E. P. and Sheshadri, A.: The Relationship between Age of Air and the Diabatic Circulation of the Stratosphere, J. Atmos. Sci., 73(11), 4507–4518, https://doi.org/10.1175/JAS-D-16-0125.1, 2016.

Miyazaki, K. and Iwasaki, T.: Diagnosis of Meridional Ozone Transport Based on Mass-Weighted Isentropic Zonal Means, J. Atmos. Sci., 62(4), 1192–1208, https://doi.org/10.1175/JAS3394.1, 2005.

Miyazaki, K., Patra, P. K., Takigawa, M., Iwasaki, T. and Nakazawa, T.: Global-scale transport of carbon dioxide in the troposphere, J. Geophys. Res. Atmos., 113(D15), D15301, https://doi.org/10.1029/2007JD009557, 2008.

Mooney, P. A., Mulligan, F. J. and Fealy, R.: Comparison of ERA-40, ERA-Interim and NCEP/NCAR reanalysis data with observed surface air temperatures over Ireland, Int. J. Climatol., 31(4), 545–557, https://doi.org/10.1002/joc.2098, 2011.

Parazoo, N. C., Denning, A. S., Kawa, S. R., Corbin, K. D., Lokupitiya, R. S. and Baker, I. T.: Mechanisms for synoptic variations of atmospheric CO_2 in North America, South America and Europe, Atmos. Chem. Phys., 8, 7239–7254, https://doi.org/10.5194/acp-8-7239-2008, 2008.

Parazoo, N. C., Denning, A. S., Berry, J. A., Wolf, A., Randall, D. A., Kawa, S. R., Pauluis, O. and Doney, S. C.: Moist synoptic transport of CO_2 along the mid-latitude storm track, Geophys. Res. Lett., 38(9), https://doi.org/10.1029/2011GL047238, 2011.

Parazoo, N. C., Denning, A. S., Kawa, S. R., Pawson, S. and Lokupitiya, R.: CO_2 flux estimation errors associated with moist atmospheric processes, Atmos. Chem. Phys., 12, 6405–6416, https://doi.org/10.5194/acp-12-6405-2012, 2012.

Pauluis, O., Czaja, A. and Korty, R.: The global atmospheric circulation on moist isentropes, Science, 321(5892), 1075–1078, https://doi.org/10.1126/science.1159649, 2008.

Pauluis, O., Czaja, A. and Korty, R.: The global atmospheric circulation in moist isentropic coordinates, J. Clim., 23(11), 3077–3093, https://doi.org/10.1175/2009JCLI2789.1, 2010.

Prather, M. J., Flynn, C. M., Fiore, A., Correa, G., Strode, S. A., Steenrod, S. D., Murray, L. T. and Lamarque, J. F.: ATom: Simulated Data Stream for Modeling ATom-like Measurements, ORNL Distributed Active Archive Center, 2018.

Randerson, T., Thompson, V., Conway, J., Fung, I. Y. and Field, B.: The contribution of terrestrial sources and sinks to trends in the seasonal cycle of atmospheric carbon dioxide, Global Biogeochem. Cycles, 11(4), 535–560, https://doi.org/10.1029/97GB02268, 1997.

Rasmussen, R. A. and Khalil, R. A. K.: Atmospheric Methane (CH_4): Trends and Seasonal Cycles, J. Geophys. Res., 86(C10), 9826–9832, https://doi.org/10.1029/JC086iC10p09826, 1981.

Rödenbeck, C., Houweling, S., Gloor, M. and Heimann, M.: CO_2 flux history 1982–2001 inferred from atmospheric data using a global inversion of atmospheric transport, Atmos. Chem. Phys., 3, 1919–1964, https://doi.org/10.5194/acp-3-1919-2003, 2003.

Santoni, G. W., Daube, B. C., Kort, E. A., Jiménez, R., Park, S., Pittman, J. V., Gottlieb, E., Xiang, B., Zahniser, M. S., Nelson, D. D., Mcmanus, J. B., Peischl, J., Ryerson, T. B., Holloway, S., Andrews, A. E., Sweeney, C., Hall, B., Hintsa, E. J., Moore, F. L., Elkins, J. W., Hurst, D. F., Stephens, B. B., Bent, J. and Wofsy, S. C.: Evaluation of the airborne quantum cascade laser spectrometer (QCLS) measurements of the carbon and greenhouse gas suite - CO_2, CH_4, N_2O, and CO - during the CalNex and HIPPO Campaigns, Atmos. Meas. Tech., 7, 1509–1526, https://doi.org/10.5194/amt-7-1509-2014, 2014.

Stephens, B. B., Morgan, E. J., Bent, J. D., Keeling, R. F., Watt, A. S., Shertz, S. R. and Daube,

B. C.: Airborne measurements of oxygen concentration from the surface to the lower stratosphere and pole to pole, Atmopsheric Meas. Tech. Discuss., https://doi.org/10.5194/amt-2020-294, 2020.

Stull, R. B.: An introduction to boundary layer meteorology, Springer Science & Business Media, 2012.

Sweeney, C., Karion, A., Wolter, S., Newberger, T., Guenther, D., Higgs, J. A., Andrews, A. E., Lang, P. M., Neff, D., Dlugokencky, E., Miller, J. B., Montzka, S. A., Miller, B. R., Masarie, K. A., Biraud, S. C., Novelli, P. C., Crotwell, M., Crotwell, A. M., Thoning, K. and Tans, P. P.: Seasonal climatology of CO_2 across North America from aircraft measurements in the NOAA/ESRL Global Greenhouse Gas Reference Network, J. Geophys. Res. Atmos., 120(10), 5155–5190, https://doi.org/10.1002/2014JD022591, 2015.

Tohjima, Y., Minejima, C., Mukai, H., MacHida, T., Yamagishi, H. and Nojiri, Y.: Analysis of seasonality and annual mean distribution of atmospheric potential oxygen (APO) in the Pacific region, Global Biogeochem. Cycles, 26(4), 1–15, https://doi.org/10.1029/2011GB004110, 2012.

Tung, K. K.: On the Two-Dimensional Transport of Stratospheric Tracer Gases in Isentropic Coordinates, J. Atmos. Sci., 39(10), 2330–2355, https://doi.org/10.1175/1520-0469(1982)039<2330:OTTDTO>2.0.CO;2, 1982.

Walin, G.: On the relation between sea-surface heat flow and thermal circulation in the ocean, Tellus, 34(2), 187–195, https://doi.org/10.3402/tellusa.v34i2.10801, 1982.

Wang, J. W., Denning, A. S., Lu, L., Baker, I. T., Corbin, K. D. and Davis, K. J.: Observations and simulations of synoptic, regional, and local variations in atmospheric CO_2, J. Geophys. Res. Atmos., 112(D4), https://doi.org/10.1029/2006JD007410, 2007.

Wexler, A.: Vapor pressure equation for water in the range 0 to 100°C, J. Res. Natl. Bur. Stand. Sect. A Phys. Chem., 80A(5-6), 775–785, https://doi.org/10.6028/jres.075a.022, 1976.

Wills, R. C. J. and Schneider, T.: Mechanisms setting the strength of orographic Rossby waves across a wide range of climates in a moist idealized GCM, J. Clim., 31(18), 7679–7700, https://doi.org/10.1175/JCLI-D-17-0700.1, 2018.

Wofsy, S.: HIPPO MEDUSA Flask Sample Trace Gas And Isotope Data. Version 1.0. UCAR/NCAR - Earth Observing Laboratory. https://doi.org/10.3334/CDIAC/HIPPO_014., 2017a.

Wofsy, S. C.: HIAPER Pole-to-Pole Observations (HIPPO): fine-grained, global-scale measurements of climatically important atmospheric gases and aerosols, Philos. Trans. R. Soc. A Math. Phys. Eng. Sci., 369(1943), 2073–2086, https://doi.org/10.1098/rsta.2010.0313, 2011.

Wofsy, S. C.: HIPPO Merged 10-Second Meteorology, Atmospheric Chemistry, and Aerosol Data. Version 1.0. UCAR/NCAR - Earth Observing Laboratory. https://doi.org/10.3334/CDIAC/HIPPO_010., 2017b.

Wofsy, S. C., Afshar, S., Allen, H., APEL, E., Asher, E., Barletta, B., Bent, J., Bian, H., Biggs, B., Blake, D. and Others: ATom: Merged Atmospheric Chemistry, Trace Gases, and Aerosols, ORNL DAAC, https://doi.org/10.3334/ORNLDAAC/1581, 2018.

Yang, H., Chen, G., Tang, Q. and Hess, P.: Quantifying isentropic stratosphere-troposphere exchange of ozone, J. Geophys. Res. Atmos., 121(7), 3372–3387, https://doi.org/10.1002/2015JD024180, 2016.

Chapter 2 Seasonal Tropospheric Distribution and Air-sea Fluxes of Atmospheric Potential Oxygen from Global Airborne Observations

Abstract

Seasonal change of atmospheric potential oxygen (APO ~ O_2 + CO_2) is a tracer for air-sea O_2 flux with little sensitivity to the terrestrial exchange of O_2 and CO_2. In this study, we present the tropospheric distribution and inventory of APO in each hemisphere with seasonal resolution, using O_2 and CO_2 measurements from discrete airborne campaigns between 2009 and 2018. The airborne data is represented on a mass-weighted isentropic coordinate ($M_{\theta e}$) as an alternative to latitude, which reduces the noise from synoptic variability in the APO cycles. We find a larger seasonal amplitude of APO inventory in the Southern Hemisphere relative to the Northern Hemisphere, and a larger amplitude in high latitudes (low $M_{\theta e}$) relative to low latitudes (high $M_{\theta e}$) within each hemisphere. With a box model, we invert the seasonal changes in APO inventory to yield estimates of air-sea flux cycles at the hemispheric scale. We find a larger seasonal net outgassing of APO in the Southern Hemisphere (518±52.6 Tmol) than the Northern Hemisphere (342±52.1 Tmol). Differences in APO phasing and amplitude between the hemispheres suggest distinct physical and biogeochemical mechanisms driving the air-sea O_2 fluxes, such as fall outgassing of photosynthetic O_2 in the Northern Hemisphere, possibly associated with the formation of the seasonal subsurface shallow oxygen maximum. We compare our estimates with four model- and observation-based products, identifying key limitations in these products or in the tools used to create them.

Plain Language Summary

Better understanding of the air-sea O_2 fluxes facilitates the study of marine productivity, global carbon cycle and ocean heat transport. Seasonal air-sea exchange of O_2 has been estimated by combining precise measurements of atmospheric O_2 and CO_2 into atmospheric potential oxygen

(APO ~ O_2 + CO_2). Using APO observations from nine global airborne campaigns between 2009 and 2018, we resolve the seasonal cycle of atmospheric APO concentration in multiple pressure and latitude bands, yielding estimates of the tropospheric APO inventory, and area-integrated air-sea APO flux of each hemisphere. To a first approximation, the ocean is a source of APO in the spring and summer but a sink in the fall and winter, tracking the seasonal warming and cooling of the ocean as well as different ocean biogeochemistry and ventilation regimes. In addition, these cycles show clear asymmetry between hemispheres and display a progressive shift in the seasonal phase and amplitude across latitudes. It is therefore important to understand the physical and biogeochemical processes that lead to these differences.

2.1 Introduction

Atmospheric potential oxygen (APO), which is effectively the sum of atmospheric O_2 and CO_2 concentrations, is primarily a tracer of ocean biogeochemistry (Stephens et al., 1998). APO is generally insensitive to photosynthesis and respiration of the land biosphere due to compensating impacts on O_2 and CO_2. APO has been observed at surface stations (e.g., Battle et al., 2006; Goto et al., 2017; Manning & Keeling, 2006; Tohjima et al., 2003, 2019), on ship transects (Ishidoya et al., 2016; Pickers & Manning, 2015; Pickers et al., 2017; Stephens et al., 2003; Thompson et al., 2007; Tohjima et al., 2012, 2015), and from aircraft (Bent, 2014; Ishidoya et al., 2022; Langenfelds, 2002; Stephens et al., 2021). A prominent feature in time series of APO are seasonal variations, driven mainly by seasonal air-sea O_2 flux due to upper-ocean biological activities, thermally-induced solubility changes, and ocean ventilation, with smaller contributions from air-sea exchanges of CO_2 and N_2 (Manning & Keeling, 2006; Stephens et al., 1998). APO is also sensitive to the burning of petroleum and natural gas, which are characterized by more negative O_2:C ratios than land photosynthexsis/respiration, but combustion of these products make a

negligible contribution to seasonal APO cycles at background stations (Manning & Keeling, 2006; Nevison et al., 2008).

Measurements of seasonal variations in atmospheric APO have been used to estimate oceanic net community production (NCP) (Goto et al., 2017; Nevison et al., 2012, 2018), evaluate the ocean biogeochemistry components of Earth System Models (Naegler et al., 2007; Nevison et al., 2015, 2016; Stephens et al., 1998), and estimate gas-exchange velocities (Keeling et al., 1998). These measurements have also been used to validate estimates of climatological seasonal air-sea O_2 flux, which are calculated based on measurements of dissolved O_2 in surface ocean (Garcia & Keeling, 2001; Keeling et al., 1998; Najjar & Keeling, 1997, 2000). Atmospheric APO observations have also been inverted to yield global air-sea APO fluxes that are optimized to best match observed APO at surface stations, thus constraining global-scale seasonal air-sea O_2 exchange (Rödenbeck et al., 2008). The accuracy of air-sea O_2 fluxes inferred from atmospheric measurements is limited, however, by uncertainties due to vertical transport in atmospheric tracer transport models as well as by the limited coverage of atmospheric measurements (Naegler et al., 2007; Nevison et al., 2008).

Here we use APO measurements from two global airborne campaigns, the HIAPER Pole-to-Pole Observations (HIPPO) project (Wofsy, 2011) and the Atmospheric Tomography (ATom) mission (Thompson et al., 2022), to quantify climatological seasonal APO distributions, tropospheric inventories, and air-sea fluxes at the hemispheric scale. The APO seasonal cycles are expressed on a mass-weighted moist isentropic coordinate, $M_{\theta e}$, developed by Jin et al. (2021), which is an alternative to latitude and effectively removes the impact of synoptic variability from airborne data. Due to the known tendency for rapid adiabatic airmass mixing (mixing along moist isentropes) (Parazoo et al., 2011; Pauluis et al., 2008), long-lived atmospheric tracers such as O_2

and CO_2 tend to be well-mixed on $M_{\theta e}$ (or θ_e), which allows hemispheric inventories to be estimated by a simple one-dimensional integration over $M_{\theta e}$. We use this method to generate hemispheric inventories of APO. We then invert these inventories using a box model to yield hemispheric scale air-sea APO fluxes. We apply our estimates as a direct test to other model and observation-based products, such as the Jena CarboScope APO inversion (Rödenbeck et al., 2008), climatological Garcia & Keeling (2001) O_2 fluxes from a heat flux based extension of dissolved O_2 measurements, and one configuration of the Community Earth System Model (CESM, Yeager et al., 2022).

2.2 Materials and Methods

2.2.1 Definition of APO and air-sea APO fluxes

Following Stephens et al. (1998), APO (per meg) is calculated from observations according

$$\mathrm{APO} = \delta(\mathrm{O_2/N_2}) + \frac{1.1}{\mathrm{X_{O_2}}}(\mathrm{CO_2} - 350) \tag{2.1}$$

with

$$\delta(\mathrm{O_2/N_2}) = \left(\frac{\left(\frac{\mathrm{O_2}}{\mathrm{N_2}}\right)_{\mathrm{sample}}}{\left(\frac{\mathrm{O_2}}{\mathrm{N_2}}\right)_{\mathrm{reference}}} - 1\right) \cdot 10^6 \tag{2.2}$$

where 1.1 is the approximate exchange ratio of O_2 production/consumption to CO_2 consumption/production from terrestrial biosphere (Severinghaus, 1995). We note that this ratio is generally between 1.01 and 1.14 from aboveground carbon pool over small temporal and spatial scales (Gallagher et al., 2017; Hockaday et al., 2009; Worrall et al., 2013). For this study, the relevant ratio is that of O_2 to CO_2 in the seasonally accumulated growth and decay of hemispheric biota, which we assume to be 1.1 following the stoichiometric and biological arguments in Severinghaus, 1995. Sensitivity results over the range of 1.1 ± 0.05 show only minor effects

($\pm$5.1% of the hemispheric average APO, for details see SI Text S2.4), as seasonal APO changes are dominated by seasonal changes in $\delta(O_2/N_2)$. $\delta(O_2/N_2)$ is conventionally multiplied by 10^6 and expressed in per meg units, and ΔCO_2 is the difference in the CO_2 dry-air mole fraction in ppm (i.e. μmol mol^{-1}) relative to a reference of 350 ppm. Here X_{O_2}(0.2094) is the reference dry-air mole fraction of O_2 used in the definition of the O_2/N_2 scale of the Scripps O_2 Program (Keeling et al., 2020). The unit of APO can be converted from per meg to ppm equivalent for flux contributions by multiplying X_{O_2}.

The seasonal cycle of atmospheric APO is altered by oceanic emission or uptake of O_2, CO_2, or N_2. We define the oceanic flux of APO ($F^{APO(ocn)}$, Tmol day^{-1}) following:

$$F^{APO(ocn)} = \left(F^{O_2} + 1.1F^{CO_2} - \frac{X_{O_2}}{X_{N_2}} F^{N_2} \right) \times A \quad (2.3)$$

where F^{O_2}, F^{CO_2}, and F^{CO_2} are air-sea flux of O_2, CO_2, and N_2, in unit of Tmol m^{-2} day^{-1}, and A is the ocean area, in unit of m^2. X_{N_2} (0.7808) is the reference dry-air mole fraction of N_2 in the atmosphere (Keeling et al., 2020). We also define the change in APO inventory as the change in the total abundance of APO (in Tmol) in a defined atmospheric volume. In a well-mixed atmospheric volume, the excess APO inventory in moles (relative to reference air) is equal to $APO \cdot X_{O_2} \cdot M \cdot 10^{-6}$, where M is the total moles of dry air in the volume.

2.2.2 Airborne campaigns and airborne APO measurements

Both the HIPPO and ATom campaigns had global coverage (Figure 1a, Table S1), extending from the Arctic to the Antarctic and from near the surface (150-300 m) to the lower stratosphere (12-15 km) (Thompson et al., 2022; Wofsy, 2011). HIPPO consisted of five campaigns between 2009 and 2011 and ATom consisted of four campaigns between 2016 and 2018. Each campaign included a southbound and a northbound transect. On HIPPO, both

southbound and northbound transects were over the Pacific Ocean, while on ATom, southbound transects were over the Pacific Ocean and northbound transects were over the Atlantic Ocean. We aggregate data from each mission into southbound and northbound transects within each hemisphere.

This study uses airborne measurements of $\delta(O_2/N_2)$ and CO_2 made with the NCAR Airborne Oxygen Instrument (AO2) (Stephens et al., 2021). The AO2 instrument was supported by flask samples collected with the NCAR/Scripps Medusa flask sampler that collects 32 air samples in each flight for later analysis at Scripps (Bent, 2014; Stephens et al., 2021). The Medusa flasks were used to identify and correct for time-dependent systematic biases in the continuous AO2 measurements. AO2 data were adjusted to match Medusa flask using a linear trend versus time of flight on a flight-by-flight average basis (Stephens et al., 2021). O_2 measurements were adjusted for surface effects and detector cell humidity interactions, while CO_2 measurements were adjusted for surface effects and o-ring permeation effects (Stephens et al., 2021). The magnitude of O_2 adjustments for each campaign is listed in Table S3 of Stephens et al. (2021), while the magnitude of CO_2 adjustments per campaign ranges from -0.3 to 0.4 ppm, with an average of 0.01 ppm and 1σ standard deviation of 0.19 ppm. Prior to being used for correcting the AO2 measurements, the Medusa data were also adjusted to reduce the impact of diffusive fractionation associated with flask sampling (Bent, 2014; Stephens et al., 2021) by computing

$$\delta\left(\frac{O_2}{N_2}\right)^{*} = \delta\left(\frac{O_2}{N_2}\right)_{obs} - \frac{1}{3.77}\,\delta\left(\frac{Ar}{N_2}\right)_{obs} \tag{2.4}$$

where $\delta(O_2/N_2)_{obs}$ is the Medusa observation, and $\delta(Ar/N_2)_{obs}$ is measured relative to an arbitrary reference of 15 per meg, chosen to approximate the global surface average (Stephens et

al., 2021). 3.77 is the ratio of the Ar/N_2 change to O_2/N_2 change associated with thermal fractionation (Bent, 2014; Keeling et al., 2004). This correction recognizes that

$$\delta\left(\frac{O_2}{N_2}\right)_{obs} = \delta\left(\frac{O_2}{N_2}\right) + \delta\left(\frac{O_2}{N_2}\right)_{fract} \quad (2.5)$$

$$\delta\left(\frac{Ar_2}{N_2}\right)_{obs} = \delta\left(\frac{Ar}{N_2}\right) + \delta\left(\frac{Ar_2}{N_2}\right)_{fract} \quad (2.6)$$

with

$$\delta\left(\frac{O_2}{N_2}\right)_{fract} = \frac{1}{3.77}\,\delta\left(\frac{Ar_2}{N_2}\right)_{fract} \quad (2.7)$$

where the *obs* subscript denotes the observed value and the *fract* subscript denotes sampling artifacts caused by thermal fractionation at the air intake or flask exit port, which we expect are the dominant sampling artifacts. Pressure-driven inlet fractionation was also apparent, but with a small enough magnitude and similar enough expected ratio to be included in a single correction (section 4.2.1 of Stephens et al., 2021).

The Medusa-corrected AO2 data are thus effectively measuring $\delta(O_2/N_2)^*$ on a mean basis per flight, from which we can compute

$$APO^* = \delta\left(\frac{O_2}{N_2}\right)^* + \frac{1.1}{X_{O_2}}(CO_2 - 350) \quad (2.8)$$

To calculate seasonal APO from APO^*, it is necessary to correct for the true $\delta(Ar/N_2)$ seasonality. Here we use modeled estimates, which we refer to as $\delta(Ar/N_2)_{model}$, and assume that $\delta(Ar/N_2)_{model} = \delta(Ar/N_2)_{true}$. The $\delta(Ar/N_2)_{model}$ is calculated from simulated air-sea N_2 exchange based on scaling ocean heat flux. Thus

$$\mathrm{APO} = \mathrm{APO}^{*} + \frac{1}{3.77}\delta\left(\frac{\mathrm{Ar}}{\mathrm{N_2}}\right)_{\mathrm{model}} \tag{2.9}$$

with

$$\begin{aligned}\delta\left(\frac{\mathrm{Ar}}{\mathrm{N_2}}\right)_{\mathrm{model}} &= \frac{1}{\mathrm{X_{Ar}}}\Delta\mathrm{Ar} - \frac{1}{\mathrm{X_{N_2}}}\Delta\mathrm{N_2} \\ &= \frac{1}{\mathrm{X_{Ar}}}\frac{1}{34}\Delta\mathrm{N_2} - \frac{1}{\mathrm{X_{N_2}}}\Delta\mathrm{N_2} \\ &= 1.87 \cdot \Delta\mathrm{N_2}\end{aligned} \tag{2.10}$$

where ΔN_2 is the modeled atmospheric N_2 anomaly driven by air-sea N_2 exchange, calculated as if N_2 were a trace gas in ppm-equivalent units (e.g. μmol mol^{-1}). X_{Ar} (0.00934) is the mole fraction of Ar in the atmosphere. 1/34 is a scaling factor, which is the ratio of Ar and N_2 air-sea fluxes driven by heat flux from Table 3 in Manizza et al. (2012). Air-sea N_2 exchange (F^{N_2}) is calculated from ocean heat fluxes (Q) from the Estimating the Circulation and Climate of the Ocean (ECCO) Version 4 Release 3, which interpolates ocean heat flux estimates to a global field by a non-linear inverse model (Forget et al., 2015)

$$\mathrm{F^{N_2}} = -\frac{1}{1.3} \cdot \frac{\mathrm{dS}}{\mathrm{dT}} \cdot \frac{\mathrm{Q}}{\mathrm{C_p}} \tag{2.11}$$

where dS/dT (mol kg^{-1} °C^{-1}) is the temperature derivative of solubility (Weiss, 1970), Q is the ocean heat flux (W m^{-2}) and C_p is the specific heat capacity of seawater (3993 J kg^{-1} °C^{-1}). Equation 2.11 is similar to that used by Keeling et al. (1992) but with the introduction of the factor of 1/1.3 by Jin et al. (2007). This factor accounts for incomplete equilibration and other processes, including mixing-induced super-saturation due to the non-linear dependence of solubility on temperature and the penetration of solar radiation below the ocean mixed layer (Dietze & Oschlies,

2005; Manizza et al., 2012). We estimate ΔN_2 by forward transporting ECCO-based air-sea N_2 exchange using the TM3 atmospheric transport model (Heimann & Körner, 2003).

The difference between APO and APO^* is small, ranging from -4 to 4 per meg (Fig. S1). This correction also has small impact on the seasonal amplitude of the APO concentrations, which scales up the seasonal amplitude of APO^* by 0.89 per meg (4.7%) and 1.38 per meg (4.9%) in the Northern and Southern Hemisphere, respectively.

2.2.3 Filtering and detrending of APO airborne observations

We exclude all measurements from the stratosphere using the criterion of Jin et al. (2021): {Water vapor (H_2O) < 50 ppm} and {O_3 >150 ppb or N_2O < 319 ppb}, where N_2O has been detrended relative to a reference year of 2009. H_2O was measured by VCSEL (Zondlo et al., 2010) for HIPPO and DLH for ATom (Diskin et al., 2002; Scott et al., 1990). O_3 was measured by the NOAA Unmanned Aerial Systems Chromatograph for Atmospheric Trace Species (UCATS, Hintsa et al., 2021). N_2O was measured by the Harvard Quantum Cascade Laser System (QCLS, Santoni et al., 2014). N_2O measurements are not available from ATom1, so the stratosphere samplings are simply defined by H_2O and O_3 for this campaign. We also exclude all observations near landing sites with the same criteria as in Jin et al. (2021), for example, samples that were collected 120s after takeoff, 600s prior to landing, and any missed approaches.

To focus on APO seasonal cycles, we detrend the airborne measurements by subtracting a smoothed interannual trend from a global mean APO time series using data from the Scripps O_2 Program (Hamme and Keeling, 2008). This APO time series is calculated as a weighted average of APO measurements from seven surface stations, with the weights based on the latitudinal coverage of each corresponding station (Table 2.5, weights are from Hamme and Keeling (2008)). The smoothing was based on a least-squares fit consisting of a stiff cubic spline function plus 4-

harmonic terms (Manning & Keeling, 2006; Reinsch, 1967). Detrended APO is referred to as ΔAPO. The latitude and pressure cross section of ΔAPO for each airborne campaign transect is shown in Figure 2.1b.

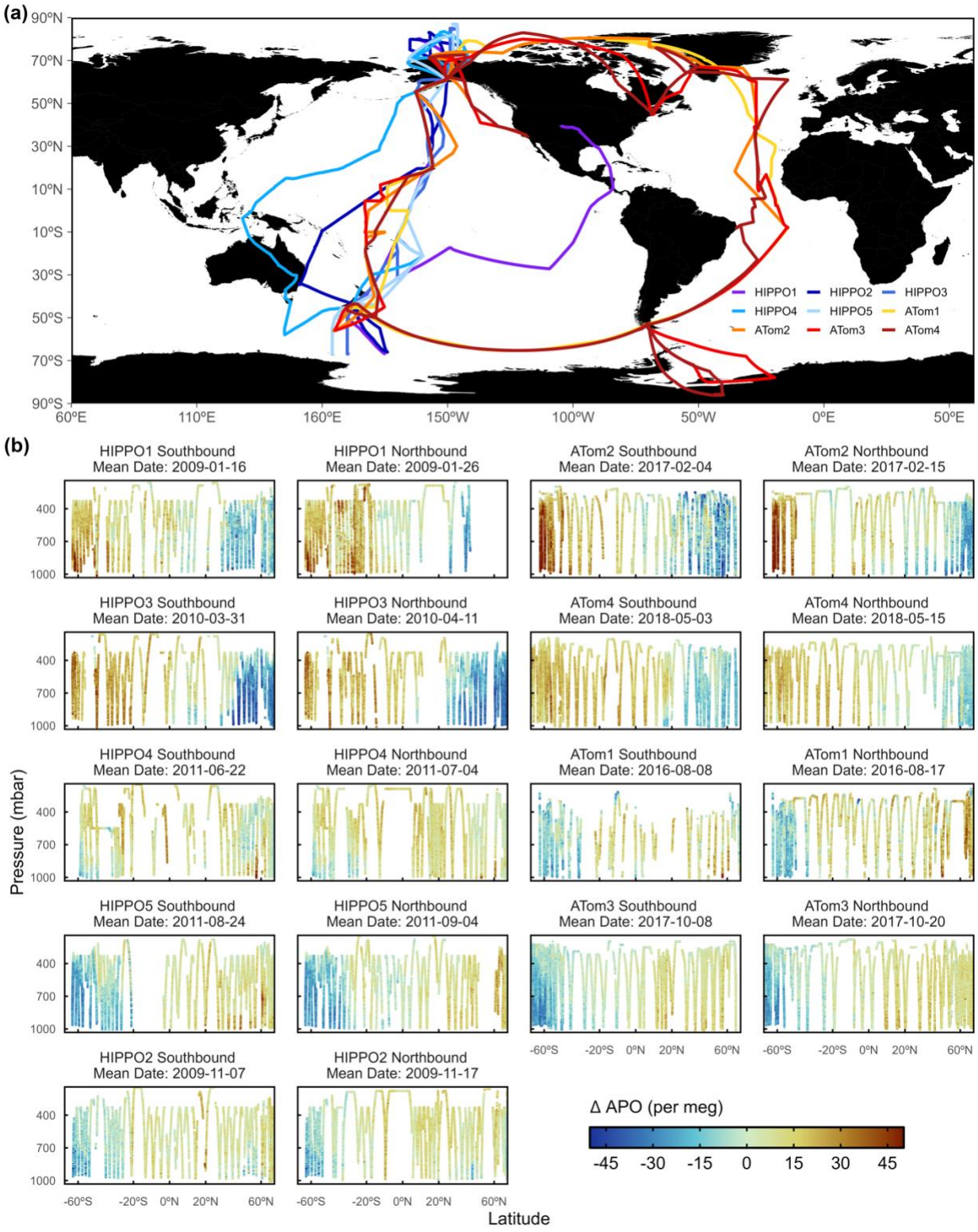

Figure 2.1: (a) HIPPO and ATom flight tracks colored by campaigns. (b) Latitude and pressure cross-sections of ΔAPO for each airborne campaign transect. Panels are ordered over the course of the season.

2.2.4 Air-sea APO flux products

We compare airborne-based estimates of seasonal air-sea APO fluxes with four alternate estimates.

The first product uses APO fluxes from the Jena CarboScope APO Inversion (referred to as the Jena inversion, version: apo99XS_v2022), which yields APO fluxes optimized to best match observed APO at stations in the Scripps O_2 Program surface flask network and at stations and on ships (Tohjima et al., 2012) from the National Institute for Environmental Studies (updates of Rödenbeck et al., 2008). Details of stations and their locations are in Table 2.4. We use the fluxes from 2009 to 2018, to match with the duration of the HIPPO and ATom campaigns.

The second product is an observation-based semi-empirical product (referred to as GKT), using year-to-year repeating climatological F^{O_2} from Garcia and Keeling (2001), climatological F^{CO_2} from Takahashi (2009), and climatological F^{N_2} calculated from ocean heat fluxes from ECCO version 4 (see section 2.2, Forget et al., 2015). F^{O_2} from Garcia and Keeling (2001) is calculated by interpolating dissolved O_2 measurements weighted by ocean heat flux anomalies. Following Morgan et al. (2021), here we scale down the F^{O_2} by 18% (i.e., multiply by a factor of 0.82) to accounts for bias in the gas transfer velocity from Wanninkhof (1992), which is used to calculate F^{O_2} from Garcia and Keeling (2001). Naegler et al. (2006) showed that the gas transfer velocity coefficient of 0.39 from Wanninkhof (1992) should be scaled down by 18% to 0.32. This scaling is also supported by Bent (2014).

The third product is based on a forced ocean-ice configuration of CESM2 (Yeager et al., 2022, refered to as CESM), which is forced by JRA55-do (Tsujino et al., 2018) atmospheric fields and prognostic ocean BGC using the Marine Biogeochemistry Library (MARBL; Long et al., 2021). The oceanic O_2 (F^{O_2}), CO_2 (F^{CO_2}) and N_2 (F^{N_2}) fluxes are provided directly as model

output, with 1° x 1° horizontal resolution and daily resolution from 1986 to 2020. We only analyze outputs from 2009 to 2018.

We calculate area-integrated daily air-sea APO flux cycles in each hemisphere from these three products, and fit with a 2-harmonic plus offset to yield average seasonal cycles (Figure 2.5). We note that the GKT is defined as a seasonal anomaly, so the annual uptake is pre-subtracted (equal to 0).

2.2.5 Atmospheric simulations

To translate APO fluxes from these products into atmospheric distributions, we rely on the TM3 transport model (Heimann & Körner, 2003) and MIROC4.0-based Atmospheric Chemistry-Transport Model (ACTM, Patra et al., 2018). TM3 was run at a 5^o longitude by 4^o latitude spatial resolution with 19 vertical levels, using winds from NCEP/NCAR reanalysis with daily temporal resolution (Kalnay et al., 1996). With the modeled fluxes as input, the TM3 model yields as output excesses or deficits of APO against a prescribed background. The simulated APO atmospheric fields are referred to as Jena-TM3, GKT-TM3, and CESM-TM3. These simulations were run from 2006 to 2018. The first three years are used for model spin-up and are discarded. We use model output from 2009 to 2018.

We also use ACTM to forward transport air-sea APO fluxes from the Jena APO inversion (referred to as Jena-ACTM), in order to provide another constraint on interhemispheric-mixing time scales (for details see Section 5.1 and Appendix A). ACTM was run from 1999 to 2019 at ~2.8° longitude by ~2.8° latitude spatial resolution with 67 vertical levels driven by JRA-55 winds (Kobayashi et al., 2015). We only use Jena-ACTM output between 2009 and 2018.

2.2.6 Calculation of $M_{\theta e}$ and $M_{\theta e}$-weighted average APO

Airborne APO observations are sorted and binned on the $M_{\theta e}$ coordinate, which is defined as the total dry air mass under a specific moist isentropic value (defined by constant θ_e) in the

troposphere of each hemisphere (Jin et al., 2021). $M_{\theta e}$ is defined separately in the Northern and Southern Hemispheres and is not continuous across the Equator. The coordinate $M_{\theta e}$ is similar to θ_e, generally increasing towards the equator and with altitude in each hemisphere (Figure 2.2b). The computation of $M_{\theta e}$ follows:

$$M_{\theta_e}(\theta_e, t) = \sum M_x(t)|_{\theta_{e_x} < \theta_e} \tag{2.12}$$

where $M_x(t)$ is the dry air mass of each grid cell x at time t, and θ_{e_x} is the equivalent potential temperature. The sum is over all air with θ_{e_x} less than θ_e in the troposphere, which is defined as PVU smaller than 2. This calculation yields a unique value of $M_{\theta e}$ for each value of θ_e. We refer to the relationship between θ_e and $M_{\theta e}$ as the "θ_e-$M_{\theta e}$ look-up table", which we generate at daily resolution for each hemisphere based on four reanalyses, which are ERA-Interim, (Dee et al., 2011), MERRA-2 (Gelaro et al., 2017), NCEP (Kalnay et al., 1996), and JRA-55 (Kobayashi et al., 2015). We use the look-up table based on ERA-Interim to organize airborne data. These look-up tables are available at https://doi.org/10.5281/zenodo.4420398.

The $M_{\theta e}$ value for each airborne observation was derived from matching the θ_e value of each observation with the ERA-Interim look-up table of the corresponding date.

We calculate θ_e (K) following Stull (2012):

$$\theta_e = \left(T + \frac{L_v(T)}{C_{pd}} w\right)\left(\frac{P_0}{P}\right)^{\frac{R_d}{C_{pd}}} \tag{2.13}$$

where w is the water vapor mixing ratio with unit of kg of water vapor per kg of air mass, R_d (287.04 J kg^{-1} K^{-1}) is the gas constant for air, C_{pd} (1005.7 J kg^{-1} K^{-1}) is the specific heat of dry air at constant pressure, P_0 (1013.25 mbar) is the reference pressure at the surface, and $L_v(T)$

($kJ\,kg^{-1}$) is the latent heat of evaporation. $L_v(T)$ is defined as $2406\,kJ\,kg^{-1}$ at 40 °C and $2501\,kJ\,kg^{-1}$ at 0 °C and scales linearly with temperature.

For HIPPO, θ_e is available from the merged file that is calculated using water vapor mole fraction measured by VCSEL (Zondlo et al., 2010). For ATom, θ_e was computed from static pressure, air temperature as measured by the Meteorological Measurement System (MMS), and relative humidity of water vapor as measured by the Diode Laser Hygrometer (DLH) (Diskin et al., 2002; Scott et al., 1990).

We also assign a $M_{\theta e}$ value for each grid of the modeled daily atmospheric APO field (TM3 and ACTM) using 3-D atmospheric $M_{\theta e}$ fields derived from the corresponding reanalysis used in the transport model. 3-D $M_{\theta e}$ fields are interpolated to the transport model grids using inverse distance weighted interpolation.

To calculate the mass-weighted average detrended APO for a given $M_{\theta e}$ band, we use a method that assumes each APO observation represents the APO value on the corresponding $M_{\theta e}$ surface throughout the hemisphere (Jin et al., 2021).We sort APO by $M_{\theta e}$ from low to high and compute a mass-weighted average APO by trapezoidal integration of APO as a function of $M_{\theta e}$, dividing by the range of $M_{\theta e}$. This method effectively weighs each measurement or modeled value by the fraction of the hemispheric airmass with the same θ_e value that it represents. The method yields accurate inventories because, as shown below, the variability in APO along $M_{\theta e}$ surfaces is small due to rapid adiabatic mixing (see also Jin et al., 2021), and because this variability is also partly addressed by averaging data from different elevations.

2.3 Seasonal atmospheric APO distributions

We examine the seasonal cycle of airborne APO grouped into five $M_{\theta e}$-pressure bins (40×10^{16} kg intervals) in each hemisphere and four pressure bins (200 mbar intervals), as shown

in Figure 2.2a. The approximate geographic distribution of each bin is illustrated by the zonal average $M_{\theta e}$ surfaces in Figure 2.2b. These cycles are calculated by 2-harmonic fits (with offset removed) to each averaged ΔAPO of the $M_{\theta e}$ and pressure bin (shown as points in Fig. 2.2a). Statistics of the cycles (amplitude and phase) in the different bins are summarized in Figure 2.2c. A comparison of observed cycles and simulated cycles (i.e., Jena-TM3, GKT-TM3, and CESM-TM3) grouped by 20 (10^{16} kg) $M_{\theta e}$ intervals is shown in Figure 8.

In Figure 2.2a, all bins show well-resolved seasonal APO cycles, with higher amplitudes in the Southern Hemisphere compared to the Northern Hemisphere at a given pressure-$M_{\theta e}$ bin. Within each hemisphere, the amplitudes show a clear gradient across $M_{\theta e}$, with larger amplitudes at lower $M_{\theta e}$ (higher latitudes). Phasing of the APO cycles also shows clear gradients over $M_{\theta e}$. Whereas the cycles within the Southern Hemisphere have earlier phasing (upward zero-crossing date) at low $M_{\theta e}$ (high latitude), the cycles in the Northern Hemisphere tend to have later phasing at low $M_{\theta e}$. These patterns in amplitude and phase are similar to those seen in summaries of surface or shipboard measurements (Keeling et al., 1998; Tohjima et al., 2012).

In a given $M_{\theta e}$ bin (Figure 2.2a and c), the amplitude decreases slightly with increasing altitude (decreasing pressure), due to the fact that surface fluxes drive the APO seasonal cycle. The weak variation with pressure (at constant $M_{\theta e}$) is expected considering that θ_e (or $M_{\theta e}$) surfaces are preferential surfaces for mixing. The phase generally shifts later with decreasing pressure, consistent with a time lag for adiabatic mixing of the APO cycle along θ_e surfaces. An exception to this pattern is seen in the high $M_{\theta e}$ (120 - 160) bins of the Northern Hemisphere, where the earliest phase is found in the mid-troposphere (800 – 400 mbar), while the lower (1000 – 800 mbar) and upper troposphere (400 – 200 mbar) show clear lags in phase (Figure 2.2a).

The gradients in seasonal phasing with respect to $M_{\theta e}$ are mainly driven by fluxes at higher latitudes in each hemisphere, and are partly driven by delayed propagation of the cycles from the opposite hemisphere (Garcia & Keeling, 2001; Keeling et al., 1998; Najjar & Keeling, 2000). These effects, together with the ~180° out-of-phase seasonal flux cycle between low-latitudes (<20°N) and high-latitudes in the Northern Hemisphere (Figure 2.13), lead to the small and noisy seasonal cycle of the highest $M_{\theta e}$ band (low latitude) in the Northern Hemisphere. We find that the upward zero-crossing date arrives ~5.5 weeks earlier in the high $M_{\theta e}$ (120 - 160) of the northern mid-troposphere (800 – 600 mbar) relative to the lower troposphere (1000 – 800 mbar), as shown in Figure 2.2a and c. This pattern is consistent with Keeling et al. (1998), who found that the observed seasonal maximum at the Mauna Loa Observatory (MLO, 3397 masl) is 2 months earlier than the seasonal maximum at Cape Kumukahi (KUM, 15 masl), which is only 82 km from MLO, but at a lower elevation.

As an alternative, we also have binned airborne observations by pressure and latitude (Figure 2.9b). This approach leads to a much larger scatter of amplitudes and phases in APO seasonal cycles with pressure level (at fixed latitude bins) compared to binning data by pressure and $M_{\theta e}$ (Figure 2.2a and Figure 2.9a). The larger scatter is expected, which illustrates the advantage of organizing airborne observations on $M_{\theta e}$. Binning airborne observations by pressure and latitude also leads to larger short-term variability (F test, $p < 0.01$) within individual pressure bins relative to the mean cycles, based on the distribution of all detrended observations (not shown as points but denoted as 1σ values in Figure 2.9), indicating larger synoptic disturbances.

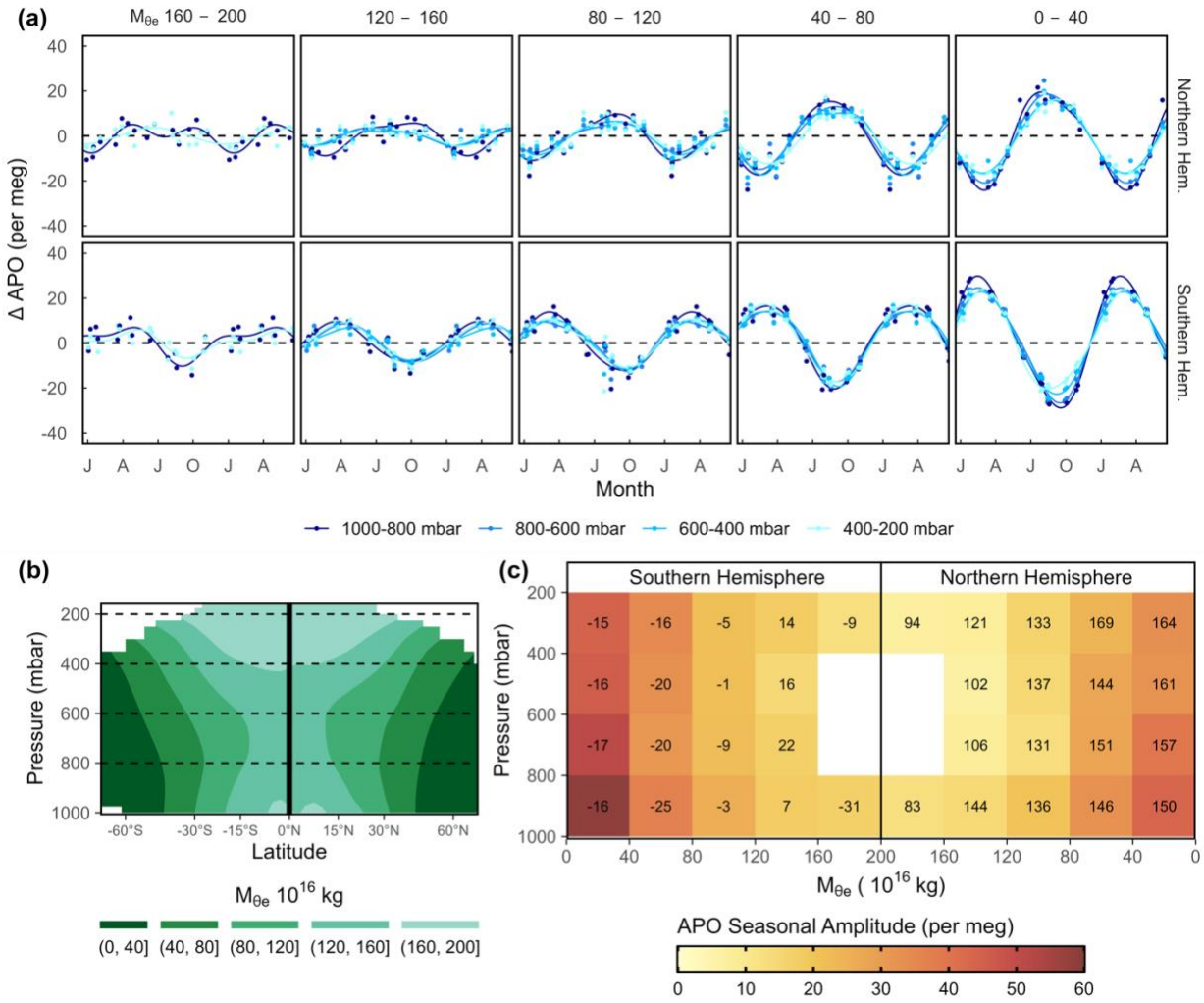

Figure 2.2: (a) Seasonal cycles of detrended airborne APO (ΔAPO) sorted by M_{θ_e}–pressure bins (columns) and hemispheres (rows). M_{θ_e} bins (10^{16} kg) are shown at the top of each panel and pressure bins are colored. Each point represents the mass-weighted average (based on M_{θ_e}) ΔAPO within the specific M_{θ_e}–pressure bins, filtering out bins with less than twenty 10-s observations. The curves represent two-harmonic fits to corresponding mass-weighted average ΔAPO of each $M_{\theta e}$ and pressure bin. Annul mean values are subtracted. The first half year is repeated in each panel. Bins in the mid-troposphere (800 – 600 mbar and 600 – 400 mbar) of the highest M_{θ_e} value (160 - 200) are dropped because these bins contain very little air mass. (b) Schematic of the contours of zonal and annual average M_{θ_e} in the Latitude-Pressure coordinate, calculates as the average M_{θ_e} in the year of 2009 using ERA-Interim. (c) Seasonal amplitude (shading) and phase (upward zero-crossing Julian date) of the fitted APO seasonal cycles in Figure 2.2a. Negative Julian dates are given from November to December. Bins in the mid-troposphere (800 – 600 mbar and 600 – 400 mbar) of the highest M_{θ_e} value (160 - 200) are dropped because these bins contain very little air mass.

2.4 Seasonal cycles of tropospheric APO inventories

2.4.1 Method

We show our estimates of APO inventory seasonal anomalies (ΔM^{APO}) of each airborne campaign transect in Figure 2.3, and their values are reported in Table 2.6 and 2.7, including uncertainties. Inventory estimates from different years are grouped into a climatological year. For each of the 18 airborne transects, we calculate mass-weighted average detrended APO ($\langle \Delta APO \rangle$) for each hemisphere. We then compute ΔM^{APO} (in moles) of each hemisphere from hemispheric mass-weighted average ΔAPO ($\langle \Delta APO \rangle$) as follows:

$$\Delta M^{APO} = \langle \Delta APO \rangle \cdot X_{O_2} \cdot M_{trop} \cdot \kappa \quad (2.14)$$

The parameter M_{trop} is the total tropospheric dry air mass of the hemisphere. Here we use a constant hemispheric dry air mass of $2.02 \cdot 10^{18}$ kg, which ensures that δM^{APO} is insensitive to changes in tropospheric air mass in the absence of changes in APO concentration. The total mass of dry air in the troposphere of each hemisphere is computed from integrating all ERA-Interim tropospheric (PVU < 2) grid cells. The changes in tropospheric air mass with season are small in any case, varying from $2.00 \cdot 10^{18}$ kg to $2.04 \cdot 10^{18}$ kg in the Southern Hemisphere and from $1.97 \cdot 10^{18}$ kg to $2.06 \cdot 10^{18}$ kg in the Northern Hemisphere. The parameter κ ($3.45 \cdot 10^{-17}$ Tmol kg^{-1}) is a constant that converts an amount of dry air mass from kg to Tmol, which consists of the product of $10^3/28.97$ (i.e., converts kg of air mass to mol of air mass), 10^{-12} (i.e., converts mol of air mass to Tmol of air mass) and 10^{-6} (i.e., converts ppm to mol/mol). Seasonal cycles of tropospheric APO inventory of each hemisphere are calculated by 2-harmonic fits with annual offset removed (Figure 2.3). Related statistics (seasonal amplitude, maximum and minimum date, upward zero-crossing date) based on 2-harmonic fits are summarized in Table 2.1.

The $M_{\theta e}$ integration method can yield unbiased tropospheric APO inventories if the spatial coverage of airborne measurements is broad enough (Jin et al., 2021). Also, APO inventories for multiple campaigns can define climatological mean seasonal cycles only if their temporal coverage is sufficient. We assess the bias due to incomplete coverage by subsampling simulated 3-D fields of APO (from Jena-TM3 and Jena-ACTM, see Figure 2.10) as detailed in SI Text S1. This approach yields estimated errors for each airborne campaign transect at the corresponding mean day of year. We only find small errors, with an average RMSE across the 18 transects of 1.67 per meg (based on TM3) or 1.21 per meg (based on ACTM) in the Northern Hemisphere, and 1.42 per meg (based on TM3) or 1.68 per meg (based on ACTM) in the Southern Hemisphere, suggesting that the airborne data and $M_{\theta e}$ integration method could represent hemispheric average APO well. We also find that TM3 and ACTM models generally agree with sign of biases (Figure 2.10). We use these calculated errors (averaged from TM3 and ACTM) to correct the observed APO inventory seasonal anomalies estimated from each airborne campaign transect (SI Text S1). For error analysis, we allow that these corrections for each individual inventory estimate have uncertainty amounting to ±100% of the correction (SI Text S2.3).

We show the corrected hemispheric ΔM^{APO} for each airborne campaign in Figure 2.3 (points), with error bars representing 1σ uncertainty as a quadrature sum from the following sources: (1) measurement imprecision and reproducibility; (2) spread of $M_{\theta e}$ values for different reanalysis products; (3) bias correction due to limited spatial and temporal coverage of the observations; (4) the uncertainty of the land biosphere O_2:CO_2 exchange ratio. To assess uncertainties in the harmonic fits, we generate an ensemble of 2000 fits. Details of the uncertainty (error bars in Figure 2.3) analysis are presented in SI Text S2.

2.4.2 Results and discussion of APO inventories

In each hemisphere, the seasonal anomaly of APO inventory generally increases in spring and summer and decreases in fall and winter (Figure 2.3), consistent with air-sea fluxes of O_2 driving the seasonal cycle of atmospheric APO. In the Southern Hemisphere, the austral spring/summer rise is more rapid than the austral fall/winter decrease by ~1.5 months. In the Northern Hemisphere, due to a broad summer peak, the rising period is ~3 months shorter than that in the Southern Hemisphere.

Figure 2.3 and Table 2.1 show that the seasonal amplitude of atmospheric APO inventory in the Southern Hemisphere (408±41.2Tmol) is significantly larger than in the Northern Hemisphere (274±44.4Tmol). The cycle in the Southern Hemisphere is heavily dominated by the first harmonic, and the phase indicated by the upward zero-crossing is 4 weeks later relative to the cycle in the Northern Hemisphere when measured relative to hemispheric solstice date.

The period of seasonal maximum APO inventory is broader in the Northern Hemisphere than in the Southern Hemisphere. Similar broad maxima are seen at northern land stations (e.g., Hateruma Island at 24.1°N, Barrow at 71.3°N, and Alert at 82.5°N) and in the subtropical (20 - 40°N) Northwest Pacific, as shown by shipborne measurements (Nevison et al., 2015; Tohjima et al., 2012, 2019).

The annual average APO is lower in the Northern Hemisphere by 6.4 ± 1.11 per meg (93.3 ± 16.21 Tmol) relative to the Southern Hemisphere, based on the annual mean from the 2-harmonic fits. In comparison, Resplandy et al. (2016) reported a northern APO deficit of 10.4 ± 0.9 per meg using HIPPO data in the mid-troposphere between 40°N and 60°N, which they use to constrain the interhemispheric ocean heat flux, based on close connection between APO and heat fluxes. These two estimates are not directly comparable because our estimate includes data from

lower latitudes, where we expect a smaller APO gradient between two hemispheres (Resplandy et al., 2016).

Each APO seasonal inventory estimate has uncertainty up to $\pm$72 Tmol (Error bars in Figure 2.3, details in Table 2.6 and 2.7). Of the several contributions to the uncertainty, the dominant contribution is measurement imprecision and reproducibility, which is mainly limited by campaign-to-campaign calibration or sampling offsets. The corrections for limited coverage and the uncertainty for corrections are small because we have sufficient observations across $M_{\theta e}$ (or on θ_e) surfaces in the hemisphere and because the along-$M_{\theta e}$ APO gradients are uniformly small (Figure 2.2a) in both high and low $M_{\theta e}$ bins. For the low $M_{\theta e}$ bins, the small gradient is due to rapid adiabatic APO mixing along $M_{\theta e}$. For the high $M_{\theta e}$ bins, the small gradient can be partially attributed to the small magnitude of surface APO flux due to weak seasonal forcing.

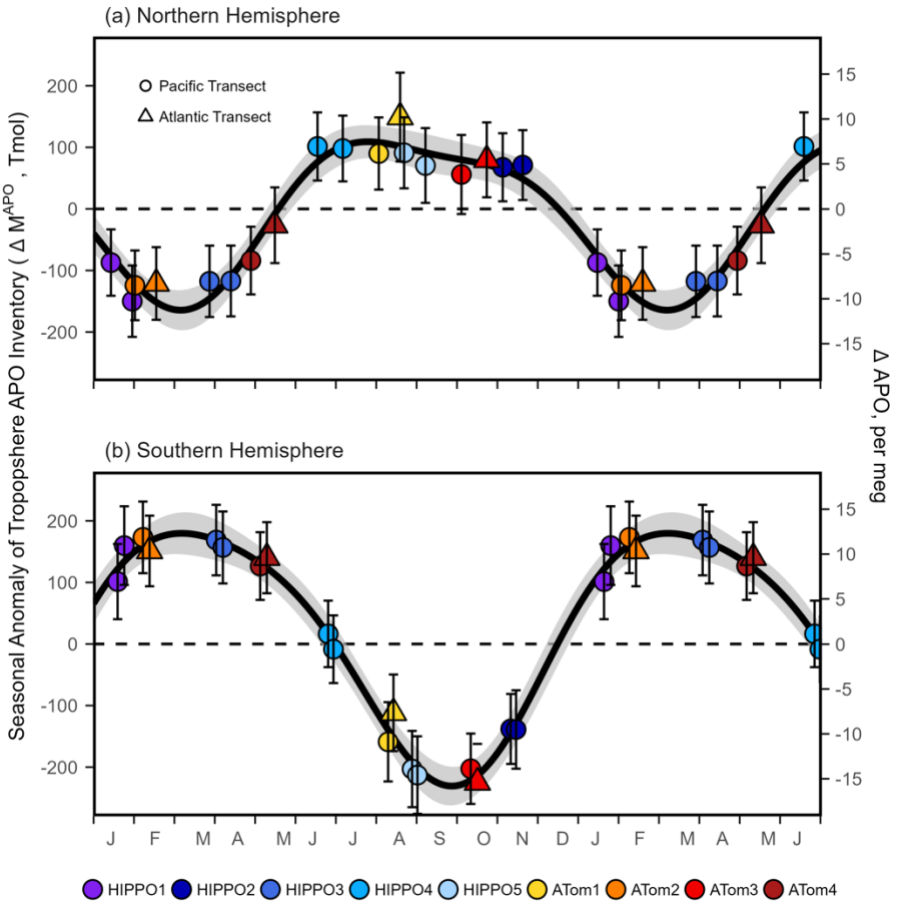

Figure 2.3: Seasonal anomaly of tropospheric APO inventory (Tmol) or concentration (per meg) in the Northern (a) and Southern (b) Hemisphere. Points show estimates of seasonal APO anomaly of each airborne campaign transect computed from the $M_{\theta e}$.

Table 2.1: Statistics of the seasonal cycle of tropospheric APO inventory (Figure 2.3) from two-harmonic fits (annual mean removed) for each hemisphere computed from airborne observations with correction for sparse spatial and temporal coverage.

Product	Hemisphere	Seasonal Amplitude (Tmol)	Maximum Date	Minimum Date	Upward-zero Crossing Date
Airborne observation	North	274±44.4	207±34.8	66±10.4	140±10.9
	South	408±41.2	66±21.4	270±8.7	349±8.2

2.5 Seasonal cycles of hemispheric air-sea APO fluxes

2.5.1 Method

We calculate total area-integrated APO fluxes (including all sources of exchange, i.e., from the ocean and fossil fuel emission) in the Northern Hemisphere (F_N^{APO}) and Southern Hemisphere (F_S^{APO}) (Tmol day^{-1}) from airborne observations, using a two-box model:

$$F_N^{APO}(t) = \frac{\partial M_N^{APO}(t)}{\partial t} + L_N(t) \quad (2.15)$$

$$F_S^{APO}(t) = \frac{\partial M_S^{APO}(t)}{\partial t} + L_S(t) \quad (2.16)$$

where $\frac{\partial M_N^{APO}(t)}{\partial t}$ and $\frac{\partial M_S^{APO}(t)}{\partial t}$ are the tropospheric APO inventory changes (Tmol day^{-1}) of each hemisphere and $L_N(t)$ and $L_S(t)$ are "leakage" terms across the Equator and tropopause. Here we calculate daily APO inventory changes in each hemisphere by combining the 2-harmonic fitted seasonal APO inventories from Section 4 with the previously removed annual average hemispheric APO and the removed long-term APO trend. Combing these components allows us to resolve both seasonal and annual mean components of the flux. We base the trend on observations from surface stations (Section 2.3), scaled to yield hemispheric inventories (Eq. 2.14). We use the same global trend for both hemispheres.

The leakage terms are included in Eq. 2.17 and 2.18 to account for the transport of ΔAPO between hemispheres, and between the troposphere and the stratosphere. Positive leakage represents the transport out of the troposphere in each hemisphere. We parameterize the leakage according to:

$$L_N(t) = \frac{\left(M_N^{APO}(t) - M_S^{APO}(t)\right)}{\tau(t)} + STE_N \quad (2.17)$$

$$L_S(t) = -\frac{\left(M_N^{APO}(t) - M_S^{APO}(t)\right)}{\tau(t)} + STE_S \quad (2.18)$$

where $\tau(t)$ is a climatological inter-hemisphere APO exchange time scale with unit of year, and $STE_N(t)$ and $STE_S(t)$ are climatological stratosphere-troposphere exchange rate (Tmol day^{-1}). We estimate $\tau(t)$, $STE_N(t)$, and $STE_N(t)$ using two transport models (TM3 and MIROC-ACTM) as described in Appendix A. We show climatological monthly $\tau(t)$, $STE_N(t)$, and $STE_N(t)$ in Figure 2.4, along with the interannual variability from 2009 to 2018 (shown as $\pm$ 1σ). To yield daily values of τ, STE_S, and STE_N for application in Eqs. 2.15 and 2.16, we fit the climatological monthly results to a two-harmonic fit (Figure 2.4).

We validate the two-box model by successfully reconstructing the daily Jena inversion APO flux using troposphere APO inventories and parameters $\tau(t)$, STE_N, and STE_S from two transport models (TM3 and ACTM), as shown in Figure 2.11. This reconstruct shows small RMSE up to 0.53 Tmol day^{-1}. Seasonal cycle of air-sea APO flux is dominated by the inventory term ($\frac{dM^{APO}}{dt}$), with relatively small contribution form the leakage term. The leakage term causes the flux amplitude to be larger than the inventory amplitude by 22.1% in the Northern Hemisphere and 23.2% in the Southern Hemisphere, as shown in Figure 2.12.

The area-integrated APO fluxes calculated using Eq. 2.15 and 2.16 include small contributions from APO fluxes directly caused by the burning of fossil-fuel ($F^{APO(ff)}$). To resolve APO fluxes due to ocean fluxes alone, we compute residual fluxes according to

$$\begin{aligned} F^{APO(ocn)} &= F^{APO} - F^{APO(ff)} \\ &= F^{APO} - \left(F^{O_2(ff)} + 1.1F^{CO_2(ff)}\right) \end{aligned} \quad (2.19)$$

where fossil fuel O_2 flux is calculated by scaling corresponding CO_2 flux

$$F^{O_2(ff)} = -1.35F^{CO_2(ff)} \quad (2.20)$$

The factor of -1.35 is supported by emission ratios from Keeling et al. (1998) and emissions by fuel type from the Global Carbon Budget (Friedlingstein et al., 2022). We use $F^{CO_2(ff)}$ averaged from Open-source Data Inventory for Anthropogenic CO_2 (ODIAC, Oda et al., 2018) and GCP-GridFEDv2022.2 (Jones et al., 2021) (for details see SI Text S3.2). Fossil fuel emission contributes significantly to the loss of APO in the Northern Hemisphere, amounting to an annual uptake of 208.5 Tmol, but its impact on the seasonal cycle is small, accounting for 1.2% of the air-sea flux seasonal amplitude (Figure 2.12). In the Southern Hemisphere, the annual APO uptake of fossil fuels is small, amounting to 15.7 Tmol and 0.06% of the air-sea flux seasonal amplitude (Figure 2.12).

We show the seasonal cycle of air-sea APO flux of each hemisphere in Figure 2.5, calculated by applying the 2-harmonic seasonal APO inventory anomalies in each hemisphere that are resolved in Section 4 to the 2-box model and correcting for the fossil fuel component. The flux uncertainties are calculated from an ensemble of model runs that uses 2000 iterations of harmonic fits from the previous section and convolving these with additional uncertainties in the box-model transport parameter and fossil fuel correction (SI Text S3). Related statistics (maximum and minimum fluxes, maximum and minimum date, APO seasonal net outgassing (SNO), upward zero-crossing date, and annual flux) are summarized in Table 2.2. SNO is defined as the area under the positive portion of the 2-harmonic fitted seasonal cycle curve after removing the annual mean flux, which is a measure of the contribution of air-sea APO flux to the seasonal cycle of atmospheric APO (Garcia & Keeling, 2001). The annual mean flux is calculated as the integration of daily flux over the course of the seasonal cycle.

2.5.2 Results and discussion of air-sea APO fluxes

We find significantly larger SNO in the Southern Hemisphere (518±52.6Tmol) than in the Northern Hemisphere (342±52.1 Tmol). Dividing SNO by the ocean area in each hemisphere, we find a flux per unit area that is also larger (within 1σ uncertainty) in the south (2.49±0.253 mol m^{-2}) than the north (2.21±0.337 mol m^{-2}).

In both hemispheres (Figure 2.5a-b), the APO flux cycle is non sinusoidal, with the rise occurring more rapidly than the decline. Compared to the hemispheric solstice date, the timing of this rise, based on the upward zero-crossing, is earlier by 3 weeks in the Northern Hemisphere (late March) compared to the Southern Hemisphere (mid-October) (Figure 2.5c and Table 2.2). Similarly, the date of maximum summer outgassing is earlier by 5 weeks in the Northern Hemisphere. These estimated phase asymmetries are not very sensitive to assumptions about interhemispheric APO leakage (Figure 2.12).

Differences are also notable in the shape of the declining portion of the cycle. The Southern Hemisphere decrease is relatively steady, while the Northern Hemisphere decrease starts with a slow drop from May to August followed by a late summer plateau till October, and then a rapid drop through January. This near zero flux during the summer plateau leads to a broad atmospheric APO peak in the Northern Hemisphere (Figure 2.3a), corresponding to a period of longer (but weaker) APO outgassing in the Northern Hemisphere (Figure 2.5c). A similar summer plateau is clearly manifested in the CESM, but is weak in the Jena inversion. This feature, however, is not observed in GKT (Figure 2.5d).

Could the phase asymmetry in the APO cycles between the hemispheres be caused by differences in the phasing of seasonal ocean warming and cooling? The simulated flux cycle from GKT, which is calculated by assuming air-sea O_2 flux is in phase with ocean heat flux, does not

support this hypothesis because it does not show such phase asymmetry between hemispheres (Figure 2.5d).

The phase asymmetry is likely caused by other physical and biogeochemical processes that drive the surface ocean O_2 change. A significant factor may be differences in the timing of the spring bloom between hemispheres. Satellite-based chlorophyll concentrations suggest that the spring bloom is roughly one month earlier in the Northern compared to the Southern Hemisphere, with the bloom peaking in April and May over the mid-latitudes (30-50°N) of the North Atlantic and Pacific and peaking in November to January at mid-latitudes (30-50°S) of the Southern Hemisphere (Sapiano et al., 2012). The earlier spring-time O_2 outgassing in the Northern Hemisphere may also be influenced by differences in O_2 equilibration time scale in the mixed layer. As shown in de Boyer Montégut et al. (2004), the mixed layer depth in the mid-latitude Northern Hemisphere is between 10 to 100 meters in spring (April), whereas the depth in the mid-latitude Southern Hemisphere is generally between 100 to 300 meters in spring (October). Assuming a gas exchange velocity of 3 m day^{-1} and a difference in mixed layer depth of 100 m, the equilibration time in the Northern Hemisphere would be about 1 month faster than in the Southern Hemisphere.

The asymmetry in the breadth of the late summer and fall outgassing period (broader and stronger in the Northern Hemisphere) may be influenced by the presence of the shallow oxygen maximum (SOM) in the North Pacific (Hayward, 1994; Shulenberger & Reid, 1981), as noted by Ishidoya et al. (2016). The SOM is generated by the strong surface ocean stratification in the summer, which traps photosynthetically-produced O_2 below the mixed layer, delaying O_2 outgassing until the fall, when the mixed layer deepens. The SOM is confirmed by Argo float measurements over western subtropical North Pacific (17.7-20.2°N and 162-164.5°E), which show

clear oxygen supersaturation beneath the mixed layer from May till November (Yang et al., 2017). We also find, in the CESM configuration, an oxygen supersaturation zone at around 40-60 meters deep over the mid-latitude (20 - 45°N) of the Northern Pacific from July to October (not shown), suggesting that the summer-to-fall plateau in CESM is SOM-related. We could not find a similarly strong late summer and fall plateau in the Southern Hemisphere in both airborne-based flux estimates and the CESM, consistent with the summer mixed layer being deeper in the Southern Hemisphere (Kara et al., 2003).

The phase and SNO differences between hemispheres may also have contributions from tropical ocean fluxes. The CESM and the Jena inversion suggest clear seasonal fluxes in the 20°S - 20°N band (Figure 2.13). The APO fluxes integrated over this band have similar phasing to fluxes in the extratropical Southern Hemisphere, with ocean APO uptake during the austral winter and outgassing during the austral summer. These tropical fluxes therefore contribute to a larger SNO in the Southern Hemisphere and smaller SNO in the Northern Hemisphere, while also contributing to earlier phasing in the north (Figure 2.13).

Table 2.2 also provides annual APO fluxes, based on the secular components of the box model, yielding net global ocean APO uptake of 207 Tmol. The gain of APO in the global ocean is expected from the ocean uptake of anthropogenic CO_2, with small impact from a climate driven net outgassing of APO due to ocean heat uptake from the atmosphere (32 ± 19.6 Tmol net releasing per year) and aerosol-related APO outgassing due to ocean fertilization driven by atmospheric deposition of anthropogenic aerosol (8 ± 4.1 Tmol net releasing per year) (Resplandy et al., 2019). Here we estimate an annual ocean anthropogenic CO_2 uptake of 2.7 ± 0.25 PgC (converted from 247 ± 22.8 Tmol of APO) by subtracting the global climate-driven APO impact and aerosol-related impact from our global annual oceanic APO uptake estimates (for method see SI Text S4). Our

estimation is close to the value (2.8±0.4 PgC) reported in Global Carbon Budget 2021 during the decade 2011-2020 (Friedlingstein et al., 2022).

The hemispheric flux estimates are transport model-dependent because we use TM3 and ACTM models to correct for sparse spatial and temporal sampling and to derive leakage terms in the box model. This impact is small because the flux cycles are dominated by the atmospheric inventory change on the hemispheric scale (Figure 2.12). Using TM3 model alone or ACTM alone only leads to a small SNO differences of 14 Tmol (4.1%) and 17 Tmol (3.3%) in the Northern and Southern Hemisphere, respectively (larger if using ACTM).

Can the airborne data resolve changes in the seasonal cycles over time? Comparing the SNO estimated using HIPPO (2009-2011) data alone or ATom (2016-2018) data alone (by harmonic fits to subsets of the transects), we find SNO of ATom is 5% and 2% larger than that of HIPPO in the Northern and Southern Hemisphere respectively. These changes are not significant compared to uncertainties.

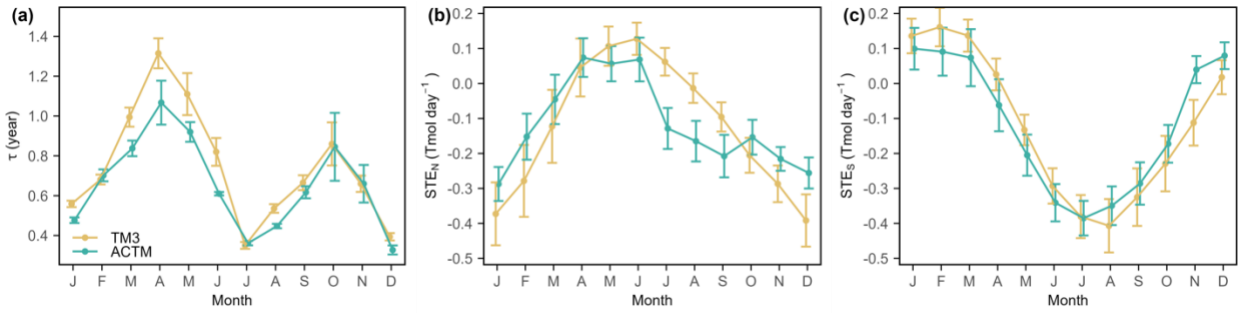

Figure 2.4: (a) Climatological monthly seasonal APO exchange time scale (τ) between the Northern and the Southern troposphere. (b) and (c) Troposphere-stratosphere APO exchange rate (Tmol day^{-1}) in the Northern Hemisphere (STE_N) and Southern Hemisphere (STE_S), respectively. Positive value denotes troposphere to stratosphere APO transport. τ, STE_N, and STE_S are computed using air-sea APO flux from Jena CarboScope APO inversion and tropospheric APO inventory from Jena-TM3 and Jena-ACTM (model descriptions see section 2.5). The 1 σ uncertainty is computed as the standard deviation of τ for each corresponding month from 2009 to 2018. Methods are presented in Appendix A.

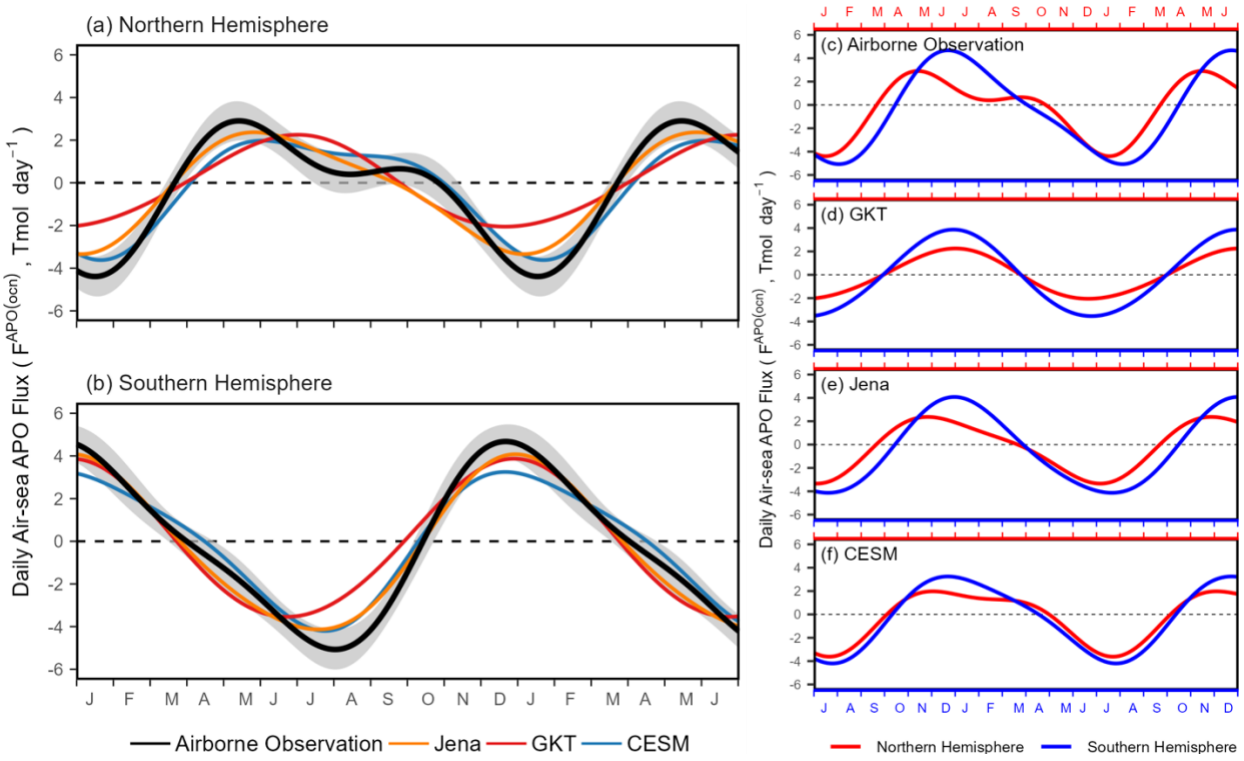

Figure 2.5: Seasonality of area-integrated daily air-sea APO fluxes in the Northern (a) and Southern (b) Hemisphere. We show our estimate of the flux cycle as black curves. The 1 σ uncertainty (gray shading) is calculated as the standard deviation of 2000 iteration of 2-harmonic fit to flux estimates (for details see SI Text S3). For comparison, we also show the modeled daily air-sea APO fluxes from Jena (orange), GKT (red), CESM (blue). The first half-year is repeated. (c) – (f) Comparing the seasonal cycle of APO fluxes from airborne observations and other products in the Northern and Southern Hemisphere, with the cycle in the Southern Hemisphere shifted by 6 months (starting from July, see blue ticks on the bottom). The first half year is repeated. We note that only GKT is adjusted to have zero annual flux.

Table 2.2: Statistical indices of the seasonal cycle of air-sea APO fluxes from two-harmonic fits for each hemisphere computed from airborne observations, Jena inversion, GKT, and CESM. We note that seasonal net outgassing (SNO) and upward zero-crossing date is calculated based on the flux cycles with annual mean flux removed.

Product	Hem.	Max. fluxes (Tmol day^{-1})	Max. Date	Min. fluxes (Tmol day^{-1})	Min. Date	SNO (Tmol)	Upward Zero-crossing Date	Annual Flux (Tmol)
Airborne observation	North	2.9±0.83	135±25.3	-4.4±0.88	16±11.9	342±52.1	79±14.4	-111±34.7
	South	4.7±0.79	354±14.1	-5.1±0.86	214±15.9	518±52.6	284±7.8	-96±34.6
Jena inversion	North	2.4	147	-3.3	5	311	77	-101
	South	4.1	363	-4.1	200	471	283	-113
GKT	North	2.3	183	-2.1	354	250	90	/
	South	3.9	362	-3.5	174	430	271	/
CESM	North	2.0	154	-3.6	21	312	92	-71
	South	3.2	354	-4.2	206	415	281	-66

2.6 Comparisons to other APO flux estimates

2.6.1 Comparison to GKT

We find systematic differences in seasonal amplitudes and phases between our airborne observation-based estimates and the GKT climatology (Figure 2.5). The comparison suggests there are significant limitations to GKT fluxes at mid- to high-latitudes of the Northern Hemisphere, based on discrepancies in the seasonal phases of APO inventory cycle in the mid- to high $M_{\theta e}$ bins (Figure 2.8). The O_2 fluxes from the GKT climatology used dissolved O_{228} data with large gaps in spatial and temporal coverage, especially over the high latitudes (Najjar & Keeling, 1997). To interpolate these sparse data, Garcia and Keeling (2001) assumed that O_2 fluxes are exactly in phase with ocean heat fluxes at a constant ratio over large latitude bands, an approach which has known limitations (Bent, 2014; Sun et al., 2017). These limitations in the coverage of samplings and assumptions lead to a significant underestimate of the northern winter-time O_2 uptake (Figure

2.5a). We find that, in the Labrador Sea, the Garcia & Keeling (2001) climatology yields winter-time (Oct. to Mar.) O_2 uptake of 9.1 mol m^{-2}, compared to more recent estimates of 22.1±2.5 mol m^{-2} for 2016 (Atamanchuk et al., 2020) and 29.1±3.8 mol m^{-2} for 2015 (Koelling et al., 2017).

2.6.2 Comparison to Jena APO inversion

We find relatively good agreement between our hemispheric flux estimates and from the Jena inversions (Figure 2.5 and Table 2.2). The most obvious differences in the Northern Hemisphere are the too weak northern summer plateau and too small northern winter-time oceanic APO uptake. The too small winter-time uptake in inversion estimates based on surface data relative to airborne-based estimates is also found in Resplandy et al. (2016), and is attributed to an underestimation of the vertical mixing by the atmospheric transport models over the north Atlantic. In the Southern Hemisphere, we find evident differences of atmospheric APO seasonal cycles in individual $M_{\theta e}$ bins, where the Jena-TM3 shows a smaller change in APO amplitude from low to high $M_{\theta e}$ than the observations (Figure 2.8). This discrepancy may point to the TM3 model overestimating mixing (across $M_{\theta e}$) in the Southern Hemisphere. This interpretation is also supported by comparison (not shown) between the Jena inversion and shipboard measurements over the Western Pacific from 5°S to 24°S from Tohjima et al. (2012) where the Jena inversion yields amplitudes that are too large by up to 40%.

2.6.3 Comparison to CESM

In the Northern Hemisphere, the CESM shows a too weak spring (MAM) APO outgassing of ~1.5 Tmol day^{-1} but too large fall (SON) outgassing of ~1.2 Tmol day^{-1}. (Figure 2.5a). These discrepancies may result from limitations in the combination of modelled spring-summer export production and fall-time ventilation, as seen in an earlier version of CESM (Nevison et al., 2015). Nevison et al. (2015) pointed out that fall deep water ventilation in multiple Earth System Models

is too weak, which reduces the transport of O_2-depleted deep water into the surface ocean during the northern fall.

In the Southern Hemisphere, the seasonal phases of the CESM are close to airborne observations but peak-to-peak amplitude and SNO are lower than the airborne results.

2.7 Summary and outlook

We use APO observations from two recent airborne projects, HIPPO and ATom, to resolve climatological seasonal APO tropospheric distributions (Section 3), tropospheric inventories (Section 4), and air-sea fluxes (Section 5) at the hemispheric scale. Airborne observations are organized on a mass-weighted moist isentropic coordinate ($M_{\theta e}$) as an alternative to latitude, to analyze atmospheric distributions and to compute tropospheric inventories.

The airborne data resolve clear seasonal APO changes within and between hemispheres (Figure 2.2). The seasonal amplitude is larger in the Southern Hemisphere and is larger in the high-latitudes (low $M_{\theta e}$) of each hemisphere. The seasonal phase also shows a clear gradient over latitudes ($M_{\theta e}$). In the Northern Hemisphere, we find an earlier phase in the lowest latitude (highest $M_{\theta e}$), while in the Southern Hemisphere, we find an earlier phase in the high latitude (lowest $M_{\theta e}$). These different patterns are also observed at surface stations and shipboard measurements over the Pacific Ocean (Keeling et al., 1998; Tohjima et al., 2012).

We also compute hemispheric-scale air-sea fluxes from hemispheric inventories using a 2-box model (Appendix A) that accounts for the surface APO flux, the inter-hemispheric APO exchange, and the troposphere-stratosphere APO exchange. We compare our box-model inverted flux to other model and observation-based products, such as the Jena APO inversion (updates of Rödenbeck et al., 2008), the Garcia and Keeling (2001) O_2 flux climatology, and one configuration of CESM, to identify limitations in these products (Section 6).

Our estimates of air-sea APO fluxes (Figure 2.5) show clear seasonal cycles in both hemispheres, with the ocean releasing APO in the spring and summer and taking up APO in the fall and winter. The cycle in the Northern Hemisphere has a smaller seasonal amplitude, an earlier (relative to the hemispheric solstice date), and a longer period of net outgassing (Figure 2.5) compared to the cycle in the Southern Hemisphere, suggesting differences between the hemispheres in physical and biogeochemical mechanisms, such as a strong subsurface oxygen maximum (SOM) and faster mixed layer equilibration time scale in the Northern Hemisphere.

Our results point to two important flux features in the Northern Hemisphere. The first feature is a strong oceanic O_2 uptake in January. This strong uptake feature is clearly underestimated in observation-based products (i.e., GKT). We attribute the bias in GKT to limited coverage of dissolved O_2 measurements over northern high latitudes and the assumption that O_2 fluxes are exactly in phase with ocean heat fluxes at a constant ratio over large latitude bands, which fails to account for processes during winter-time deep convection events.

The second feature is a period of weak APO outgassing in the northern late summer and fall. This signal is likely related to the development of the SOM, which stores spring-time photosynthetically produced O_2 below the mixed layer, and delays the O_2 outgassing until the fall, when the mixed layer deepens. In comparison with airborne-based estimates during the northern late summer and fall, the CESM shows too strong APO outgassing. On the other hand, two observation-based products (GKT and the Jena inversion) do not capture this northern APO outgassing during the late summer and fall.

Given the evident limitations of the Garcia and Keeling (2001) O_2 flux climatology, our study motivates creation of an improved climatology, taking advantage of expanded measurements of O_2 with atmospheric calibration on biogeochemical Argo floats (Bittig & Körtzinger, 2015,

2017; Bushinsky et al., 2016, 2017; Claustre et al., 2020; Johnson et al., 2015). Our study also motivates future work focusing on regions with winter-time deep convection (e.g., Labrador Sea and western boundary currents) and summer-time stratification (e.g., northwest Pacific) from both modeling and observational perspectives. More realistic depictions of ocean ventilation in general circulation models (e.g., CESM) are needed, along with improved coverage in atmospheric APO station measurements that better target convective regions along with improved skill of modeled atmospheric transport over these regions. Finally, a regular program of hemispheric to global scale airborne transects, such as HIPPO and ATom but at higher frequency, would greatly improve our ability to constrain APO fluxes and resolve interannual variations and trends tied to climate and biogeochemical forcing.

2.8 Appendix A: Box model

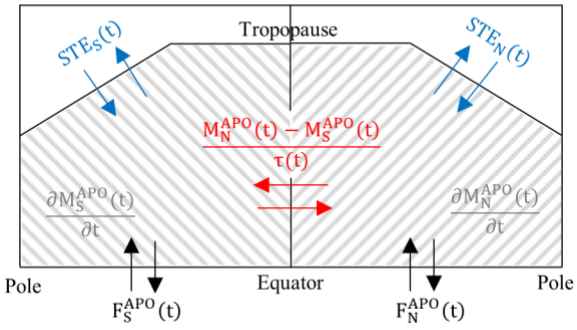

Figure 2.6: Schematic of the box model.

We use a box model (Figure 2.6) as a modified version of the two-box model in Lintner et al. (2004) and Patra et al. (2009) to quantify the hemispheric APO leakage. The model follows:

$$L_N(t) = F_N^{APO}(t) - \frac{\partial M_N^{APO}(t)}{\partial t} = \frac{\left(M_N^{APO}(t) - M_S^{APO}(t)\right)}{\tau(t)} + STE_N(t) \qquad (2.21)$$

$$L_S(t) = F_S^{APO}(t) - \frac{\partial M_S^{APO}(t)}{\partial t} = -\frac{\left(M_N^{APO}(t) - M_S^{APO}(t)\right)}{\tau(t)} + STE_S(t) \quad (2.22)$$

with climatological monthly $\tau(t)$ as the inter-hemisphere APO exchange time with unit of year, and monthly STE_N and STE_S as the stratosphere-troposphere APO exchange with unit of Tmol day^{-1}.

STE_N and STE_S are directly calculated from daily Jena-TM3 and Jena-ACTM as the time derivative of stratosphere APO inventory of each hemisphere, assuming interhemispheric APO exchange in the stratosphere is negligible compared to the exchange across tropopause (Butchart, 2014; Stohl et al., 2003), following:

$$STE_N(t) = \frac{\partial M_N^{APO(Strat)}(t)}{\partial t} \quad (2.23)$$

$$STE_S(t) = \frac{\partial M_S^{APO(Strat)}(t)}{\partial t} \quad (2.24)$$

where $M_N^{APO(Strat)}(t)$ and $M_S^{APO(Strat)}(t)$ are the stratosphere APO inventory in the Northern and Southern Hemisphere, respectively. We report climatological monthly STE in Figure 2.4b and c, with the 1σ uncertainty showing interannual variability.

We solve for the parameter $\tau(t)$ according to:

$$\tau(t) = \frac{2\left(M_N^{APO}(t) - M_S^{APO}(t)\right)}{F_N^{APO}(t) - F_S^{APO}(t) - \frac{\partial\left(M_N^{APO}(t) - M_S^{APO}(t)\right)}{\partial t} - STE_N(t) + STE_S(t)} \quad (2.25)$$

We use monthly $F_N^{APO}(t)$ and $F_S^{APO}(t)$ averaged from daily Jena inversion APO flux, and monthly $M_N^{APO}(t)$ and $M_S^{APO}(t)$ averaged from daily Jena-TM3 or Jena-ACTM, to compute the

climatological monthly $\tau(t)$ (averaged for each month from 2009 to 2018). We report $\tau(t)$ of each model in Figure 2.4a, with the 1σ uncertainty showing interannual variability. In Figure 2.4a, we show that both TM3 and ACTM transport model suggest a faster inter-hemisphere mixing in summer and winter, and a slower mixing in spring and fall.

To examine the skill of the box model in producing daily air-sea APO fluxes, we compare simulated APO fluxes (Jena inversion) with reconstructed APO fluxes calculated using simulated APO inventories based on the Jena inversion APO flux forward transported by the TM3 model (Jena-TM3), and the ACTM model (Jena-ACTM), together with corresponding climatological TM3-based or ACTM-based τ and STE (Figure 2.11). The daily τ and STE is computed by a 2-harmonic fit to climatological monthly τ and climatological monthly STE. We show (Figure 2.11) that this box model can reconstruct the hemispheric air-sea APO flux reasonably well, with RMSE of daily flux smaller than 0.53 Tmol day^{-1}. This method does not bias the SNO results, as we find a small difference of averaged SNO (2009-2018) between the reconstructed APO flux and the original APO flux of 18 Tmol (5.8%) in the Northern Hemisphere and 32 Tmol (6.3%) in the Southern Hemisphere.

2.9 Data Availability Statement

All HIPPO 10 s merge data are available from https://doi.org/10.3334/CDIAC/HIPPO_010 (Wofsy, 2017). Besides, all HIPPO Medusa merge data are available from https://doi.org/10.3334/CDIAC/HIPPO_014 (Wofsy, 2017). All ATom 10s and Medusa merge data are available from https://doi.org/10.3334/ORNLDAAC/1581 (Wofsy et al., 2018).

Jena CarboScope APO inversion (version: apo99XS_v2022) is available from https://www.bgc-jena.mpg.de/CarboScope/?ID=apo99XS_v2022 (Rödenbeck et al., 2008). Garcia and Keeling (2001) climatological monthly O_2 flux data and climatological monthly N_2

flux data from ECCO version 4 are available from https://doi.org/10.5281/zenodo.6516046. The CESM air-sea APO flux fields are available upon request. The atmospheric field of APO forward transported by TM3 and ACTM model are available upon request.

θ_e–M_{θ_e} look-up tables with daily resolution and 1 K intervals in θ_e from 1980 to 2018 computed from ERA-Interim are available at https://doi.org/10.5281/zenodo.4420398 (Jin, 2021).

2.10 Supplement

2.10.1 Possible Sampling Biases in APO Inventories

We identify three potential sampling biases in the estimated climatological cycles of atmospheric APO inventory: (1) limited seasonal coverage (18 transects over the climatological year); (2) limited interannual coverage (sampling particular years instead of all years); (3) limited spatial coverage (under-sampling the full troposphere of each hemisphere). To constrain the likely magnitude of these biases, we compared the true simulated (Jena-TM3 and ACTM-TM3) APO inventory seasonal anomaly averaged over the full 2009-2018 period (computed by integrating over all daily model detrended tropospheric grid cells with a cutoff at PVU = 2) to the "subsampled" anomaly estimated by subsampling simulated APO atmospheric fields (detrended) along 18 flight tracks on corresponding flight dates and using the $M_{\theta e}$ integration method. Simulated 3-D APO fields are first detrended by subtracting a daily smoothed interannual trend from a global mean APO time series using observed data from the Scripps O_2 Program (Hamme & Keeling, 2008). The true seasonal anomaly is calculated using the detrended daily 3-D APO atmospheric field from 2009 to 2018, which yields a true climatological hemispheric APO inventory anomaly cycle based on 2-harmonic fit to daily detrended inventory estimates. We conduct this comparison for each airborne campaign transect at the corresponding mean day of year, calculating the difference between true anomaly and subsampled anomaly, as shown in Figure 2.10. For each transect, the difference between the true anomaly and subsampled anomaly

is small, with an average RMSE across the 18 transects of 1.67 per meg (based on TM3) or 1.21 per meg (based on ACTM) in the Northern Hemisphere, and 1.42 per meg (based on TM3) or 1.68 per meg (based on ACTM) in the Southern Hemisphere. We therefore apply these differences (Figure 2.10) to correct observed hemispheric seasonal APO anomaly of each airborne campaign transect. The uncertainties in these biases are hard to quantify, and are likely transport model dependent, so we take ±100 % as a conservative estimate.

2.10.2 Uncertainties in the seasonal cycle of troposphere APO inventory

We allow for random error in the estimation of each observed ΔM^{APO} (points in Figure 2.3) with the following sources of uncertainty: (1) The irreproducibility of the Medusa and corrected AO2 measurements, potentially causing flight or campaign specific offsets; (2) the computation of $M_{\theta e}$ associated with different reanalysis products; (3) the uncertainty of the above-mentioned spatial and temporal bias correction in SI Text S1; (4) the uncertainty of the exchange ratio of O_2 production/consumption to CO_2 consumption/production from terrestrial biosphere. We now discuss these errors in turn.

2.10.2.1 Measurement imprecision and reproducibility

The $\delta(O_2/N_2)$ measurements from the Medusa flasks and from the AO2 instrument adjusted to match Medusa have several potential sources of bias, including errors in propagating calibration scales, surface effects in flasks or tubing, and sample fractionation, as discussed in detail by Stephens et al. (2021). The imprecision in AO2 is negligible after averaging 1000s of measurements. A comparability imprecision of the Medusa $\delta(O_2/N_2)$ measurements is presented in Stephens et al. (2021), which compared AO2 measurements, adjusted to match Medusa, to 10 stations in the Scripps O_2 Program network, with very broad coincidence criteria (±1000 km horizontally, ±1000 m altitude, and ±10 days). The mean offsets per campaign were typically within ±5 per meg. These means had a standard deviation of ±3.3 per meg, reflecting a

conservative estimate as they are based on many fewer flasks than the full hemispheric inventory. We also allow for uncertainty in the calibration of the $\delta(O_2/N_2)$ and CO_2 measurements due to possible long-term drift in calibration gases in the lab at Scripps, which amounts to ±2 per meg per campaign. We report a quadrature 1σ uncertainty of hemispheric average APO concentration per campaign of ±3.86 per meg, equaling to ±56.31 Tmol of the troposphere inventory of each hemisphere, which is systematic for each airborne campaign.

2.10.2.2 Spread of Mθe values for different reanalysis products

Different reanalysis products produce different daily θ_e-$M_{\theta e}$ relationships. To quantify the sensitivity of ΔM^{APO} to the choice of reanalysis product, we alternately use θ_e-$M_{\theta e}$ look-up table tables generated from NCEP, JRA-55 and MERRA-2 (Gelaro et al., 2017; Kalnay et al., 1996; Kobayashi et al., 2015). Uncertainty is then calculated as the standard deviation of the difference in hemispheric average APO computed from the look-up table generated by using ERA-Interim, NCEP, and MERRA-2 for all airborne campaign transects (18 in each hemisphere). We report that the use of different reanalysis products leads to uncertainty of hemispheric APO inventory amounting to $\pm$ 3.65 Tmol and $\pm$ 2.19 Tmol in the Northern and Southern Hemisphere, respectively.

2.10.2.3 Spatial and temporal bias correction

Each estimate of seasonal APO inventory anomaly could be biased by spatial and temporal sparseness of airborne observations. We correct these biases, as shown above (in Supplement Text 2.10.1). The uncertainty of the correction is assumed to be ±100 % of the corresponding correction to each airborne campaign transect.

2.10.2.4 Biosphere O2:CO2 exchange ratio

We conduct sensitivity test by generating ensemble of hemispheric average APO estimates using the exchange ratio over the range of 1.1 ± 0.05. We find that the varying ratio would alter

each estimate by $\pm$5.1%. We use $\pm$5.1% of the averaged ΔM^{APO} value as the uncertainty of corresponding airborne campaign transect due to the uncertainty of exchange ratio.

2.10.2.5 Overall uncertainties

We calculate the quadrature 1σ uncertainty of each atmospheric seasonal APO inventory anomaly based on uncertainty sources reported above (SI Text S2.1-S2.4). To quantify the 1σ uncertainty of seasonal cycles based on 2-harmonic fits, we generate 2000 iterations of 2-harmonic fits to airborne observed ΔM^{APO} with random 1σ uncertainty reported above to yield ensembles of fits. We note that the uncertainty induced by measurement imprecision of each campaign and in each iteration has the same value in both hemispheres and from both transects. We report uncertainties of the 2-harmonic fitted seasonal cycles (black curves in Figure 2.3) as the standard deviation of these 2000 iterations.

2.10.3 Uncertainties in the seasonal cycle of air-sea APO flux

We allow for random error in the estimation of 2-harmonic fitted seasonal air-sea APO flux estimates with the following sources of uncertainty: (1) uncertainty of 2-harmonic fitted seasonal APO inventory (described in SI Text S2); (2) the uncertainty of the hemispheric APO leakage which comes from the uncertainty of τ(t) and STE (for details see Appendix A); and (3) the uncertainty of the fossil fuel CO_2 emission correction ($F^{APO(ff)}$). We note that $F^{APO(ocn)}$ are mostly driven by the time derivative of APO inventory ($\frac{\partial M^{APO}}{\partial t}$), with small contribution from leakage (Figure 2.12). We now discuss these errors in turn.

2.10.3.1 Uncertainty of leakage correction

We report the climatological monthly τ(t), STE_N, and STE_S based on Jena-TM3 and Jena-ACTM in Appendix A. For 2000 iterations of seasonal APO inventory cycles in each hemisphere, we use monthly τ(t) and STE including 1σ uncertainties from two transport models to invert the seasonal surface APO fluxes. Therefore, 1000 iterations are applied to TM3-based τ and STE,

while another 1000 iterations are applied to ACTM-based τ and STE. The uncertainty of leakage correction is included in the spread of inverted flux estimates.

2.10.3.2 Uncertainty of fossil fuel CO_2 flux correction

We use the average of two monthly fossil fuel CO_2 emission dataset to correct for $F^{APO(ff)}$. One is the Open-source Data Inventory for Anthropogenic CO_2 (ODIAC, Oda et al., 2018). Another one is the GCP-GridFED (Jones et al., 2021). For both datasets, we first calculate a climatological (2009-2018) monthly average CO_2 emission for each hemisphere. We then interpolate monthly flux to daily using linear interpolation. ODIAC suggests an annual fossil fuel CO_2 emission (2009 to 2018 average) of 8.51 PgC yr^{-1} and 0.64 PgC yr^{-1} in the Northern and Southern Hemisphere respectively. GCP-GridFED suggests an annual fossil fuel CO_2 emission (2009 to 2018 average) of 8.25 PgC yr^{-1} and 0.62 PgC yr^{-1} in the Northern and Southern Hemisphere respectively. The annual emission is highly comparable between these two datasets, but GCP-GridFED suggests a seasonal amplitude that is twice as large as that in ODIAC.

Converting anthropogenic CO_2 emission to $F^{APO(ff)}$ (Eq. 2.19 and 2.20), we yield 208.5 Tmol yr^{-1} and 15.7 Tmol yr^{-1} APO lost in the Northern and Southern Hemisphere. The uncertainty in the Northern Hemisphere is particularly important due to large emission, which we assumed to be $\pm$0.5 PgC yr^{-1} based on the uncertainty of global fossil CO_2 emission in Global Carbon Budget of $\pm$0.5 PgC yr^{-1} (Friedlingstein et al., 2022). The uncertainty in the Southern Hemisphere is assumed to be $\pm$0.10 PgC yr^{-1} as a conservative estimate. Therefore, we report uncertainty of daily $F^{APO(ff)}$ to be $\pm$0.034 Tmol d^{-1} and $\pm$0.006 Tmol d^{-1} in the Northern and Southern Hemisphere respectively. We also generate 2000 iterations of climatological cycle of daily $F^{APO(ff)}$ in each hemisphere.

2.10.3.3 Overall uncertainty

The overall uncertainties of 2-harmonic fitted seasonal air-sea APO flux cycles are further computed as the standard deviation of 2000 iterations of box-model inverted flux cycle with fossil fuel APO exchange ($F^{APO(ff)}$) corrected (for details see Section 5.1). We note that we do not explicitly quantify the uncertainty of multi-stations average long-term APO trend, which is expected to be negligibly small compared to the uncertainty of airborne APO measurements.

S4 Deriving annual ocean uptake of anthropogenic CO_2 from annual ocean APO uptake

We first calculate the net APO changes due to ocean sink for anthropogenic carbon ($\mathbf{F^{AO(Cant)}}$) following Resplandy et al (2019):

$$F^{APO(Cant)} = F^{APO(ocn)} - F^{APO(Climate)} - F^{APO(AtmD)} \quad (2.26)$$

where $F^{APO(Climate)}$ is climate driven net outgassing of APO due to ocean heat uptake from the atmosphere (32 ± 19.6 Tmol net releasing per year), and $F^{APO(AtmD)}$ is aerosol-related APO outgassing due to ocean fertilization driven by atmospheric deposition of anthropogenic aerosol (8 ± 4.1 Tmol net releasing per year), as reported in Resplandy et al. (2019).

Net ocean anthropogenic CO_2 uptake ($F^{Cant)}$) can be estimated from $F^{APO(Cant)}$ following:

$$F^{APO(Cant)} = \frac{F^{APO(Cant)}}{1.1} \quad (2.27)$$

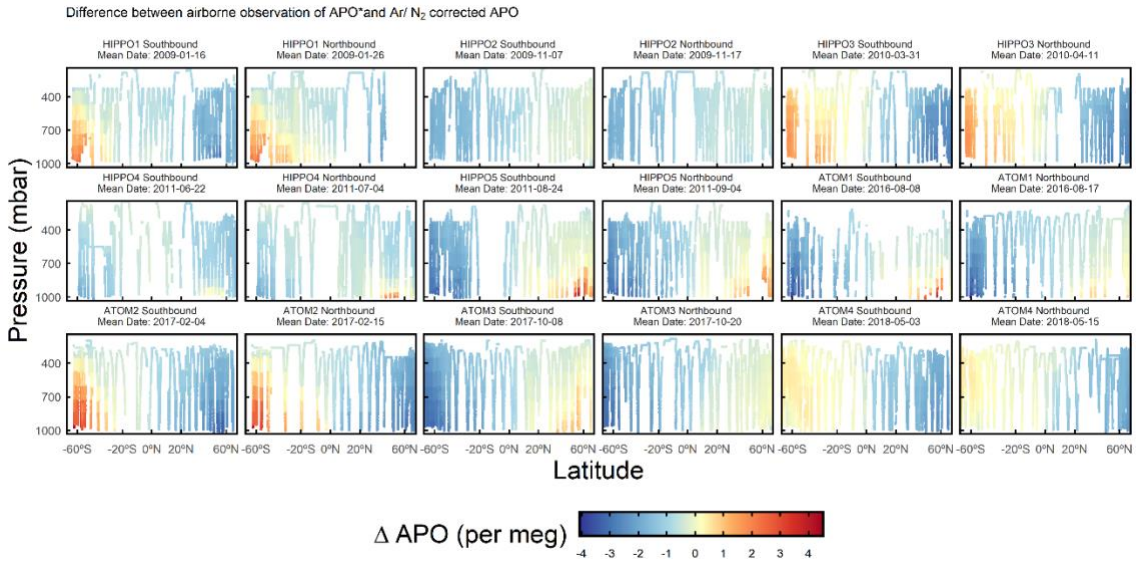

Figure 2.7: Difference between airborne observation of Ar/N2-corrected APO (ΔAPO) and ΔAPO*, computed as ΔAPO-ΔAPO*.

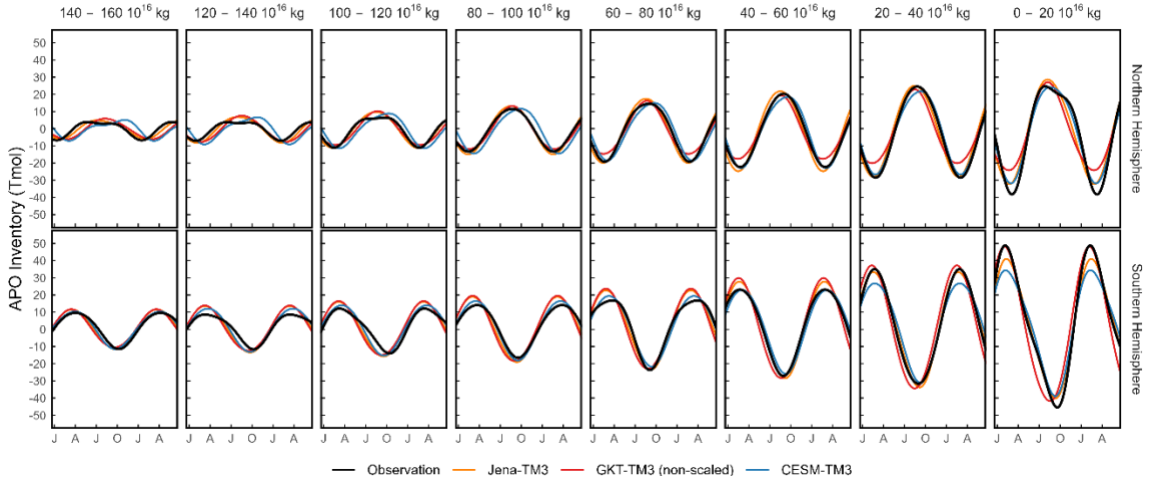

Figure 2.8: APO inventory seasonal cycle (annual mean subtracted) of selected M_θ bins. Cycles are calculated by 2-harmonic fit to mass-weighted average detrended APO of each $M_{\theta e}$ bin with offset removed. We compare airborne observations (black) with four simulations which are Jena-TM3 (orange), non-scaled GKT-TM3 (red), CESM-TM3 (blue), and CESM2-TM3 (light blue) . The first half year is repeated. The calculation of daily simulated APO inventory of each $M_{\theta e}$ band follows Eq. 2.14, using the same troposphere criteria (PVU < 2).

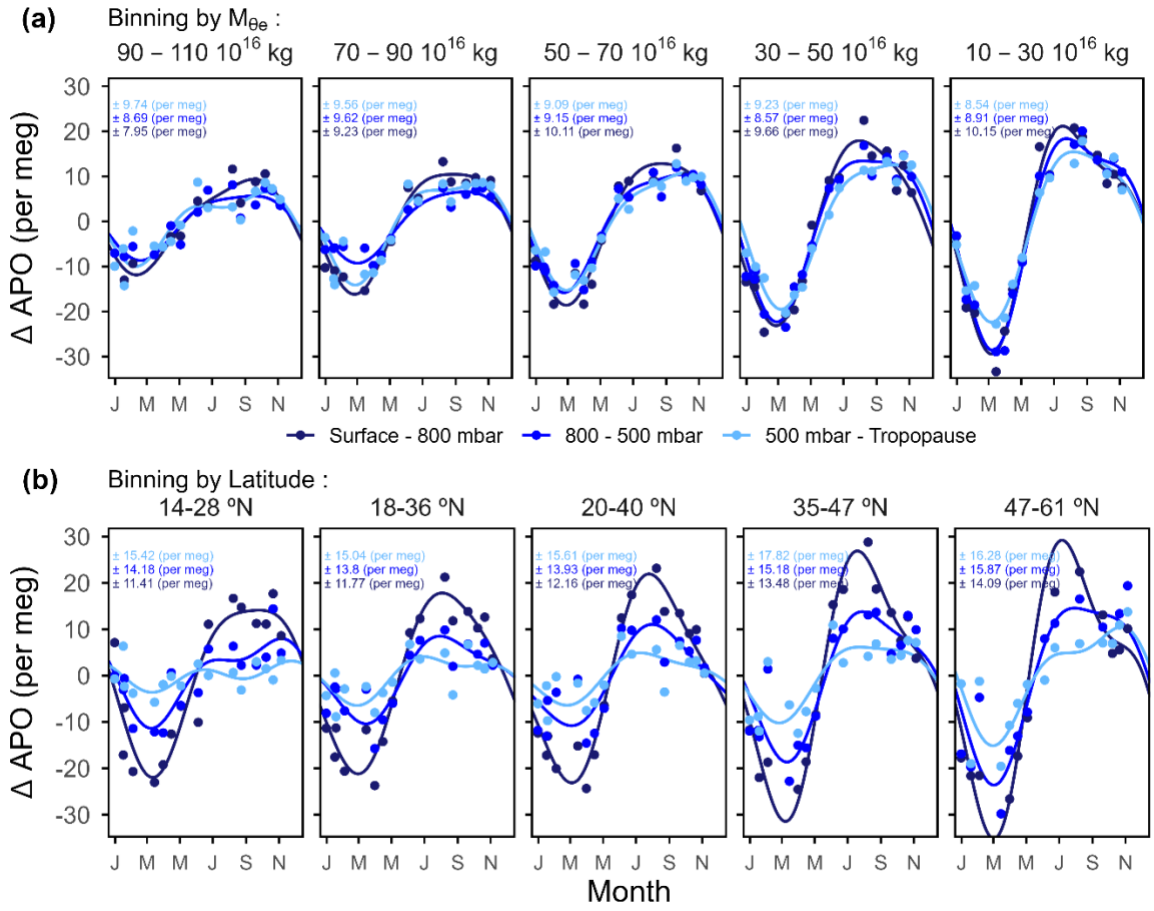

Figure 2.9: Seasonal cycles of airborne Northern Hemisphere APO data sorted by (a) $M_{\theta e}$-pressure bins and (b) latitude-pressure bins. $M_{\theta e}$ bins (10^{16} kg) and latitude bins are shown on the top of each panel. Panel (a) is similar to figure 2a, but with different $M_{\theta e}$ bin. The latitude bounds are chosen to approximate the meridional coverage of each corresponding $M_{\theta e}$ bin in the lower troposphere. Airborne APO observations are first grouped into $M_{\theta e}$-pressure or latitude-pressure bins, and then averaged for each airborne campaign transect, shown as points. We filter out the points averaged from less than twenty 10-sec observations. The 1σ variability about the seasonal cycle fits for each $M_{\theta e}$-pressure or latitude-pressure bin are labelled on top of each panel. These 1σ values are based on the distribution of all binned observations (not shown), rather than the distribution of average APO of each bin and airborne campaign transect (shown).

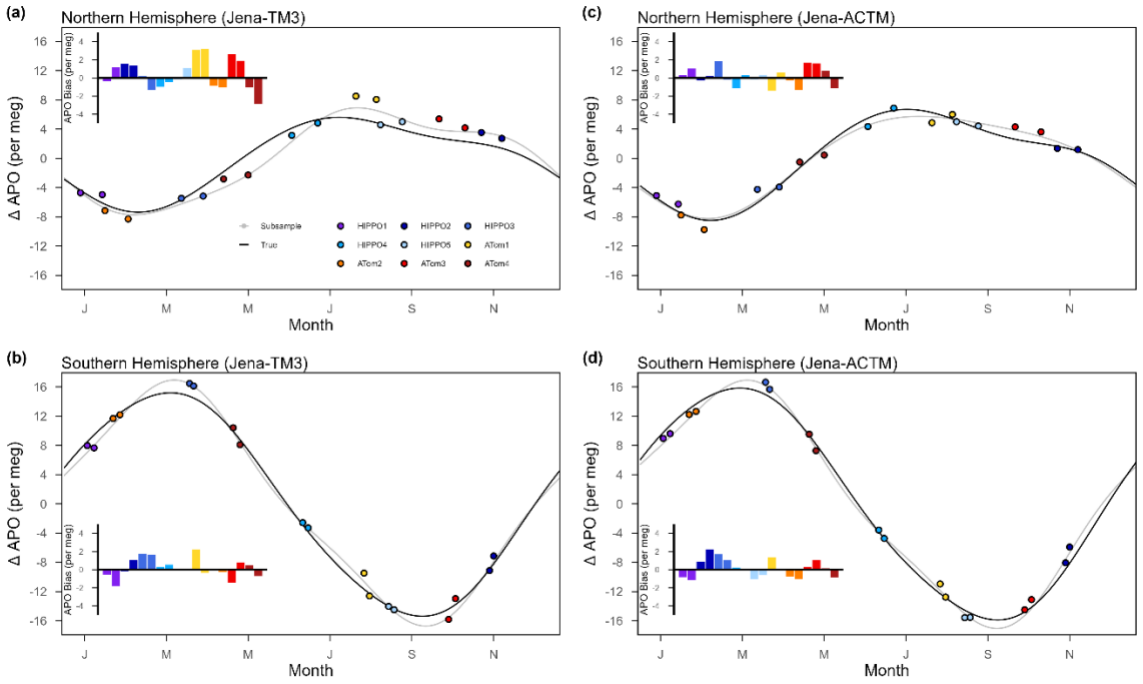

Figure 2.10: Quantification of biases in estimates of hemispheric average troposphere seasonal APO anomaly due to the limited temporal and spatial coverage of HIPPO and ATom airborne campaigns, and the $M_{\theta e}$ integration method, based on simulated atmospheric data using fluxes from the Jena APO inversion and TM3 in (a) and (b), or based on ACTM in (c) and (d). The black line shows the true modeled hemispheric average APO seasonal cycle, which is computed by integrating all detrended model tropospheric (cutoff at PVU = 2) grid cells in each hemisphere from 2009 to 2018 and fitted by a 2-harmonic. Points show the hemispheric average APO calculated using the method from Section 4.1, based on subsampling models (Jena-TM3 and Jena-ACTM) with the coverage of the flight track at corresponding flight dates. The differences between subsampled averages and corresponding true average in each hemisphere are shown in the inserted histogram. These histograms use the same color assignment to represent airborne campaigns as in the main figures (points).

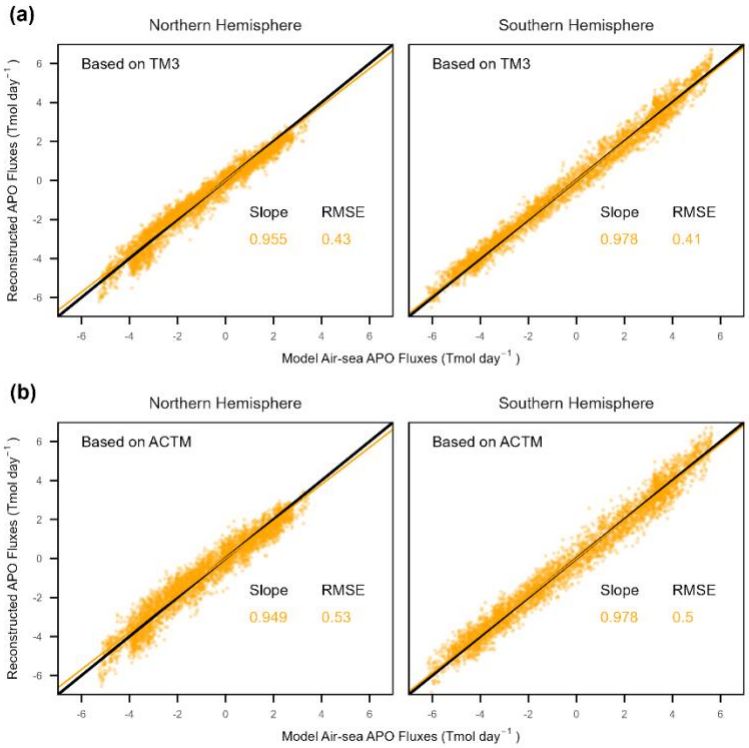

Figure 2.11: Comparison between simulated air-sea APO fluxes (from Jena inversion) and box model reconstructed flux. This reconstruction follows Eq. 2.21-25, with the knowledge of model tropospheric APO inventory and parameter $\tau(t)$ and STE computed from TM3 model in (a) and from ACTM model in (b). We show the linear fit of simulated and reconstructed fluxes as orange line, and compute the slope of the fit and Root-mean-square error (RMSE).

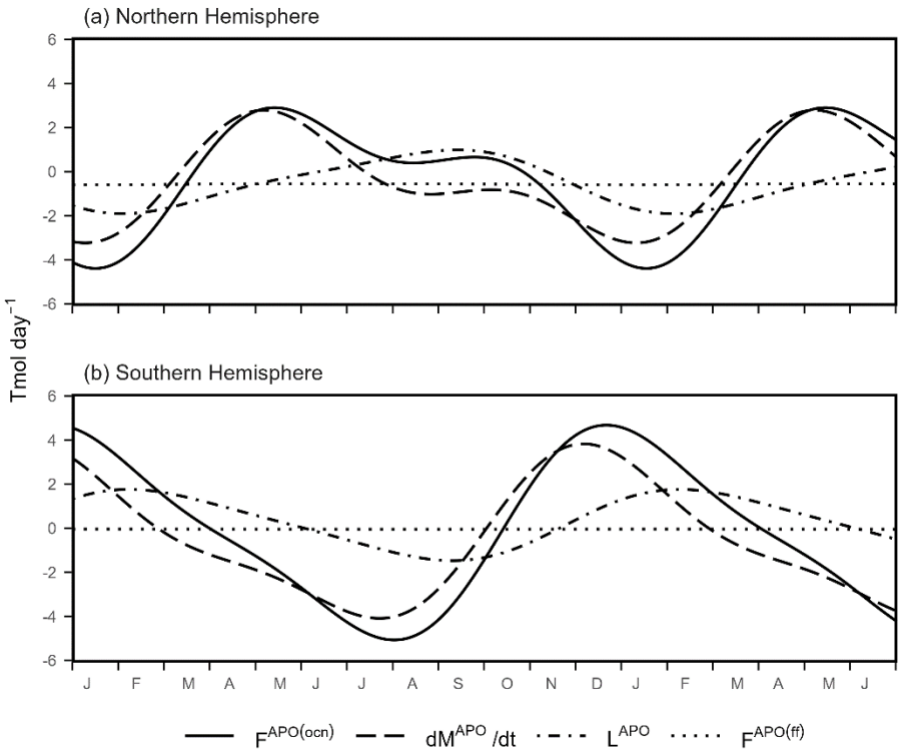

Figure 2.12: Seasonal cycles of air-sea APO fluxes ($F^{APO(ocn)}$, same as the black line in Figure 2.5a and b), with additional components that sum to yield $F^{APO(ocn)}$, as detailed in Eqs. 2.15, 2.16, and 2.19. These components include the time derivative of total atmospheric APO inventory ($\frac{\partial M^{APO}}{\partial t}$), leakage ($L^{APO}$, positive as transport out of the hemisphere) and atmospheric APO inventory change due to fossil fuel emission ($F^{APO(ff)}$, negative as APO lost in the atmosphere). The first half year is repeated.

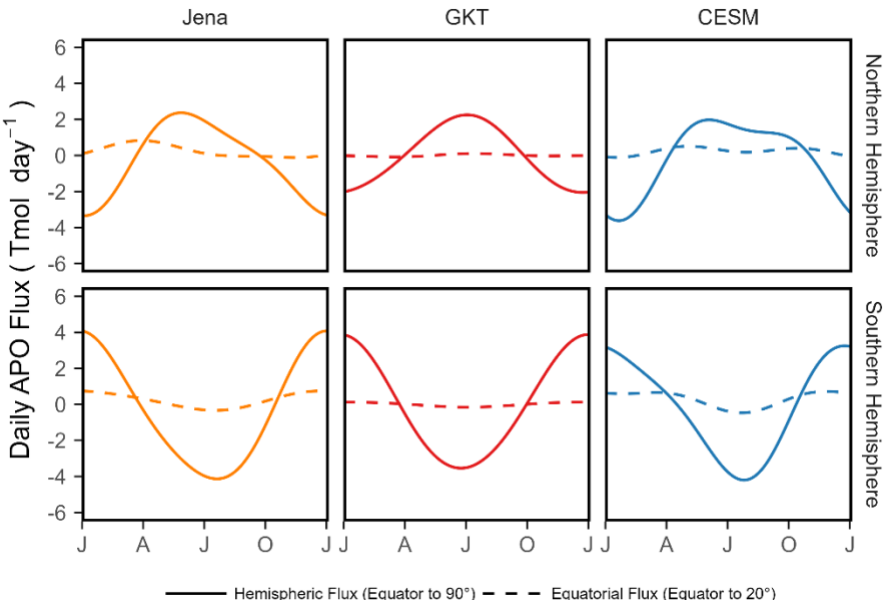

Figure 2.13: Comparing simulated air-sea APO fluxes from the hemispheric scale (Equator to 90°, solid line) and equatorial region (Equator to 20°, dashed line) in each hemisphere.

Table 2.3: Summary of longitude, latitude, and time range of each airborne campaign transect. Each airborne campaign transect is consisted of campaign name, leg name, and correspondent hemisphere.

Campaign	Transect	Hemisphere	Longitude	Latitude	Duration
HIPPO1	Northbound	North	105.0W - 84.0W	0.3N - 39.8N	2009.01.28 – 2009.01.30
		South	169.4E - 94.4W	66.2S – 1.5S	2009.01.20 – 2009.01.28
	Southbound	North	165.3W - 147.7W	0.5N - 80.1N	2009.01.12 - 2009.01.17
		South	169.5E - 165.9W	66.2S – 1.4S	2009.01.17 - 2009.01.21
HIPPO2	Northbound	North	171.9E - 147.8W	0.0N – 83.1N	2009.11.17 – 2009.11.22
		South	151.3E - 174.0 W	66.0S – 0.0S	2009.11.11 – 2009.11.17
	Southbound	North	165.0W – 145.0W	15.0N – 80.0N	2009.11.02 – 2009.11.07
		South	172.3E – 160.4W	66.0S – 1.6S	2009.11.08 - 2009.11.12
HIPPO3	Northbound	North	165.3W – 147.7W	0.6N -85.1N	2010.04.10 – 2010.04.16
		South	169.6E – 165.7W	66.9S – 0.7S	2010.04.05 – 2010.04.10
	Southbound	North	165.4W – 147.0W	0.0N – 84.8N	2010.03.26 – 2010.03.31
		South	169.6E – 165.4W	66.9S – 0.0S	2010.03.31 – 2010.04.06
HIPPO4	Northbound	North	132.2E – 143.0W	0.35N – 82.1N	2011.07.03 – 2011.07.11
		South	128.2E – 172.5E	58.0S – 0.3S	2011.06.28 – 2011.07.03
	Southbound	North	165.0W – 141.5W	0.0N -83.6N	2011.06.16 – 2011.06.23
		South	145.0E – 160.0W	58.0S – 0.0S	2011.06.23 – 2011.06.29
HIPPO5	Northbound	North	165.0W – 145.2W	0.0N – 87.0N	2011.09.04 – 2011.09.08
		South	163.9E – 159.9W	67.2S – 0.0S	2011.08.29 – 2011.09.04
	Southbound	North	165.5W – 147.5W	0.5N – 82.0N	2011.08.19 - 2011.08.24
		South	163.9E – 159.8W	67.2S – 0.6S	2011.08.24 – 2011.08.30

Table 2.4: A list of stations used in the Jena APO Inversion s99XS_v2022. The ship data used in this study is from Tohjima et al. (2012).

Station name	Abbreviation	Latitude	Longitude	Altitude (masl)
Alert	ALT	82.45°N	62.52°W	210
Cold Bay	CBA	55.20°N	162.72°W	25
Cape Ochiishi	COI	43.16°N	145.50°E	55
La Jolla	LJO	32.87°N	117.25°W	15
Hateruma Island	HAT	24.06°N	123.81°E	47
Mauna Loa	MLO	19.53°N	155.58°W	3397
Cape Kumukahi	KUM	19.52°N	154.82°W	3
American Samoa	SMO	14.25°S	170.57°W	42
Cape Grim	CGO	40.68°S	144.68°E	94
Palmer Station	PSA	64.92°S	64.00°W	10
South Pole	SPO	89.98°S	24.8°W	2810

Table 2.5: A list of stations used in calculating global mean APO time series (based on the latitudinal weights from Hamme & Keeling, 2008).

Station name	Abbreviation	Latitude	Longitude	Altitude (masl)	Latitudinal weights
Alert	ALT	82.45°N	62.52°W	210	0.05
Cold Bay	CBA	55.20°N	162.72°W	25	0.11
La Jolla	LJO	32.87°N	117.25°W	15	0.12
Cape Kumukahi	KUM	19.52°N	154.82°W	3	0.2
American Samoa	SMO	14.25°S	170.57°W	42	0.24
Cape Grim	CGO	40.68°S	144.68°E	94	0.17
Palmer Station	PSA	64.92°S	64.00°W	10	0.11

Table 2.6: Airborne observation of APO inventory seasonal anomalies in the Northern Hemisphere, including overall uncertainty of each estimate. We also include each APO inventory anomaly estimate without correction for sparse spatial and temporal coverage of airborne observations. These uncorrected values and the corrections are shown Figure 2.10. We note that the inventory anomalies are estimated relative to the annual average inventory. In the transect column, SB refers to a southbound transect, NB refers to as a northbound transect, P is referred to as the Pacific transect, while A is referred to as the Atlantic transect.

Airborne campaign	Transect	Mean date (DOY)	APO inventory anomaly (Tmol)	Non-corrected APO inventory anomaly (Tmol)
HIPPO1	SB (P)	2009-01-14 (14)	-87±53.9	-88
	NB (P)	2009-01-30 (30)	-150±58.0	-137
HIPPO2	SB (P)	2009-11-04 (308)	68±55.3	82
	NB (P)	2009-11-19 (323)	71±56.7	87
HIPPO3	SB (P)	2010-03-29 (88)	-118±57.9	-101
	NB (P)	2010-04-14 (104)	-117±57.5	-124
HIPPO4	SB (P)	2010-06-18 (169)	101±55.3	86
	NB (P)	2010-07-07 (188)	98±53.4	93
HIPPO5	SB (P)	2011-08-22 (234)	91±57.6	102
	NB (P)	2011-09-07 (250)	71±60.7	97
ATom1	SB (P)	2016-08-03 (215)	90±58.6	106
	NB (A)	2016-08-19 (231)	149±72.1	193
ATom2	SB (P)	2017-02-01 (32)	-124±56.6	-134
	NB (A)	2017-02-17 (48)	-121±59.0	-141
ATom3	SB (P)	2017-10-04 (277)	56±64.2	88
	NB (A)	2017-10-23 (296)	80±60.8	106
ATom4	SB (P)	2018-04-29 (119)	-84±55.0	-89
	NB (A)	2018-05-17 (137)	-27±61.5	-59

Table 2.7: Similar to Table 2.6, but showing the seasonal anomalies of APO inventory in the Southern Hemisphere.

Airborne campaign	Transect	Mean date (DOY)	APO inventory anomaly (Tmol)	Non-corrected APO inventory anomaly (Tmol)
HIPPO1	SB (P)	2009-01-19 (19)	101±61.1	74
	NB (P)	2009-01-24 (24)	160±63.8	123
HIPPO2	SB (P)	2009-11-10 (314)	-138±56.8	-121
	NB (P)	2009-11-14 (318)	-139±63.7	-104
HIPPO3	SB (P)	2010-04-03 (93)	169±57.3	180
	NB (P)	2010-04-08 (98)	157±58.5	166
HIPPO4	SB (P)	2010-06-26 (177)	16±54.0	20
	NB (P)	2010-07-30 (181)	-9±55.0	-5
HIPPO5	SB (P)	2011-08-28 (240)	-203±61.9	-183
	NB (P)	2011-09-01 (244)	-213±62.9	-187
ATom1	SB (P)	2016-08-10 (222)	-159±64.4	-126
	NB (A)	2016-08-14 (226)	-112±62.2	-85
ATom2	SB (P)	2017-02-07 (38)	173±58.1	190
	NB (A)	2017-02-12 (43)	151±57.3	163
ATom3	SB (P)	2017-10-11 (282)	-203±57.2	-212
	NB (A)	2017-10-16 (289)	-225±62.7	-197
ATom4	SB (P)	2018-05-06 (126)	127±55.0	128
	NB (A)	2018-05-11 (131)	140±57.7	125

2.11 Acknowledgments

We would like to acknowledge the efforts of the full HIPPO and ATom science teams and the pilots and crew of the NSF/NCAR GV and NASA DC-8 as well as the NCAR and NASA project managers, field support staff, and logistics experts. In this work, we have used the HIPPO and ATom 10 s merge files. We thank the Harvard QCLS, Harvard OMS, NOAA UCATS, and NOAA Picarro teams for sharing measurements. The recent atmospheric measurements of the Scripps O_2 program have been supported via funding from the NSF and the National Oceanographic and Atmospheric Administration (NOAA) under grants OPP-1922922 and

NA20OAR4320278, respectively. Y. Jin was supported under a grant from NSF (AGS-1623748) and under a grant from Earth Networks. NCAR is sponsored by the National Science Foundation under Cooperative Agreement No. 1852977. HIPPO is supported by NSF ATM-0628519 and ATM-0628388, ATom1 is supported by NSF AGS-1547626 and AGS-1547797. ATom2-4 are supported by NSF AGS-1623745 and AGS-1623748. Any opinions, findings, conclusions, and recommendations expressed in this material are those of the authors and do not necessarily reflect the views of NSF, NOAA, or DOE.

Chapter 2, in full, is a reprint of the material as it appears in Jin. Y., Stephens, B. B, Keeling, R. F., Morgan, E. J., Rödenbeck, C., Patra, P., Long, M. C.: Seasonal Tropospheric Distribution and Air-sea Fluxes of Atmospheric Potential Oxygen from Global Airborne Observations, Global Biogeochemical Cycles, 37, e2023GB007827. https://doi.org/10.1029/2023GB007827. The dissertation author was the primary investigator and author of this paper.

Reference

Atamanchuk, D., Koelling, J., Send, U., & Wallace, D. W. R. (2020). Rapid transfer of oxygen to the deep ocean mediated by bubbles. *Nature Geoscience*, *13*, 232–237. https://doi.org/10.1038/s41561-020-0532-2

Battle, M., Fletcher, S. M., Bender, M. L., Keeling, R. F., Manning, A. C., Gruber, N., et al. (2006). Atmospheric potential oxygen: New observations and their implications for some atmospheric and oceanic models. *Global Biogeochemical Cycles*, *20*(1). https://doi.org/10.1029/2005GB002534

Bent, J. D. (2014). *Airborne oxygen measurements over the Southern Ocean as an integrated constraint of seasonal biogeochemical processes*. University of California, San Diego.

Bittig, H. C., & Körtzinger, A. (2015). Tackling oxygen optode drift: Near-surface and in-air oxygen optode measurements on a float provide an accurate in situ reference. *Journal of*

Atmospheric and Oceanic Technology, *32*(8), 1536–1543. https://doi.org/10.1175/JTECH-D-14-00162.1

Bittig, H. C., & Körtzinger, A. (2017). Technical note: Update on response times, in-air measurements, and in situ drift for oxygen optodes on profiling platforms. *Ocean Science*, *13*(1), 1–11. https://doi.org/10.5194/os-13-1-2017

Bushinsky, S. M., Emerson, S. R., Riser, S. C., & Swift, D. D. (2016). Accurate oxygen measurements on modified argo floats using in situ air calibrations. *Limnology and Oceanography: Methods*, *14*(8), 491–505. https://doi.org/10.1002/lom3.10107

Bushinsky, S. M., Gray, A. R., Johnson, K. S., & Sarmiento, J. L. (2017). Oxygen in the Southern Ocean From Argo Floats: Determination of Processes Driving Air-Sea Fluxes. *Journal of Geophysical Research: Oceans*, *122*(11), 8661–8682. https://doi.org/10.1002/2017JC012923

Butchart, N. (2014). The Brewer-Dobson circulation. *Reviews of Geophysics*, *52*(2), 157–184. https://doi.org/10.1002/2013RG000448

Claustre, H., Johnson, K. S., & Takeshita, Y. (2020). Observing the Global Ocean with Biogeochemical-Argo. *Annual Review of Marine Science*, *12*, 23–48. https://doi.org/10.1146/annurev-marine-010419-010956

Dee, D. P., Uppala, S. M., Simmons, A. J., Berrisford, P., Poli, P., Kobayashi, S., et al. (2011). The ERA-Interim reanalysis: Configuration and performance of the data assimilation system. *Quarterly Journal of the Royal Meteorological Society*, *137*(656), 553–597. https://doi.org/10.1002/qj.828

Dietze, H., & Oschlies, A. (2005). On the correlation between air-sea heat flux and abiotically induced oxygen gas exchange in a circulation model of the North Atlantic. *Journal of*

Geophysical Research C: Oceans, *110*(C9). https://doi.org/10.1029/2004JC002453

Diskin, G. S., Podolske, J. R., Sachse, G. W., & Slate, T. A. (2002). Open-path airborne tunable diode laser hygrometer. *Diode Lasers and Applications in Atmospheric Sensing*, *4817*, 196–204. https://doi.org/10.1117/12.453736

Forget, G., Campin, J. M., Heimbach, P., Hill, C. N., Ponte, R. M., & Wunsch, C. (2015). ECCO version 4: An integrated framework for non-linear inverse modeling and global ocean state estimation. *Geoscientific Model Development*, *8*(10), 3071–3104. https://doi.org/10.5194/gmd-8-3071-2015

Friedlingstein, P., Jones, M. W., Sullivan, M. O., Andrew, R. M., Bakker, D. C. E., Hauck, J., et al. (2022). Global Carbon Budget 2021. *Earth System Science Data*, *14*(4), 1917–2005. https://doi.org/10.5194/essd-14-1917-2022

Gallagher, M. E., Liljestrand, F. L., Hockaday, W. C., & Masiello, C. A. (2017). Plant species, not climate, controls aboveground biomass O_2 : CO_2 exchange ratios in deciduous and coniferous ecosystems. *Journal of Geophysical Research: Biogeosciences*, *122*(9), 2314–2324. https://doi.org/10.1002/2017JG003847

Garcia, E., & Keeling, F. (2001). On the global oxygen anomaly and air-sea flux. *Journal of Geophysical Research*, *106*(C12), 31155–31166. https://doi.org/10.1029/1999JC000200

Gelaro, R., McCarty, W., Suárez, M. J., Todling, R., Molod, A., Takacs, L., et al. (2017). The Modern-Era Retrospective Analysis for Research and Applications, Version 2 (MERRA-2). *Journal of Climate*, *30*(14), 5419–5454. https://doi.org/https://doi.org/10.1175/JCLI-D-16-0758.1

Goto, D., Morimoto, S., Aoki, S., Patra, P. K., & Nakazawa, T. (2017). Seasonal and short-term variations in atmospheric potential oxygen at Ny-Ålesund, Svalbard. *Tellus, Series B:*

Chemical and Physical Meteorology, *69*(1). https://doi.org/10.1080/16000889.2017.1311767

Hamme, R. C., & Keeling, R. F. (2008). Ocean ventilation as a driver of interannual variability in atmospheric potential oxygen. *Tellus, Series B: Chemical and Physical Meteorology*, *60*(5), 706–717. https://doi.org/10.1111/j.1600-0889.2008.00376.x

Hayward, T. L. (1994). The shallow oxygen maximum layer and primary production. *Deep-Sea Research Part I*, *41*(3), 559–574. https://doi.org/10.1016/0967-0637(94)90095-7

Heimann, M., & Körner, S. (2003). *The global atmospheric tracer model TM3: Model description and user's manual Release 3.8 a*. MPI-BGC.

Hintsa, E. J., Moore, F. L., Hurst, D. F., Dutton, G. S., Hall, B. D., Nance, J. D., et al. (2021). UAS Chromatograph for Atmospheric Trace Species (UCATS) - A versatile instrument for trace gas measurements on airborne platforms. *Atmospheric Measurement Techniques*, *14*(10), 6795–6819. https://doi.org/10.5194/amt-14-6795-2021

Hockaday, W. C., Masiello, C. A., Randerson, J. T., Smernik, R. J., Baldock, J. A., Chadwick, O. A., & Harden, J. W. (2009). Measurement of soil carbon oxidation state and oxidative ratio by 13C nuclear magnetic resonance. *Journal of Geophysical Research: Biogeosciences*, *114*(2), 1–14. https://doi.org/10.1029/2008JG000803

Ishidoya, S., Uchida, H., Sasano, D., Kosugi, N., Taguchi, S., Ishii, M., et al. (2016). Ship-based observations of atmospheric potential oxygen and regional air-sea O_2 flux in the northern North Pacific and the Arctic Ocean. *Tellus, Series B: Chemical and Physical Meteorology*, *68*(1). https://doi.org/10.3402/tellusb.v68.29972

Ishidoya, S., Tsuboi, K., Niwa, Y., Matsueda, H., Murayama, S., Ishijima, K., & Saito, K. (2022). Spatiotemporal variations of the $\delta(O_2/N_2)$, CO_2 and δ(APO) in the troposphere over

the western North Pacific. *Atmospheric Chemistry and Physics*, *22*(10), 6953–6970. https://doi.org/10.5194/acp-22-6953-2022

Jin, X., Najjar, R. G., Louanchi, F., & Doney, S. C. (2007). A modeling study of the seasonal oxygen budget of the global ocean. *Journal of Geophysical Research: Oceans*, *112*(C5). https://doi.org/10.1029/2006JC003731

Jin, Y. (2021). θ-Mθe Lookup Table (ERA-Interim) (Version v1.0.0) [Data set], Zenodo. https://doi.org/https://doi.org/10.5281/zenodo.4420398

Jin, Y., Keeling, R., Morgan, E., Ray, E., Parazoo, N., & Stephens, B. (2021). A mass-weighted atmospheric isentropic coordinate for mapping chemical tracers and computing inventories. *Atmospheric Chemistry and Physics*, *21*, 217–238. https://doi.org/10.5194/acp-2020-841

Johnson, K. S., Plant, J. N., Riser, S. C., & Gilbert, D. (2015). Air oxygen calibration of oxygen optodes on a profiling float array. *Journal of Atmospheric and Oceanic Technology*, *32*(11), 2160–2172. https://doi.org/10.1175/JTECH-D-15-0101.1

Jones, M. W., Andrew, R. M., Peters, G. P., Janssens-Maenhout, G., De-Gol, A. J., Ciais, P., et al. (2021). Gridded fossil CO_2 emissions and related O_2 combustion consistent with national inventories 1959–2018. *Scientific Data*, *8*(1), 1–23. https://doi.org/10.1038/s41597-020-00779-6

Kalnay, E., Kanamitsu, M., Kistler, R., & Collins, W. (1996). The NCEP/NCAR 40-Year Reanalysis Project. *Bulletin of the American Meteorological Society*, *77*(3), 437–472. https://doi.org/10.1175/1520-0477(1996)077<0437:TNYRP>2.0.CO;2

Kara, A. B., Rochford, P. A., & Hurlburt, H. E. (2003). Mixed layer depth variability over the global ocean. *Journal of Geophysical Research C: Oceans*, *108*(C3). https://doi.org/10.1029/2000jc000736

Keeling, R. F., Stephens, B. B., Najjar, R. G., Doney, S. C., Archer, D., & Heimann, M. (1998). Seasonal variations in the atmospheric O_2/N_2 ratio in relation to the kinetics of air-sea gas exchange. *Global Biogeochemical Cycles*, *12*(1), 141–163. https://doi.org/10.1029/97GB02339

Keeling, R. F., Blaine, T., Paplawsky, B., Katz, L., Atwood, C., & Brockwell, T. (2004). Measurement of changes in atmospheric Ar/N_2 ratio using a rapid-switching, single-capillary mass spectrometer system. *Tellus B: Chemical and Physical Meteorology*, *56*(4), 322–338. https://doi.org/10.3402/tellusb.v56i4.16453

Keeling, R. F., Walker, S. J., & Paplawsky, W. (2020). *Span Sensitivity of the Scripps Interferometric Oxygen Analyzer*.

Kobayashi, S., Ota, Y., Harada, Y., Ebita, A., Moriya, M., Onoda, H., et al. (2015). The JRA-55 reanalysis: General specifications and basic characteristics. *Journal of the Meteorological Society of Japan*, *93*(1), 5–48. https://doi.org/10.2151/jmsj.2015-001

Koelling, J., Wallace, D. W. R., Send, U., & Karstensen, J. (2017). Intense oceanic uptake of oxygen during 2014–2015 winter convection in the Labrador Sea. *Geophysical Research Letters*, *44*(15), 7855–7864. https://doi.org/10.1002/2017GL073933

Langenfelds, R. L. (2002). *Studies of the global carbon cycle using atmospheric oxygen and associated tracers*. University of Tasmania.

Lintner, B. R., Gilliland, A. B., & Fung, I. Y. (2004). Mechanisms of convection-induced modulation of passive tracer interhemispheric transport interannual variability. *Journal of Geophysical Research D: Atmospheres*, *109*(D13102). https://doi.org/10.1029/2003JD004306

Long, M. C., Moore, J. K., Lindsay, K., Levy, M., Doney, S. C., Luo, J. Y., et al. (2021).

Simulations With the Marine Biogeochemistry Library (MARBL). *Journal of Advances in Modeling Earth Systems*, *13*(12), e2021MS002647. https://doi.org/10.1029/2021MS002647

Manizza, M., Keeling, R. F., & Nevison, C. D. (2012). On the processes controlling the seasonal cycles of the air–sea fluxes of O_2 and N_2O: A modelling study. *Tellus B: Chemical and Physical Meteorology*, *64*(1), 18429. https://doi.org/10.3402/tellusb.v64i0.18429

Manning, A. C., & Keeling, R. F. (2006). Global oceanic and land biotic carbon sinks from the scripps atmospheric oxygen flask sampling network. *Tellus, Series B: Chemical and Physical Meteorology*, *58*(2), 95–116. https://doi.org/10.1111/j.1600-0889.2006.00175.x

Montegut, C. de B., Madec, G., Fischer, A. S., Lazar, A., & Iudicone, D. (2004). Mixed layer depth over the global ocean: An examination of profile data and a profile-based climatology. *Journal of Geophysical Research: Oceans*, *109*(12), 1–20. https://doi.org/10.1029/2004JC002378

Morgan, E. J., Manizza, M., Keeling, R. F., Resplandy, L., Mikaloff-Fletcher, S. E., Nevison, C. D., et al. (2021). An atmospheric constraint on the seasonal air–sea exchange of oxygen and heat in the extratropics. *Journal of Geophysical Research: Oceans*, *126*(8), e2021JC017510. https://doi.org/10.1029/2021jc017510

Naegler, T., Ciais, P., Rodgers, K., & Levin, I. (2006). Excess radiocarbon constraints on air-sea gas exchange and the uptake of CO_2 by the oceans. *Geophysical Research Letters*, *33*(L11802). https://doi.org/10.1029/2005GL025408

Naegler, T., Ciais, P., Orr, J. C., Aumont, O., & Rödenbeck, C. (2007). On evaluating ocean models with atmospheric potential oxygen. *Tellus*, *59B*, 138–156. https://doi.org/10.1111/j.1600-0889.2006.00197.x

Najjar, R. G., & Keeling, R. F. (1997). Analysis of the mean annual cycle of the dissolved

oxygen anomaly in the World Ocean. *Journal of Marine Research*, *55*, 117–151. https://doi.org/10.1357/0022240973224481

Najjar, R. G., & Keeling, R. F. (2000). Mean annual cycle of the air-Sea oxygen flux: A global view. *Global Biogeochemical Cycles*, *14*(2), 573–584. https://doi.org/10.1029/1999GB900086

Nevison, C., Munro, D., Lovenduski, N., Cassar, N., Keeling, R., Krummel, P., & Tjiputra, J. (2018). Net Community Production in the Southern Ocean: Insights From Comparing Atmospheric Potential Oxygen to Satellite Ocean Color Algorithms and Ocean Models. *Geophysical Research Letters*, *45*(19), 10549–10559. https://doi.org/10.1029/2018GL079575

Nevison, C. D., Mahowald, N. M., Doney, S. C., Lima, I. D., & Cassar, N. (2008). Impact of variable air-sea O_2 and CO_2 fluxes on atmospheric potential oxygen (APO) and land-ocean carbon sink partitioning. *Biogeosciences*, *5*(3), 875–889. https://doi.org/10.5194/bg-5-875-2008

Nevison, C. D., Keeling, R. F., Kahru, M., Manizza, M., Mitchell, B. G., & Cassar, N. (2012). Estimating net community production in the Southern Ocean based on atmospheric potential oxygen and satellite ocean color data. *Global Biogeochemical Cycles*, *26*, GB1020. https://doi.org/10.1029/2011GB004040

Nevison, C. D., Manizza, M., Keeling, R. F., Kahru, M., Bopp, L., Dunne, J., et al. (2015). Evaluating the ocean biogeochemical components of Earth system models using atmospheric potential oxygen and ocean color data. *Biogeosciences*, *12*, 193–208. https://doi.org/10.5194/bg-12-193-2015

Nevison, C. D., Manizza, M., Keeling, R. F., Stephens, B. B., Bent, J. D., Dunne, J., et al.

(2016). Evaluating CMIP5 ocean biogeochemistry and Southern Ocean carbon uptake using atmospheric potential oxygen: Present-day performance and future projection. *Geophysical Research Letters*, *43*(5), 2077–2085. https://doi.org/10.1002/2015GL067584

Oda, T., Maksyutov, S., & Andres, R. J. (2018). The Open-source Data Inventory for Anthropogenic CO_2, version 2016 (ODIAC2016): A global monthly fossil fuel CO_2 gridded emissions data product for tracer transport simulations and surface flux inversions. *Earth System Science Data*, *10*(1), 87–107. https://doi.org/10.5194/essd-10-87-2018

Parazoo, N. C., Denning, A. S., Berry, J. A., Wolf, A., Randall, D. A., Kawa, S. R., et al. (2011). Moist synoptic transport of CO_2 along the mid-latitude storm track. *Geophysical Research Letters*, *38*, L09804. https://doi.org/https://doi.org/10.1029/2011GL047238

Patra, P. K., Takigawa, M., Dutton, G. S., Uhse, K., Ishijima, K., Lintner, B. R., et al. (2009). Transport mechanisms for synoptic, seasonal and interannual SF_6 variations and "age" of air in troposphere. *Atmospheric Chemistry and Physics*, *9*(4), 1209–1225. https://doi.org/10.5194/acp-9-1209-2009

Patra, Prabir K., Takigawa, M., Watanabe, S., Chandra, N., Ishijima, K., & Yamashita, Y. (2018). Improved chemical tracer simulation by MIROC4.0-based atmospheric chemistry-transport model (MIROC4-ACTM). *Scientific Online Letters on the Atmosphere*, *14*, 91–96. https://doi.org/10.2151/SOLA.2018-016

Pauluis, O., Czaja, A., & Korty, R. (2008). The global atmospheric circulation on moist isentropes. *Science*, *321*(5892), 1075–1078. https://doi.org/https://doi.org/10.1126/science.1159649

Pickers, P. A., & Manning, A. C. (2015). Investigating bias in the application of curve fitting programs to atmospheric time series. *Atmospheric Measurement Techniques*, *8*(3), 1469–

1489. https://doi.org/10.5194/amt-8-1469-2015

Pickers, Penelope A., Manning, A. C., Sturges, W. T., Le Quéré, C., Mikaloff Fletcher, S. E., Wilson, P. A., & Etchells, A. J. (2017). In situ measurements of atmospheric O_2 and CO_2 reveal an unexpected O_2 signal over the tropical Atlantic Ocean. *Global Biogeochemical Cycles*, *31*(8), 1289–1305. https://doi.org/10.1002/2017GB005631

Reinsch, C. H. (1967). Smoothing by spline functions. *Numerische Mathematik*, *10*, 177–183. https://doi.org/10.1007/BF02169154

Resplandy, L., Keeling, R. F., Stephens, B. B., Bent, J. D., Jacobson, A., Rödenbeck, C., & Khatiwala, S. (2016). Constraints on oceanic meridional heat transport from combined measurements of oxygen and carbon. *Climate Dynamics*, *47*, 3335–3357. https://doi.org/https://doi.org/10.1007/s00382-016-3029-3

Resplandy, L., Keeling, R. F., Eddebbar, Y., Brooks, M., Wang, R., Bopp, L., et al. (2019). Quantification of ocean heat uptake from changes in atmospheric O_2 and CO_2 composition. *Scientific Reports*, *9*(1), 1–10. https://doi.org/10.1038/s41598-019-56490-z

Rödenbeck, C., Le Quéré, C., Heimann, M., & Keeling, R. F. (2008). Interannual variability in oceanic biogeochemical processes inferred by inversion of atmospheric O_2/N_2 and CO_2 data. *Tellus B: Chemical and Physical Meteorology*, *60*(5), 685–705. https://doi.org/10.1111/j.1600-0889.2008.00375.x

Santoni, G. W., Daube, B. C., Kort, E. A., Jiménez, R., Park, S., Pittman, J. V., et al. (2014). Evaluation of the airborne quantum cascade laser spectrometer (QCLS) measurements of the carbon and greenhouse gas suite - CO_2, CH_4, N_2O, and CO - during the CalNex and HIPPO Campaigns. *Atmospheric Measurement Techniques*, *7*, 1509–1526. https://doi.org/https://doi.org/10.5194/amt-7-1509-2014

Sapiano, M. R. P., Brown, C. W., Schollaert Uz, S., & Vargas, M. (2012). Establishing a global climatology of marine phytoplankton phenological characteristics. *Journal of Geophysical Research: Oceans*, *117*(8), 1–16. https://doi.org/10.1029/2012JC007958

Scott, S. G., Bui, T. P., Chan, K. R., & Bowen, S. W. (1990). The meteorological measurement system on the NASA ER-2 aircraft. *Journal of Atmospheric & Oceanic Technology*, *7*(4), 525–540. https://doi.org/10.1175/1520-0426(1990)007<0525:tmmsot>2.0.co;2

Severinghaus, J. P. (1995). *Studies of the terrestrial O_2 and carbon cycles in sand dune gases and in Biosphere 2*. Columbia University.

Shulenberger, E., & Reid, J. L. (1981). The Pacific shallow oxygen maximum, deep chlorophyll maximum, and primary productivity, reconsidered. *Deep Sea Research Part A, Oceanographic Research Papers*, *28*(9), 901–919. https://doi.org/10.1016/0198-0149(81)90009-1

Stephens, B. B., Keeling, R. F., Heimann, M., Six, K. D., Murnane, R., & Caldeira, K. (1998). Testing global ocean carbon cycle models using measurements of atmospheric O_2 and CO_2 concentration. *Global Biogeochemical Cycles*, *12*(2), 213–230. https://doi.org/10.1029/97GB03500

Stephens, B. B., Keeling, R. F., & Paplawsky, W. J. (2011). Shipboard measurements of atmospheric oxygen using a vacuum-ultraviolet absorption technique. *Tellus B: Chemical and Physical Meteorology*, *55*(4), 857–878. https://doi.org/10.3402/tellusb.v55i4.16386

Stephens, B. B., Morgan, E. J., Bent, J. D., Keeling, R. F., Watt, A. S., Shertz, S. R., & Daube, B. C. (2021). Airborne measurements of oxygen concentration from the surface to the lower stratosphere and pole to pole. *Atmospheric Measurement Techniques*, *14*(3), 2543–2574. https://doi.org/10.5194/amt-14-2543-2021

Stohl, A., Bonasoni, P., Cristofanelli, P., Collins, W., Feichter, J., Frank, A., et al. (2003). Stratosphere-troposphere exchange: A review, and what we have learned from STACCATO. *Journal of Geophysical Research Atmospheres*, *108*(12). https://doi.org/10.1029/2002jd002490

Stull, R. B. (2012). *An introduction to boundary layer meteorology*. Springer Science & Business Media.

Sun, D., Ito, T., & Bracco, A. (2017). Oceanic Uptake of Oxygen During Deep Convection Events Through Diffusive and Bubble-Mediated Gas Exchange. *Global Biogeochemical Cycles*, *31*(10), 1579–1591. https://doi.org/10.1002/2017GB005716

Takahashi, T., Sutherland, S. C., Wanninkhof, R., Sweeney, C., Feely, R. A., Chipman, D. W., et al. (2009). Climatological mean and decadal change in surface ocean pCO_2, and net sea-air CO_2 flux over the global oceans. *Deep-Sea Research Part II: Topical Studies in Oceanography*, *56*(8–10), 554–577. https://doi.org/10.1016/j.dsr2.2008.12.009

Thompson, C. R., Wofsy, S. C., Prather, M. J., Newman, P. A., Hanisco, T. F., Ryerson, T. B., et al. (2022). The NASA Atmospheric Tomography (ATom) Mission: Imaging the Chemistry of the Global Atmosphere. *Bulletin of the American Meteorological Society*, *103*(3), 761–790. https://doi.org/10.1175/BAMS-D-20-0315.1

Thompson, R. L., Manning, A. C., Lowe, D. C., & Weatherburn, D. C. (2007). A ship-based methodology for high precision atmospheric oxygen measurements and its application in the Southern Ocean region. *Tellus, Series B: Chemical and Physical Meteorology*, *59*(4), 643–653. https://doi.org/10.1111/j.1600-0889.2007.00292.x

Tohjima, Y., Mukai, H., Machida, T., & Nojiri, Y. (2003). Gas-chromatographic measurements of the atmospheric oxygen/nitrogen ratio at Hateruma Island and Cape Ochi-ishi, Japan.

Geophysical Research Letters, *30*(12). https://doi.org/10.1029/2003GL017282

Tohjima, Yasunori, Minejima, C., Mukai, H., MacHida, T., Yamagishi, H., & Nojiri, Y. (2012). Analysis of seasonality and annual mean distribution of atmospheric potential oxygen (APO) in the Pacific region. *Global Biogeochemical Cycles*, *26*, GB4008. https://doi.org/10.1029/2011GB004110

Tohjima, Yasunori, Terao, Y., Mukai, H., Machida, T., Nojiri, Y., & Maksyutov, S. (2015). ENSO-related variability in latitudinal distribution of annual mean atmospheric potential oxygen (APO) in the equatorial Western Pacific. *Tellus, Series B: Chemical and Physical Meteorology*, *67*(1), 25869. https://doi.org/10.3402/tellusb.v67.25869

Tohjima, Yasunori, Mukai, H., MacHida, T., Hoshina, Y., & Nakaoka, S. I. (2019). Global carbon budgets estimated from atmospheric O_2/N_2 and CO_2 observations in the western Pacific region over a 15-year period. *Atmospheric Chemistry and Physics*, *19*(14), 9269–9285. https://doi.org/10.5194/acp-19-9269-2019

Tsujino, H., Urakawa, S., Nakano, H., Small, R. J., Kim, W. M., Yeager, S. G., et al. (2018). JRA-55 based surface dataset for driving ocean–sea-ice models (JRA55-do). *Ocean Modelling*, *130*, 79–139. https://doi.org/10.1016/j.ocemod.2018.07.002

Wanninkhof, R. (1992). Relationship between wind speed and gas exchange over the ocean revisited. *Limnology and Oceanography: Methods*, *97*(C5), 7373–7382. https://doi.org/10.4319/lom.2014.12.351

Weiss, R. F. (1970). The solubility of nitrogen, oxygen and argon in water and seawater. *Deep-Sea Research and Oceanographic Abstracts*, *17*(4), 721–735. https://doi.org/10.1016/0011-7471(70)90037-9

Wofsy, S. HIPPO MEDUSA Flask Sample Trace Gas And Isotope Data. Version 1.0.

UCAR/NCAR - Earth Observing Laboratory. https://doi.org/10.3334/CDIAC/HIPPO_014. (2017).

Wofsy, S. C. (2011). HIAPER Pole-to-Pole Observations (HIPPO): fine-grained, global-scale measurements of climatically important atmospheric gases and aerosols. *Philosophical Transactions of the Royal Society A: Mathematical, Physical and Engineering Sciences*, *369*(1943), 2073–2086. https://doi.org/https://doi.org/10.1098/rsta.2010.0313

Wofsy, S. C. HIPPO Merged 10-Second Meteorology, Atmospheric Chemistry, and Aerosol Data. Version 1.0. UCAR/NCAR - Earth Observing Laboratory. https://doi.org/10.3334/CDIAC/HIPPO_010. (2017).

Wofsy, S. C., Afshar, S., Allen, H., APEL, E., Asher, E., Barletta, B., et al. (2018). ATom: Merged Atmospheric Chemistry, Trace Gases, and Aerosols. *ORNL DAAC*. https://doi.org/https://doi.org/10.3334/ORNLDAAC/1581

Worrall, F., Clay, G. D., Masiello, C. A., & Mynheer, G. (2013). Estimating the oxidative ratio of the global terrestrial biosphere carbon. *Biogeochemistry*, *115*, 23–32. https://doi.org/10.1007/s10533-013-9877-6

Yang, B., Emerson, S. R., & Bushinsky, S. M. (2017). Annual net community production in the subtropical Pacific Ocean from in situ oxygen measurements on profiling floats. *Global Biogeochemical Cycles*, *31*(4), 728–744. https://doi.org/10.1002/2016GB005545

Yeager, S. G., Rosenbloom, N., Glanville, A. A., Wu, X., Simpson, I., Li, H., et al. (2022). The Seasonal-to-Multiyear Large Ensemble (SMYLE) prediction system using the Community Earth System Model version 2. *Geoscientific Model Development*, *15*(16), 6451–6493. https://doi.org/10.5194/gmd-15-6451-2022

Zondlo, M. A., Paige, M. E., Massick, S. M., & Silver, J. A. (2010). Vertical cavity laser

hygrometer for the National Science Foundation Gulfstream-V aircraft. *Journal of Geophysical Research Atmospheres*, *115*, D20309. https://doi.org/10.1029/2010JD014445

Chapter 3 Improved Atmospheric Constraints on Southern Ocean CO_2 Exchange

Abstract

The net air-sea CO_2 exchange over the Southern Ocean (SO), which includes a significant anthropogenic carbon sink superimposed on strong natural fluxes, is poorly constrained due to sparse observations. Here we present an improved estimate of SO CO_2 exchange over three latitude bands using atmospheric CO_2 measurements from global airborne campaigns and an atmospheric 4-box model based on a mass-indexed isentropic coordinate ($M_{\theta e}$). Our estimates show two features not clearly resolved by previous atmospheric measurements: a weak winter-time outgassing in the polar region, and a sharp phase transition of the seasonal flux cycles between polar/subpolar and subtropical regions. Our estimates suggest much stronger summer-time uptake in the polar/subpolar regions than estimated using pCO_2 derived from profiling floats, but somewhat weaker uptake than a recent study by Long et al (Long et al., 2021) that used the same airborne data as this study while quantifying atmospheric transport using atmospheric transport models (ATMs). The box-model approach requires knowledge of diabatic air mixing rates between boxes (transport across θ_e or $M_{\theta e}$ surfaces), which we estimate from moist static energy (MSE) budgets derived from meteorological reanalyses. This mixing rate can also be derived from ATMs, but we show clear summer-time discrepancies with the MSE-based mixing rates. These discrepancies of mixing rates and differences between simulated and observed CO_2 gradients indicate that most ATMs tend to have excessive diabatic mixing at high southern latitudes in austral summer.

Significance Statement

Precise estimates of Southern Ocean (SO) CO_2 uptake are lacking due to sparse surface-ocean observations. This study presents an alternate approach applying airborne CO_2 observations

to constrain the SO air-sea CO_2 flux using a multi-box atmospheric model aligned with moist isentropes. This study improves upon prior studies that estimate flux based on atmospheric CO_2 measurements by using better-constrained estimates of atmospheric diabatic transport (transport across moist isentropes). It also allows fluxes to be resolved in finer latitude bands, thus facilitating a closer comparison with surface ocean pCO_2 observations and identifying CO_2 flux components driven by marine photosynthesis, ventilation, and warming/cooling. Our study underscores the value of aircraft measurements for precisely quantifying long-term changes in CO_2 uptake by the SO.

3.1 Introduction

Precise assessments of the air-sea CO_2 flux of the Southern Ocean (SO), which includes both natural and anthropogenic components, are of critical importance to understanding the global carbon cycle and to predicting future oceanic carbon uptake under climate change (2–5). The high-latitude SO (<58°S) was likely a significant natural source of CO_2 to the atmosphere in the preindustrial era, but has switched to being a net sink in the present-day (6). Available estimates suggest that uptake over the entire SO (<35°S) strengthened from 1980 to 2015, with significant decadal variability (5, 7–11).

Observation-based flux estimates of the entire SO remain highly uncertain. The net SO CO_2 flux has been quantified using pCO_2 measurements from ship-based and Argo float observations (12–18) and from atmospheric CO_2 measurements at surface stations that are inverted by atmospheric transport models (ATMs) (19–25). These products, however, show a large spread of flux estimates, and are limited by sparse observations, possible measurement biases, and uncertainties in near-surface wind speed, gas exchange coefficients, and modeled atmospheric transport.

Recently, Long et al. (1, henceforth Long21) used atmospheric CO_2 observations from a series of global airborne campaigns to estimate the seasonal cycle of SO (90°S to 45°S) CO_2 flux, averaged from 2009 to 2018, and reported an annual oceanic uptake of 0.53 ± 0.23 PgC yr^{-1}. This annual sink estimate is consistent with the average of atmospheric inversion products (henceforth 3-D inversions) and ship-based pCO_2 products (Surface Ocean CO_2 Atlas, SOCAT), but larger than recent pCO_2-based estimates using profiling floats data from Southern Ocean Carbon and Climate Observations and Modeling project (SOCCOM) (16, 18). Long21 also identified a larger summer-time CO_2 uptake compared to the SOCCOM-based flux estimates and the average of multiple atmospheric inversion products. The method of Long21 uses the atmospheric CO_2 gradient across potential temperature (θ) as an emergent constraint on the underlying air-sea flux, taking advantage of the tendency of CO_2 to be well-mixed on θ surfaces (26–28).

Here we apply the same airborne datasets (detailed in Material and Methods and *SI Appendix,* Fig. 3.6) as Long21 to infer seasonal cycles of air-sea CO_2 flux using a novel 4-box tropospheric inverse method (Fig. 3.1a, henceforth 4-box inversion), in which the boxes are aligned with a mass-indexed moist isentropic coordinate, $M_{\theta e}$ (29). This coordinate has a nearly constant relationship with latitude and season over the SO and, like both θ and θ_e coordinates, is the preferential mixing surface of CO_2 in the troposphere (27, 29). The method invokes a mass balance, accounting for the CO_2 inventory change within each box using observations and the exchange of CO_2 between boxes determined by cross-$M_{\theta e}$ diabatic transport calculated as the product of observed CO_2 gradients and parameterized diabatic mixing rates from the moist static energy (MSE) budgets of meteorological reanalyses. The 4-box inversion allows fluxes to be resolved at scales smaller than in Long21, in three zonal bands between 90°S and ~37°S (Fig. 3.1b and *SI Appendix,* Fig. 3.7) which we label as "polar," "subpolar," and "subtropical," and identifies

finer-scale discrepancies with pCO_2-based flux products (16, 30–34). Our flux estimates also help to identify the latitudinal structure of processes driving seasonal pCO_2 changes and CO_2, such as the interactions between marine photosynthesis, ocean ventilation, and warming/cooling (35, 36).

Accurate assessment of atmospheric transport, especially diabatic transport, is critical for inverting surface CO_2 fluxes. Diabatic transport is conventionally determined using ATMs (37), but these models show a large spread of simulated transport, which is related to uncertainty in advection, convection and boundary height parameterizations (21, 38–40). Prior studies have identified errors in ATMs by pointing to vertical CO_2 gradients being overestimated in simulations at mid-latitude (41, 42).

In this paper, we start by describing the structure of the $M_{\theta e}$-aligned box-model inversion and validate this method. We conduct a systematic analysis of uncertainty in simulated diabatic mixing rates across three $M_{\theta e}$ surfaces over the mid- to high-latitude SO by developing two relevant constraints, one based on moist static energy (MSE) budgets and the other based on atmospheric CO_2 gradients across $M_{\theta e}$ surfaces. We present our airborne-based seasonal flux estimates and discuss key features and mechanisms that cause the flux cycles to vary meridionally. Estimates obtained from airborne measurements are further compared with other flux products to identify any limitations these products may have. We also discuss the broad implications of our method for resolving decadal variability and long-term trends in SO CO_2 fluxes, resolving surface fluxes of other species and in other regions, and the potential to improve ATMs in general.

3.2 Results and Discussions

3.2.1 Box-model Architecture and Evaluation

The 4-box inversion model, shown in Figure 3.1a (detailed in Materials and Methods) divides the troposphere in the Southern Hemisphere into discrete boxes, with lateral boundaries aligned with fixed values of $M_{\theta e}$ (26). The $M_{\theta e}$ coordinate is aligned with θ_e, but a given $M_{\theta e}$

surface constantly adjusts to keep the total dry airmass under it conserved. Each $M_{\theta e}$ surface is indexed to the corresponding contained airmass (29). The three primary boxes of the model each contain 15×10^{16} kg of dry air, and intersect the surface of the Earth in zonal bands (Fig. 3.1b). The northern-most fourth box provides a boundary condition for the third box. The CO_2 flux at the bottom of each primary box is calculated from mass balance, based on diagnosed CO_2 transport between boxes and observed inventory changes within the boxes (Eq. 3.1). A key assumption of the 4-box model is that the adiabatic transport (along θ_e or $M_{\theta e}$ transport) is sufficiently rapid that CO_2 meridional transport is mainly controlled by bi-directional diabatic transport (across θ_e or $M_{\theta e}$ transport) between boxes, thus effectively reducing the troposphere to a discrete 1-dimensional mixing system. This assumption and performance of the box-model is validated below. In this model, diabatic transport is parameterized based on the cross-$M_{\theta e}$ CO_2 gradient and a seasonally-dependent diabatic mixing rate, expressed in $kg^2\ day^{-1}$ (Eq. 3.2). Because airmass (kg) has replaced latitude or length in our box model, these mixing rates are analogous to diffusion coefficients, with the advantage of representing fundamental properties of the atmosphere that are independent of model discretization.

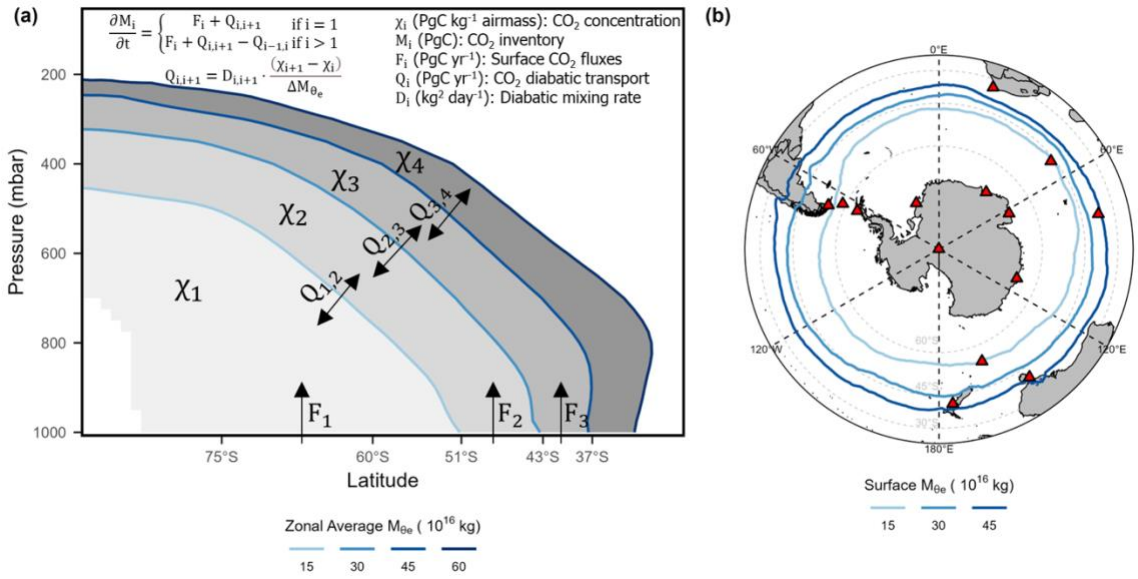

Figure 3.1: (a) Schematic of the box model. Boundaries of the box model are selected $M_{\theta e}$ surfaces at 15, 30, 45, and 60 $M_{\theta e}$ values (10^{16} kg), which are shown as zonal and 2009-2018 averages. (b) Selected near-surface $M_{\theta e}$ contours as 2009-2018 averages. $M_{\theta e}$ is computed from 3-hourly MERRA-2 reanalysis. These $M_{\theta e}$ bands are nearly fixed with season (*SI Appendix*, Fig. 3.7). Red triangles show the location of surface stations that are used in the Carbon Tracker 2019b 3-D CO_2 inversion product.

We calculate climatological monthly diabatic mixing rates using two approaches, one based on atmospheric transport model simulations of total CO_2 (ATM-based mixing rates), and one based on moist static energy budgets derived from MERRA-2 and JRA-55 reanalyses (MSE-based mixing rates) (see Materials and Methods). We find a large difference among ATM-based mixing rates, while the two MSE-based mixing rates are highly consistent, and are generally smaller than ATM-based mixing rates, especially in austral summer (Fig. 3.2 and *SI Appendix*, Fig. 3.8). MSE-based mixing rates are also more precisely defined, because MSE is exactly parallel with the $M_{\theta e}$ coordinate by definition and because MSE has strong gain/loss and gradients (as needed to diagnose diabatic mixing rates) in all seasons.

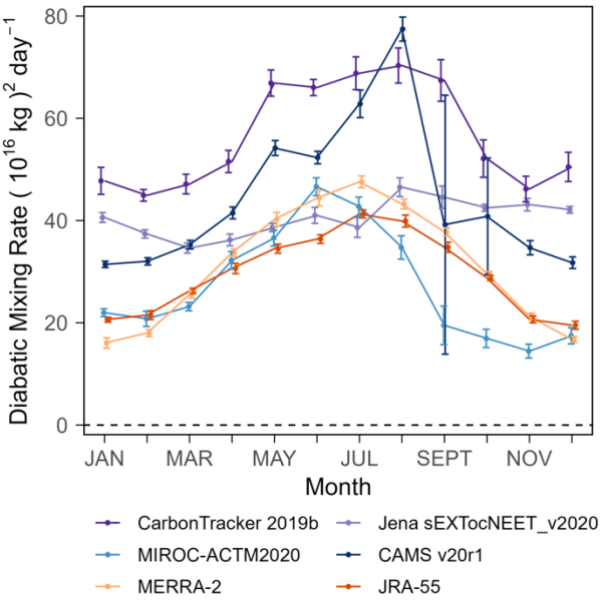

Figure 3.2: Diabatic mixing rates of the 30 (10^{16} kg) $M_{\theta e}$ surface. These mixing rates are parameterized from four 3-D CO_2 inversion products and moist static energy budget of two reanalysis products (MERRA-2 and JRA-55). Error bars represent only the interannual variability of parameterized mixing rates, which is shown to be small, with the exception of CAMS in September because of the close-to-zero CO_2 gradient across the 30 (10^{16} kg) $M_{\theta e}$ surface. Diabatic mixing rates of the 15 and 45 (10^{16} kg) $M_{\theta e}$ surface are shown in *SI Appendix,* Fig. 3.8.

We validate the 4-box inversion approach by applying the method to reconstruct surface CO_2 fluxes in each 3-D inversion (Fig. 3.3), using the full 3-D gridded atmospheric CO_2 fields of each product, averaged over each box, and using the corresponding parameterized climatological ATM-based mixing rates from the same model (detailed in Materials and Methods). This method provides an internally consistent system for each 3-D inversion, and the reconstructed surface fluxes align well with original inverted fluxes over each zonal band (RMSE $\leq$ 0.12 PgC yr^{-1}, Fig. 3.3a, *SI Appendix,* Fig. 3.9-3.11, *SI Appendix,* Table 3.1), especially over the climatological seasonal cycle (Fig. 3.3b). The 4-box inversion also reconstructs the interannual variability (IAV) of fluxes (e.g., Fig. 3.3a), even with the box-model CO_2 transport being driven by interannually-constant mixing rates, showing that flux IAV can be learned from variations in atmospheric CO_2 gradients, while the impact of IAV in the atmospheric dynamics is relatively small. The validation

confirms that the complex 3-dimensional circulation of the atmosphere at high southern latitudes can be approximated by mixing along one dimension (the coordinate $M_{\theta e}$), at least for the purpose of resolving zonally-averaged SO CO_2 fluxes.

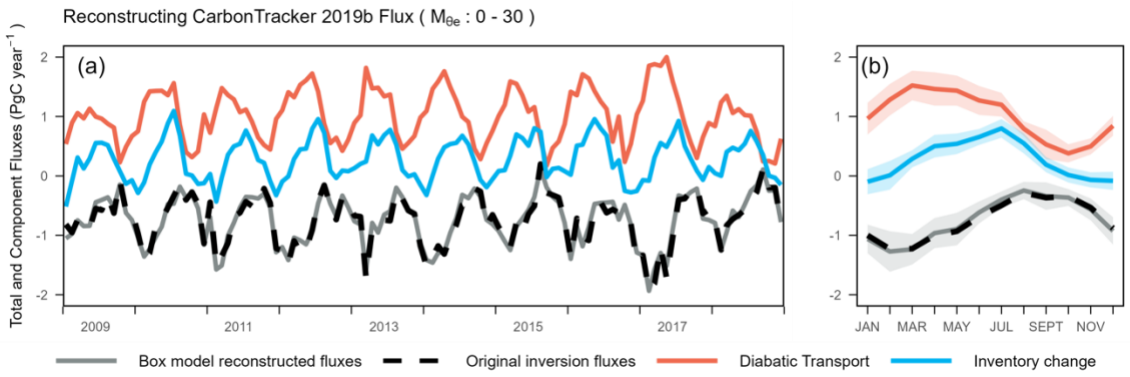

Figure 3.3: (a) Monthly reconstructed air-sea CO_2 fluxes (solid gray) for the 0-30 (10^{16} kg) $M_{\theta e}$ band (south of ~ 43°S near the Earth surface) based on CarbonTracker 2019b, compared with the original monthly 3-D inversion fluxes for the same $M_{\theta e}$ band (dashed black). The other components (i.e., diabatic CO_2 transport and CO_2 inventory change, detailed in Materials and Methods, and Eq. 3.1) of the box-model reconstruction are shown as well. Positive values of the diabatic transport represent CO_2 transport into the 0-30 $M_{\theta e}$ band (poleward transport). We note that the inventory change (blue) equals the sum of fluxes (black) and diabatic transport (red). (b) Similar to (a), but showing the flux and other components as climatological monthly averages (2009 to 2018). Shaded regions show interannual variability, which is calculated as the standard deviation over 10 years for the corresponding month. We also show these reconstructions for other 3-D inversion products and other surface $M_{\theta e}$ bands in *SI Appendix*, Fig. 3.9-3.11.

3.2.2 Diabatic Mixing Rate Evaluation

The large spread in ATM-based mixing rates and the systematic difference from MSE-based mixing rates (Fig. 3.2) in austral summer emphasize the need for constraints on this critical mixing parameter. We find that the ATM-simulated gradients are strongly anti-correlated with corresponding ATM-based mixing rates (Fig. 3.4), which is expected because a larger mixing rate corresponds to more rapid homogenization across $M_{\theta e}$ surfaces, leading to a smaller gradient. Based on the intercept of the fits to the ATM gradient-mixing rates relationship, the two MSE-based mixing rates are highly comparable to observed CO_2 gradients (Fig. 3.4), suggesting that the two sets of MSE-based mixing rates are more realistic than estimates of ATM-based mixing rate.

All but one of the ATMs simulate CO_2 gradients that are too small compared to observations, suggesting these ATMs overestimate summer-time mixing. The exception is the ACTM model, which yields a realistic summer gradient and mixing rates compatible with the MSE budget. In the rest of the year, both MSE-based mixing rates and ATM-based mixing rates, as well as simulated and observed CO_2 gradients are generally within the 1σ uncertainty of the observed gradients and close to two MSE-based mixing rates (*SI Appendix,* Fig. 3.12).

For the 4-box inversions presented here, we alternately use two sets of MSE-based mixing rates to invert airborne CO_2 observations, where we allow for uncertainty in mixing based on the spread between these two estimates and their small IAV (detailed in *SI Appendix*, Text 3.7.2).

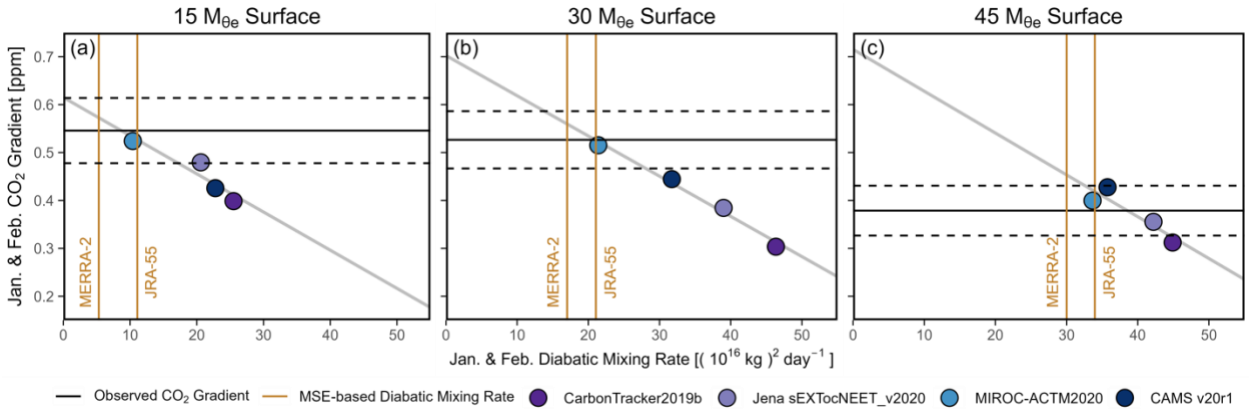

Figure 3.4: Exploring the correlation between Jan. and Feb. ATM-based mixing rates at each $M_{\theta e}$ surface and simulated atmospheric CO_2 gradients across the corresponding $M_{\theta e}$ surface of four transport models (3-D CO_2 inversion products). Simulated gradients are from 3-D concentration fields averaged at the mean dates of five airborne campaigns or sub-campaigns that took place during January and February (HIPPO1, ATom2, and ORCAS1-3). The corresponding ATM-based mixing rate is calculated as the January and February average. For comparison, we show the observed CO_2 gradients (spatial bias corrected, as detailed in *SI Appendix*, Text 3.7.1) as horizontal black lines, which are calculated as the average of the same five campaigns or sub-campaigns, while the dashed lines show the $1\,\boldsymbol{\sigma}$ uncertainty (measurement and spatial bias correction uncertainty). We also show two MSE-based mixing rates (January and Feburary average) as vertical brown lines. A similar figure exploring the correlation between April to November averaged CO_2 gradient and averaged diabatic mixing rate is presented in *SI Appendix*, Fig. 3.12.

3.2.3 Airborne-based air-sea CO_2 fluxes

We calculate air-sea CO_2 fluxes using the observed CO_2 inventory of each $M_{\theta e}$ box and CO_2 gradients across $M_{\theta e}$ surfaces from each airborne campaign, which are resolved by binning airborne data into four $M_{\theta e}$ bands (detailed in Materials and Methods). We correct for small biases in CO_2 inventory and gradient induced by sparse spatial coverage of the airborne observations (*SI Appendix,* Text 3.7.1 and Table 3.5) by comparing averaged CO_2 from full 3-D model data and flight track-subsampled model data. We also correct the contribution of small non-oceanic CO_2 flux to the CO_2 mass balance based on flux estimates in four inversion products (*SI Appendix,* Figure 3.13). We conduct a thorough analysis of flux uncertainty induced by CO_2 measurement imprecision, spread and IAV of MSE-based diabatic mixing rates, spatial coverage corrections, flux interannual variability due to insufficient temporal sampling, and non-oceanic CO_2 flux corrections (*SI Appendix,* Text 3.71-3.7.2).

Figure 3.5: (a)-(d) Seasonal cycle of air-sea CO_2 fluxes (negative as net oceanic uptake) estimated using 4-box model based on airborne CO_2 observations and two sets of MSE-based diabatic mixing rates (see Materials and Methods). Each individual point represents the calculated fluxes using airborne observations from the corresponding campaign, centering on the mean date of each campaign, while the black line is a 2-harmonic fit. Error bars represent the 1σ uncertainty of each flux estimate, while shaded regions represent the 1σ uncertainty of the 2-harmonic fits (detailed in *SI Appendix*, Text 3.7.1-3.7.2). Values of air-sea CO_2 fluxes calculated for each airborne campaign transect and for each band are summarized in *SI Appendix*, Table 3.4. Annual fluxes are from the constant term of the 2-harmonic fitted climatological flux cycles, which is equivalent to integrating the fit over a year. These approximate latitude bands (see top of each panel) are calculated as the zonal average latitude of the corresponding annual average (2009 to 2018) $M_{\theta e}$ surface over the ocean (*SI Appendix*, Fig. 3.7). We also show box-model resolved fluxes calculated using the average of 6 sets of mixing rate and each set of mixing rate in *SI Appendix*, Fig. 3.15 and 3.16. In (e)-(h), we compare our estimates with four 3-D CO_2 inversion products, and two neural network interpolated surface ocean pCO_2 products using SOCAT pCO_2 observations alone and SOCCOM pCO_2 observations alone. Details of these products are in *SI Appendix*, Text 3.7.6. The SOCCOM product is a sensitivity run where all shipboard data from SOCAT were excluded (only SOCCOM float data were included). We note that the ocean CO_2 flux in Jena sEXTocNEET_v2020 is a prior, which is provided by assimilation of surface ocean pCO_2 observations (i.e., not neural-network derived pCO_2) from SOCAT (63) by the Jena mixed-layer scheme (64). The seasonal cycle of each product is calculated as the average between 2009 and 2018, except for SOCCOM, which is averaged from 2015 to 2017. In (i)-(l), we compare our estimates with thermally-driven air-sea CO_2 flux cycles (dashed red, methods in *SI Appendix*, Text 3.7.3), which is derived from assuming 4% pCO_2 increase per degree Celsius increase in sea-surface temperature (SST) and using wind-speed dependent gas exchange. We calculate the correlation between the airborne observed flux cycle and the estimated thermal-driven flux cycle of each band. Black solid curves and shaded regions in (e)-(l) are corresponding airborne observed fluxes and 1σ uncertainty. Panels (i) to (l) have a different y-axis range compared to panels (a) to (h). We also compare our estimates with nine global ocean biogeochemistry models that are used in the Global Carbon Budget 2020 (8, 49) in *SI Appendix*, Fig. 3.14.

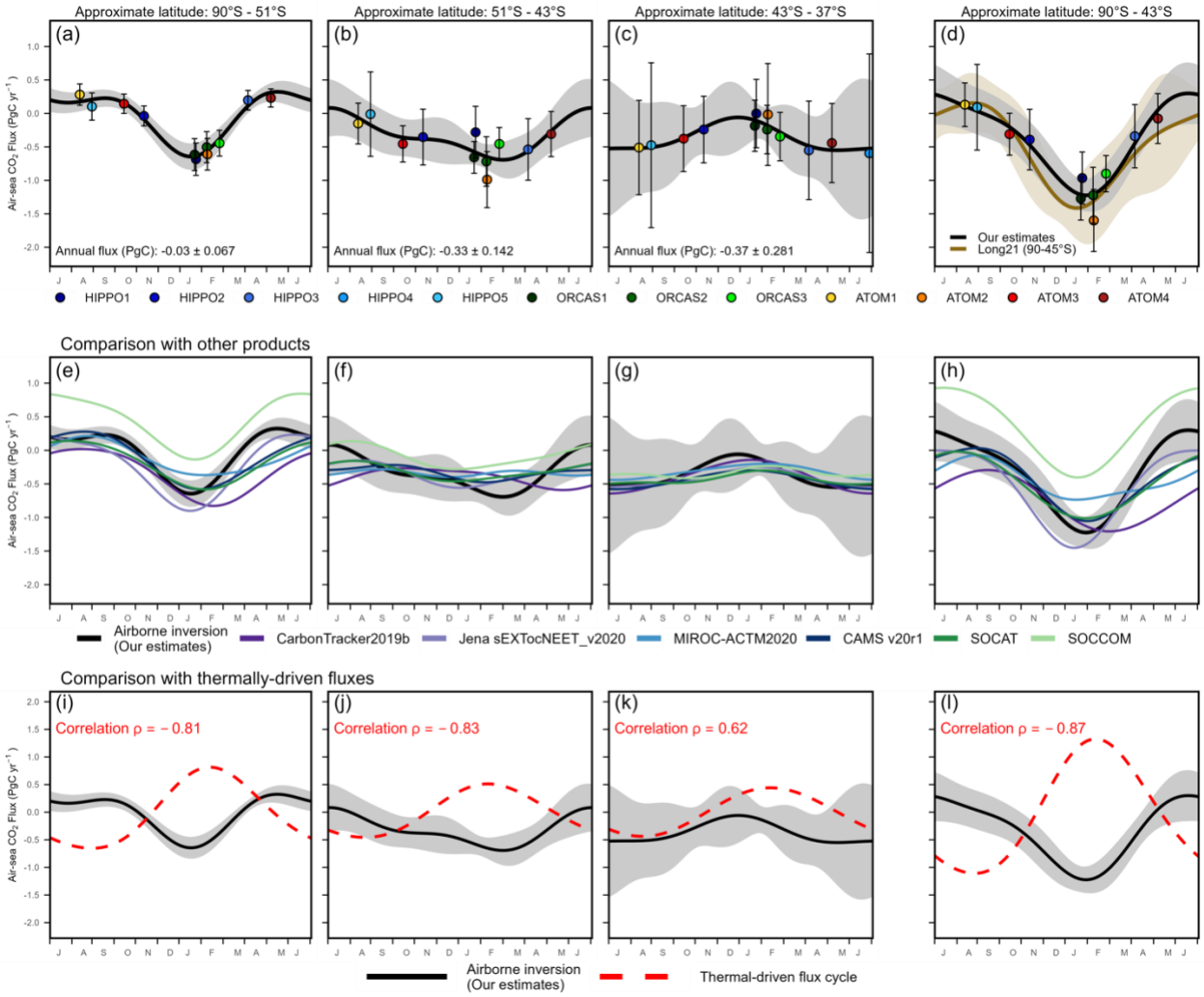
Approximate latitude: 90°S - 51°S
Approximate latitude: 51°S - 43°S
Approximate latitude: 43°S - 37°S
Approximate latitude: 90°S - 43°S
(a)
(b)
(c)
(d)
Air-sea CO2 Flux (PgC yr−1)
Annual flux (PgC): -0.03 ± 0.067
Annual flux (PgC): -0.33 ± 0.142
Annual flux (PgC): -0.37 ± 0.281
Our estimates
Long21 (90-45°S)
J A S O N D J F M A M J
HIPPO1
HIPPO2
HIPPO3
HIPPO4
HIPPO5
ORCAS1
ORCAS2
ORCAS3
ATOM1
ATOM2
ATOM3
ATOM4
Comparison with other products
(e)
(f)
(g)
(h)
Airborne inversion
(Our estimates)
CarbonTracker2019b
Jena sEXTocNEET_v2020
MIROC-ACTM2020
CAMS v20r1
SOCAT
SOCCOM
Comparison with thermally-driven fluxes
(i)
(j)
(k)
(l)
Correlation ρ = − 0.81
Correlation ρ = − 0.83
Correlation ρ = 0.62
Correlation ρ = − 0.87
Airborne inversion
(Our estimates)
Thermal-driven flux cycle

The 4-box inversion resolves clear seasonal cycles of air-sea CO_2 flux in all three latitude bands, with clear differences in amplitude and phasing between the bands. Over the polar band (Fig. 3.5a), we find a strong CO_2 uptake in the summer (DJF) and a weak outgassing in the winter (JJA). Over the subpolar band (Fig. 3.5b), we find a strong uptake in the summer and a weak uptake in the winter. In the subtropical band (Fig. 3.5c), the seasonality is reversed, with a weak uptake in the summer and a strong uptake in the rest of the year. Averaged over the full year, all bands show net uptake. We now discuss each of these prominent features in turn.

The airborne-based estimates suggest a weak winter-time CO_2 outgassing of 0.05 ± 0.03 PgC integrated from June to August (equivalent to 0.56 ± 0.35 gC m^{-2} mon^{-1}) in the polar band (Fig. 3.5a). Winter outgassing is expected from strong winter-time upwelling which brings carbon-rich deep water to the surface (7). This outgassing pattern is consistent with several recent pCO_2-based flux estimates, for example, observations from uncrewed surface vehicles in the Antarctic Zone during June and July of 2019 (0.7 gC m^{-2} mo^{-1}) (33), reconstructed winter-time (July, 2004-2014 average) fluxes using summer-time measurements (0.04 ± 0.008 PgC) (34), and ship-based SOCAT measurements (0.03 PgC, Fig. 3.5e) (17), but is smaller than estimates solely based on recent profiling floats deployed by the SOCCOM project during 2014 and 2017 (~ 0.23 PgC, Fig. 3.5e) (16, 32). The small winter-time outgassing in our results is also consistent with several 3-D inversions that used surface station CO_2 observations (Jena inversion, ACTM, and CAMS), but is significantly more positive than one 3-D inversion (CT 2019b, Fig. 3.5e).

The airborne-based flux estimates show a clear phase shift between the polar/subpolar bands (Fig. 3.5a-b) and the subtropical band (Fig. 3.5c). The boundary between these two boxes in the 4-box model roughly aligns with the subtropical front over the Atlantic and the Indian Ocean but is ~5° south of the subtropical front over the Pacific Ocean. This phase shift is likely due to

the latitudinal change of the dominant mechanism that drives the surface-ocean pCO_2 seasonal changes. To the north of this boundary, the pCO_2 cycle is dominated by temperature-related solubility changes. To the south, it is dominated by biological production/mixing processes driving seasonal changes in dissolved inorganic carbon (DIC) (35, 36, 43). A similar shift across ~40°S has been resolved in surface ocean pCO_2 data (36, 43, 44) and also in flux estimates based on these pCO_2 data, but the seasonal amplitudes of fluxes in these estimates are weaker in both regions than we find from airborne data (Fig. 3.5e-g). The phase shift, however, is not clearly resolved in the 3-D inversions (Fig. 3.5e-g).

To quantify the contribution of temperature-related solubility changes to the CO_2 fluxes (Fig. 3.5i-l), we compare the airborne-based fluxes to results from a simple thermal model, which assumes pCO_2 increases by 4% per degree Celsius increase in sea-surface temperature (SST) change and uses wind-speed dependent gas exchange (methods in *SI Appendix*, Text 3.7.3) (45, 46). In the polar zone (Fig. 3.5i-j), the thermal model yields fluxes that are strongly out of phase compared with observations (correlation ρ = -0.81 and -0.83). In the subtropical region (Fig. 3.5k), the cycle from the thermal model broadly aligns with the observed cycle (ρ =0.62).

Despite the correlation, the observed flux cycle in the subtropical band has significant deviations in the austral spring compared to the thermal-driven cycle. The strengthening of CO_2 uptake from January to April is faster than expected from warming alone (Fig. 3.5k), which requires a contribution from biologically-driven changes, possibly associated with the fall phytoplankton bloom (47, 48).

We find a summer-time ocean CO_2 uptake of 0.13 ± 0.04 PgC (integrated from December to February, DJF) in the polar band (Fig. 3.5a) and 0.14 ± 0.04 PgC in the subpolar band (Fig. 3.5b), which contributes to most of the annual uptake of 0.36 ± 0.16 PgC south of ~43°S (Fig. 3.5d). Our

results are qualitatively consistent with prior estimates using the same airborne observations (Long21). However, our annual uptake estimate integrated over the polar and subpolar band is smaller (within uncertainty) than that of Long21 (0.53 ± 0.23 PgC) (Fig. 3.5d). The difference is mainly explained by larger summer-time CO_2 uptake in Long21, but the comparison is complicated by small differences in ocean domains between these two studies (the 30 $M_{\theta e}$ surface, compared to 45°S, displaces ~2° southward over the western Pacific and ~3° in other basins). The larger summer uptake in Long21 can be attributed to the dependence on ATMs, which we suggest have unrealistically fast mixing rates in summer (Fig. 3.2). Summertime fluxes from our box model are especially sensitive to the diabatic mixing rate because summertime cross-$M_{\theta e}$ gradients are large, and the inventory change is small (Fig. 3.4). The winter-time fluxes are less sensitive to the diabatic mixing rate because wintertime CO_2 gradients are small, and the inverted flux is mainly diagnosed from the observed atmospheric CO_2 inventory change.

Our airborne based flux estimates generally agree with 3-D inversions. Our estimates suggest a weaker winter-time sink (within uncertainty) in the subpolar region (Fig. 3.5f), and show a more pronounced change in phasing between subtropical and subpolar regions. These deviations can partly be attributed to the excess diabatic transport in most models, as suggested by the CO_2 gradient constraint (Fig. 3.4).

Our airborne-based flux estimates differ significantly from an estimate solely based on neural-network interpolation of SOCCOM float data. We find that the SOCCOM-based estimate, compared to our airborne-based estimate, suggests a too weak CO_2 uptake in all seasons in both the polar (significant, Fig. 3.5e) and subpolar regions (within uncertainty, Fig. 3.5f), as well as a too weak seasonal cycle in the subtropical band (Fig. 3.5g). Flux estimates based on SOCAT measurements are generally consistent with our estimates but also suggest a too weak seasonality

in the subtropical band (Fig. 3.5g). Possible bias in SOCCOM pCO_2 data has been identified by Wu et al. (30), and SOCCOM float data remain sparse in our lowest latitude band 43-37°S (16).

Our airborne-based estimates also show large differences from global ocean biogeochemistry models, which have known difficulties in representing CO_2 exchange over the Southern Ocean (49, 50) given the large competing process drivers. We find several models that suggest a similar phase shift, but we did not find any model that agrees well with our estimates in all three bands (*SI Appendix*, Fig. 3.14).

3.3 Overview and outlook

We have resolved air-sea CO_2 fluxes over three zonal bands of the SO using airborne data and a 4-box inversion approach based on $M_{\theta e}$ coordinates. This framework adequately describes large-scale CO_2 transports needed for resolving fluxes at the scale of three zonal bands over the mid- to high latitudes of the SO, showing that the complex meridional CO_2 transport can be simplified to diabatic transport. This framework also incorporates constraints on the diabatic mixing rate from MSE budgets of atmospheric reanalyses, without requiring an atmospheric transport model. We demonstrate that the diabatic mixing rates inferred from the MSE budgets are realistic, based on a CO_2 gradient-mixing rate constraint, but the mixing in most ATMs is too fast in the austral summer. These differences in representing mixing led to our summer uptake estimates being somewhat smaller than uptake estimated by Long21, despite using the same airborne CO_2 data. In the austral winter, ATM- and MSE-based mixing rates are generally comparable.

Our study illustrates the potential for using MSE as a constraint on diabatic transport, which has implications for improving ATMs in general. The MSE constraints are relevant for improving estimates of vertical mixing, which has been highlighted as a major source of error in CO_2 fluxes estimated via inverse model calculations using both satellite and in situ data (41, 42). Vertical

mixing in the mid-troposphere has both along- and cross-$M_{\theta e}$ components, and the cross-$M_{\theta e}$ mixing (diabatic) component would typically be rate limiting because the along-$M_{\theta e}$ (adiabatic) mixing is more rapid. We find a larger spread in diabatic mixing rates between four ATM-based mixing rates compared to two MSE-based mixing rates (Fig. 3.2), which suggests that errors are introduced during the construction of ATMs. Future studies should focus on better understanding the inconsistency between transport models and reanalyses, which are likely to be associated with coarser resolution in models relative to the original reanalysis and multiple schemes of model parameterizations.

Our study motivates obtaining airborne data with higher temporal coverage. Here we only attempted to resolve a seasonal climatology of the SO CO_2 flux, but resolving flux interannually would be feasible given regular sampling on future aircraft campaigns, with spatial coverage over the SO similar to HIPPO, ORCAS, and ATom. Our box model framework is suitable also for studying the sources and sinks of other tracers, for example, computing the surface O_2 flux, and atmospheric CH_4 chemical loss rate.

3.4 Materials and methods

3.4.1 Airborne campaigns and airborne CO2 observations

We use airborne CO_2 observations from three aircraft campaigns, the HAIPER Pole-to-Pole Observation project (HIPPO, (51)), the O_2/N_2 Ratio and CO_2 Airborne Southern Ocean Study (ORCAS, (52)), and the Atmospheric Tomography Mission (ATom, (53)). HIPPO and ATom have global coverage, mostly along a Pacific or Atlantic transect, while ORCAS focused on the Southern Ocean adjacent to Drake Passage (horizontal flight tracks are shown in *SI Appendix*, Fig. 3.6). HIPPO consisted of five campaigns (HIPPO1-5) and ATom consisted of four campaigns (ATom1-4), each with several flights south of 35°S. ORCAS was a single 6-week campaign, but with much denser temporal sampling, so we have split it into three sub-campaigns (ORCAS1-3)

in our analysis. Detailed descriptions of these airborne campaigns are in *SI Appendix,* Text 3.7.4 and *SI Appendix*, Table 3.2. We primarily use CO_2 airborne measurements collected by the NCAR AO2 instrument (54). To evaluate potential uncertainty (detailed in *SI Appendix,* Text 3.7.2.1), we also use measurements from three other in-situ instruments, the Harvard QCLS instrument (55), Harvard OMS instrument (56), and NOAA Picarro, and measurements from two flask samplers, the NCAR/Scripps Medusa flask sampler (51, 54) and NOAA Portable Flask Packages (PFP, 55). AO2 and QCLS are available on all campaigns. However, OMS did not fly on ORCAS or ATom, NOAA PFPs did not fly on ORCAS, and the NOAA Picarro did not fly on HIPPO. The in-situ measurements are averaged to 10-sec intervals.

3.4.2 Mass-indexed moist isentropic coordinate ($M_{\theta e}$)

The $M_{\theta e}$ coordinate, first introduced in Jin et al. (29), is defined as the total dry air mass under a specific moist isentropic surface (θ_e) in the troposphere of a given hemisphere. Surfaces of constant $M_{\theta e}$ align with surfaces of constant θ_e but the relationship changes with season, as the atmosphere warms and cools. A schematic of annual zonal average atmospheric $M_{\theta e}$ value is in shown Fig. 3.1a, while climatological positions of the near-Earth surface contours of three $M_{\theta e}$ surfaces (15, 30, and 45 10^{16} kg) are shown in Fig. 3.1b and *SI Appendix,* Fig. 3.7. Details of the calculation of $M_{\theta e}$ are described in *SI Appendix*, Text 3.7.5.

We also relate bands of constant $M_{\theta e}$ to approximate latitude bands (see Fig. 3.5) based on the zonal average latitude of corresponding daily surface $M_{\theta e}$ (averaged from 2009 to 2018) over the ocean.

3.4.3 Box model architecture and diabatic mixing rates

We build a 4-box atmospheric model using selected $M_{\theta e}$ surfaces (15, 30, 45, and 60, 10^{16} kg) as boundaries, shown in Fig. 3.1a. This box model takes advantage of θ_e (or $M_{\theta e}$) being the preferential mixing surface of CO_2 throughout the hemisphere, especially over mid-latitude storm

tracks (26, 27). The box model allows surface CO_2 fluxes (F_i, PgC year^{-1}) to be computed from the CO_2 mass balance of each $M_{\theta e}$ box, based on the knowledge of atmospheric CO_2 inventory (M_i, PgC) in each box and the diabatic transport of CO_2 between boxes ($Q_{i,i+1}$, PgC year^{-1})

$$\frac{\partial M_i}{\partial t} = \begin{cases} F_i + Q_{i,i+1} & \text{if } i = 1 \\ F_i + Q_{i,i+1} - Q_{i-1,i} & \text{if } i > 1 \end{cases} \quad (3.1)$$

where i = 1 is the highest latitude (lowest $M_{\theta e}$) box.

In Eq. 3.1, $Q_{i,i+1}$ represents the transport (PgC year^{-1}) of CO_2 between the ith and i+1th box, with poleward flux as positive. $Q_{i,i+1}$ is parameterized according to:

$$Q_{i,i+1} = D_{i,i+1} \cdot \frac{(\chi_{i+1} - \chi_i)}{\Delta M_{\theta_e}} \quad (3.2)$$

where $D_{i,i+1}$ is the diabatic mixing rate (kg^2 day^{-1}) that represents the mixing rate across the boundary of box i and i+1, χ_i is the CO_2 concentration (PgC per kg air mass) of the ith box, calculated as CO_2 inventory of the box divided by the total airmass of the box (15×10^{16} kg), and $\Delta M_{\theta e}$ is the distance in $M_{\theta e}$ coordinates between box centers, which for evenly spaced boxes is the same as the total airmass of each box. Equation 3.2 is a variant of Fick's law, with $M_{\theta e}$ as an effective distance coordinate, and $\frac{(\chi_{i+1}-\chi_i)}{\Delta M_{\theta_e}}$ is a measure of the CO_2 concentration gradient. With this approach, $D_{i,i+1}$ is a property of the corresponding $M_{\theta e}$ surface and is insensitive to the choice of box size.

We adopt two independent methods to estimate climatological (2009 to 2018 average) monthly diabatic mixing rates ($D_{i,i+1}$). The first method extracts diabatic mixing rates from transport models using total CO_2 fields from 3-D inversion products (*SI Appendix*, Table 3.3). We first use the daily 3-D atmospheric field of $M_{\theta e}$ computed from MERRA-2 to assign a $M_{\theta e}$ value to each daily model grid cell from 2009 to 2018. The atmospheric 3-D CO_2 fields and surface CO_2

flux fields of inversions are interpolated to the MERRA-2 reanalysis grids (1°x1°, 26 vertical levels from 1000 mbar to 100 mbar). We then calculate a daily CO_2 inventory (M_i) of each $M_{\theta e}$ band as the sum of CO_2 mass for all 3-D grid boxes within the corresponding $M_{\theta e}$ domain. We calculate monthly CO_2 inventory change ($\frac{dM_i}{dt}$) by taking the time derivative of monthly atmospheric CO_2 inventory. We note that monthly CO_2 inventory change is computed by first averaging daily CO_2 inventory by month but shifting the phase of the averaging window by 15 days to center at the beginning of each month, and then differencing these values to obtain a rate of change centered mid-month. We calculate monthly CO_2 gradients between two $M_{\theta e}$ boxes (χ_{i+1}-χ_i) by averaging daily gradients. We calculate monthly surface CO_2 flux (F_i) by averaging daily flux, which is computed by integrating all daily 3-D inversion flux grids with surface $M_{\theta e}$ values within the corresponding $M_{\theta e}$ range.

The CO_2 transport across the north boundary of each $M_{\theta e}$ box in the model can be calculated from the CO_2 inventory change and surface flux of that box and the boxes further southward, according to:

$$Q_{i,i+1}(t) = \sum_{i'=1}^{i'=i} \left(\frac{dM_{i'}(t)}{dt} - F_{i'}(t) \right) \tag{3.3}$$

Combining Eq. 3.2 and 3.3, climatological average (2009 to 2018 average) monthly $D_{i,i+1}$ is calculated following:

$$D_{i,i+1}(t) = \frac{[\sum_{i'=1}^{i'=i} \left(\frac{dM_{i'}(t)}{dt} - F_{i'}(t) \right)]}{[\chi_{i+1}(t) - \chi_i(t)]} \cdot \Delta M_{\theta_e} \tag{3.4}$$

where [] denotes the average of corresponding monthly values of all years (2009 to 2018). The 1σ uncertainty is calculated as the standard deviation of resolved $D_{i,i+1}(t)$ for that month over all years, representing the interannual variability, which is shown to be small (Fig. 3.2 and *SI*

Appendix, Fig. 3.8), with the exception of CAMS in September because of close-to-zero CO_2 gradients across the 30 (10^{16} kg) $M_{\theta e}$ surface.

The second method relies on moist static energy (MSE) budgets from meteorological reanalyses, of which we use MERRA-2 and JRA-55 (59, 60). MSE is a measure of static energy that is conserved in adiabatic ascent/descent and during latent heat release due to condensation, and is thus aligned with surfaces of θ_e or $M_{\theta e}$. This method provides a much more well-defined D because finite MSE gradients exist in each reanalysis time step and do not reverse sign, in contrast to CO_2. MSE is defined following

$$\mathrm{MSE(t)} = \mathrm{C_p \cdot T(t) + g \cdot z + L_v(T) \cdot q(t)} \tag{3.5}$$

where $\mathrm{C_p}$ (1005.7 J $\mathrm{kg^{-1}\,K^{-1}}$) is the specific heat of dry air at a constant pressure, T is temperature (K), g is the gravity constant assumed to be 9.81 m $\mathrm{s^{-2}}$, q is the specific humidity of air (kg water vapor per kg air mass), and $\mathrm{L_v}$ is the latent heat of evaporation at temperature T (K). $\mathrm{L_v}$ is defined as 2406 kJ $\mathrm{kg^{-1}}$ at 40°C and 2501 kJ $\mathrm{kg^{-1}}$ at 0°C and scales linearly with temperature.

MSE transport at the northern boundary of each box is calculated by energy conservation within the box, which follows Eq. 3.3 but has a small modification to account for atmospheric energy sources or sinks (E_i, J $\mathrm{day^{-1}}$):

$$\mathrm{Q_{i,i+1}(t)} = \sum_{\mathrm{i'=1}}^{\mathrm{i'=i}} \left(\frac{\mathrm{dS_{i'}(t)}}{\mathrm{dt}} - \mathrm{F_{i'}(t)} - \mathrm{E_{i'}}(t) \right) \tag{3.6}$$

where S is the total MSE (J) that is calculated using temperature (T) and specific humidity (q) from corresponding reanalyses (Eq. 3.5). F_i is modified as surface heat flux (J $\mathrm{day^{-1}}$), including surface sensible and latent heat flux, which is directly available from MERRA-2 and JRA-55. E_i is defined as heating rate due to radiative imbalance, and is calculated using temperature tendency analysis ($\frac{\partial T_i}{\partial t}$, K $\mathrm{day^{-1}}$) of these reanalyses, following:

$$E_i(t) = C_p(T) \cdot \frac{\partial T_i(t)}{\partial t} \cdot M_{\theta_e} \quad (3.7)$$

With MERRA-2, the temperature tendency due to radiative imbalance is directly available, while with JRA-55, it is calculated as the sum of heating rates due to longwave and shortwave radiation.

To estimate climatological monthly $D_{i,i+1}$ from reanalysis, the gradient $(\chi_{i+1} - \chi_i)$ in Eq. 3.4 is modified to be the energy density gradient (J per kg airmass), calculated from the total MSE of each box divided by the total airmass of the box (15×10^{16} kg in this study).

We thus calculate monthly $\frac{dS_{i'}(t)}{dt}$, $F_{i'}(t)$, $E_{i'}(t)$ from 2009 to 2018 by averaging 6-hourly data from MERRA-2 and JRA-55, with 6-hourly S_i shifted by 15 days before calculating $\frac{dS_{i'}(t)}{dt}$, as for ATM CO_2.

The calculation of monthly D based on MSE is according to a modified version of Eq. 3.4:

$$D_{i,i+1}(t) = \frac{[\sum_{i'=1}^{i'=i} \left(\frac{dS_{i'}(t)}{dt} - F_{i'}(t) - E_{i'}(t)\right)]}{[\chi_{i+1}(t) - \chi_i(t)]} \cdot \Delta M_{\theta_e} \quad (3.8)$$

We show six (four ATM-based and two MSE-based) sets of monthly diabatic mixing rates for the $M_{\theta e}$ surfaces at 15, 30, and 45 (10^{16} kg) in Fig. 3.2 and *SI Appendix*, Fig. 3.8. Climatological daily mixing rates are further calculated by 4-harmonic fits to monthly data.

3.4.4 Validation of box-model approach

We validate the use of the 4-box model for estimating surface CO_2 flux by showing that this approach successfully reconstructs monthly surface CO_2 fluxes for each of the four 3-D CO_2 inversion products. This approach uses Eq. 3.1 and 3.2, with χ_i based on the gridded atmospheric CO_2 fields averaged over grid cells within corresponding $M_{\theta e}$ box and uses $D_{i,i+1}$ calculated using CO_2 gradients from each transport model as described in the previous section. We then average

daily reconstructed fluxes to monthly, centered at the middle of each month, shown as solid black curves in Fig. 3.3 and *SI Appendix,* Fig. 3.9-3.11.

3.4.5 Airborne estimates of air-sea CO_2 fluxes

We use the 4-box model (Eq. 3.1 and 3.2) and airborne CO_2 observations to calculate air-sea CO_2 fluxes for each surface $M_{\theta e}$ band and each airborne campaign, centering on the mean date of the campaign, shown as points in Figure 3.5a-d. This calculation includes the following steps.

We first detrend airborne CO_2 observations by subtracting a smoothed interannual CO_2 trend at the South Pole (SPO) (61). The trend is calculated by a stiff cubic spline function to the monthly average SPO data (62).We then compute detrended average CO_2 ($\widehat{\chi_i}$) for each campaign and each box by trapezoidal integration of detrended CO_2 as a function of $M_{\theta e}$ (as in Jin et al. (29)), and dividing by the $M_{\theta e}$ range of the box (i.e., 15×10^{16} kg). (62). Prior to trapezoidal integration, we extrapolate airborne observations to $M_{\theta e} = 0$ surface using the average of the 100 observations with the lowest $M_{\theta e}$ values near 0. The extrapolation only results in a slightly different averaged CO_2 for the lowest $M_{\theta e}$ box compared to the value without extrapolation (< 0.03 ppm) because we have sufficient measurements across $M_{\theta e}$ surfaces. The exceptions are HIPPO1 and 4 (difference $\approx$0.1 ppm), in which we do not have observations on low $M_{\theta e}$ surfaces (*SI Appendix*, Fig. 3.20). For HIPPO4, however, we extrapolate to $M_{\theta e}$ = 15 (10^{16} kg) using the average of the 100 observations with the lowest $M_{\theta e}$ values near 15 because due to the absence of observations in the entire first $M_{\theta e}$ box, and only estimate fluxes for the 30-45 (10^{16} kg) box. We then correct for bias in CO_2 estimates due to limited spatial coverage (detailed in *SI Appendix,* Text 3.7.1). For each $M_{\theta e}$ box, we conduct a 2-harmonic fit with annual offset to $\widehat{\chi_i}$ of 12 campaigns, yielding a fitted seasonal cycle (with offset) of $\widehat{\chi_i}$. We then compute the long-term (2009 to 2018) time series of observed χ_i as the sum of the climatological seasonal cycle of $\widehat{\chi_i}$ and the CO_2 trend at SPO. We note that we use the same trend for each $M_{\theta e}$ band, preserving each band's annual mean offset

from SPO. The time series of CO_2 inventory (M_i) of each box is therefore computed by multiplying χ_i and the $M_{\theta e}$ range of the box (i.e., 15×10^{16} kg in this study). Fitted χ_i and M_i values of each campaign are defined as the values at the mean date of the corresponding campaign. Observed surface CO_2 fluxes for each airborne campaign is then calculated as the combination of two components, namely the CO_2 inventory change $\frac{\partial M_i}{\partial t}$ and CO_2 diabatic transport $Q_{i,i+1}$, following Eq. 3.1 and 3.2. We calculate the component $\frac{\partial M_i}{\partial t}$ as the time derivative of the daily timeseries of M_i from the combined seasonal plus SPO trend fit. The component $Q_{i,i+1}$ for each airborne campaign mean date is calculated as the product of the observed atmospheric CO_2 gradient (without fitting) between two boxes and the 4-harmonic fitted diabatic mixing rate at the campaign mean date (average of 2 MSE-based mixing rates) of the corresponding $M_{\theta e}$ surface.

The surface CO_2 fluxes estimated from the 4-box model are the total fluxes that also contain any land ecosystem CO_2 emission/uptake and fossil fuel CO_2 emission. We correct for these non-oceanic components by subtracting the corresponding flux components using the average of four 3-D CO_2 inversion products. The magnitude of this correction is small compared to the total air-sea fluxes, as shown in *SI Appendix,* Fig. 3.13.

We estimate the uncertainty of each individual flux estimate and the seasonal flux cycle by generating an ensemble (2000 iterations) of flux estimates, allowing for uncertainty of these sources: (1) uncertainty of CO_2 measurements; (2) uncertainty of the correction for spatial bias due to insufficient airborne coverage; (3) interannual variability of the diabatic mixing rate; (4) spread of the diabatic mixing rate between the two reanalyses; (5) correction for the biosphere and fossil fuel CO_2 flux; and (6) interannual variability of the flux. Detailed bias and uncertainty analyses are presented in *SI Appendix,* Text 3.7.1-3.7.2. The overall uncertainties of each flux

estimate are shown as error bars in Fig. 3.5a-d. The overall uncertainties of 2-harmonic fitted seasonal flux cycles are shown as shaded regions in Fig. 3.5a-d.

We also show the averaged air-sea CO_2 fluxes calculated using 6 sets of diabatic mixing rates (4 sets of ATM-based and 2 sets of MSE-based) in *SI* Appendix, Fig. 3.15. These are estimated using the average and 1σ uncertainty of 6000 iterations of flux estimates, with 1000 iterations for each set of mixing rates. We also show the air-sea CO_2 fluxes calculated using each set of mixing rates in *SI* Appendix, Fig. 3.16.

We calculate the annual CO_2 uptake of each $M_{\theta e}$ box from the constant term of the 2-harmonic fitted seasonal flux cycles (shown as text in Fig. 3.5).

3.5 Acknowledgement

We thank the efforts of the full HIPPO, ORCAS, and ATom science teams and the pilots and crew of the NSF/NCAR GV and NASA DC-8 as well as the NCAR and NASA project managers, field support staff, and logistics experts. In this work, we have used the HIPPO, ORCAS, and ATom 10-s merge files. We thank the NCAR AO2, Harvard QCLS, Harvard OMS, NOAA UCATS, and NOAA Picarro, NOAA PFP, and NCAR/Scripps Medusa teams for sharing CO_2 measurements. These include Sara Afshar, Jonathan Bent, John Budney, Róisín Commane, Bruce Daube, Glenn Diskin, Rodrigo Jimenez, Kathryn McKain, Fred Moore, Tim Newberger, Jasna Pittman, Bill Paplawsky, Sunyoung Park, Greg Santoni, Stephen Shertz, MacKenzie Smith, Andy Watt, Steven Wofsy, and Bin Xiang. For sharing O_3, N_2O, and H_2O measurements, we also thank Jim Elkins, Eric Hintsa, and Fred Moore for ATom-1 N_2O data; Ru-Shan Gao and Ryan Spackman for HIPPO O_3 data; Ilann Bourgeois, Jeff Peischl, Tom Ryerson, and Chelsea Thompson for ATom O_3 data; Stuart Beaton, Minghui Diao, and Mark Zondlo for HIPPO and ORCAS H_2O data; and Glenn Diskin and Josh DiGangi for ATom H_2O data. Yuming Jin was supported under a grant from NSF (AGS-1623748) and under a grant from Earth Networks.

This material is based on work supported by the National Center for Atmospheric Research, which is a major facility sponsored by the NSF under Cooperative Agreement No. 1852977. HIPPO was supported by NSF grants ATM-0628575, ATM-0628452, ATM-0628519, and ATM-0628388. ORCAS was supported by grants NSF PLR-1501993, PLR-1502301, PLR-1501997, and PLR-1501292. ATom was supported by NASA grant NNX15AJ23G. The NOAA CO_2 ATom measurements were supported by NASA grant NNX16AL92A. NCAR and Scripps AO2 and Medusa measurements in ATom were supported by NSF AGS-1547626 and AGS-1547797 for ATom1 and by NSF AGS-1623745 and AGS-1623748 for ATom 2-4. Recent CO_2 measurements at SPO station have been supported by NASA (NNX17AE74G) and by Eric and Wendy Schmidt via recommendation of the Schmidt Futures program. Any opinions, findings, conclusions, and recommendations expressed in this material are those of the authors and do not necessarily reflect the views of NSF, NOAA, or DOE.

Chapter 3, in full, has been submitted for publication of the material as it may appear in Jin, Y., Keeling, R. F., Long, M. C., Stephens, B. B., Patra, P., Rödenbeck, C., Morgan, E. J.: Improved Atmospheric Constraint of the Southern Ocean CO_2 Exchange, PNAS. The dissertation author was the primary investigator and author of this paper.

3.6 Reference

1. Long, M. C., Stephens, B. B., McKain, K., Sweeney, C., Keeling, R. F., Kort, E. A., et al. (2021). Strong Southern Ocean carbon uptake evident in airborne observations. *Science*, *374*(6572), 1275–1280. https://doi.org/10.1126/science.abi4355
2. Gruber, N., Clement, D., Carter, B. R., Feely, R. A., van Heuven, S., Hoppema, M., et al. (2019). The oceanic sink for anthropogenic CO_2 from 1994 to 2007. *Science*, *363*(6432), 1193–1199. https://doi.org/10.1126/science.aau5153
3. Hauck, J., Völker, C., Wolf-Gladrow, D. A., Laufkötter, C., Vogt, M., Aumont, O., et al.

(2015). On the Southern Ocean CO_2 uptake and the role of the biological carbon pump in the 21st century. *Global Biogeochemical Cycles*, *29*(9), 1451–1470. https://doi.org/10.1002/2015GB005140

4. Kessler, A., & Tjiputra, J. (2016). The Southern Ocean as a constraint to reduce uncertainty in future ocean carbon sinks. *Earth System Dynamics*, *7*(2), 295–312. https://doi.org/10.5194/esd-7-295-2016
5. Lovenduski, N. S., McKinley, G. A., Fay, A. R., Lindsay, K., & Long, M. C. (2016). Partitioning uncertainty in ocean carbon uptake projections: Internal variability, emission scenario, and model structure. *Global Biogeochemical Cycles*, *30*(9), 1276–1287. https://doi.org/10.1002/2016GB005426
6. Gloor, M., Gruber, N., Sarmiento, J., Sabine, C. L., Feely, R. A., & Rödenbeck, C. (2003). A first estimate of present and preindustrial air-sea CO_2 flux patterns based on ocean interior carbon measurements and models. *Geophysical Research Letters*, *30*(1). https://doi.org/10.1029/2002gl015594
7. Gruber, N., Landschutzer, P., & Lovenduski, N. S. (2019). The Variable Southern Ocean Carbon Sink. *Annual Review of Marine Science*, *11*, 159–186. https://doi.org/10.1126/sciadv.aav6471
8. Friedlingstein, P., O'Sullivan, M., Jones, M. W., Andrew, R. M., Hauck, J., Olsen, A., et al. (2020). Global Carbon Budget 2020. *Earth System Science Data*, *12*(4), 3269–3340. https://doi.org/10.5194/essd-12-3269-2020
9. Le Quéré, C., Rödenbeck, C., Buitenhuis, E. T., Conway, T. J., Langenfelds, R., Gomez, A., et al. (2007). Saturation of the southern ocean CO_2 sink due to recent climate change. *Science*, *316*(5832), 1735–1738. https://doi.org/10.1126/science.1136188

10. Lovenduski, N. S., Gruber, N., & Doney, S. C. (2008). Toward a mechanistic understanding of the decadal trends in the Southern Ocean carbon sink. *Global Biogeochemical Cycles*, *22*, GB3016. https://doi.org/10.1029/2007GB003139
11. Nevison, C. D., Munro, D. R., Lovenduski, N. S., Keeling, R. F., Manizza, M., Morgan, E. J., & Rödenbeck, C. (2020). Southern Annular Mode Influence on Wintertime Ventilation of the Southern Ocean Detected in Atmospheric O_2 and CO_2 Measurements. *Geophysical Research Letters*, *47*(4), e2019GL085667. https://doi.org/10.1029/2019GL085667
12. Gregor, L., Kok, S., & Monteiro, P. M. S. (2018). Interannual drivers of the seasonal cycle of CO_2 in the Southern Ocean. *Biogeosciences*, *15*(8), 2361–2378. https://doi.org/10.5194/bg-15-2361-2018
13. Landschützer, P., Gruber, N., Bakker, D. C. E., & Schuster, U. (2014). Recent variability of the global ocean carbon sink. *Global Biogeochemical Cycles*, *28*(9), 927–949. https://doi.org/10.1111/1462-2920.13280
14. Ritter, R., Landschützer, P., Gruber, N., Fay, A. R., Iida, Y., Jones, S., et al. (2017). Observation-Based Trends of the Southern Ocean Carbon Sink. *Geophysical Research Letters*, *44*(24), 12339–12348. https://doi.org/10.1002/2017GL074837
15. Rödenbeck, C., Bakker, D. C. E., Gruber, N., Iida, Y., Jacobson, A. R., Jones, S., et al. (2015). Data-based estimates of the ocean carbon sink variability - First results of the Surface Ocean pCO_2 Mapping intercomparison (SOCOM). *Biogeosciences*, *12*(23), 7251–7278. https://doi.org/10.5194/bg-12-7251-2015
16. Bushinsky, S. M., Landschützer, P., Rödenbeck, C., Gray, A. R., Baker, D., Mazloff, M. R., et al. (2019). Reassessing Southern Ocean Air-Sea CO_2 Flux Estimates With the Addition of Biogeochemical Float Observations. *Global Biogeochemical Cycles*, *33*(11), 1370–1388.

https://doi.org/10.1029/2019GB006176

17. Landschützer, P., Gruber, N., & Bakker, D. C. E. (2020). *An observation-based global monthly gridded sea surface pCO_2 product from 1982 onward and its monthly climatology (NCEI Accession 0160558). Version 5.5. NOAA National Centers for Environmental Information. Dataset. https://doi.org/10.7289/V5Z89*.
18. Landschützer, Peter, Bushinsky, S. M., & Gray, A. R. (2019). A combined globally mapped carbon dioxide (CO_2) flux estimate based on the Surface Ocean CO_2 Atlas Database (SOCAT) and Southern Ocean Carbon and Climate Observations and Modeling (SOCCOM) biogeochemistry floats from 1982 to 2017 (NC. https://doi.org/10.25921/9hsn-xq82.
19. Rödenbeck, C., Houweling, S., Gloor, M., & Heimann, M. (2003). CO_2 flux history 1982–2001 inferred from atmospheric data using a global inversion of atmospheric transport. *Atmospheric Chemistry and Physics*, *3*, 1919–1964. https://doi.org/https://doi.org/10.5194/acp-3-1919-2003
20. Jacobson, A. R., Schuldt, K. N., Miller, J. B., Oda, T., Tans, P., Andrews, A., & J. Mund, L. Ott, G. J. Collatz, T. Aalto, S. Afshar, K. Aikin, S. Aoki, F. Apadula, B. Baier, P. Bergamaschi, A. Beyersdorf, S. C. Biraud, A. Bollenbacher, D. Bowling, G. Brailsford, J. B. Abshire, G. Chen, H. Chen, L. Chmura, Sites Climadat, A. Colomb, S, and M. Z. (2020). CarbonTracker CT2019B. https://doi.org/10.25925/20201008
21. Patra, P. K., Takigawa, M., Watanabe, S., Chandra, N., Ishijima, K., & Yamashita, Y. (2018). Improved chemical tracer simulation by MIROC4.0-based atmospheric chemistry-transport model (MIROC4-ACTM). *Scientific Online Letters on the Atmosphere*, *14*, 91–96. https://doi.org/10.2151/SOLA.2018-016

22. Chandra, N., Patra, P. K., Niwa, Y., Ito, A., Iida, Y., Goto, D., et al. (2022). Estimated regional CO_2 flux and uncertainty based on an ensemble of atmospheric CO_2 inversions. *Atmospheric Chemistry and Physics*, *22*(14), 9215–9243. https://doi.org/10.5194/acp-22-9215-2022

23. Chevallier, F., Fisher, M., Peylin, P., Serrar, S., Bousquet, P., Bréon, F. M., et al. (2005). Inferring CO_2 sources and sinks from satellite observations: Method and application to TOVS data. *Journal of Geophysical Research Atmospheres*, *110*, D24309. https://doi.org/10.1029/2005JD006390

24. Chevallier, F. (2013). On the parallelization of atmospheric inversions of CO_2 surface fluxes within a variational framework. *Geoscientific Model Development*, *6*(3), 783–790. https://doi.org/10.5194/gmd-6-783-2013

25. Chevallier, F., Ciais, P., Conway, T. J., Aalto, T., Anderson, B. E., Bousquet, P., et al. (2010). CO_2 surface fluxes at grid point scale estimated from a global 21 year reanalysis of atmospheric measurements. *Journal of Geophysical Research Atmospheres*, *115*, D21307. https://doi.org/10.1029/2010JD013887

26. Barnes, E. A., N. Parazoo, C. Orbe, and A. S. Denning, 2016. Isentropic transport and the seasonal cycle amplitude of CO_2. Jour. Geophys. Res Atmos., doi:10.1002/2016/JD025109.

27. Parazoo, N. C., Denning, A. S., Berry, J. A., Wolf, A., Randall, D. A., Kawa, S. R., et al. (2011). Moist synoptic transport of CO_2 along the mid-latitude storm track. *Geophysical Research Letters*, *38*, L09804. https://doi.org/10.1029/2011GL047238

28. Parazoo, N. C., Denning, A. S., Kawa, S. R., Pawson, S., & Lokupitiya, R. (2012). CO_2 flux estimation errors associated with moist atmospheric processes. *Atmospheric Chemistry and*

Physics, *12*, 6405–6416. https://doi.org/10.5194/acp-12-6405-2012

29. Jin, Y., Keeling, R., Morgan, E., Ray, E., Parazoo, N., & Stephens, B. (2021). A mass-weighted atmospheric isentropic coordinate for mapping chemical tracers and computing inventories. *Atmospheric Chemistry and Physics*, *21*, 217–238. https://doi.org/10.5194/acp-2020-841
30. Wu, Y., Bakker, D. C. E., Achterberg, E. P., Silva, A. N., Pickup, D. D., Li, X., et al. (2022). Integrated analysis of carbon dioxide and oxygen concentrations as a quality control of ocean float data. *Communications Earth & Environment*, *3*, 92. https://doi.org/10.1038/s43247-022-00421-w
31. Johnson, K. S., Plant, J. N., Coletti, L. J., Jannasch, H. W., Sakamoto, C. M., Riser, S. C., et al. (2017). Biogeochemical sensor performance in the SOCCOM profiling float array. *Journal of Geophysical Research: Oceans*, *122*(8), 6416–6436. https://doi.org/10.1002/2017JC012838
32. Gray, A. R., Johnson, K. S., Bushinsky, S. M., Riser, S. C., Russell, J. L., Talley, L. D., et al. (2018). Autonomous Biogeochemical Floats Detect Significant Carbon Dioxide Outgassing in the High-Latitude Southern Ocean. *Geophysical Research Letters*, *45*(17), 9049–9057. https://doi.org/10.1029/2018GL078013
33. Sutton, A. J., Williams, N. L., & Tilbrook, B. (2021). Constraining Southern Ocean CO_2 Flux Uncertainty Using Uncrewed Surface Vehicle Observations. *Geophysical Research Letters*, *48*, e2020GL091748. https://doi.org/10.1029/2020GL091748
34. Mackay, N., & Watson, A. (2021). Winter Air-Sea CO_2 Fluxes Constructed From Summer Observations of the Polar Southern Ocean Suggest Weak Outgassing. *Journal of Geophysical Research: Oceans*, *126*, e2020JC016600.

https://doi.org/10.1029/2020JC016600

35. Prend, C. J., Hunt, J. M., Mazloff, M. R., Gille, S. T., & Talley, L. D. (2022). Controls on the Boundary Between Thermally and Non-Thermally Driven pCO_2 Regimes in the South Pacific. *Geophysical Research Letters*, *49*, e2021GL095797. https://doi.org/10.1029/2021GL095797
36. Sarmiento, J. L., & Gruber, N. (2006). *Ocean Biogeochemical Dynamics*. Princeton University Press.
37. Miyazaki, K., Patra, P. K., Takigawa, M., Iwasaki, T., & Nakazawa, T. (2008). Global-scale transport of carbon dioxide in the troposphere. *Journal of Geophysical Research: Atmospheres*, *113*(D15), D15301. https://doi.org/https://doi.org/10.1029/2007JD009557
38. Belikov, D. A., Maksyutov, S., Krol, M., Fraser, A., Rigby, M., Bian, H., et al. (2013). Off-line algorithm for calculation of vertical tracer transport in the troposphere due to deep convection. *Atmospheric Chemistry and Physics*, *13*(3), 1093–1114. https://doi.org/10.5194/acp-13-1093-2013
39. Krol, M., De Bruine, M., Killaars, L., Ouwersloot, H., Pozzer, A., Yin, Y., et al. (2018). Age of air as a diagnostic for transport timescales in global models. *Geoscientific Model Development*, *11*(8), 3109–3130. https://doi.org/10.5194/gmd-11-3109-2018
40. Schuh, A. E., Jacobson, A. R., Basu, S., Weir, B., Baker, D., Bowman, K., et al. (2019). Quantifying the Impact of Atmospheric Transport Uncertainty on CO_2 Surface Flux Estimates. *Global Biogeochemical Cycles*, *33*(4), 484–500. https://doi.org/10.1029/2018GB006086
41. Gaubert, B., Stephens, B. B., Basu, S., Chevallier, F., Deng, F., Kort, E. A., et al. (2019). Global atmospheric CO_2 inverse models converging on neutral tropical land exchange, but

disagreeing on fossil fuel and atmospheric growth rate. *Biogeosciences*, *16*(1), 117–134. https://doi.org/10.5194/bg-16-117-2019

42. Stephens, B. B., Gurney, K. R., Tans, P. P., Sweeney, C., Peters, W., Bruhwiler, L., et al. (2007). Weak Northern and Strong Tropical Land Carbon Uptake from Vertical Profiles of Atmospheric CO_2. *Science*, *316*(5832), 1732–1735. https://doi.org/10.1126/science.1137004
43. Landschützer, Peter, Gruber, N., Bakker, D. C. E., Stemmler, I., & Six, K. D. (2018). Strengthening seasonal marine CO_2 variations due to increasing atmospheric CO_2. *Nature Climate Change*, *8*(2), 146–150. https://doi.org/10.1038/s41558-017-0057-x
44. Gurney, K. R., Law, R. M., Denning, A. S., Rayner, P. J., Baker, D., Bousquet, P., et al. (2002). Towards robust regional estimates of annual mean CO_2 sources and sinks. *Nature*, *415*, 626–630. doi:10.1038/415626a.
45. Takahashi, T., Sutherland, S. C., Wanninkhof, R., Sweeney, C., Feely, R. A., Chipman, D. W., et al. (2009). Climatological mean and decadal change in surface ocean pCO_2, and net sea-air CO_2 flux over the global oceans. *Deep-Sea Research Part II: Topical Studies in Oceanography*, *56*(8–10), 554–577. https://doi.org/10.1016/j.dsr2.2008.12.009
46. Wanninkhof, R., Asher, W. E., Ho, D. T., Sweeney, C., & McGillis, W. R. (2009). Advances in Quantifying Air-Sea Gas Exchange and Environmental Forcing. *Annual Review of Marine Science*, *1*(1), 213–244. https://doi.org/10.1146/annurev.marine.010908.163742
47. Behrenfeld, M. J., & Falkowski, P. G. (1997). Photosynthetic rates derived from satellite-based chlorophyll concentration. *Limnology and Oceanography*, *41*(1), 1–20. https://doi.org/10.4319/lo.1997.42.1.0001.
48. Moore, J. K., & Abbott, M. R. (2000). Phytoplankton chlorophyll distributions and primary

production in the Southern Ocean. *Journal of Geophysical Research: Oceans*, *105*(C12), 28709–28722. https://doi.org/10.1029/1999jc000043

49. Hauck, Judith, Zeising, M., Le Quéré, C., Gruber, N., Bakker, D. C. E., Bopp, L., et al. (2020). Consistency and Challenges in the Ocean Carbon Sink Estimate for the Global Carbon Budget. *Frontiers in Marine Science*, *7*, 571720. https://doi.org/10.3389/fmars.2020.571720
50. Fay, A. R., & McKinley, G. A. (2021). Observed Regional Fluxes to Constrain Modeled Estimates of the Ocean Carbon Sink. *Geophysical Research Letters*, *48*, e2021GL095325. https://doi.org/10.1029/2021gl095325
51. Wofsy, S. C. (2011). HIAPER Pole-to-Pole Observations (HIPPO): fine-grained, global-scale measurements of climatically important atmospheric gases and aerosols. *Philosophical Transactions of the Royal Society A: Mathematical, Physical and Engineering Sciences*, *369*(1943), 2073–2086. https://doi.org/10.1098/rsta.2010.0313
52. Stephens, B. B., Long, M. C., Keeling, R. F., Kort, E. A., Sweeney, C., Apel, E. C., et al. (2018). The O_2/N_2 ratio and CO_2 airborne Southern Ocean study. *Bulletin of the American Meteorological Society*, *99*(2), 381–402. https://doi.org/10.1175/BAMS-D-16-0206.1
53. Thompson, C. R., Wofsy, S. C., Prather, M. J., Newman, P. A., Hanisco, T. F., Ryerson, T. B., et al. (2022). The NASA Atmospheric Tomography (ATom) Mission: Imaging the Chemistry of the Global Atmosphere. *Bulletin of the American Meteorological Society*, *103*(3), 761–790. https://doi.org/10.1175/BAMS-D-20-0315.1
54. Stephens, B. B., Long, M. C., Keeling, R. F., Kort, E. A., Sweeney, C., Apel, E. C., et al. (2018). The O_2/N_2 ratio and CO_2 airborne Southern Ocean study. *Bulletin of the American Meteorological Society*, *99*(2), 381–402. https://doi.org/10.1175/BAMS-D-16-0206.1

55. Santoni, G. W., Daube, B. C., Kort, E. A., Jiménez, R., Park, S., Pittman, J. V., et al. (2014). Evaluation of the airborne quantum cascade laser spectrometer (QCLS) measurements of the carbon and greenhouse gas suite - CO_2, CH_4, N_2O, and CO - during the CalNex and HIPPO Campaigns. *Atmospheric Measurement Techniques*, *7*, 1509–1526. https://doi.org/10.5194/amt-7-1509-2014

56. Daube, J. C., Boering, K. A., Andrews, A. E., & Wofsy, S. C. (2002). A high-precision fast-response airborne CO_2 analyzer for in situ sampling from the surface to the middle stratosphere. *Journal of Atmospheric and Oceanic Technology*, *19*(10), 1532–1543. https://doi.org/10.1175/1520-0426(2002)019<1532:AHPFRA>2.0.CO;2

57. Bent, J. D. (2014). *Airborne oxygen measurements over the Southern Ocean as an integrated constraint of seasonal biogeochemical processes*. University of California, San Diego.

58. Sweeney, C., Karion, A., Wolter, S., Newberger, T., Guenther, D., Higgs, J. A., et al. (2015). Seasonal climatology of CO_2 across North America from aircraft measurements in the NOAA/ESRL Global Greenhouse Gas Reference Network. *Journal of Geophysical Research : Atmospheres*, *120*(10), https://doi.org/10.1002/2014JD022591

59. Gelaro, R., McCarty, W., Suárez, M. J., Todling, R., Molod, A., Takacs, L., et al. (2017). The Modern-Era Retrospective Analysis for Research and Applications, Version 2 (MERRA-2). *Journal of Climate*, *30*(14), 5419–5454. https://doi.org/10.1175/JCLI-D-16-0758.1

60. Kobayashi, S., Ota, Y., Harada, Y., Ebita, A., Moriya, M., Onoda, H., et al. (2015). The JRA-55 reanalysis: General specifications and basic characteristics. *Journal of the Meteorological Society of Japan*, *93*(1), 5–48. https://doi.org/10.2151/jmsj.2015-001

61. Keeling, R. F., & Keeling, C. D. (2017). *Atmospheric Flask CO_2 and Isotopic Data Sets – Multiple Sampling Stations (Archive 2021-07-01). In Scripps CO_2 Program Data. UC San Diego Library Digital Collections. https://doi.org/10.6075/J0HQ3X30*.

62. Keeling, C. D., Piper, S. C., Bacastow, R. B., Wahlen, M., Whorf, T. P., Heimann, M., & Meijer, H. A. (2001). *Exchanges of atmospheric CO_2 and $^{13}CO_2$ with the terrestrial biosphere and oceans from 1978 to 2000. I. Global aspects, SIO Reference Series, No. 01-06, Scripps Institution of Oceanography, San Diego, 88 pages*.

63. Bakker, D. C. E., Pfeil, B., Smith, K., Hankin, S., Olsen, A., Alin, S. R., et al. (2014). An update to the surface ocean CO_2 atlas (SOCAT version 2). *Earth System Science Data*, *6*(1), 69–90. https://doi.org/10.5194/essd-6-69-2014

64. Rödenbeck, C., Bakker, D. C. E., Metzl, N., Olsen, A., Sabine, C., Cassar, N., et al. (2014). Interannual sea-air CO_2 flux variability from an observation-driven ocean mixed-layer scheme. *Biogeosciences*, *11*(17), 4599–4613. https://doi.org/10.5194/bg-11-4599-2014

3.7 Supporting Information Appendix

3.7.1: Bias due to sparse airborne spatial coverage

We showed in Fig. 3.3 and *SI Appendix*, Fig. 3.9-3.11 that, using the true 3-D atmospheric fields of models, we could successfully reconstruct the underlying surface CO_2 fluxes from knowledge of the true inventories of CO_2 within the $M_{\theta e}$ bands. Our estimated inventories from the airborne data may be biased, however, due to sparse coverage. To assess this bias, we compare the true χ_i of models (i.e., the 3-D atmospheric field of each inversion product) with χ_i calculated by subsampling the model atmospheric field along flight tracks. The true model χ_i is computed by averaging over all inversion product tropospheric grid cells (cutoff at PVU = 2) of flight dates of each airborne campaign within the corresponding $M_{\theta e}$ surfaces. The subsampled average χ_i is

computed by subsampling model data along the flight tracks at flight dates and by trapezoidal integration of subsampled model data as a function of $M_{\theta e}$, as in Jin et al. (2021), using $M_{\theta e}$ calculated from MERRA-2 and interpolated to the model grids. Prior to the trapezoidal integration, the subsampled data is also extrapolated to $M_{\theta e}$ = 0 surface using the average of the 100 observations with the lowest $M_{\theta e}$ values, except for HIPPO4, in which we only extrapolate to $M_{\theta e}$ = 15. We show the differences between true and subsampled average in *SI Appendix*, Fig. 3.17 and Table 3.5. This comparison is conducted for each inversion posterior atmospheric CO_2 field, for each airborne campaign and for each $M_{\theta e}$ band. These four inversion products generally agree on the sign of the bias in CO_2 concentration due to sparse airborne spatial coverage. We correct our χ_i calculated from airborne observations for each $M_{\theta e}$ band and each airborne mission using the corresponding bias averaged over 4 inversion products. The 1σ uncertainty of the correction for each campaign (or sub-campaign) and $M_{\theta e}$ band is assumed to be the standard deviation of the corresponding corrections of four 3-D CO_2 inversions. The day-to-day variability (1σ) in model χ_i computed from the 3-D fields is small (< 0.05 ppm), thus this correction for sparse spatial sampling also effectively corrects for any temporal sampling biases from sampling on particular flight days.

3.7.2: Uncertainty

We access the uncertainty of airborne-based seasonal air-sea CO_2 flux estimates of each $M_{\theta e}$ band by generating a large ensemble (2000 iterations) of flux estimates incorporating uncertainty from the following sources: (1) uncertainty of airborne CO_2 measurements of instrument; (2) uncertainty of the bias correction for CO_2 concentration of each $M_{\theta e}$ band due to sparse airborne spatial coverage; (3) interannual variability of the diabatic mixing rates; (4) differences of diabatic mixing rates between two reanalyses; (5) uncertainty of correction for the biosphere and fossil fuel CO_2 flux; (6) interannual variability of air-sea CO_2 flux.

We first generate 2000 iterations of the airborne AO2 data that accounts for AO2 CO_2 measurement uncertainty (detailed below in *SI Appendix*, Text 3.7.2.1). For each iteration, we resolve detrended CO_2 for each $M_{\theta e}$ band and each airborne campaign or sub-campaign, while correcting for spatial bias with 1σ uncertainty of the correction incorporated (detailed in *SI Appendix,* Text 3.7.1). We then apply each iteration to the 4-box model to calculate surface CO_2 flux estimates for each $M_{\theta e}$ band and for each airborne campaign. We apply MERRA-based mixing rates to the first 1000 iterations and JRA-based mixing rates to last 1000 iterations, with both sets incorporating interannual variability of the diabatic mixing rates as random errors (detailed in Materials and Methods). For individual flux (12 estimates) in each iteration, we add additional uncertainty due to flux interannual variability as suggested by MIROC-ACTM (details see below in *SI Appendix,* Text 3.7.2.2). Flux estimates from each campaign or sub-campaign and iteration are corrected for the small non-oceanic flux as the average of corresponding fluxes from four 3-D inversion models, while allowing 1σ uncertainty amounting to the standard deviation of four models (detailed in Materials and Methods). For each campaign, the overall 1σ uncertainty of flux (error bars in Fig. 3.5a-d) is calculated as the standard deviation of the 2000 iterations of flux estimates. We also calculate an ensemble of daily seasonal CO_2 flux cycles by carrying out 2-harmonic fits to each iteration of CO_2 flux estimates (12 campaigns or sub-campaigns) and for each $M_{\theta e}$ band. The 1σ uncertainty is calculated as the standard deviation of the 2-harmonic fitted daily flux of the large ensemble (2000 iterations), shown as shaded regions in Fig. 3.5a-d.

3.7.2.1: Uncertainty of AO2 CO_2 measurement

The AO2 instrument is primarily an atmospheric oxygen instrument, which also includes a CO_2 sensor. Although this sensor is not as precise as the other sensors flown in these campaigns, the short-term random error essentially averages out over the large spatial integrals used here. However, we allow that the AO2 CO_2 measurements may have systematic errors due to drift in

calibration or other artifacts during or between flights. To address measurement error, we generate an ensemble (2000 iterations) of 10-sec airborne measurements (aligned with data in HIPPO, ORCAS, and ATom merged files), with each iteration representing a plausible representation of the AO2 CO_2 signal with error, following:

$$\mathrm{CO_2^i}(t) = \mathrm{CO_2^{AO2}}(t) + [\text{within flight error}] + [\text{between flight error}] \quad \text{(S1)}$$

where $\mathrm{CO_2^i}(t)$ represents the i^{th} iteration of CO_2, where i runs from 1 to 2000, and $\mathrm{CO_2^{AO2}}$ represents the original AO2 CO_2 data. Both within- and between-flight errors are estimated based on the differences in CO_2 ($\mathrm{CO_2^{Diff}}$) measured between the AO2 instrument and other in-situ instruments (Harvard QCLS, Harvard OMS, or NOAA Picarro), assuming that the other measurements are correct and AO2 is wrong, which effectively provides a conservative assumption of errors in AO2. In this study, we estimate the error using AO2 and QCLS or OMS for HIPPO flights, and using AO2 and QCLS or NOAA Picarro for ORCAS and ATom flights.

The within-flight error is modeled as a random variable across all flights and measurements. For each flight and each pair of instruments (AO2 and the other), we build an autoregressive model using the method of Elorrieta et al. (1), which is suitable for irregular time series due to sampling gaps. The within-flight error is modeled as follows:

$$\mathrm{CO_2^{Diff}}(t) = \mathrm{AR_{10-sec}^{j,k}} \cdot \mathrm{CO_2^{Diff}}(t-1) + \epsilon^{j,k}(t) \quad \text{(S2)}$$

where $\mathrm{AR_{10-sec}^{j,k}}$ is the autocorrelation coefficient that indicates the dependence of CO_2 of current time step $\mathrm{CO_2^{Diff}}(t)$ on that of previous time step $\mathrm{CO_2^{Diff}}(t-1)$, and $\epsilon^{j,k}(t)$ is the random error, drawn from a Gaussian distribution, with a new sample drawn for each data point. Both the AR coefficient and the standard deviation (1σ) of $\epsilon(t)$ are unique for each flight (j) and for each instrument pair (k), which we summarize in *SI Appendix*, Table 3.7. The 1σ random error is dominated by short-term imprecision of the AO2 instrument. We note that the mean CO_2 offset of

the flight (j) between two instruments is pre-subtracted while constructing the autoregressive model (Eq. S2), because between-flight error is considered separately. For HIPPO flights, 1000 iterations are based on coefficients resulting from AO2 minus QCLS and 1000 iterations are based on AO2 minus OMS. For ORCAS and ATom flights, 1000 iterations are based on coefficients resulted from AO2 minus QCLS and 1000 iterations are based on AO2 minus NOAA Picarro. The order of these 2000 iterations is randomized for other error analysis. For flights where one of the instruments is unavailable (the target instrument AO2 and/or other instruments), we use the averaged AR coefficient and the averaged 1σ value for $\epsilon(t)$ of the corresponding campaign sub-campaign and the corresponding instrument to generate simulated $CO_2^{Diff}(t)$.

The between-flight error is sampled from a Gaussian distribution centered on zero with a new sample drawn for each flight and applied as a uniform offset to all data in that flight. We use a standard deviation (1σ) of ± 0.26 ppm for all HIPPO flights, and ± 0.13 for all ATom and ORCAS flights based on AO2-QCLS differences. To establish these 1σ values, we compare the averaged CO_2 differences of each flight between AO2 and QCLS. The 1σ values are therefore calculated as the standard deviation of all flight-averaged CO_2 differences between two instruments, as shown in *SI Appendix*, Fig. 3.18. This approach gives a conservative estimate of AO2 flight-to-flight stability, as some variability could result from biases in the other sensor. Fig. 3.18 also shows differences between AO2 and other in-situ instruments (i.e., OMS and NOAA-Picarro) and NOAA portable flask packages (PFP) (2). Using ± 0.25 ppm for HIPPO based on AO2-OMS differences, ± 0.13 ppm for ORCAS and ATom based on AO2-NOAA Picarro differences, or ± 0.23 ppm for ORCAS and ATom based on AO2-PFP differences would not significantly change our results. The larger 1σ value for PFP comparisons might result from less data per flights with the flask system. We did not compare with another flask dataset (Medusa)

because the AO2 CO_2 measurements are already adjusted to match Medusa on a flight-average basis (3).

3.7.2.2: Flux interannual variability (IAV)

In this study, we estimate 12 separate snapshots of the flux on particular dates that spread over 10 years, and fit a 2-harmonic seasonal flux cycle. Due to interannual variability of the flux, our approximate seasonal cycle estimate will not conform to a true climatology. To estimate errors relative to a true climatology, we rely on IAV from inverted oceanic CO_2 fluxes estimated using MIROC-ACTM. We access the flux bias due to limited temporal sampling for each airborne campaign (or sub-campaign) by comparing the ACTM modeled flux of a 15-day flight window and a 10-year averaged flux of the same 15-day window repeating from 2009 to 2018 (*SI Appendix*, Fig. 3.19). The 15-day flight window is selected as the mean campaign flight day ±7 days. We could correct for interannual variability, in principle, based on the difference of the modeled flux in a specific year and the 10-year averaged flux for each campaign. We find, however, only a small potential correction (bars in *SI Appendix*, Fig. 3.19, mean absolute correction of 0.04 PgC yr^{-1}). This bias also does not contribute to a clear seasonal flux cycle bias (black curves in *SI Appendix*, Fig. 3.19). Therefore, we do not correct for this bias but rather consider flux IAV of each campaign (sub-campaign) as a random error, calculated as the standard deviation of the 15-day averaged flux from 2009 to 2018, as summarized in *SI Appendix*, Table 3.8. We use MIROC-ACTM to evaluate IAV because the simulated diabatic mixing rates and CO_2 gradients of ACTM match best with reanalysis and airborne observations.

3.7.3 Thermal-driven CO_2 flux cycle

We estimate the thermal-driven flux cycle (Fig. 3.5m-p) using the following expression as suggested by Takahashi et al. (2009).

$$F_{CO_2}^{thermal} = k \cdot \alpha \cdot pCO_2^{eq} \cdot 0.04 \cdot (SST - < SST >) \quad (S3)$$

where k is the CO_2 gas transfer velocity (cm hr^{-1}), α is the CO_2 solubility in sea water (mmol m^{-3} atm^{-1}), pCO_2^{eq} is the CO_2 partial pressure at equilibrium, assumed to be 400 μatm, SST is the sea surface temperature, $< SST >$ represents the annual average SST. 0.04 denotes a 4% pCO_2 change per 1°C SST change, also as suggested by Takahashi et al. (2009).

We use monthly gridded (lon × lat = 1° × 1°) SST data from the NOAA Optimum Interpolation (OI) SST V2 product (5). The $\alpha \cdot pCO_2^{eq}$ term is a function of sea surface temperature (SST) and is calculated from CO2cal (6), by assuming salinity at 34 PSU, total alkalinity at 2250 μmol $kgSW^{-1}$, sea water density at 1.02 g cm^{-3}, and using monthly SST data from the NOAA OISST V2 product (5).

The gas exchange coefficient k is calculated following Wanninkhof, 1992 (7):

$$k = 0.31 \cdot U_{10}^2 \cdot \left(\frac{Sc}{660}\right)^{-\frac{1}{2}} \quad (S4)$$

where U_{10} is 10-m surface wind speed, which we obtained from MERRA-2 reanalysis (8), Sc is the Schmidt number, and 660 is the Schmidt number of CO_2 in seawater at 20°C. We calculate gridded monthly Sc from 2009 to 2018 using the expression below, as suggested in Wanninkhof, 1992 (7) :

$$Sc = 2073.1 - 125.62 \cdot SST + 3.6276 \cdot SST^2 - 0.043219 \cdot SST^3 \quad (S5)$$

where we use monthly SST data from NOAA OISST V2 (5).

3.7.4: Airborne campaigns

Both the HIPPO and ATom campaigns had broad coverage in the Southern Hemisphere, extending from the Equator to the Antarctic, and from near the surface (150-300 m) to the lower stratosphere (12-15 km) (*SI Appendix*, Fig. 3.6). HIPPO consisted of five missions (referred to as HIPPO1-5) between 2009 and 2011 and ATom consisted of four missions (refer to as ATom1-4)

between 2016 and 2018 (detailed in *SI Appendix*, Table 3.2). HIPPO missions were over the Pacific Ocean, while ATom missions covered both the Pacific Ocean and the Atlantic Ocean.

ORCAS had 19 research flights during Jan. and Feb. of 2016, with spatial coverage from ~35°S to 75°S. These flights collected samples over the Drake Passage and surrounding South America and Antarctic Peninsula coastal regions. Since the ORCAS campaign spans about two months, we divide ORCAS flights into three groups (detailed in *SI Appendix*, Table 3.2) to yield the average CO_2 of each $M_{\theta e}$ band.

We exclude all observations near landing sites with the same criteria as in Jin et al. (2021), for example, samples that were collected 120s after takeoff, 600 s prior to landing, and likewise for any missed approaches.

3.7.5: Calculation of $M_{\theta e}$ for each airborne observation

The computation of $M_{\theta e}$ is presented in Jin et al. (9), follows:

$$M_{\theta_e}(\theta_e, t) = \sum M_x(t)|_{\theta_{e_x} < \theta_e} \quad (S7)$$

where x indicates an individual grid cell of the atmospheric field, $M_x(t)$ is the dry air mass of each grid cell x at time t, and θ_{e_x} is the equivalent potential temperature of the grid cell. For a given θ_e threshold, the corresponding $M_{\theta e}$ value is calculated by integrating the airmass of all grid cells with θ_e value smaller than the threshold. We only integrate airmass in the troposphere, which is defined as potential vorticity unit (PVU) smaller than 2. This calculation yields a unique value of $M_{\theta e}$ for each value of θ_e as well as a 3-D field of atmospheric $M_{\theta e}$, which we generate at daily resolution in the Southern Hemisphere based on MERRA-2 reanalysis (8). We also calculate $M_{\theta e}$ using other reanalyses (NCEP, JRA-55, and ERA-5) and we find that the differences are generally small (9).

We define surface $M_{\theta e}$ as the $M_{\theta e}$ value of the lowest altitude level in the MERRA-2 reanalysis at a given longitude and latitude.

The $M_{\theta e}$ value of each airborne observation is computed by matching the observed θ_e value with our daily θ_e-$M_{\theta e}$ lookup table. We compute observed θ_e following

$$\theta_e = \left(T + \frac{L_v(T)}{C_p} q\right)\left(\frac{P_0}{P}\right)^{\frac{R_d}{C_p}} \quad \text{(S8)}$$

where T (K) is the temperature of air; q (kg of water vapor per kg of air mass) is the water vapor mixing ratio; R_d (287.04 J kg^{-1} K^{-1}) is the gas constant for air; C_{pd} (1005.7 J kg^{-1} K^{-1}) is the specific heat of dry air at constant pressure; P_0 (1013.25 mbar) is the reference pressure at the surface, and $L_v(T)$ is the latent heat of evaporation at temperature T. $L_v(T)$ is defined as 2406 kJ kg^{-1} at 40°C and 2501 kJ kg^{-1} at 0°C and scales linearly with temperature.

For HIPPO and ORCAS, we calculate θ_e using the recommended static pressure and air temperature variables (PSX and ATX), and water vapor mole fraction measured by VCSEL (10; H2Oppmv_vxl for HIPPO and VMR_VXL for ORCAS). We interpolate specific humidity in MERRA-2 to any missing water vapor mole fraction measurement along HIPPO flights. For ATom, we calculate θ_e from static pressure and air temperature as measured by the Meteorological Measurement System (MMS, P), and relative humidity of water vapor as measured by the Diode Laser Hygrometer (DLH, Sat_Vapor_Press_H2O) (11, 12).

3.7.6: Atmospheric CO_2 inversion products, empirical surface ocean pCO_2 products, global biogeochemistry models, and prior airborne estimate

We use estimated air-sea CO_2 fluxes and posterior atmospheric CO_2 concentration from four atmospheric inversion products. The transport model, resolution, and meteorology of each inversion product is summarized in *SI Appendix*, Table 3.3. In these inversions, the fossil fuel and fire CO_2 fluxes are prescribed, while the ocean and land CO_2 fluxes are optimized to match in-situ CO_2 observations, except Jena sEXTocNEET_v2020 which uses prescribed ocean CO_2 fluxes

provided by assimilation of surface ocean pCO_2 observations from SOCAT (13) by the Jena mixed-layer scheme (14). The land fluxes in Jena sEXTocNEET_v2020 are optimized.

Surface ocean pCO_2 products used forcomparison purposes in this study were derived using neural-network approaches to interpolate pCO_2 data from SOCAT (13) or SOCCOM (15), as described in Landschützer et al. (16). Here we use two different flux estimates from Landschützer et al. (17, 18), with the methodology presented by Bushinsky et al. (19) and listed here by the names used in Figure 3.5i-l:

1. SOCAT: only shipboard pCO_2 measurements were used to train the neural network and generate extrapolated pCO_2 fields used to estimate fluxes, no profiling float data were included.

2. SOCCOM(only): a sensitivity run where all shipboard data from SOCAT were excluded (only SOCCOM float data were included) south of 35°S after the year 2014.

We compare to modeled air-sea CO_2 flux fields from nine global ocean biogeochemistry models that were submitted to the Global Carbon Budget 2020 (20). These models are all general circulation models coupled with biogeochemistry modules. Details can be found in Hauck et al. (21) and Table A2 of Friedlingstein et al. (20). We downloaded flux fields from Hauck et al. (21), which have been previously regridded to 1° x 1°.

We use monthly surface $M_{\theta e}$ maps (averaged from the daily maps based on MERRA-2) that are interpolated to model grids to assign a $M_{\theta e}$ value to each surface grid of the CO_2 flux fields. Total fluxes of each month are calculated by integrating all selected grids of the corresponding $M_{\theta e}$ range. Seasonal cycles of total fluxes are calculated by a 2-harmonic fit to the monthly fluxes from 2009 to 2018, except for SOCCOM and FESOM, which are from 2015 to 2017, and from 2009 to 2017, respectively.

For each product, we calculate annual uptake by integrating the monthly fluxes of each year, and we report the mean annual uptake from 2009 to 2018, with 1σ uncertainty as the standard deviation of 10 years.

3.7.7: Discussion of diabatic mixing rates

We find that diabatic mixing rates are generally larger at a high $M_{\theta e}$ surface (lower latitudes) relative to a low surface (Fig. 3.2 and *SI Appendix*, Fig. 3.8), suggesting a faster diabatic transport time scale in low latitudes. Diabatic mixing rates also show a clear seasonal cycle at higher $M_{\theta e}$ surfaces (30 and 45), which display slower transport time scales (low values) in the austral summer relative to the winter. We show a large spread of mixing rates that are calculated from four different inversion products, corresponding to four different atmospheric transport models driven by four different reanalysis wind products (*SI Appendix,* Table 3.8). Among all four ATM-based mixing rates, CT-based mixing rates display the fastest transport, while ACTM-based mixing rates display the slowest transport. Jena-based mixing rates only show a small seasonal cycle and is close to ACTM-based mixing rates in the winter (small mixing rate), but relatively close to CT-based mixing rates in the summer (larger mixing rate). CAM-based mixing rates show a fast transport in the winter that is close to CT-based mixing rates, but show a slow transport in the summer that is close to ACTM-based mixing rates. On the other hand, mixing rates computed using moist static energy from reanalyses (MSE-based mixing rates) generally show a slower transport compared to the average of ATM-based mixing rates. The two MSE-based mixing rates are highly comparable and show a slow transport time scale that is close to ACTM-based mixing rates in the summer. Diabatic mixing rates only show very small interannual variability at each $M_{\theta e}$ surface and from each product, indicated by the small 1σ uncertainty bars in Fig. 3.2 and *SI Appendix,* Figure 3.8. We note that ATM-based mixing rates are poorly constrained when the atmospheric CO_2 gradient across $M_{\theta e}$ is small (e.g., from September to November in CAMS). This

suggests that, provided we use the same transport model, a different mixing rate would be derived if we base our calculations on a single component of atmospheric CO_2 (e.g., ocean flux alone), or if we use other chemical tracers (e.g., O_2) that have different gradients compared to CO_2.

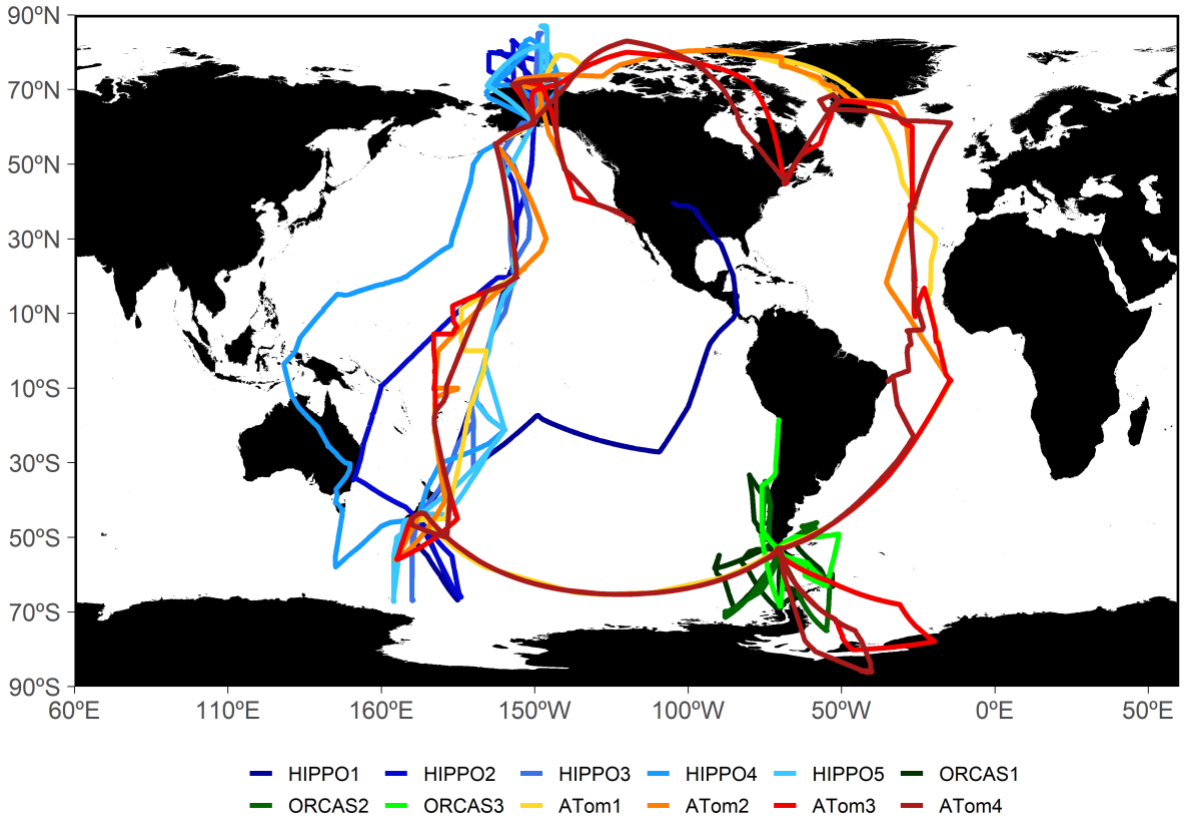

Figure 3.6: HIPPO, ORCAS and ATom horizonal flight tracks, colored by campaigns or sub-campaigns. The aircraft profiled continuously from near the ocean surface to 12-14 km (see Fig. 3.6 in Long et al. 2021 (22)).

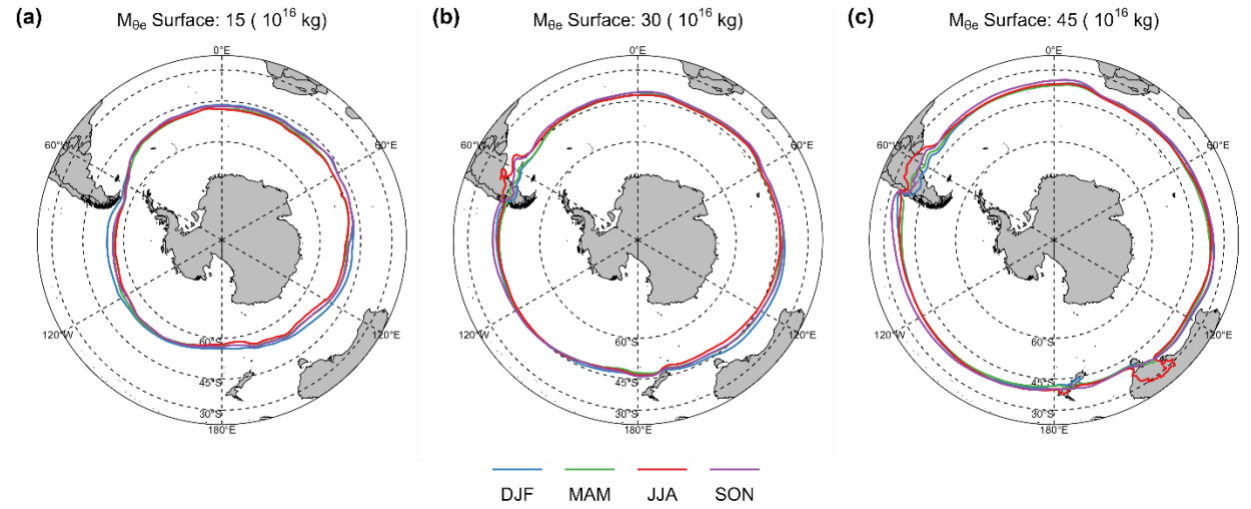

Figure 3.7: Similar to Fig. 3.1b, but showing $M_{\theta e}$ surface contours for each season (by color, averaged from 2009 to 2018 based on MERRA-2 reanalysis) of three $M_{\theta e}$ surfaces (10^{16} kg).

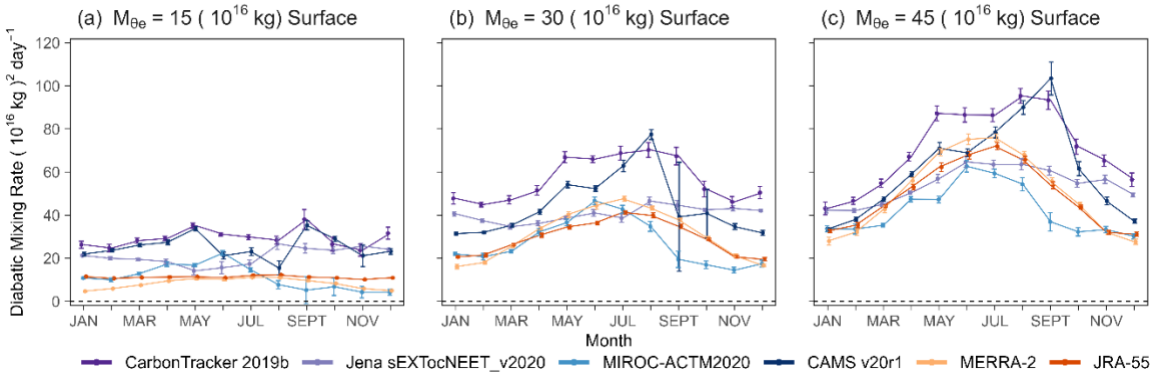

Figure 3.8: Diabatic mixing rates of the (a) 15 (10^{16} kg), (b) 30 (10^{16} kg), and (c) 45 (10^{16} kg) $M_{\theta e}$ surface. These mixing rates are parameterized from four 3-D CO_2 inversion products and moist static energy budgets of two reanalysis products. Error bars represent only the interannual variability of parameterized mixing rates, which is shown to be small. Panel (b) is identical to Figure 3.2, but with a larger y-range.

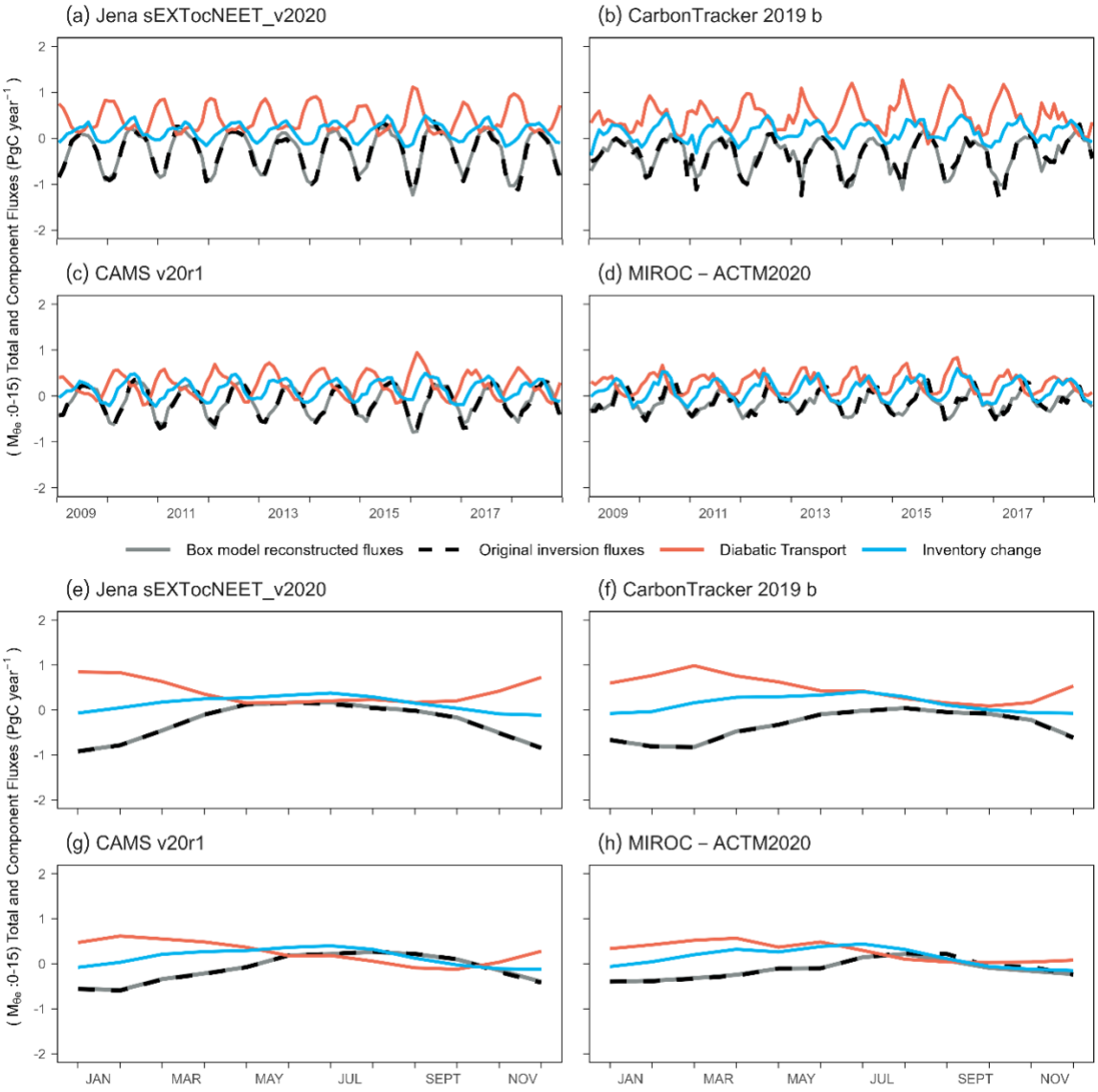

Figure 3.9: (a) – (d) Monthly reconstructed air-sea CO_2 fluxes (solid black) of the 0-15 (10^{16} kg) $M_{\theta e}$ band (~ south of 51°S near the Earth surface, detailed in Fig. 3.1b and SI Appendix, Fig. 3.6) based on four 3-D inversions, comparing with the original monthly inversion fluxes of the same $M_{\theta e}$ band (dashed black). Each component (i.e., diabatic CO_2 transport and CO_2 inventory change, detailed in Materials and Methods, and Eq. 3.1) of the box-model reconstruction is shown as well. Negative values of the diabatic transport represents CO_2 transport into the 0-15 $M_{\theta e}$ band (poleward transport). (e) – (h) Similar to (a) – (d), but showing the flux and each component as a climatological monthly average (2009 to 2018).

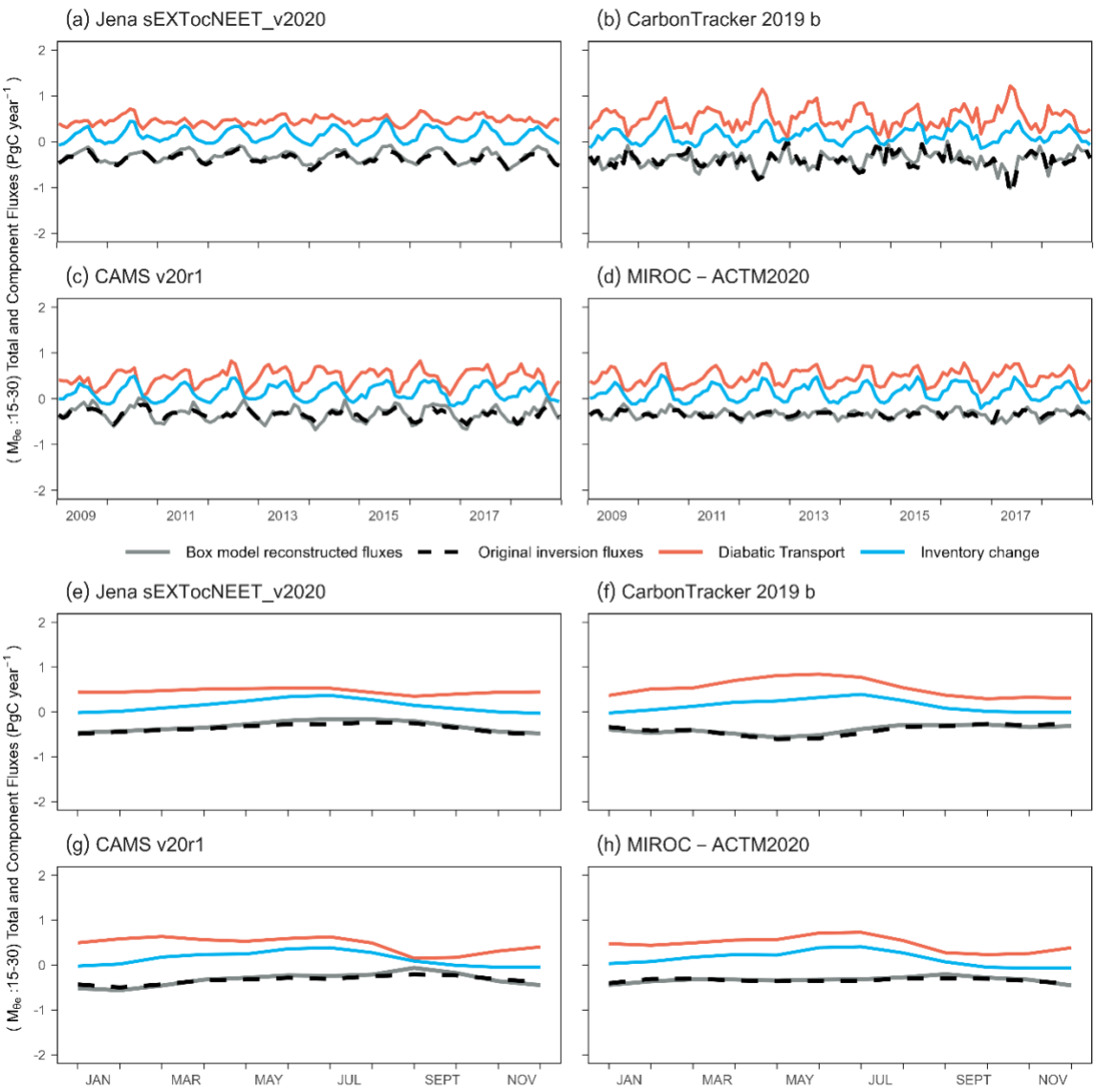

Figure 3.10: Similar to Figure 3.7, but showing reconstruction of surface CO_2 flux for the $M_{\theta e}$ band of 15 to 30 (10^{16} kg).

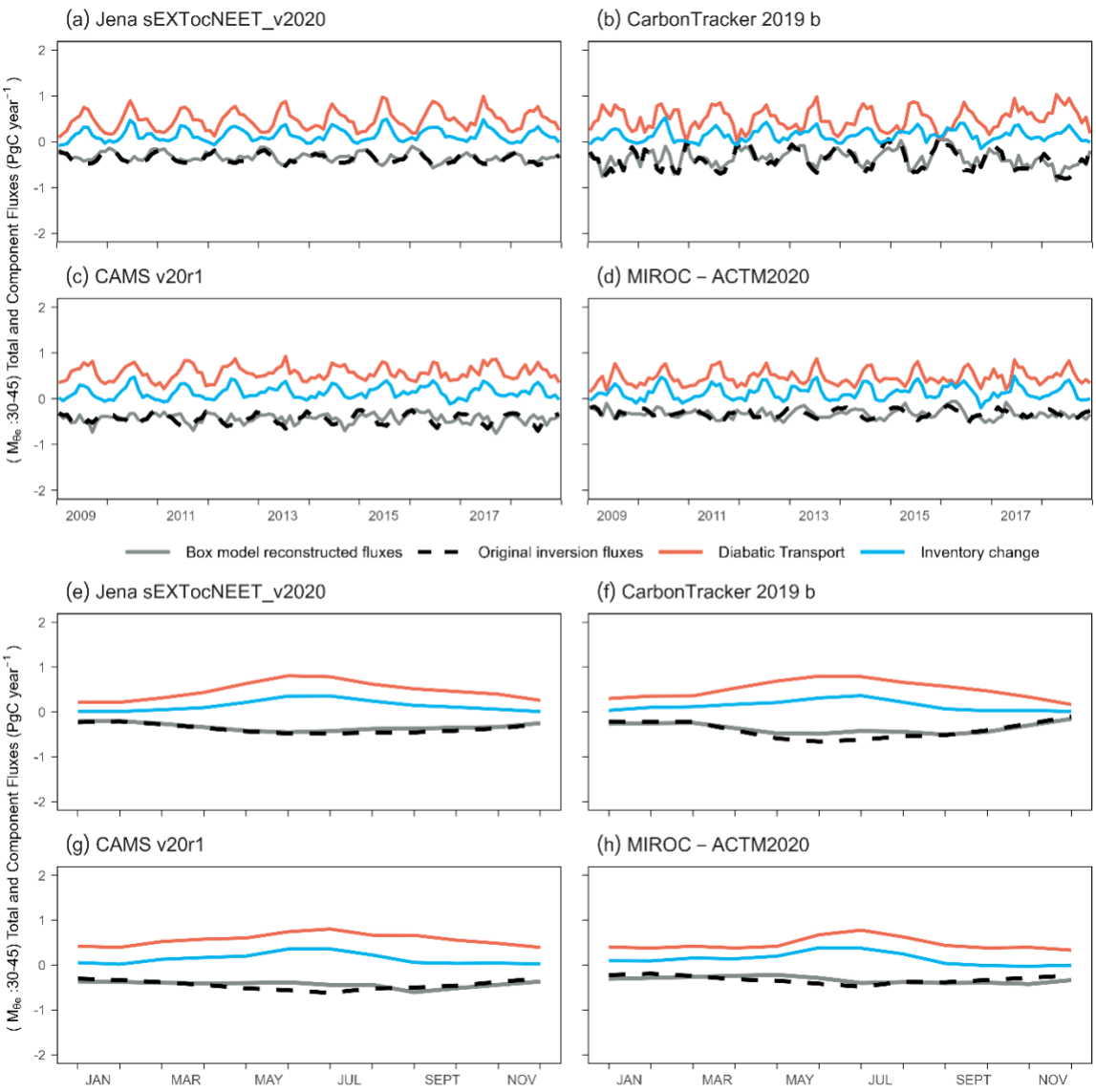

Figure 3.11: Similar to Figure 3.7, but showing reconstruction of surface CO_2 flux for the $M_{\theta e}$ band of 30 to 45 (10^{16} kg).

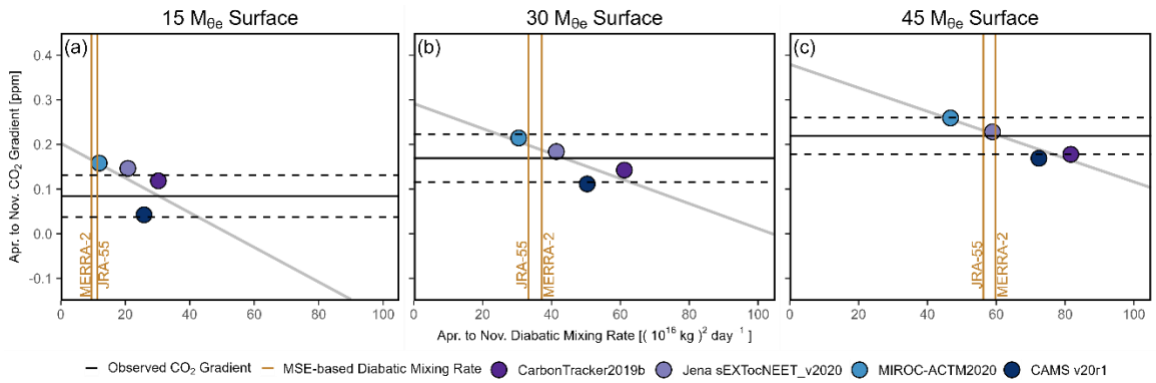

Figure 3.12: Similar to Fig. 3.4a-c but exploring the correlation between April to November averaged ATM-based mixing rates for three $M_{\theta e}$ surfaces and simulated atmospheric CO_2 gradients across the corresponding $M_{\theta e}$ surfaces of four transport models (inversion products). Simulated gradients are averaged at the mean dates of seven airborne campaigns that took place during April to November (HIPPO2-5, and ATom1, 3, 4). The corresponding ATM-based mixing rate is calculated as the April to November average. For comparison, we show the observed CO_2 gradients (spatial bias corrected) in horizontal black lines, which are calculated as the average of the same seven campaigns, while the dashed lines show the 1σ uncertainty (measurement and spatial bias correction uncertainty). We also show two MSE-based mixing rates (April to November average) as vertical brown lines.

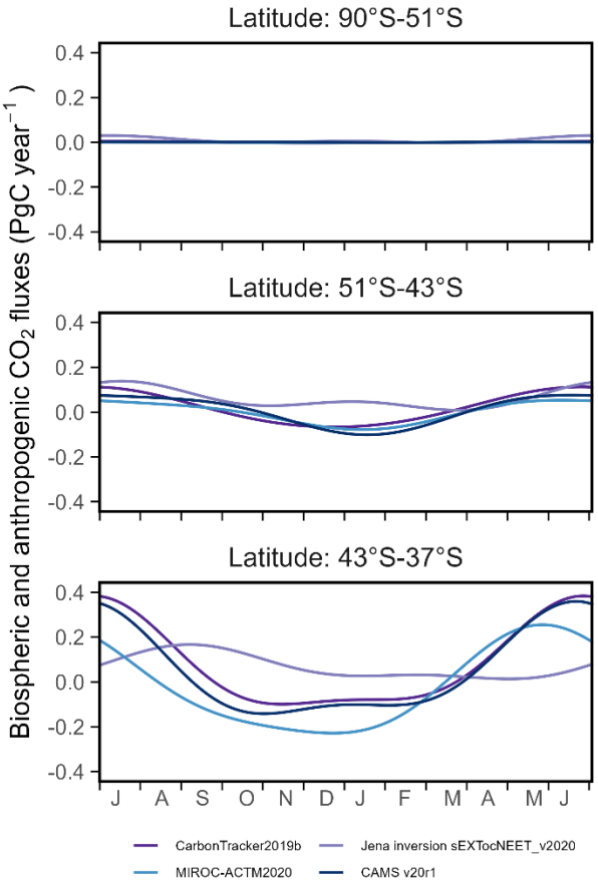

Figure 3.13: Seasonal cycles (2009 to 2018 average) of biosphere and anthropogenic CO_2 fluxes estimated by the atmospheric inversion products for three approximate latitude bands (calculated based on surface $M_{\theta e}$ range). The seasonal cycles are calculated by 2-harmonic fits to monthly fluxes from 2009 to 2018. For each $M_{\theta e}$ band, we subtract the mean biospheric and anthropogenic flux (averaged from the four flux estimates) from our surface CO_2 flux estimates (based on airborne observation and box model) to yield air-sea CO_2 fluxes. This correction has 1 σ uncertainty amounting to the standard deviation of the four flux estimates.

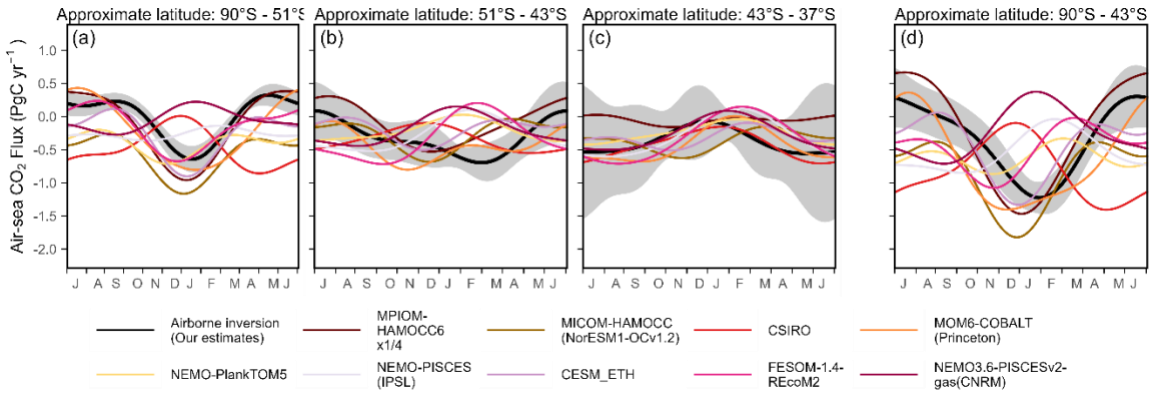

Figure 3.14: Similar to Fig. 3.5e-h, but comparing our airborne-based estimates (black) with ocean biogeochemistry models that are used in Global Carbon Project 2020 (20, 21).

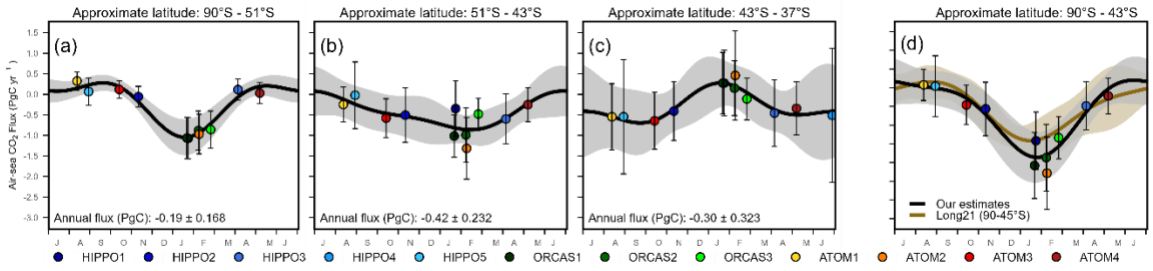

Figure 3.15: Similar to Fig. 3.5a–d but showing the fitted flux cycles calculated using the mean of four ATM-based mixing rates and 2 MSE-based mixing rates.

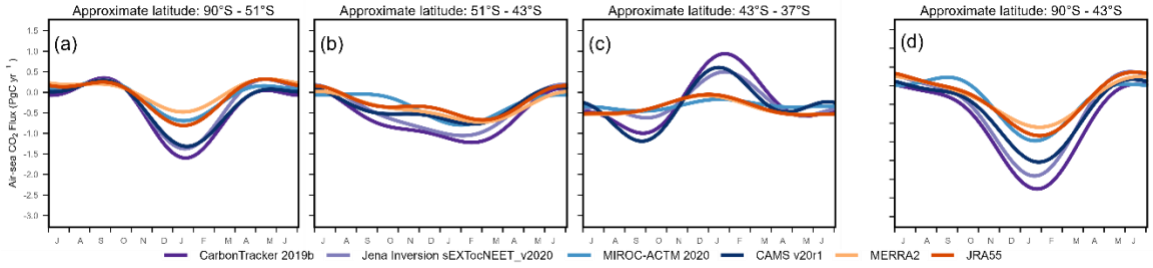

Figure 3.16: Similar to Fig. 3.5a–d but showing the fitted flux cycles calculated using each set of diabatic mixing rate (i.e., 4 ATM-based and 2 MST-based).

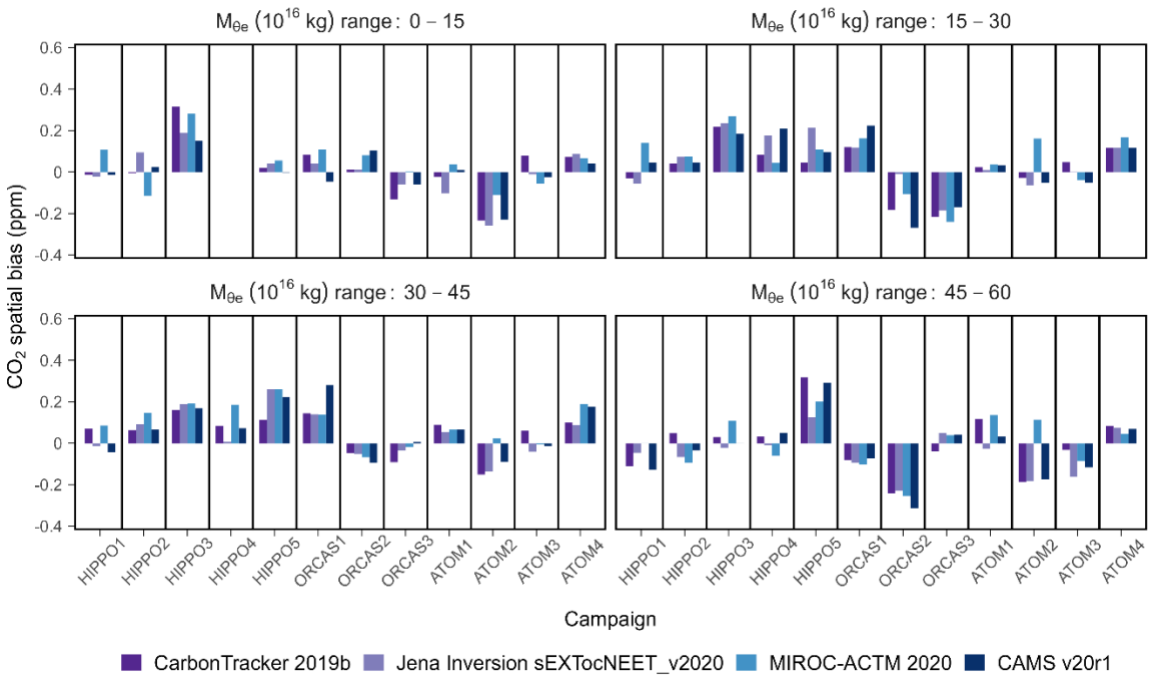

Figure 3.17: Identifying bias in our estimates of CO_2 concentration for each $M_{\theta e}$ box due to limited spatial coverage of the airborne CO_2 measurements. We compare the true model CO_2 (i.e., calculated from the 3-D atmospheric field of each inversion product) with values calculated by subsampling the model atmospheric field along the flight track of each airborne mission (method see *SI Appendix*, Text 3.7.1) and processing identically to the observations. The bias is calculated as the subsampled average minus the true average, and therefore, a positive bias indicates that the limited spatial coverage biases the estimated CO_2 concentration too large. We adjust our measurements using the average across models for each campaign or sub-campaign.

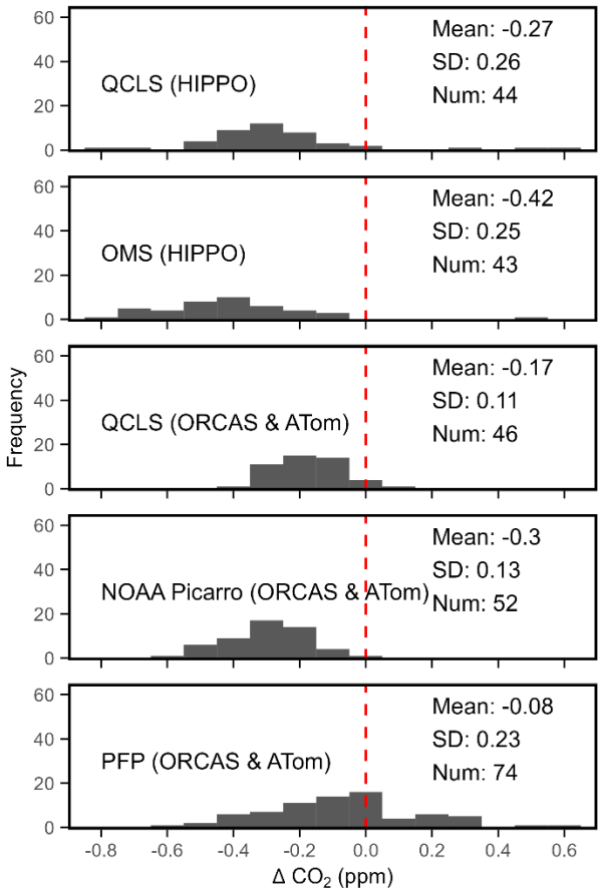

Figure 3.18: Histogram of CO_2 differences, averaged over each flight, between the AO2 instrument and other instruments (for method see *SI Appendix,* Text 3.7.2.1). One value is generated per flight and the histogram shows these differences across all flights and campaigns. We also show the mean and standard deviation of CO_2 offsets for each instrument, and the number of flights that are available.

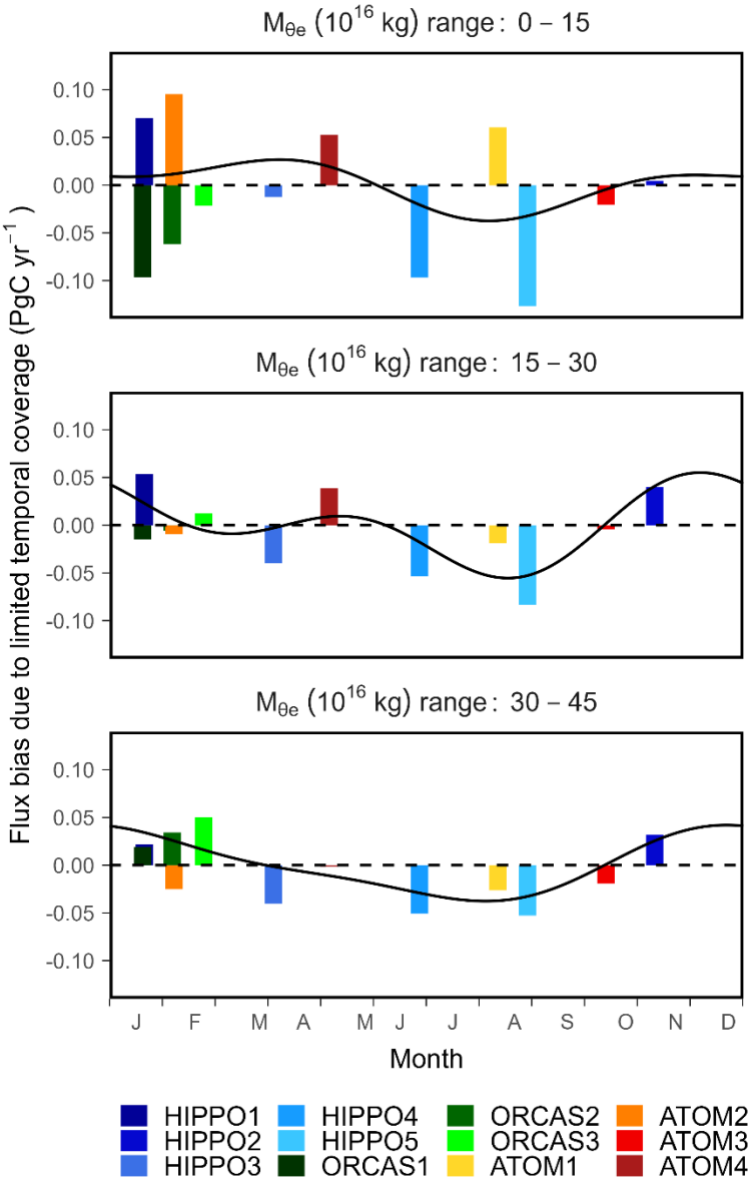

Figure 3.19: Identifying bias in CO_2 flux estimates for each $M_{\theta e}$ box and each airborne campaign or sub-campaign due to limited temporal coverage (interannual variability), based on estimated flux from MIROC-ACTM. For each campaign, we quantify the bias (shown as bars) as the differences between modelled flux of a 15-day flight window around the corresponding campaign mean date and the 10-year averaged flux of the same 15-day window repeating from 2009 to 2018. The 15-day flight window is selected as the mean campaign flight day ±7 days. A positive bias indicates that the limited temporal coverage biases the estimated air-sea CO_2 flux too large (more outgassing or less uptake). We also show the corresponding seasonal cycle of these interannual flux biases as black curves, estimated by 2-harmonic fits of corresponding bars for each $M_{\theta e}$ band. We do not adjust for interannual sampling biases, but do include a component in our uncertainty budget from inverted flux in MIROC-ACTM.

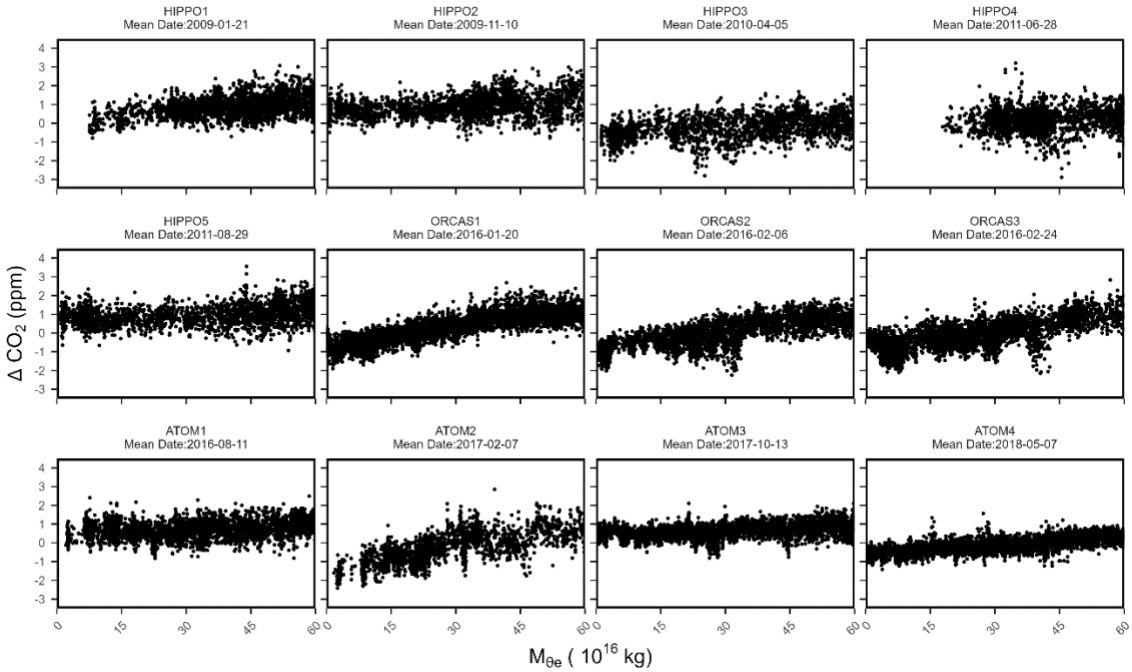

Figure 3.20: Detrended airborne CO_2 observations (ΔCO_2) expressed on the $M_{\theta e}$ coordinate. We note that we have dense measurements across all $M_{\theta e}$ surfaces in each campaign except close-to-0 $M_{\theta e}$ during HIPPO1, ATom1, and ATom2. We also do not have measurements in the entire first $M_{\theta e}$ band during HIPPO4 (no observation lower than 17.88 $M_{\theta e}$).

Table 3.1: RMSE (PgC yr^{-1}) of reconstructed monthly surface CO_2 fluxes compared to the original fluxes.

M_{θ_e} band (10^{16} kg)	RMSE of each inversion products			
	Jena CO_2 inversion sEXTocNEET_v2020	CarbonTracker 2019b	CAMS V20r1	MIROC-ACTM2020
0-15	0.067	0.097	0.048	0.094
15-30	0.066	0.086	0.081	0.067
30-45	0.083	0.118	0.113	0.109

Table 3.2: Summary of research flight number latitude coverage, and duration of each airborne mission in the Southern Hemisphere.

Campaign	Flight numbers	Latitude coverage	Date
HIPPO1	5 – 10	66.2°S – 0.0°S	2009.01.16 – 2009.01.28
HIPPO2	4 – 8	66.0°S – 0.0°S	2009.11.07 – 2009.11.16
HIPPO3	4 – 8	66.9°S – 0.0°S	2010.03.31 – 2010.04.10
HIPPO4	4 – 8	58.0°S – 0.0°S	2011.06.22 – 2011.07.03
HIPPO5	7 – 11	67.2°S – 0.0°S	2011.08.24 – 2011.09.03
ORCAS1	1 – 6	69.0°S – 33.3°S	2016.01.15 – 2016.01.25
ORCAS2	7 – 11	75.0°S – 35.0°S	2016.01.30 – 2016.02.12
ORCAS3	12 – 19	68.5°S – 18.3°S	2016.02.18 – 2016.02.29
ATom1	4 – 8	65.3°S – 0.0°S	2016.08.06 – 2016.08.17
ATom2	4 – 8	65.3°S – 0.0°S	2017.02.03 – 2017.02.15
ATom3	4 – 9	80.1°S – 0.0°S	2017.10.06 – 2017.10.19
ATom4	4 – 9	86.2°S – 0.0°S	2018.05.01 – 2018.05.14

Table 3.3: Atmospheric inversion products.

Product	Years	Transport Model	Resolution (lon x lat x vertical level)	Meteorology	Reference
Jena Inversion sEXTocNEET_v2020	1999-2019	TM3	4 x 5 x 19	NCEP	(23)
Carbon Tracker 2019b	2000-2018	TM5	3 x 2 x 25	ERA-Interim	(24)
CAMS v20r1	1979-2020	LMDZ6A	3.75 x 1.875 x 39	ERA5	(25–27)
MIROC-ACTM2020	1996-2019	MIROC4-ACTM	2.8 x 2.8 x 67	JRA-55	(28)

Table 3.4: Airborne-based air-sea CO_2 fluxes estimated for each campaign and $M_{\theta e}$ band. The mean day of year of each airborne campaign is also listed. Positive flux denotes net outgassing into the atmosphere. Latitudes represent mean annual locations of $M_{\theta e}$ boundaries. We did not resolve flux estimates in the first two bands of HIPPO4 because there is no observation data within the entire first $M_{\theta e}$ band (0-15 10^{16} kg).

Campaign	Day of year	M_{θ_e}(10^{16} kg): 0-15 Latitude: 90°S - 51°S		M_{θ_e}(10^{16} kg): 15-30 Latitude: 51°S - 43°S		M_{θ_e}(10^{16} kg): 30-45 Latitude: 43°S - 39°S		M_{θ_e}(10^{16} kg): 0-30 Latitude: 90°S - 43°S	
		Flux (PgC yr^{-1})	Uncertainty (PgC yr^{-1})	Flux (PgC yr^{-1})	Uncertainty (PgC yr^{-1})	Flux (PgC yr^{-1})	Uncertainty (PgC yr^{-1})	Flux (PgC yr^{-1})	Uncertainty (PgC yr^{-1})
HIPPO1	22	-0.68	0.24	-0.28	0.39	-0.01	0.50	-0.97	0.40
HIPPO2	314	-0.03	0.15	-0.35	0.42	-0.24	0.50	-0.39	0.46
HIPPO3	95	0.20	0.15	-0.54	0.46	-0.54	0.74	-0.34	0.47
HIPPO4	179	/	/	/	/	-0.61	1.48	/	/
HIPPO5	241	0.10	0.21	-0.02	0.63	-0.47	1.21	0.08	0.64
ORCAS1	20	-0.61	0.24	-0.66	0.24	-0.19	0.39	-1.27	0.32
ORCAS2	37	-0.50	0.24	-0.73	0.37	-0.25	0.36	-1.23	0.42
ORCAS3	55	-0.44	0.19	-0.45	0.25	-0.34	0.36	-0.90	0.28
ATom1	223	0.28	0.16	-0.15	0.30	-0.52	0.73	0.13	0.32
ATom2	40	-0.61	0.24	-0.99	0.41	-0.02	0.77	-1.61	0.46
ATom3	286	0.15	0.14	-0.46	0.28	-0.38	0.49	-0.31	0.33
ATom4	127	0.23	0.14	-0.30	0.34	-0.45	0.60	-0.07	0.38

Table 3.5: Atmospheric CO_2 gradients across $M_{\theta e}$ bands observed by each airborne campaign. The adjusted gradient is also shown here, which is calculated by subtracting the bias due to limited spatial coverage (detailed in *SI Appendix*, Text 3.7.1 and Fig. 3.18)

Campaign	$M_{\theta_e}^{15-30}$-$M_{\theta_e}^{0-15}$			$M_{\theta_e}^{30-45}$-$M_{\theta_e}^{15-30}$			$M_{\theta_e}^{45-60}$-$M_{\theta_e}^{30-45}$		
	Gradient (ppm)	Adjusted gradient (ppm)	Uncertainty (ppm)	Gradient (ppm)	Adjusted gradient (ppm)	Uncertainty (ppm)	Gradient (ppm)	Adjusted gradient (ppm)	Uncertainty (ppm)
HIPPO1	0.53	0.51	0.16	0.32	0.32	0.17	0.08	0.18	0.10
HIPPO2	0.09	0.03	0.11	0.23	0.20	0.17	0.14	0.27	0.10
HIPPO3	0.08	0.09	0.11	0.18	0.23	0.15	0.08	0.23	0.13
HIPPO4	/	/	/	0.08	0.12	0.21	0.08	0.16	0.13
HIPPO5	0.14	0.05	0.15	0.16	0.06	0.14	0.15	0.14	0.14
ORCAS1	0.71	0.60	0.09	0.66	0.64	0.10	0.20	0.47	0.08
ORCAS2	0.31	0.50	0.15	0.65	0.57	0.12	0.22	0.42	0.07
ORCAS3	0.38	0.53	0.09	0.59	0.42	0.08	0.39	0.44	0.07
ATom1	-0.01	-0.06	0.10	0.12	0.07	0.06	0.14	0.15	0.09
ATom2	0.68	0.47	0.16	0.52	0.62	0.15	0.31	0.32	0.19
ATom3	0.03	0.03	0.08	0.24	0.23	0.08	0.21	0.31	0.08
ATom4	0.29	0.22	0.05	0.13	0.22	0.08	0.14	0.21	0.06

Table 3.6: Bias of averaged CO_2 concentration due to limited spatial coverage (detailed in *SI Appendix*, Text 3.7.1). A positive value indicates that the limited spatial coverage would bias the observed average CO_2 of the corresponding $M_{\theta e}$ band too high. We also show the 1σ uncertainty of these corrections (± values), which are calculated as the standard deviation of the correction of four models for each campaign or sub-campaign and $M_{\theta e}$ band.

Campaign (sub-campaign)	$M_{\theta_e}(10^{16}$ kg) band			
	0-15	15-30	30-45	45-60
HIPPO1	0.01±0.06	0.02±0.09	0.02±0.06	-0.07±0.06
HIPPO2	0.00±0.09	0.06±0.02	0.09±0.04	-0.04±0.06
HIPPO3	0.23±0.08	0.22±0.03	0.18±0.02	0.03±0.06
HIPPO4	/	0.13±0.08	0.09±0.07	0.00±0.05
HIPPO5	0.03±0.03	0.12±0.07	0.21±0.07	0.23±0.09
ORCAS1	0.05±0.07	0.16±0.05	0.18±0.07	-0.09±0.01
ORCAS2	0.05±0.05	-0.14±0.11	-0.07±0.02	-0.26±0.04
ORCAS3	-0.06±0.05	-0.20±0.03	-0.03±0.04	0.02±0.04
ATom1	-0.02±0.06	0.02±0.01	0.07±0.01	0.06±0.08
ATom2	-0.21±0.07	0.00±0.11	-0.09±0.08	-0.11±0.15
ATom3	0.00±0.06	-0.01±0.04	0.00±0.04	-0.10±0.05
ATom4	0.07±0.02	0.13±0.03	0.14±0.05	0.07±0.02

Table 3.7: AR_{10-sec} coefficient (unitless) and 1σ uncertainty (ppm) of random error $\epsilon(t)$ estimated from the autoregressive model for each pair of in situ instruments (detailed in SI Appendix, Text 3.7.2.1). Here we only show the mean values for each campaign, averaged from all flights of the campaign. We note that the variability of parameters within a campaign is generally small.

Campaign (sub-campaign)	Instrument					
	AO2 - QCLS		AO2 - OMS		AO2 - NOAA Picarro	
	$AR_{10\text{-sec}}$	1σ of $\epsilon(t)$	$AR_{10\text{-sec}}$	1σ of $\epsilon(t)$	$AR_{10\text{-sec}}$	1σ of $\epsilon(t)$
HIPPO1	0.85	0.41	0.83	0.44		
HIPPO2	0.83	0.43	0.83	0.47		
HIPPO3	0.82	0.44	0.84	0.46		
HIPPO4	0.80	0.45	0.82	0.46		
HIPPO5	0.82	0.47	0.82	0.48		
ORCAS1	0.83	0.27			0.83	0.27
ORCAS2	0.85	0.30			0.83	0.26
ORCAS3	0.85	0.29			0.85	0.29
ATom1	0.77	0.47			0.74	0.47
ATom2	0.79	0.51			0.79	0.52
ATom3	0.84	0.28			0.83	0.27
ATom4	0.81	0.27			0.82	0.27

Table 3.8: 1σ Interannual variability (IAV, PgC yr^{-1}) of air-sea CO_2 flux for each $M_{\theta e}$ band and each airborne campaign or sub-campaign, as suggested by the MIROC-ACTM model. IAV is calculated as detailed in *SI Appendix*, Text 3.7.2.2.

Campaign	M_{θ_e} (10^{16} kg) band		
	0-15	15-30	30-45
HIPPO1	0.090	0.042	0.044
HIPPO2	0.062	0.032	0.023
HIPPO3	0.076	0.038	0.039
HIPPO4	/	0.049	0.032
HIPPO5	0.085	0.045	0.045
ORCAS1	0.091	0.043	0.045
ORCAS2	0.076	0.027	0.024
ORCAS3	0.071	0.024	0.023
ATom1	0.090	0.048	0.048
ATom2	0.077	0.026	0.023
ATom3	0.083	0.043	0.026
ATom4	0.064	0.037	0.041

3.7.8 Reference of Supporting Information

1. Elorrieta, F., Eyheramendy, S., & Palma, W. (2019). Discrete-time autoregressive model for unequally spaced time-series observations. *Astronomy and Astrophysics*, *627*, A120. https://doi.org/10.1051/0004-6361/201935560

2. Sweeney, C., Karion, A., Wolter, S., Newberger, T., Guenther, D., Higgs, J. A., et al. (2015). Seasonal climatology of CO_2 across North America from aircraft measurements in the NOAA/ESRL Global Greenhouse Gas Reference Network. *Journal of Geophysical Research : Atmospheres*, *120*(10), 5155–5190. https://doi.org/https://doi.org/10.1002/2014JD022591

3. Stephens, B. B., Morgan, E. J., Bent, J. D., Keeling, R. F., Watt, A. S., Shertz, S. R., & Daube, B. C. (2021). Airborne measurements of oxygen concentration from the surface to

the lower stratosphere and pole to pole. *Atmospheric Measurement Techniques*, *14*(3), 2543–2574. https://doi.org/10.5194/amt-14-2543-2021

4. Takahashi, T., Sutherland, S. C., Wanninkhof, R., Sweeney, C., Feely, R. A., Chipman, D. W., et al. (2009). Climatological mean and decadal change in surface ocean pCO_2, and net sea-air CO_2 flux over the global oceans. *Deep-Sea Research Part II: Topical Studies in Oceanography*, *56*(8–10), 554–577. https://doi.org/10.1016/j.dsr2.2008.12.009

5. Reynolds, R. W., Rayner, N. A., Smith, T. M., Stokes, D. C., & Wang, W. (2002). An improved in situ and satellite SST analysis for climate. *Journal of Climate*, *15*(13), 1609–1625. https://doi.org/10.1175/1520-0442(2002)015<1609:AIISAS>2.0.CO;2

6. Robbins, L. L., Hansen, M. E., Kleypas, J. A., & Meylan, S. C. (2010). CO2calc: A user-friendly carbon calculator for Windows , Mac OS X , and iOS (iPhone). *U.S. Geological Survey*, 17. Retrieved from https://pubs.usgs.gov/of/2010/1280/pdf/ofr_2010-1280.pdf%0Ahttps://pubs.er.usgs.gov/publication/ofr20101280

7. Wanninkhof, R. (1992). Relationship between wind speed and gas exchange over the ocean revisited. *Limnology and Oceanography: Methods*, *97*(C5), 7373–7382. https://doi.org/10.4319/lom.2014.12.351

8. Gelaro, R., McCarty, W., Suárez, M. J., Todling, R., Molod, A., Takacs, L., et al. (2017). The Modern-Era Retrospective Analysis for Research and Applications, Version 2 (MERRA-2). *Journal of Climate*, *30*(14), 5419–5454. https://doi.org/10.1175/JCLI-D-16-0758.1

9. Jin, Y., Keeling, R., Morgan, E., Ray, E., Parazoo, N., & Stephens, B. (2021). A mass-weighted atmospheric isentropic coordinate for mapping chemical tracers and computing

inventories. *Atmospheric Chemistry and Physics*, *21*, 217–238. https://doi.org/10.5194/acp-2020-841

10. Zondlo, M. A., Paige, M. E., Massick, S. M., & Silver, J. A. (2010). Vertical cavity laser hygrometer for the National Science Foundation Gulfstream-V aircraft. *Journal of Geophysical Research Atmospheres*, *115*, D20309. https://doi.org/10.1029/2010JD014445

11. Scott, S. G., Bui, T. P., Chan, K. R., & Bowen, S. W. (1990). The meteorological measurement system on the NASA ER-2 aircraft. *Journal of Atmospheric & Oceanic Technology*, *7*(4), 525–540. https://doi.org/10.1175/1520-0426(1990)007<0525:tmmsot>2.0.co;2

12. Diskin, G. S., Podolske, J. R., Sachse, G. W., & Slate, T. A. (2002). Open-path airborne tunable diode laser hygrometer. *Diode Lasers and Applications in Atmospheric Sensing*, *4817*, 196–204. https://doi.org/10.1117/12.453736

13. Bakker, D. C. E., Pfeil, B., Smith, K., Hankin, S., Olsen, A., Alin, S. R., et al. (2014). An update to the surface ocean CO_2 atlas (SOCAT version 2). *Earth System Science Data*, *6*(1), 69–90. https://doi.org/10.5194/essd-6-69-2014

14. Rödenbeck, C., Bakker, D. C. E., Metzl, N., Olsen, A., Sabine, C., Cassar, N., et al. (2014). Interannual sea-air CO_2 flux variability from an observation-driven ocean mixed-layer scheme. *Biogeosciences*, *11*(17), 4599–4613. https://doi.org/10.5194/bg-11-4599-2014

15. Johnson, K. S., Plant, J. N., Coletti, L. J., Jannasch, H. W., Sakamoto, C. M., Riser, S. C., et al. (2017). Biogeochemical sensor performance in the SOCCOM profiling float array. *Journal of Geophysical Research: Oceans*, *122*(8), 6416–6436. https://doi.org/10.1002/2017JC012838

16. Landschützer, P., Gruber, N., Bakker, D. C. E., & Schuster, U. (2014). Recent variability of the global ocean carbon sink. *Global Biogeochemical Cycles*, *28*(9), 927–949. https://doi.org/10.1111/1462-2920.13280

17. Landschützer, Peter, Bushinsky, S. M., & Gray, A. R. (2019). A combined globally mapped carbon dioxide (CO_2) flux estimate based on the Surface Ocean CO_2 Atlas Database (SOCAT) and Southern Ocean Carbon and Climate Observations and Modeling (SOCCOM) biogeochemistry floats from 1982 to 2017 (NC. https://doi.org/10.25921/9hsn-xq82.

18. Landschützer, P., Gruber, N., & Bakker, D. C. E. (2020). *An observation-based global monthly gridded sea surface pCO_2 product from 1982 onward and its monthly climatology (NCEI Accession 0160558). Version 5.5. NOAA National Centers for Environmental Information. Dataset. https://doi.org/10.7289/V5Z89*.

19. Bushinsky, S. M., Landschützer, P., Rödenbeck, C., Gray, A. R., Baker, D., Mazloff, M. R., et al. (2019). Reassessing Southern Ocean Air-Sea CO_2 Flux Estimates With the Addition of Biogeochemical Float Observations. *Global Biogeochemical Cycles*, *33*(11), 1370–1388. https://doi.org/10.1029/2019GB006176

20. Friedlingstein, P., O'Sullivan, M., Jones, M. W., Andrew, R. M., Hauck, J., Olsen, A., et al. (2020). Global Carbon Budget 2020. *Earth System Science Data*, *12*(4), 3269–3340. https://doi.org/10.5194/essd-12-3269-2020

21. Hauck, J., Zeising, M., Le Quéré, C., Gruber, N., Bakker, D. C. E., Bopp, L., et al. (2020). Consistency and Challenges in the Ocean Carbon Sink Estimate for the Global Carbon Budget. *Frontiers in Marine Science*, *7*, 571720. https://doi.org/10.3389/fmars.2020.571720

22. Long, M. C., Stephens, B. B., McKain, K., Sweeney, C., Keeling, R. F., Kort, E. A., et al. (2021). Strong Southern Ocean carbon uptake evident in airborne observations. *Science*, *374*(6572), 1275–1280. https://doi.org/10.1126/science.abi4355

23. Rödenbeck, C., Houweling, S., Gloor, M., & Heimann, M. (2003). CO_2 flux history 1982–2001 inferred from atmospheric data using a global inversion of atmospheric transport. *Atmospheric Chemistry and Physics*, *3*, 1919–1964. https://doi.org/10.5194/acp-3-1919-2003

24. Jacobson, A. R., Schuldt, K. N., Miller, J. B., Oda, T., Tans, P., Andrews, A., & J. Mund, L. Ott, G. J. Collatz, T. Aalto, S. Afshar, K. Aikin, S. Aoki, F. Apadula, B. Baier, P. Bergamaschi, A. Beyersdorf, S. C. Biraud, A. Bollenbacher, D. Bowling, G. Brailsford, J. B. Abshire, G. Chen, H. Chen, L. Chmura, Sites Climadat, A. Colomb, S, and M. Z. (2020). CarbonTracker CT2019B. https://doi.org/10.25925/20201008

25. Chevallier, F. (2013). On the parallelization of atmospheric inversions of CO_2 surface fluxes within a variational framework. *Geoscientific Model Development*, *6*(3), 783–790. https://doi.org/10.5194/gmd-6-783-2013

26. Chevallier, F., Fisher, M., Peylin, P., Serrar, S., Bousquet, P., Bréon, F. M., et al. (2005). Inferring CO_2 sources and sinks from satellite observations: Method and application to TOVS data. *Journal of Geophysical Research Atmospheres*, *110*, D24309. https://doi.org/10.1029/2005JD006390

27. Chevallier, F., Ciais, P., Conway, T. J., Aalto, T., Anderson, B. E., Bousquet, P., et al. (2010). CO_2 surface fluxes at grid point scale estimated from a global 21 year reanalysis of atmospheric measurements. *Journal of Geophysical Research Atmospheres*, *115*, D21307.

https://doi.org/10.1029/2010JD013887

28. Chandra, N., Patra, P. K., Niwa, Y., Ito, A., Iida, Y., Goto, D., et al. (2022). Estimated regional CO_2 flux and uncertainty based on an ensemble of atmospheric CO_2 inversions. *Atmospheric Chemistry and Physics*, *22*(14), 9215–9243. https://doi.org/10.5194/acp-22-9215-2022

Chapter 4 Impact of Changing Winds on the Mauna Loa CO_2 Seasonal Cycle in Relation to the Pacific Decadal Oscillation

Abstract

Long-term measurements at the Mauna Loa Observatory (MLO) show that the CO_2 seasonal cycle amplitude (SCA) increased from 1959 through 2019 at an overall rate of 0.22 ± 0.034 ppm decade^{-1} while also varying on interannual to decadal time scales. These SCA changes are a signature of changes in land ecological CO_2 fluxes as well as shifting winds. Simulations with the TM3 tracer transport model and CO_2 fluxes from the Jena CarboScope CO_2 inversion suggest that shifting winds alone have contributed to a decrease in SCA of -0.10 ± 0.022 ppm decade^{-1} from 1959 to 2019, partly offsetting the observed long-term SCA increase associated with enhanced ecosystem net primary production. According to these simulations and MIROC-ACTM simulations, the shorter-term variability of MLO SCA is nearly equally driven by varying ecological CO_2 fluxes (49%) and varying winds (51%). We also show that the MLO SCA is strongly correlated with the Pacific Decadal Oscillation (PDO) due to varying winds, as well as with a closely-related wind index (U-PDO). Since 1980, 44 % of the wind-driven SCA decrease has been tied to a secular trend in the U-PDO, which is associated with a progressive weakening of westerly winds at 700mbar over the central Pacific from 20°N to 40°N. Similar impacts of varying winds on the SCA are seen in simulations at other low-latitude Pacific stations, illustrating the difficulty of constraining trend and variability of land CO_2 fluxes using observations from low latitudes due to the complexity of circulation changes.

Plain Language Summary

The CO_2 seasonal amplitude is an indicator of the growing season productivity of land ecosystems. CO_2 observation at Mauna Loa Observatory (MLO) showed an increasing amplitude from 1959 through 2019, probably due to significantly enhanced productivity over the Eurasia

temperate and boreal forest. In this study, we show that about a third of this observed amplitude increase at MLO was offset by long-term circulation changes, which isolated the air at low latitudes from the influence of northern high-latitude ecosystems. This wind-driven impact is also important at other low latitude Pacific stations. The CO_2 seasonal amplitude at MLO also has considerable short-term variability (on the scale of multiple years to decades), roughly half of which is regulated by the changing winds, while the remaining half is driven by the variability of ecological CO_2 fluxes. We show that the wind influence is closely associated with a climate index known as the Pacific Decadal Oscillation. Our study indicates that the attribution of amplitude changes at low latitudes stations to ecosystem changes is complicated by wind shifts.

4.1 Introduction

In the Northern Hemisphere, the concentration of CO_2 at remote atmospheric stations undergoes a clear seasonal cycle driven mostly by CO_2 uptake and release from the land biosphere (Keeling, 1960; Randerson et al., 1997) as modulated by atmospheric mixing. Since the early 1960s, an increase in the CO_2 seasonal cycle amplitude (SCA) has been observed at surface stations and airborne transects, with a larger relative increase at higher latitudes (Forkel et al., 2016; Graven et al., 2013). At Mauna Loa (MLO, 19.5° N), a ~ 15% increase has been observed from 1959 to the early 2010s, while at northern high-latitude station Barrow (BRW, 71.3° N), the increase of the same time period is ~ 35% (Graven et al., 2013). These long-term amplitude trends (henceforth "trend") are superimposed on considerable interannual to decadal variability (henceforth "variability") (Keeling et al., 1996). For example, at MLO, as shown in Figure 4.1a, the amplitude was relatively constant from 1960 to 1970, and grew by 15% over the 1970s, but then increased by only 5% from 1980 to 2020 with considerable interannual variability.

The SCA increase is an important indicator of enhanced growing-season ecosystem productivity over the northern temperate and boreal forest (Graven et al., 2013; Lin et al., 2020).

Increasing SCA has been used as an emergent constraint on CO_2 fertilization of primary production (Wenzel et al., 2016), which is possible because simulations from land ecosystem models that are coupled with atmospheric transport models attribute much of the simulated SCA increase to CO_2 fertilization (Bastos et al., 2019; Ito et al., 2016; Piao et al., 2017; Zhao et al., 2016). However, most of these coupled models systematically underestimate the SCA increase at high latitudes and in the mid-troposphere (500mbar) from 1960-2010, suggesting that the ecosystem models are missing key mechanisms (Graven et al., 2013; Thomas et al., 2016). Possibilities include underestimating CO_2 fertilization on light-use efficiency (Haverd et al., 2020; Thomas et al., 2016), or underestimating response of changing land carbon cycle to climate change. Early studies which examined SCA changes up until the mid-1990s attributed the SCA increase to enhanced photosynthetic CO_2 uptake due to warming-induced lengthening of the growing season, especially in spring (Keeling et al., 1996; Randerson et al., 1999). In contrast, recent studies focusing on trends after 1990 suggest that the CO_2 uptake has become increasingly limited by water stress tied to continued warming (Lian et al., 2020; Peñuelas et al., 2017; Smith et al., 2021; Wang et al., 2018; Zhang et al., 2020). The SCA trend has likely also been strongly influenced by warming-driven changes in vegetation cover (Forkel et al., 2016; Liu et al., 2020), and changes in agriculture and other land-use changes (Gray et al., 2014; Zeng et al., 2014). Interannual to decadal climate change, including soil temperature and water supply availability, has been suggested as a major source of SCA variability (Buermann et al., 2007).

Our ability to infer changes in growing-season productivity or constrain CO_2 fertilization from changes in SCA may be complicated, however, by variations in atmospheric circulation. Taguchi et al. (2003) and Lintner et al. (2006) found that the MLO SCA is sensitive to the interannual variations in the airflow from Siberia, where the biospheric CO_2 signal is especially

strong. Murayama et al. (2007) found significant year-to-year variabilities of the seasonal cycle at two high-latitude stations (BRW and Alert) caused by changing atmospheric circulation alone. Higuchi et al. (2002) showed that atmospheric transport alone produced significant variations in SCA on interannual to quasi-decadal timescales at both MLO and at high-latitude station BRW. Wang et al. (2020) showed that, since 1959, MLO has become more influenced by CO_2 exchanges from Amazonia, which could be connected with an expansion of the Hadley Cell in the Southern Hemisphere. These studies, which explore the connection between SCA changes and atmospheric circulation, however, did not discuss connections between decadal climate modes and wind influences on SCA, and did not discuss possible impacts of long-term wind shifts within the Northern Hemisphere.

Here we study the contribution of varying winds and varying ecological CO_2 fluxes to the trend and variability of SCA, using surface-to-atmosphere CO_2 fluxes transported by the Atmospheric Tracer Model 3 (TM3, Heimann & Körner, 2003), and the MIROC4.0-based Atmospheric Chemistry-Transport Model (ACTM, Patra et al., 2018). We focus primarily on impacts at MLO, but also briefly examine impacts on other low-latitude stations as well as high-latitude station BRW. For MLO, we examine the correlation between MLO SCA and several climate indices, including the Pacific Decadal Oscillation (PDO, Mantua et al., 1997), a closely-related wind index U-PDO (based on the first EOF of subtropical 700 mbar winds), land temperature and Palmer Drought Severity Index (PDSI). We also examine MLO 10-day back trajectories under different phases of the PDO to better understand transport pathways. We discuss these results in connection with changes in MLO SCA variability and circulation changes on the interannual to decadal scale and the long-term trend. The results highlight the significant role of changing circulation on the variability and SCA trend at MLO as well as other low-latitude

stations, which complicates using SCA at these stations to quantify large-scale ecological changes (e.g., Wenzel et al., 2016).

4.2 Data and Methods

4.2.1 CO_2 observation and its seasonal cycle amplitude

We use monthly averaged atmospheric in situ CO_2 measurements at MLO, from the Scripps CO_2 Program (Keeling et al., 2001). All the missing values from February to April in 1964 are filled by linear interpolation. We compute the seasonal cycle amplitude (SCA) by using the Thoning function following the steps below (Thoning and Tans, 1989):

1. Fit the observed MLO SCA with a cubic polynomial for the trend and 4-harmonics for the climatological seasonal cycle (Eq. 4.1).

$$CO_2(t) = \sum_{i=0}^{i=3} a_i t^i + \sum_{j=1}^{j=4} [b_i \sin(2j\pi t) + c_i \cos(2j\pi t)] + \sigma(t) \quad (4.1)$$

where t is the decimal year; a_i are coefficients for the long-term trend; b_j and c_j are coefficients for the climatological seasonal cycle; and $\sigma(t)$ is the residual term.

2. Apply a Butterworth band-pass filter to the residual ($\sigma(t)$) with 90- and 540-day cutoffs.

3. Compute the seasonal amplitude of the sum of the harmonic and band-passed residual, using the peak and trough values for each calendar year.

We note that our choice of parameters is slightly different compared to the default setup of the Thoning function, but the impact on calculated SCA is negligibly small with RMSE of 0.023 ppm from 1959 to 2019. We then compute the long-term growth rate (ppm decade^{-1}) of CO_2 SCA using generalized least-square (GLS) regression (Fox & Weisberg, 2019; Pinheiro et al., 2021). We choose this method in order to address serial correlation, as we find significant first-order autocorrelation of the SCA time series suggested by partial autocorrelation function.

4.2.2 Modeled MLO CO_2 seasonal cycle

We simulate CO_2 concentrations at MLO using two models. The first model is the global Atmospheric Tracer Model 3 (TM3, Heimann and Körner, 2003), which was run at 5° in longitude and 4° in latitude with 19 vertical levels, using 6-hourly NCEP/NCAR reanalysis meteorological fields (Kalnay et al., 1996) from 1951 to 2019, and surface fluxes from the Jena CarboScope CO_2 Inversion (version ID: s57Xoc_v2020, Rödenbeck et al., 2003; 2018a). The first six years (1951 to 1956) are model spin-up period. The inversion only uses available CO_2 observations from 4 stations (MLO, BRW, La Jolla, and South Pole) over the period of 1958 to 2019. We use two TM3 simulations: one driven by year-to-year variations in both winds and fluxes (Jena-WF), and one driven by year-to-year varying winds but climatological average cyclostationary fluxes from 1957 to 2019 (Jena-W). The difference between Jena-WF and Jena-W is referred to as Jena-F, which can approximate the impact of varying ecological CO_2 fluxes alone on the variability and trend of MLO SCA. On average, Jena-WF overestimates the MLO SCA by 5% compared to the observation. To correct for this systematic offset, we scale these simulated SCA (Jena-WF, Jena-W, and Jena-F) down by 5%. This correction only has a small impact on our analysis, since we primarily focus on the SCA variability relative to each other, and the long-term SCA trend.

In order to account for uncertainties of the transport model and reanalysis wind fields, we also simulate CO_2 with MIRCO-ACTM (Patra et al., 2018). The ACTM model was run at ~2.8° in longitude and ~2.8° in latitude with 67 vertical levels driven by JRA-55 winds (Kobayashi et al., 2015) from 1981 to 2019, with the first four years (1981 to 1984) as model spin-up period. The simulation (ACTM-W) uses cyclostationary fluxes for the ocean from Takahashi et al. (2009), and for the land from CASA (Randerson et al., 1997). It also uses fossil-fuel fluxes from Jones et al. (2021) which vary both by month and by year. The impact of changing fossil-fuel emissions on

MLO SCA is very small (Nevison et al., 2008; Wang et al., 2020). We also found the impact of biomass burning to the MLO SCA is negligibly small in the ACTM simulations.

For the modeled MLO CO_2 time series, we compute seasonal cycle amplitudes and the growth rate of the amplitude using the same approach as for observations (Section 4.2.1).

4.2.3 Climate data

As in Buermann et al. (2007), we compute 11-year moving-window correlations between MLO SCA and several climate indices to understand which time periods show the strongest correlation. These climate indices include PDO, land temperature, and Palmer Drought Severity Index (PDSI), with each time series detrended by removing the long-term linear trend and smoothed by a five-point binomial filter to focus on interannual to decadal variability. The p-value of correlations is computed using 1000 iterations of 2-tail random phase test (Ebisuzaki, 1997).

The monthly PDO index is provided by National Centers for Environmental Information (NCEI) computed from NOAA's extended reconstruction of SSTs (ERSST Version 5) (Huang et al., 2017; Mantua et al., 1997; Zhang et al., 1997). We compute the annual average PDO as the average of the twelve monthly PDO values for each calendar year.

We use the monthly land temperature data at $1° \times 1°$ spatial resolution provided by Berkeley Earth (Muller et al., 2013). We use the monthly Palmer Drought Severity Index (PDSI) index at $0.5° \times 0.5°$ spatial resolution provided by the Climatic Research Unit (Van Der Schrier et al., 2013). We compute the growing-season average land temperature and PDSI as the average from May to October of each year, and an area-weighted average for Eurasia ($LandT_{EU}$, $PDSI_{EU}$) and North America ($LandT_{NA}$, $PDSI_{NA}$). Eurasia is defined as all land within 30°N to 70°N and 120°N to 160°N, while North America is defined as all land between 20°N to 70°N.

We also generate a wind-based climate index, which we call the U-PDO, based on the first EOF of the 700mbar monthly wind field from NCEP/NCAR within the domain of 10°N to 40°N

and 120°E to 100°W (method see Legler (1983) and Appendix Text S1). The U-PDO is the U-wind component (West-East) of this first EOF, as discussed below in Figure 4.4 and section 4.3.3. The choice of 700mbar is to approximate the pressure level of MLO at ~680mbar.

4.2.4 Backward trajectories

We calculate 10-day back trajectories at MLO using the HYSPLIT program (Draxler & Rolph, 2010; Stein et al., 2015) driven by NCEP/NCAR winds every 6 hours from 1985 to 2019 (Kalnay et al., 1996). The choice of 10-day conforms with prior studies of airmass originates at MLO (Harris et al., 1992; Harris & Kahl, 1990; Hess, 1996; Miller, 1981). Particles are released at 19.53°N, 155.58°W, and 3437.00 m.a.s.l.. The vertical motion is forced to be along isentropes. All trajectories that reach above 10000 m altitudes are excluded in our analysis. We compute the fraction of backward trajectories that end above Eurasia or North America on day 10 as a function of the month and the monthly PDO index value.

4.3 Results

4.3.1 Observed and modeled seasonal cycle amplitude at MLO

In Figure 4.1a, we show the observed MLO SCA (1960-2019) compared with simulations using Jena-WF. The Jena-WF model approximates the observed variability well (RMSE = 0.27 ppm, r = 0.86). Over the whole record from 1959 to 2019, Jena-WF simulates a long-term SCA increase of 0.21 ± 0.040 ppm decade^{-1}, close to the observed increase of 0.22 ± 0.034 ppm decade^{-1}. Jena-WF also captures well the slowing of the SCA growth since the mid-1980s and all-time largest amplitudes around 2015-2017. The simulated growth from 1986 to 2019 is 0.14 ± 0.103 ppm decade^{-1}, compared to 0.16 ± 0.095 ppm decade^{-1} from observations.

In Figure 4.1b, we show the two components of MLO SCA, one driven by varying winds alone (Jena-W), and one driven by varying ecological CO_2 fluxes alone (Jena-F). Jena-F shows a persistent increase of SCA over time with a growth rate at 0.31 ± 0.024 ppm decade^{-1} over the

whole record and 0.29±0.086 ppm decade^{-1} since 1986. In contrast, the Jena-W shows a SCA decrease of -0.10±0.022 ppm decade^{-1} over the whole record, accelerating to -0.15±0.057 ppm decade^{-1} after 1986. In comparison, ACTM-W simulates a relatively smaller SCA decrease of -0.09±0.068 ppm decade^{-1} from 1986 to 2019 (see Table 4.1, not shown in Figure). The growth rate of the SCA trend based on observation, Jena-WF, Jena-W, and ACTM-W are also summarized in Table 4.1.

In Figure 4.1c, we show detrended time series for the observations, Jena-WF, Jena-W, and Jena-F, where the detrending involves subtracting a long-term linear trend. Projecting the detrended Jena-W and detrended Jena-F onto the detrended Jena-WF (method see Supplement Text 4.7.2), we find the varying winds alone and varying ecological CO_2 fluxes alone play equal roles in driving the SCA variability from 1959 to 2019, accounting for 51% and 49% of the variability, respectively. The SCA variability explained by winds alone increases slightly to 60% during the period from 1986 to 2019.

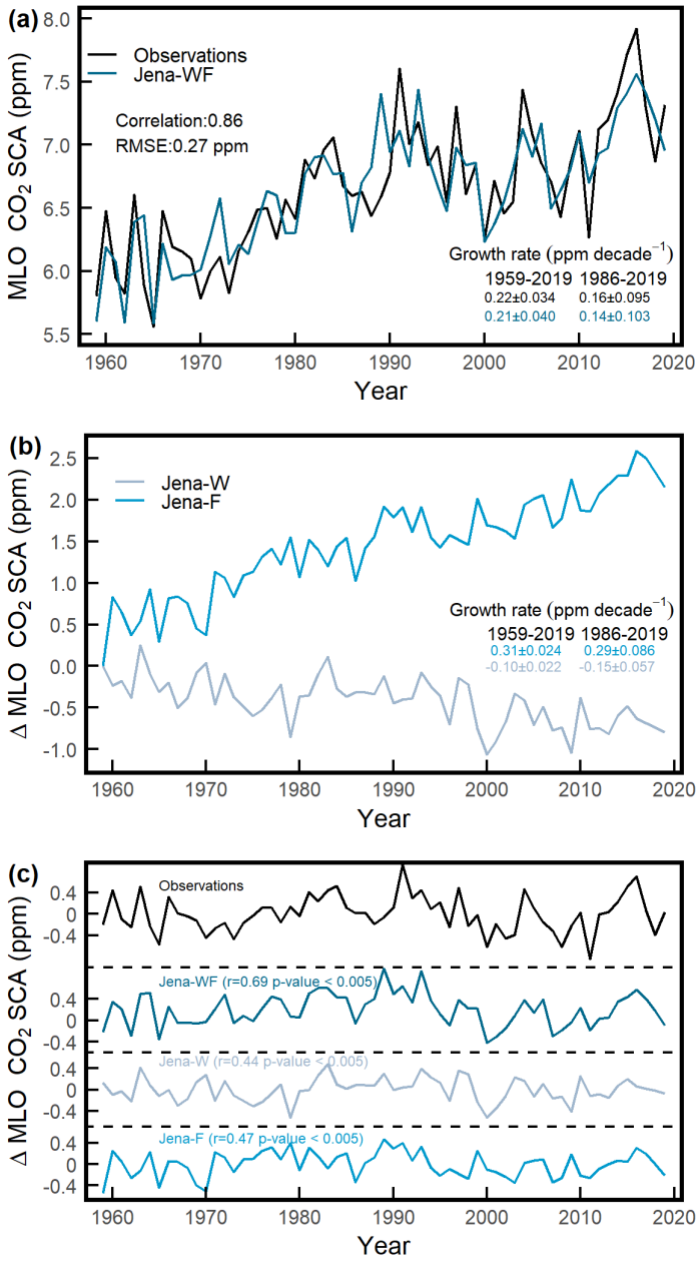

Figure 4.1: (a) Observed MLO SCA and modeled MLO SCA from Jena-WF. The Jena-WF simulation is scaled down by 5% since it systematically overestimates the SCA. (b) Anomalies (reference year 1959) of MLO SCA components simulated by Jena-W and Jena F. Each simulation is scaled down by 5%. The growth rates in (a) and (b) are computed by GLS method (see Section 4.2.1), from 1959 to 2019, and from 1986 to 2019. (c) Anomalies of detrended MLO SCA, simulated and detrended MLO SCA from Jena-WF, Jena-W, and Jena-F. Each time series is detrended by removing its long-term linear trend. We also show the correlation (r) between each detrended simulation and detrended observations, and the corresponding p-value based on 1000 iterations of 2-tailed random phase test of each correlation (Ebisuzaki, 1997).

Table 4.1: Observed and simulated (Jena-WF, Jena-W, and ACTM-W) long-term SCA trends in ppm decade^{-1} at selected stations (methods see Section 4.2.1). Observation data at MLO, BRW, KUM, and CHR are from Scripps CO_2 Program. Observation data at MID are from NOAA ObsPack (Schuldt et al., 2021). Trends are computed using GLS method (see section 4.2.1).

Stations	Years	SCA trend (ppm decade^{-1})			
		Observation	Jena-WF	Jena-W	ACTM-W
Mauna Loa (MLO, 19.5° N, 155.6° W)	1959-2019	0.22±0.034	0.21±0.040	-0.10±0.022	
	1986-2019	0.16±0.095	0.14±0.103	-0.15±0.057	-0.09±0.068
Barrow (BRW, 71.2° N, 156.4° W)	1961-2019	0.81±0.099	0.83±0.076	0.01±0.054	
	1986-2019	0.96±0.183	0.95±0.156	-0.07±0.127	-0.10±0.206
Midway Island (MID, 27.8° N, 176.7 W)	1986-2019	0.53±0.211	0.21±0.101	-0.10±0.051	-0.05±0.072
Cape Kumukahi (KUM, 19.5° N, 154.8° W)	1976-2019	0.19±0.060	0.18±0.043	-0.08±0.047	
	1986-2019	0.24±0.071	0.19±0.072	-0.10±0.081	-0.05±0.061
Christmas Island (CHR, 2.0° N, 157.3° W)	1975-2019	0.06±0.104	0.05±0.049	-0.06±0.031	
	1986-2019	0.05±0.137	0.02±0.062	-0.04±0.036	-0.01±0.082

4.3.2 Correlation between MLO CO_2 seasonal cycle amplitude and climate indices

To understand the sources of variability of MLO SCA, we examine the correlation between the observed MLO SCA and a suite of climate indices in Figure 4.2. This analysis duplicates the method of Buermann et al. (2007), but updates to 2019 and adds PDO and U-PDO to the suite of indices. Over the full record from 1959 to 2019, the correlation with PDO ($r = 0.71$, p-value < 0.005) and U-PDO ($r = 0.52$, p-value < 0.005) are both relatively strong. A marginally significant correlation is also found between MLO SCA and $PDSI_{NA}$ ($r = 0.42$, p-value $= 0.021$). There is no significant correlation between MLO SCA and other climate indices ($PDSI_{EU}$, $LandT_{EU}$, and $LandT_{NA}$).

The moving-window correlation with the PDO remains uniformly high ($r \gtrsim 0.5$) throughout the record, except for the period from 1984 to 1995. The correlation with U-PDO shows similar time variations. There is no persistent high correlation between MLO SCA and other

climate indices. As noted in Buermann et al. (2007), the correlation between the MLO SCA and $PDSI_{NA}$ increased after the late 1970s, with a high correlation found from 1980 to 1990, from 1995 to 2004. Our analysis also shows that correlation with the $PDSI_{NA}$ is similarly high over the recent period from 2011 to 2019.

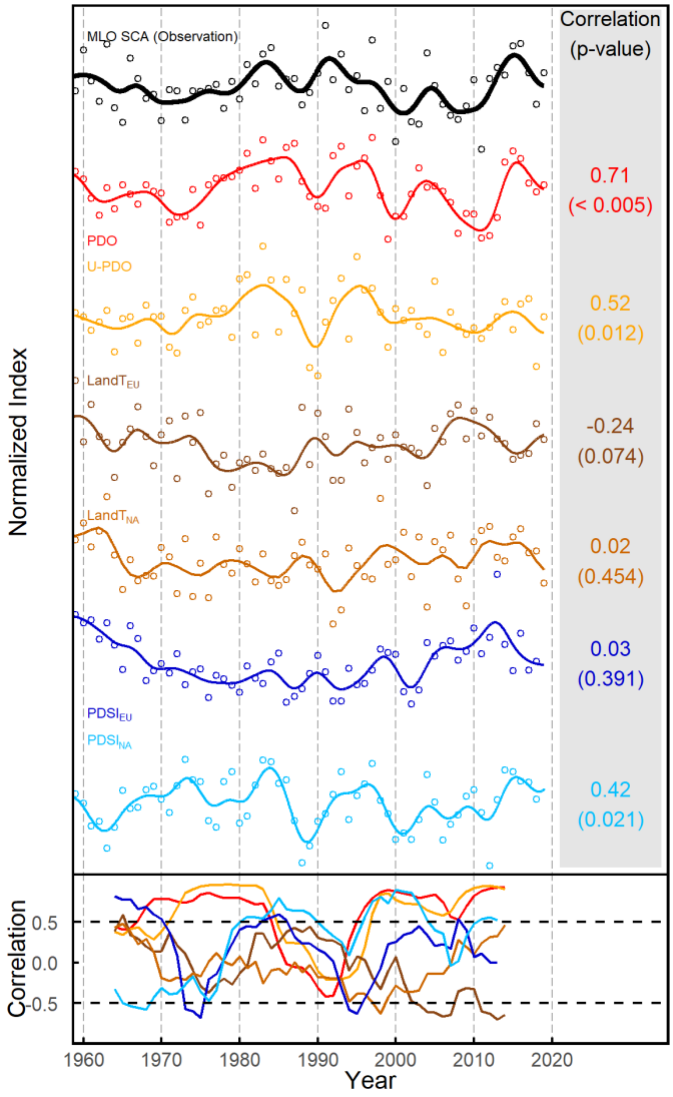

Figure 4.2: Correlations between MLO SCA (observation), and various climate indices: annual average PDO, annual average U-PDO, annual growing season (May to October) average land temperature, and Palmer Drought Severity Index (PDSI) over the Eastern Eurasia ($LandT_{EU}$, $PDSI_{EU}$) and Northern America ($LandT_{NA}$, $PDSI_{NA}$). Eastern Eurasia is defined as 30°N to 70°N and 120°N to 160°N over the Eurasia land while North America is defined as 20°N to 70°N over the North America land. Each time series (points) is first detrended by removing the long-term linear trend and normalized by its standard deviation. We also smooth each time series using a five-point binomial filter, shown as curves. We compute the correlation between each smoothed time series and MLO SCA (observation) in the right of the upper panel, while the p-value is computed by 1000 iterations of 2-tailed random phase test (Ebisuzaki, 1997). In the bottom, we show the 11-year moving window correlation between each smoothed time series and MLO SCA (observation). The moving-window correlations are plotted by using the same color assignments as in the upper panel. The correlation and moving-window correlation between MLO SCA (Observation) and land temperature is computed with land temperature leading by 1 year, following Keeling et al. (1996). Black dashed lines in the lower panel denote the ± 0.5 value.

4.3.3 Correlation between components of amplitude variability and PDSI or PDO

To address whether the SCA-$PDSI_{NA}$ and SCA-PDO correlations are flux- or wind-driven, we examine the separate correlations with ACTM-W, Jena-W, and Jena-F, as shown in Figure 4.3. Each time series is detrended, normalized, and smoothed, using the same method as described in section 4.3.2. As shown in Figure 4.3a, we find a high correlation between PDO and ACTM-W ($r = 0.68$, p-value = 0.007), and Jena-W ($r = 0.73$, p-value = 0.008), showing the importance of wind-shifts in driving variability in SCA associated with the PDO. The correlation between PDO and Jena-W is stronger since 1980 ($r = 0.89$, p-value < 0.005). The 11-year moving-window correlation in the lower panel of Figure 4.3a suggests that the connection between PDO and Jena-W is relatively low before 1977 and around 1990, while the connection between PDO and ACTM-W is relatively low before 1993 and from 2003 to 2009. The PDO index shows a relatively weak correlation between Jena-F at 0.31 (p-value = 0.142), as in Figure 4.3a. The 11-year moving-window correlation (lower panel of Figure 4.3a) switches between positive and negative, with a positive high correlation only found around 1975 and since 2008, and a negative high correlation found from 1979 to 1994. Replacing PDO with U-PDO, the moving-window correlations between ACTM-W, Jena-W, and Jena-F are very similar (Figure 4.7).

As shown in Figure 4.3b, we do not find a high correlation between $PDSI_{NA}$ with either Jena-W ($r = 0.29$, p-value = 0.302) or Jena-F ($r = 0.06$, p-value = 0.958) over the full record from 1959 to 2018. However, the 11-year moving-window correlation in the bottom panel suggests a relatively tight connection between Jena-W and $PDSI_{NA}$ around 1980, around 1990, from 1995 to 2005, and from 2009 onward. We also find a relatively high correlation between $PDSI_{NA}$ and ACTM-W ($r = 0.56$, p-value = 0.041) from 1986 to 2018, with a relatively low connection before 1995.

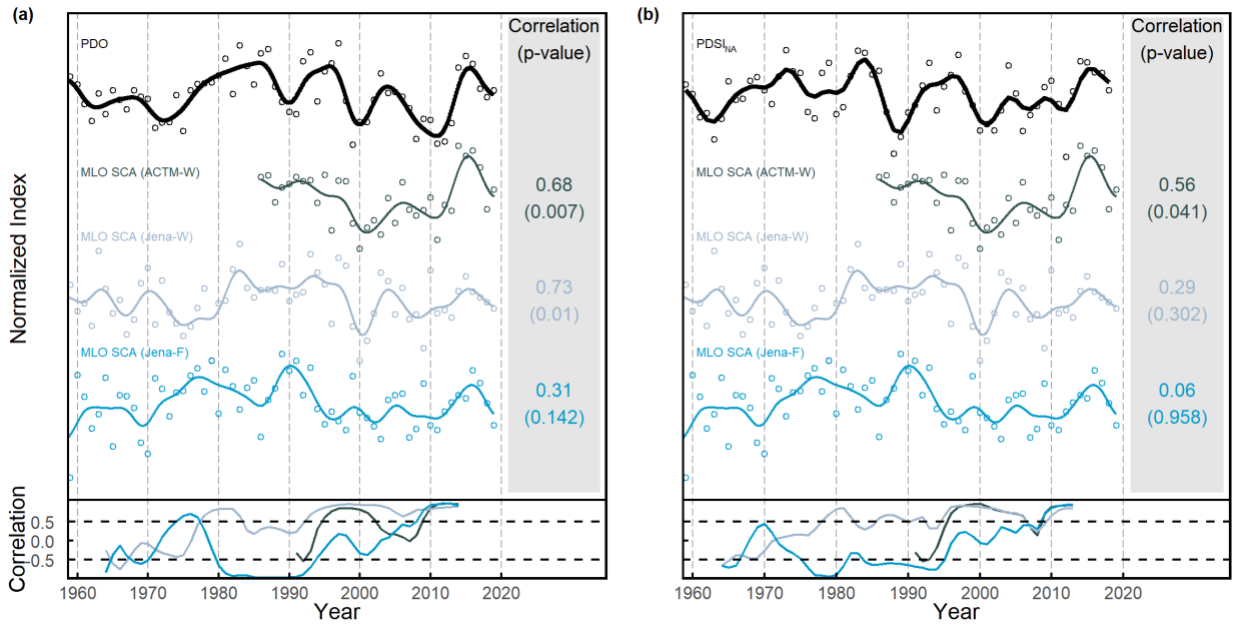

Figure 4.3: Correlations between (a) annual average PDO or (b) between $PDSI_{NA}$ and various decompositions of the MLO SCA variations: modeled MLO SCA from ACTM-W, Jena-W, and Jena-F. Each time series is detrended, normalized, and smoothed using the same method in Figure 4.2. We compute the correlation between each smoothed time series and the corresponding target (thick black curve) in the right of the upper panel. The target is annual average PDO in (a), and $PDSI_{NA}$ in (b). The p-value of the correlation is computed by 1000 iterations of two-tailed random phase test (Ebisuzaki, 1997). In the bottom panel, we show the 11-year moving window correlation between each smoothed time series and corresponding target (thick black curve in the upper panel). The moving-window correlations are plotted by using the same color assignments as in the upper. Black dashed lines in the lower panel denote the ± 0.5 value.

4.3.4 Large-scale wind-patterns associated with PDO variability

To explore the mechanism by which wind shifts impact the MLO SCA variability in association with the PDO, we examine the related U-PDO index, defined based on the first EOF of the Pacific wind field at 700mbar (Section 4.2.3). The spatial pattern of the wind EOF is shown in Figure 4.4a and the temporal variations are shown in Figure 4.4b. The temporal variation demonstrates a very close association between the U-PDO and the PDO ($r = 0.83$, p-value < 0.005). The high temporal variability of the east-west (U) component of the EOF (i.e. the U-PDO) shows the importance of shifting zonal wind strength in connection with the PDO. When the PDO and

U-PDO are positive, a stronger westerly anomaly occurs in the domain from 20°N to 40°N, together with a stronger northerly anomaly in the spatial domain west of 160°E but a stronger southerly anomaly in the spatial domain from 130°W to 160°W. This pattern makes MLO more exposed to air transported from Eurasia in a positive PDO year. We note that, around MLO, the flow pattern shows both western and eastern air-mass origins at all times of a year, but generally progresses from more westerly in winter to easterly in summer (Harris et al., 1992; Harris & Kahl, 1990).

Similar insight is found using HYSPLIT back trajectories at Mauna Loa (Figure 4.5 and Figure 4.8), which show a larger Eurasian footprint and smaller North American footprint associated with positive PDO (Figure 4.5 and Figure 4.8). The back-trajectories also resolve seasonality in this pattern. From September to May, the back trajectories favor Eurasian air-mass origins, and from July to August, they favor North American origins. This is true regardless of the phase of the PDO, but the North American influence is strengthened at all seasons during low PDO years, while the Eurasian influence is strengthened from Sept-May during high PDO years. Analysis of individual back trajectories (Figure 4.8) shows that during the winter (DJF) of positive PDO years, most trajectories originate to the west of MLO centered between 20° to 40°N, suggesting strong zonal flow. In contrast, during the winter of negative PDO years, the trajectories originate over a much wider range of latitudes, both north and south. These winters still have a cluster of trajectories from the west, typically following a curved pathway involving eastward flow at higher latitudes (e.g. 30-50°N) and bending south or southwest on the approach to MLO.

The PDO-related wind shifts are closely associated with the strength of the Aleutian Low (Newman et al., 2016), as shown in Figure 4.6. In a positive PDO year (Figure 4.6a), the Aleutian low strengthens and moves equatorward, exposing MLO to the influence of westerly winds. In a

negative PDO year (Figure 4.6b), the Aleutian low shrinks and moves poleward, leaving MLO more exposed to air from North America and the eastern Pacific.

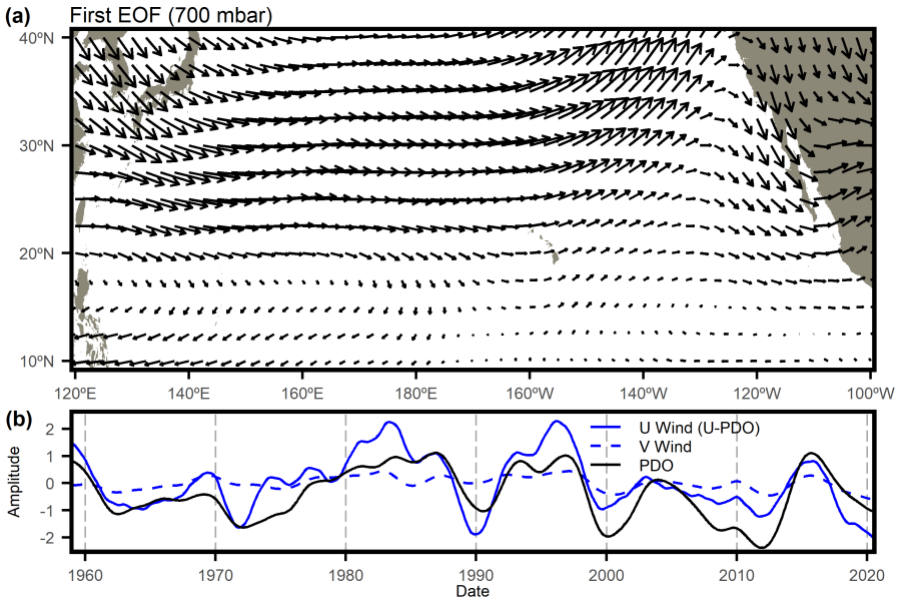

Figure 4.4: (a) Spatial pattern of the first EOF of 700 mbar monthly average wind (NCEP/NCAR) from 1959 to 2020 within the domain of 10°N to 40°N and 120°E to 100°W. (b) Temporal pattern of U (solid blue, U-PDO) and V (dashed blue) winds of the first EOF, and PDO (solid black). Each time series with the monthly resolution is smoothed by a five-point binomial filter and normalized by its standard deviation. A positive amplitude of U wind temporal pattern represents a stronger westerly anomaly in the domain from 20°N to 40°N, while a positive amplitude of V wind temporal pattern represents a stronger northerly anomaly in the spatial domain west of 160°E but a stronger southerly anomaly in the spatial domain from 160°W to 130°W. Normalized monthly PDO (black) smoothed by the same filter are compared here.

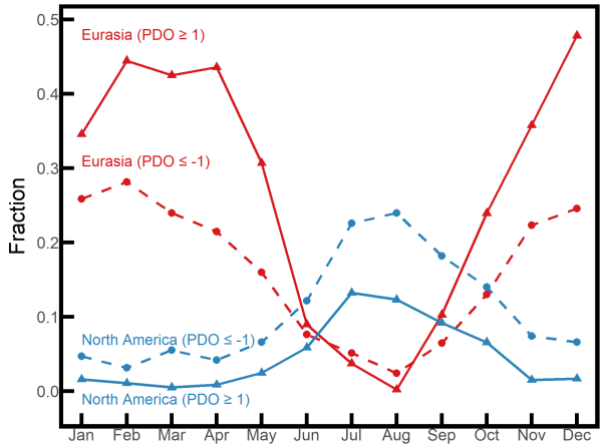

Figure 4.5: Seasonally-varying fraction of MLO 10-day back-trajectories that originate from Eurasia (red) versus North America (blue), sorted by PDO range.

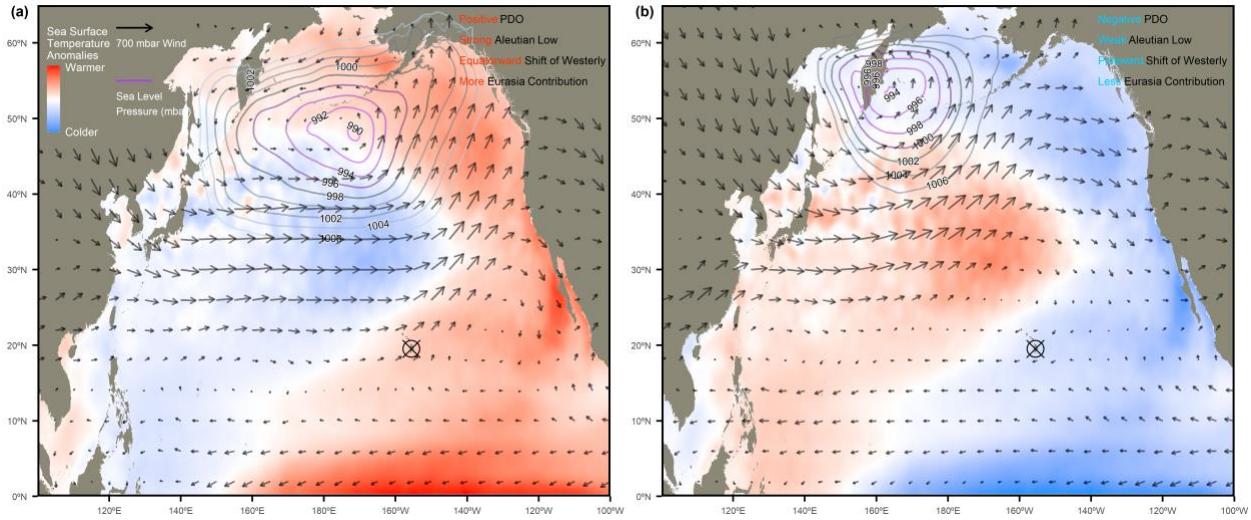

Figure 4.6: (a) Example of a map of climate variables for a positive PDO year (1997). (b) Example of a map of climate variables for a negative PDO year (2008). The North Pacific sea level pressure and 700 mbar winds (not anomalies) are presented as the January average of the corresponding year, while the sea surface temperature anomaly is presented as the spatial pattern of the first EOF of the monthly Pacific sea surface temperature data from 1980 to 2019. Climate data used here are from MERRA-2 (Gelaro et al., 2017). The location of MLO is marked by the circle cross symbol.

4.4 Discussion

4.4.1 The impact of varying winds on the SCA trend

Our analysis allows dividing the observed MLO SCA increase of 0.22±0.034 ppm decade^{-1} (3.3±0.51 % decade^{-1}) from 1959 to 2019 into components driven by variable winds and variable ecological CO_2 fluxes. From winds alone, we find a decreasing trend of -0.10±0.022 ppm decade^{-1} (-1.5±0.33 % decade^{-1}) since 1959 based on Jena-W simulations, offsetting ~30% of the increase of 0.22+0.10 = 0.32 ppm decade^{-1} (4.8 % decade^{-1}) expected from ecological flux changes alone. This decreasing trend accelerates to -0.15±0.057 ppm decade^{-1} from 1986 to 2019. Simulations with ACTM-W suggests a slightly smaller decreasing trend (-0.09±0.068 ppm decade^{-1}) from 1986 to 2019. Over the whole record from 1959 to 2019, our results based on Jena-W show a larger wind effect than found by Wang et al. (2020), who suggested a negligibly small overall trend due to changing winds alone. Over the period from 1986 to 2019, the impacts of wind in our study are

consistent with Wang et al. (2020), who reported a trend of -0.1 to -0.2 ppm decade^{-1}. This wind impact appears to be an important factor contributing to the relatively smaller SCA increase at MLO (low latitude at 19.5°N) compared to BRW (high latitude at 71.2°N), where Jena-W suggests an insignificant wind-induced trend of 0.01 ± 0.054 ppm decade^{-1} (p-value = 0.97 based on Cox-Stuart trend test) from 1961 to 2019. Similarly, ACTM-W suggests an insignificant trend at BRW of -0.07 ± 0.127 ppm decade^{-1} (p-value = 0.83 based on Cox-Stuart trend test) from 1986 to 2019, as shown in Table 4.1. The long-term winds impact at MLO is mostly driven by reduced Eurasia influence, with additional small contributions from reduced North America influence (Figure 4.9).

Wind shifts also lead to a smaller SCA at other low-latitude stations, offsetting the observed increases. As shown in Table 4.1, Jena-W yields similar SCA trends between -0.06 to -0.10 ppm decade^{-1} at the nearby Pacific stations of Midway Island (MID, 27.8° N, 176.7 W) from 1986 to 2019, at Cape Kumukahi (KUM, 19.5° N, 154.8° W) from 1979 to 2019, and at Christmas Island (CHR, 2.0° N, 157.3° W) from 1975 to 2019. Wind shifts thereby offset 16% (at MID), 30% (at KUM), and 50% (at CHR) of the SCA trend expected from ecological flux changes alone. ACTM-W also suggests decreasing SCA from 1986 to 2019 at these three stations, but the magnitude is smaller than that of Jena-W (Table 4.1). We note that, although Jena-WF underestimated the SCA trend at MID by 50% compared to observation (Table 4.1), this discrepancy is not necessarily due to error in winds, as it might alternately result from errors in the CO_2 fluxes fields.

The impact of winds at KUM is of importance in relation to the study of Wenzel et al. (2016), who applied the SCA trend at KUM as an emergent constraint on the magnitude of global CO_2 fertilization effect on gross primary production. However, their study did not evaluate the impact of wind shifts on this constraint.

The long-term wind-driven influence on MLO SCA trend and at other stations may have a connection with a poleward shift and weakening of the subtropical jet stream in the Northern Hemisphere (Archer & Caldeira, 2008). This change leads to a weakened influence of fluxes from northern high latitudes of both Eurasia and North America at MLO (Figure 4.9c). These northern landmasses are the main contributors to the MLO SCA variability and trend (Figure 4.9b), explaining 58.6% of the total SCA variabilities (method see Supplement Text 4.7.2).

The changes of subtropical jet stream are also reflected in the U-PDO index (Figure 4.4). A notable feature of the U-PDO, which is distinct from the PDO, is a stronger downward trend since 1980, which indicates a progressive weakening of westerly anomalies at 700mbar within the domain from 20°N to 40°N. To assess the contribution of the U-PDO index to the long-term wind-driven SCA trend since 1980, we use a simple statistical model $\mathrm{SCA}(\mathrm{year}) = \alpha \cdot \mathrm{year} + \gamma + \beta \cdot \overline{\mathrm{U\text{-}PDO}}(\mathrm{year})$, where $\overline{\mathrm{U\text{-}PDO}}$ is the annual average U-PDO. The parameters are computed using GLS method (similar to Section 4.2.1). The parameter β (0.21 ± 0.105, ppm U-PDO^{-1}) is largely independent of α, indicated by a negligibly small correlation between β and α ($|r| < 0.05$), and the same model with detrended SCA only leads to a slightly smaller β (0.19 ± 0.132 ppm U-PDO^{-1}). Using $\beta = 0.21$, the trend in U-PDO from 1980-2019 yields an SCA trend of -0.07 ± 0.032 ppm decade^{-1} which explains ~ 44 % of the full wind-driven effect estimated by Jena-W over this period. Over the full record from 1959 to 2019, the U-PDO term yields an SCA trend of -0.01 ± 0.041 ppm decade^{-1}, which is not significant.

The poleward shift of the subtropical jet stream is possibly tied to a long-term expansion of the Hadley cell. Wang et al. (2020) argued that a southward expansion of the Hadley cell in the Southern Hemisphere made MLO more influenced by CO_2 fluxes from Amazonia, which reduce the CO_2 SCA at MLO because the phase is approximately opposite of the signal from the northern

hemisphere. Our analysis partly agrees with Wang et al. (2020), but we only find small increasing tropical influence since 2010, as shown in Figure 4.9. Here we suggest that the northward displacement of the northern boundary of the Hadley cell may also have been important (Figure 4.11, method see Text S3 and Adam et al. (2018)), associated with northward displacement of Aleutian Low under greenhouse warming, corresponding to a wider region of easterly trade winds (Gan et al., 2017; Grise et al., 2019; Staten et al., 2019).

One important caveat in our study is the reliability of winds fields and transport models. The Jena-W (based on TM3 transport model and NCEP reanalysis), the ACTM-W (based on MIROC-ACTM model and JRA-55 reanalysis) simulations and the Wang et al. (2020) study all yield slightly different estimates of the wind impact on the MLO SCA trend from 1986 to 2019 (Table 4.1). Even larger uncertainties may apply to our estimated trends from 1959 to 2019, which entirely depends on TM3 and NCEP reanalysis. NCEP might have larger errors before the satellite era starting in 1979 (Bromwich & Fogt, 2004). Although climate models and reanalysis products generally show an expanding Hadley cell in the Southern Hemisphere, the similar expansion in the Northern Hemisphere is highly uncertain, with a larger trend from reanalyses than from model ensemble means (Allen et al., 2014; Allen & Kovilakam, 2017; Grise et al., 2019; Johanson & Fu, 2009; Lu et al., 2007; Staten et al., 2018; Tao et al., 2016).

Will shifting winds continue to contribute to decreasing SCA at low latitudes in the future? The answer may depend on whether the Hadley cell expansion over the past decades has resulted from an internal climate mode or from anthropogenic forcing. This topic remains controversial, with some studies arguing for connection with increasing greenhouse gases (Lu et al., 2007, 2009), and anthropogenic aerosols (Allen et al., 2012, 2014; Allen & Ajoku, 2016), and others pointing

to connections with PDO and ENSO indices (Allen et al., 2014; Allen & Kovilakam, 2017; Amaya et al., 2018; Grassi et al., 2012).

4.4.2 The impact of varying winds on the variability of MLO SCA

We find that varying winds alone contribute significantly (~51%) to the interannual/decadal variability of MLO SCA. Much of the wind-related variability is tied to the PDO, which modulates the relative impact of Eurasian versus North American influences on the MLO SCA variability. Years with high PDO tend to have large Eurasian influence and larger seasonal cycles. This result is consistent with Lintner et al. (2006), who reported that during the months from April to June (near the seasonal CO_2 peak at MLO), synoptic patterns favoring strong Eurasia influence are associated with high springtime CO_2 anomalies, and patterns favoring North American influence are associated with low springtime CO_2 anomalies. Buermann et al. (2007) similarly attributed part of the long-term MLO SCA decreasing in the early 1990s to the progressively declining Eurasia influence in the northern spring. However, neither of these previous studies noted the close association with the PDO. As shown in Figure 4.12 we also find high correlation between MLO SCA and ENSO index (NOAA ONI) in some periods, but not consistently over the whole period from 1959 to 2019. Lintner et al. (2006) suggested that the connection between SCA and ENSO index can be explained by the flow patterns associated with ENSO phases. This connection can also be tied to the PDO phases, as PDO resembles ENSO on the decadal scale.

We find that the contribution from variations in ecological CO_2 fluxes to the PDO-SCA correlation is small, as indicated by the weak correlation between PDO and Jena-F of 0.33 (Figure 4.3b). A relatively weak correlation is expected considering that the changes in land temperature or precipitation/evaporation associated with the PDO are quite heterogeneous in space and time (Figure 4.10).

Our analysis suggests that the controls of winds on the MLO SCA variability were unusually weak during the period from the mid-1980s to the early 1990s. The SCA was low in the late 1980s and higher in the early 1990s. During the 1985-1995 period, the SCA-PDO correlation (Figure 4.3a, r = -0.18, not smoothed) and the SCA-Jena-W correlation (Figure 4.1c, r = -0.03, not smoothed) was unusually weak, while the SCA-Jena-F correlation was relatively stronger (Figure 4.1c, r = 0.45, not smoothed), suggesting that the variability within this period was dominated by fluxes that were not associated with the PDO. A severe drought in North America in 1988 may have reduced the North American contribution to the SCA variability (Schwalm et al., 2012), while the eruption of the Mt. Pinatubo in 1991 may have strengthened summer CO_2 uptake throughout the Northern Hemisphere (Angert et al., 2004; Gu et al., 2003; C. D. Jones & Cox, 2005).

The long-term wind shifts might complicate the attribution of the MLO SCA trend to ecological changes. For example, Buermann et al. (2007) suggested that the decrease or stable SCA trend from 1990 to 2003 was mostly due to more frequent droughts over North America, with additional contributions from wind shifts that led to an overall weakening of spring-time Eurasia influence. Our results partially agree with Buermann et al. (2007), as Jena-F driven by mid-latitude North America fluxes alone (Figure 4.9c) shows decreasing SCA anomalies from 1990 to 2000. Over the long-term, however, Jena-F shows North American fluxes contributing to the overall increasing trend in SCA, with this trend persisting after 2000. Also, we do not find a persistent high correlation between $PDSI_{NA}$ and Jena-F, as shown in Figure 4.3b, but we do find a generally high correlation of $PDSI_{NA}$ with Jena-W since 1980, which is also when $PDSI_{NA}$ show a significant correlation with observed MLO SCA, as in Figure 4.2. This suggests that the higher PDSI-SCA correlation since the mid-1980s (Figure 4.2 and in Buermann et al. (2007)) was not driven primarily by CO_2 fluxes tied to drought but rather by wind variability that happens to be correlated

with the $PDSI_{NA}$. On the other hand, the $PDSI_{NA}$-Jena-F correlation is high after 2008, possibly implying an increased role of hydrological variability after 2008. More generally, Jena-WF shows that the SCA variability is dominated by the Eurasia influence due to both varying winds and varying ecological CO_2 fluxes, with relatively small contributions from North America (Figure 4.9b).

4.5 Summary and conclusion

We find that varying winds alone contribute significantly to the trend and variability of MLO SCA.

Since 1959, the Jena-W simulations suggest that varying winds by themselves caused a downward SCA trend of -0.10 ± 0.022 ppm decade^{-1}, offsetting ~30% of the long-term SCA increase (0.22+0.1=0.32 ppm decade^{-1}) due to ecological CO_2 flux changes alone. The wind-driven decrease simulated by Jena-W accelerated after 1986 to -0.15 ± 0.057 ppm decade^{-1}, while this decrease simulated by ACTM-W since 1986 is relatively smaller at -0.09 ± 0.068 ppm decade^{-1}. Both of these two simulations are consistent within uncertainties to Wang et al. (2020), who reported SCA decreasing between -0.1 to -0.2 ppm decade^{-1} driven by changing circulation alone after 1986. Roughly 44% of the post-1980 downward trend is explained by a secular trend of U-PDO (Figure 4.4b). We also find a wind-driven decreasing tendency in SCA at other low-latitude stations (MID, KUM, and CHR), with Jena-W suggests a larger decrease than ACTM-W (Table 4.1). Whereas Wang et al. (2020) speculated that the wind effect may be related to Hadley cell expansion in the Southern Hemisphere, we suggest a possibly important role of poleward expansion in the Northern Hemisphere, which acts to isolate the air at low latitudes from the influence of northern high-latitude ecosystems.

On interannual/decadal timescales, we find a high correlation between detrended MLO SCA and the annual average PDO index, as well as a closely related wind index, U-PDO. This

high correlation is closely tied to PDO-related wind patterns: (1) In a positive PDO year (Figure 4.6a), the Aleutian Low is stronger and moves equatorward, resulting in a stronger and equatorward-displaced westerly jet over the Pacific which transports air from Eurasia to MLO. (2) In a negative PDO year (Figure 4.6b), the Aleutian Low shrinks and moves poleward and westward, leading to a weaker and poleward-displaced westerly jet, and leaving MLO more exposed to CO_2 transported from North America and the Eastern Pacific.

Our analyses suggest that long-term circulation changes can partly explain the smaller relative SCA growth rate at low latitudes compared to high latitudes, observed at both surface stations and mid-troposphere airborne data, as shown in Graven et al. (2013). Especially at low latitudes, the changing circulation makes it hardto simply relate SCA changes to ecological changes, such as the enhanced magnitude of CO_2 fertilization effect (Wenzel et al., 2016) and North America drought (Buermann et al., 2007).

4.6 Data Availability Statement

CO_2 observations at MLO, KUM, and CHR are available from the Scripps CO_2 Program at https://scrippsco2.ucsd.edu/ (last access: March 15, 2021). CO_2 observations at MID are provided by the NOAA CML cooperative global air sampling network (CO_2 GLOBALVIEWplus v6.1 ObsPack) and downloaded from http://doi.org/10.25925/20201204 (Schuldt et al., 2021).

The monthly PDO index is provided by National Centers for Environmental Information and downloaded from https://www.ncdc.noaa.gov/teleconnections/pdo/ (last access: April 10, 2021) (Huang et al., 2017; Mantua et al., 1997; Zhang et al., 1997). The monthly Oceanic Niño Index (ONI) data are provided by NOAA and downloaded from https://origin.cpc.ncep.noaa.gov/products/analysis_monitoring/ensostuff/ONI_v5.php (last access: Jan 4, 2022). Land temperature data are provided by Berkeley Earth and downloaded from http://berkeleyearth.lbl.gov/auto/Global/Complete_TAVG_complete.txt (last access: October 23,

2020) (Muller et al., 2013). PDSI data are provided by the Climatic Research Unit and downloaded from https://crudata.uea.ac.uk/cru/data/drought/ (last access: August 28, 2020) (Van Der Schrier et al., 2013).

Wind data that are used to conduct EOF analysis are from NCEP/NCAR reanalysis and downloaded from https://psl.noaa.gov/data/gridded/data.ncep.reanalysis.pressure.html (last access: December 10, 2020) (Kalnay et al., 1996).

Simulated CO_2 time series data based on Jena CO_2 inversion and TM3 transport model, and MIROC-ACTM are available from https://doi.org/10.5281/zenodo.5514400.

4.7 Supplement

4.7.1 Empirical orthogonal function (EOF) analysis of winds

Following Legler (1983), the U and V winds components are combined into one vector as a complex number at each geographic location and time step, following

$$W(\lambda, \Phi, t) = U(\lambda, \Phi, t) + iV(\lambda, \Phi, t) \tag{4.2}$$

where λ denotes longitude, Φ denotes latitude, and t denotes a time step.

Elements of $W(\lambda, \Phi, t)$ are organized into a matrix with N ($\lambda \times \Phi$) geographic locations and M time steps,

$$W = \begin{bmatrix} W_{1,1} & \cdots & W_{1,M} \\ \vdots & \ddots & \vdots \\ W_{N,1} & \cdots & W_{N,M} \end{bmatrix} \tag{4.3}$$

The mean values over the full time series at each location (row of matrix W) is subtracted to sharply focus on variability following,

$$W' = W - \overline{W_{N,*}} \tag{4.4}$$

We then apply singular value decomposition to the matrix W', to decompose it into three components, which include the spatial pattern (S), the matrix of singular values (Σ), and the temporal pattern (T), following:

$$W' = S\Sigma T \tag{4.5}$$

with

$$S = \begin{bmatrix} S_{1,1} & \cdots & S_{1,\min(N,M)} \\ \vdots & \ddots & \vdots \\ S_{N,1} & \cdots & S_{N,\min(N,M)} \end{bmatrix} \tag{4.6}$$

$$T = \begin{bmatrix} T_{1,1} & \cdots & T_{1,\min(N,M)} \\ \vdots & \ddots & \vdots \\ T_{M,1} & \cdots & T_{M,\min(N,M)} \end{bmatrix} \tag{4.7}$$

and Σ as a diagonal matrix whose diagonal entries contain the singular values.

Each column in the S and T matrices represents the spatial and temporal pattern of winds W' of the M^{th} EOF. We note that each vector in matrix S and T is a complex number, with the real part as U winds direction and the imaginary part as V winds direction. Therefore, the temporal pattern of the M^{th} EOF of U winds and V winds is represented by the real part of $S_{*,M}$, and the imaginary part of $S_{*,M}$, respectively, with '*' representing the entire column.

4.7.2 Vector projection method

The fractional contributions of either varying winds (Jena-W, x_w) or varying fluxes (Jena-F, x_F) to the overall CO_2 SCA variability (Jena-WF) are computed by using a vector projection method (Graven et al., 2013). In this method, Jena-W or Jena-F is projected onto Jena-WF via:

$$x_W = \frac{\sum_t [\text{Jena-W}(t) \cdot \text{Jena-WF}(t)]}{\sum_t [\text{Jena-WF}(t) \cdot \text{Jena-WF}(t)]} \tag{S8}$$

$$x_F = \frac{\sum_t [\text{Jena-F}(t) \cdot \text{Jena-WF}(t)]}{\sum_t [\text{Jena-WF}(t) \cdot \text{Jena-WF}(t)]} \tag{S9}$$

We note that Jena-W, Jena-F, Jena-WF are pre-detrended and satisfy

$$\text{Jena-WF}(t) = \text{Jena-W}(t) + \text{Jena-F}(t) \tag{S10}$$

4.7.3 North edge of the Hadley cell

We compute the latitude of the Hadley cell north edge using seven commonly-used metrics (see Figure 4.10) following Adam et al. (2018). These calculations yield annual average latitudes, which are based on wind, temperature, and pressure fields from NCEP/NCAR reanalysis data with monthly resolution (Kalnay et al., 1996). A brief description of each method is presented here:

1. PSI: the latitude which the streamfuction at 500 mbar shifts from negative to positive in the Northern Hemisphere.

2. PSL: the latitude with maximum zonal average sea level pressure.

3. TPB: the latitude with maximum poleward zonal average tropopause height decreasing, while tropopause is defined as height with lapse rate decreases to 2K km^{-1}, and remains lower than this between this level and all higher levels within 2 km.

4. STJ: the latitude of the maximum zonal wind difference between upper-level (200 mbar) and lower-level (850 mbar).

5. EDJ: the latitude with the maximum zonal average zonal wind at 850 mbar.

6. UAS: the latitude which zonal wind shifts from easterlies to westerlies at 1000 mbar.

7. OLR: the first latitude which maximum outgoing long-wave radiation drops to 20 W/m^2 below its peak value.

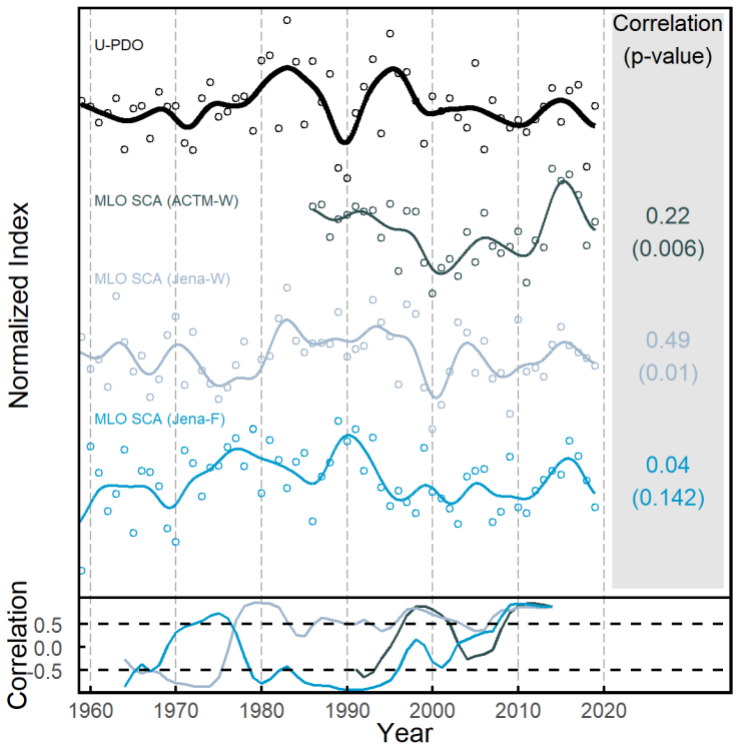

Figure 4.7: Similar to Figure 4.3 but exploring the correlations between annual average U-PDO and various decompositions of the MLO SCA variations: modeled MLO SCA from ACTM-W, Jena-W, and Jena-F. Each time series is detrended, normalized, and smoothed using the same method in Figure 4.2. We compute the correlation between each smoothed time series and U-PDO in the right of the upper panel. The p-value of the correlation is computed by 1000 iterations of two-tailed random phase test (Ebisuzaki, 1997). In the bottom panel, we show the 11-year moving window correlation between each smoothed time series and U-PDO. The moving-window correlations are plotted by using the same color assignments as in the upper. Black dashed lines in the lower panel denote the ± 0.5 value.

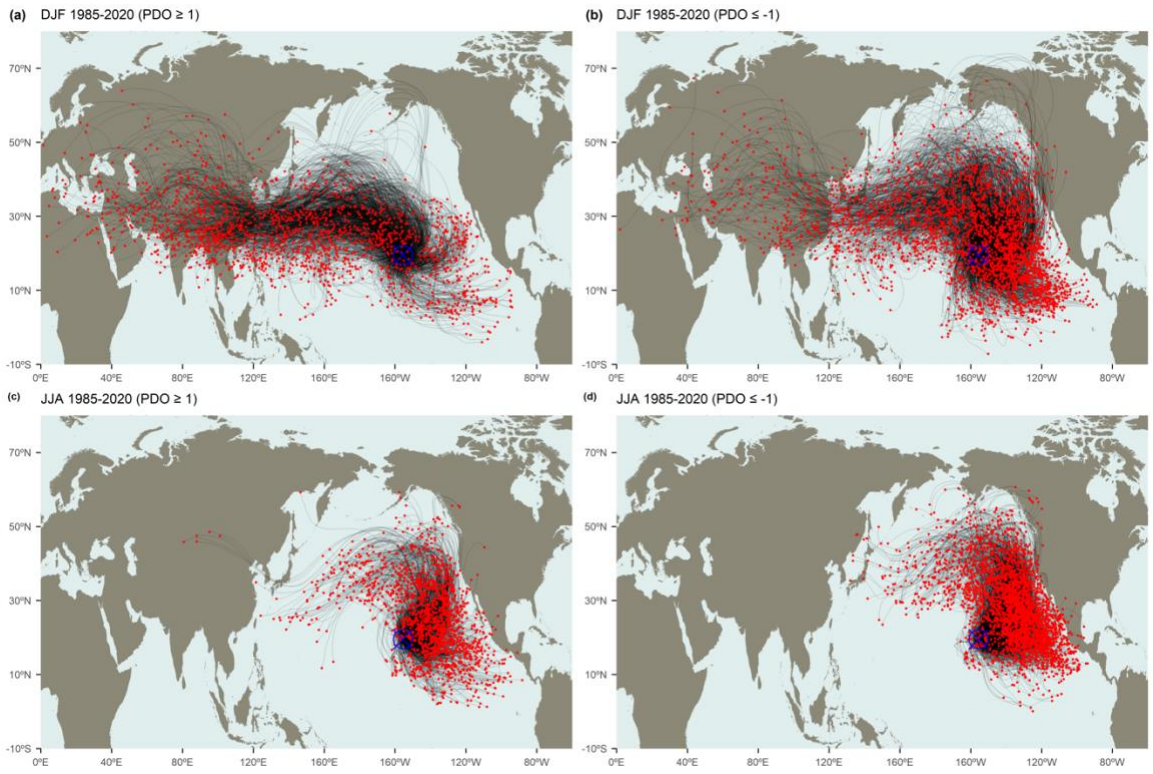

Figure 4.8: HYSPLIT back trajectories of different seasons and PDO phases. (a) DJF of positive PDO years (PDO index ≥ 1), (b) DJF of positive PDO years (PDO index ≤ -1), (c) JJA positive PDO years (PDO index ≥ 1), and (d) JJA of positive PDO years (PDO index ≤ -1).

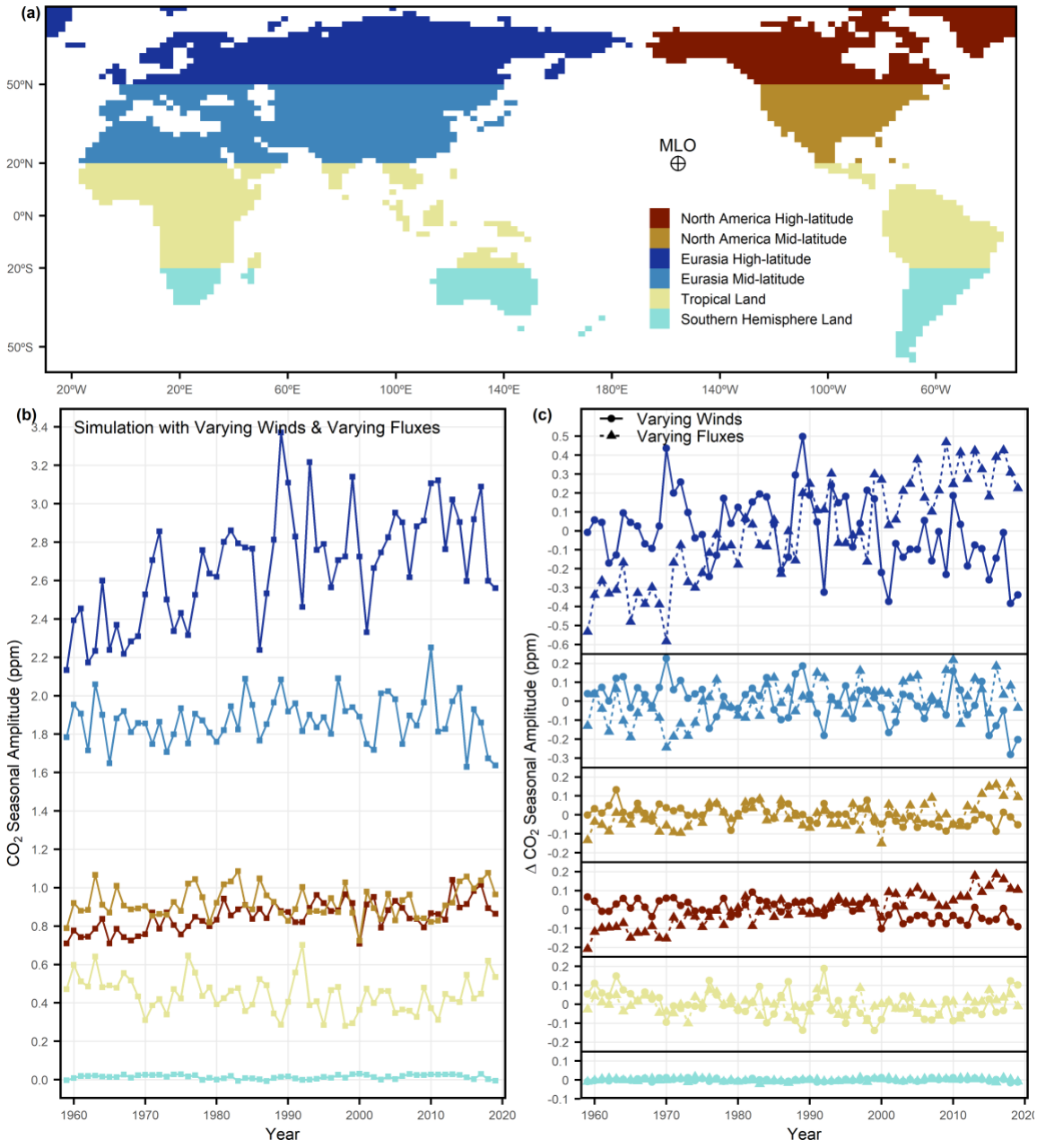

Figure 4.9: Simulated MLO CO_2 seasonal amplitude using fluxes from each tagged region (map in (a)) of Jena CarboScope CO_2 Inversion (version ID: s57Xoc_v2020) transported by TM3 model. We show simulations driven by both varying winds and fluxes in (b) and simulations driven by either varying winds or varying fluxes in (c).

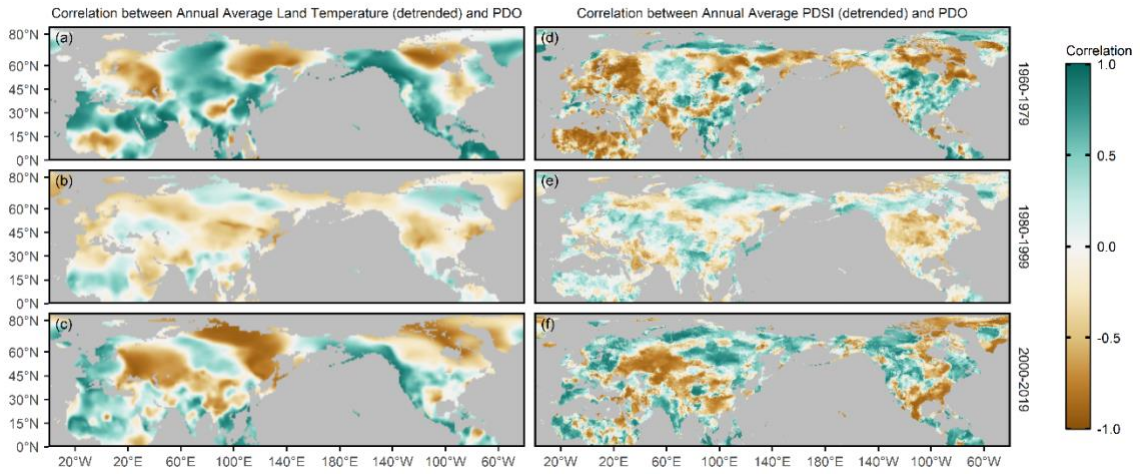

Figure 4.10: Correlation between annual average PDO and land temperature (detrended) within the time slice from (a) 1960 to 1979, (b) 1980 to 1999, and (c) 2000 to 2019. Correlation between annual average PDO and PDSI (detrended) within the time slice from (d) 1960 to 1979, (e) 1980 to 1999, and (f) 2000 to 2019. Land temperature and PDSI are detrended by removing the long-term linear trend for each grid cell. We show that the correlation between PDO and land temperature or PDSI is heterogeneous in time and space.

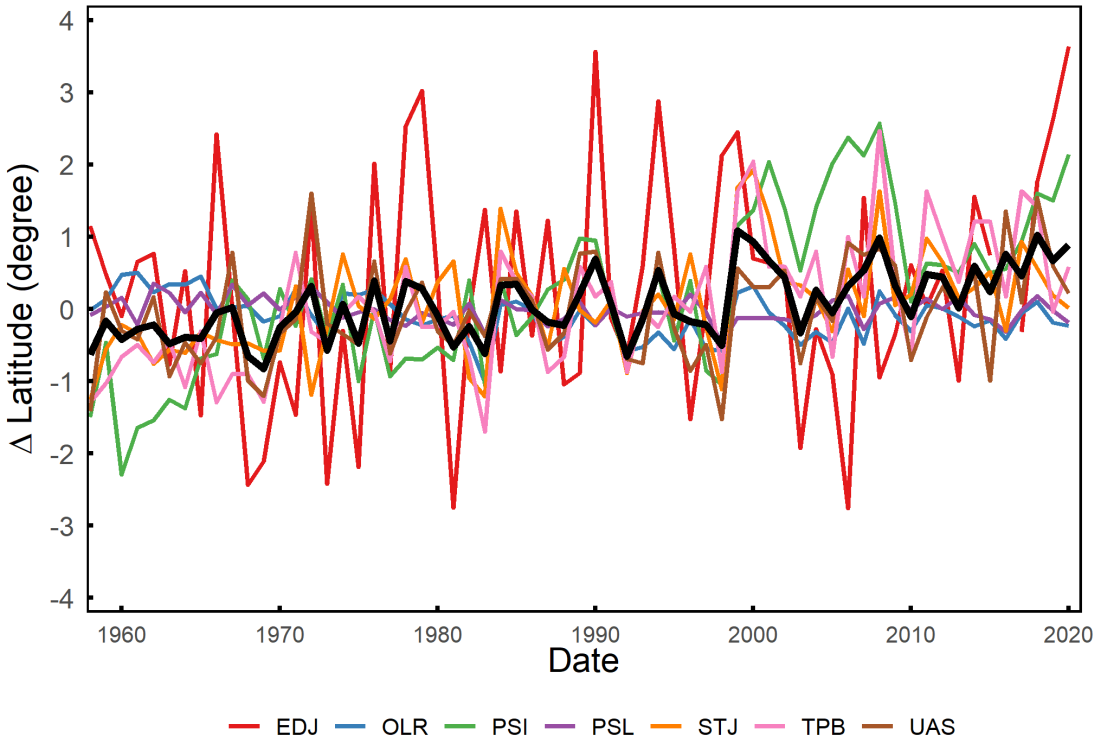

Figure 4.11: Anomaly of the annual average latitude of the Hadley cell north edge from 1959 to 2019 computed based on NCEP reanalysis. Curves of different colors correspond to different definitions of the northern boundary, as shown in Text 4.7.3, following Adam et al. (2018). The black curve shows the average of the seven individual estimates.

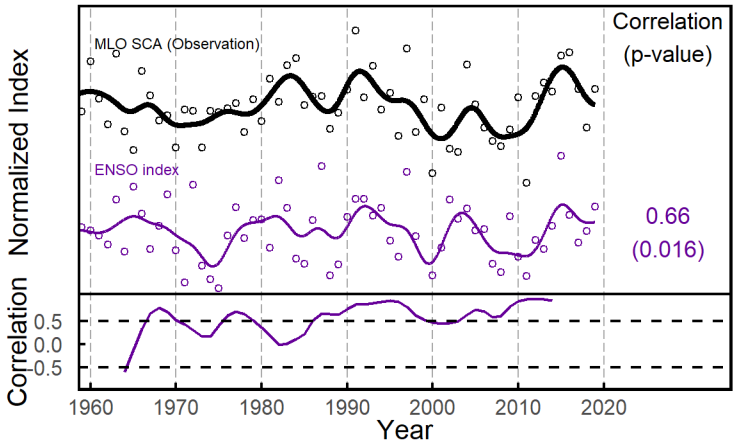

Figure 4.12: Similar to Figure 4.3 but exploring the correlations between observed MLO SCA and annual average ENSO index. We use NOAA Oceanic Niño Index (ONI). Each time series is detrended, normalized, and smoothed using the same method in Figure 4.2. In the bottom panel, we show the 11-year moving window correlation. Black dashed lines in the lower panel denote the ± 0.5 value.

4.8 Acknowledgments

Y. Jin was supported under a grant from NSF (AGS-1623748) and under a grant from Earth Networks. The historical measurements of the Scripps CO_2 program at MLO, KUM, CHR, BRW, have been supported by numerous grants from NSF and DOE and by staff at the Mauna Loa Observatory, which is supported by NOAA. Recent measurements at these stations have been supported by NASA (NNX17AE74G), NSF (OPP-1304270, OPP-1922922) and by Eric and Wendy Schmidt via recommendation of the Schmidt Futures program, with support for the instrumentation at MLO provided by Earth Networks. We also thank two anonymous reviewers and Dr. Benjamin Lintner for their valuable comments and efforts. Any opinions, findings, conclusions, and recommendations expressed in this material are those of the authors and do not necessarily reflect the views of NSF, NOAA, or DOE.

Chapter 4, in full, is a reprint of the material as it appears in Jin, Y., Keeling, R. F., Rödenbeck, C., Patra, P. K., Piper, S. C., & Schwartzman, A., 2022. Impact of changing winds on the Mauna Loa CO2 seasonal cycle in relation to the Pacific decadal oscillation. *Journal of*

Geophysical Research: Atmospheres, *127*(13), e2021JD035892. https://doi.org/10.1029/2021JD035892. The dissertation author was the primary investigator and author of this paper.

Reference

Adam, O., Grise, K. M., Staten, P., Simpson, I. R., Davis, S. M., Davis, N. A., et al. (2018). The TropD software package (v1): Standardized methods for calculating tropical-width diagnostics. *Geoscientific Model Development*, *11*(10), 4339–4357. https://doi.org/10.5194/gmd-11-4339-2018

Allen, R. J., & Ajoku, O. (2016). Future aerosol reductions and widening of the northern tropical belt. *Journal of Geophysical Research*, *121*(12), 6765–6786. https://doi.org/10.1002/2016JD024803

Allen, R. J., & Kovilakam, M. (2017). The role of natural climate variability in recent tropical expansion. *Journal of Climate*, *30*(16), 6329–6350. https://doi.org/10.1175/JCLI-D-16-0735.1

Allen, R. J., Sherwood, S. C., Norris, J. R., & Zender, C. S. (2012). Recent Northern Hemisphere tropical expansion primarily driven by black carbon and tropospheric ozone. *Nature*, *485*, 350–354. https://doi.org/10.1038/nature11097

Allen, R. J., Norris, J. R., & Kovilakam, M. (2014). Influence of anthropogenic aerosols and the Pacific Decadal Oscillation on tropical belt width. *Nature Geoscience*, *7*, 270–274. https://doi.org/10.1038/ngeo2091

Amaya, D. J., Siler, N., Xie, S. P., & Miller, A. J. (2018). The interplay of internal and forced modes of Hadley Cell expansion: lessons from the global warming hiatus. *Climate Dynamics*, *51*, 305–319. https://doi.org/10.1007/s00382-017-3921-5

Angert, A., Biraud, S., Bonfils, C., Buermann, W., & Fung, I. (2004). CO_2 seasonality indicates

origins of post-Pinatubo sink. *Geophysical Research Letters*, *31*, L11103. https://doi.org/10.1029/2004GL019760

Archer, C. L., & Caldeira, K. (2008). Historical trends in the jet streams. *Geophysical Research Letters*, *35*(8), 1–6. https://doi.org/10.1029/2008GL033614

Bastos, A., Ciais, P., Chevallier, F., Rödenbeck, C., Ballantyne, A. P., Maignan, F., et al. (2019). Contrasting effects of CO_2 fertilization, land-use change and warming on seasonal amplitude of Northern Hemisphere CO_2 exchange. *Atmospheric Chemistry and Physics*, *19*(19), 12361–12375. https://doi.org/https://doi.org/10.5194/acp-19-12361-2019

Bromwich, D. H., & Fogt, R. L. (2004). Strong trends in the skill of the ERA-40 and NCEP-NCAR reanalyses in the high and midlatitudes of the southern hemisphere, 1958-2001. *Journal of Climate*, *17*(23), 4603–4620. https://doi.org/10.1175/3241.1

Buermann, W., Lintner, B. R., Koven, C. D., Angert, A., Pinzon, J. E., Tucker, C. J., & Fung, I. Y. (2007). The changing carbon cycle at Mauna Loa Observatory. *Proceedings of the National Academy of Sciences*, *104*(11), 4249–4254. https://doi.org/https://doi.org/10.1073/pnas.0611224104

Draxler, R. R., & Rolph, G. D. (2010). HYSPLIT (Hybrid Single-Particle Lagrangian Integrated Trajectory) Model access via NOAA ARL READY Website (http://ready.arl.noaa.gov/HYSPLIT. php), NOAA Air Resources Laboratory, Silver Spring, MD [Software].

Ebisuzaki, W. (1997). A method to estimate the statistical significance of a correlation when the data are serially correlated. *Journal of Climate*, *10*(9), 2147–2153. https://doi.org/10.1175/1520-0442(1997)010<2147:AMTETS>2.0.CO;2

Forkel, M., Carvalhais, N., Rödenbeck, C., Keeling, R., Heimann, M., Thonicke, K., et al.

(2016). Enhanced seasonal CO_2 exchange caused by amplified plant productivity in northern ecosystems. *Science*, *351*(6274), 696–699. https://doi.org/10.1126/science.aac4971

Fox, J., & Weisberg, S. (2019). *An R Companion to Applied Regression, Third Edition*. Sage, Thousand Oaks, CA.

Gan, B., Wu, L., Jia, F., Li, S., Cai, W., Nakamura, H., et al. (2017). On the Response of the Aleutian Low to Greenhouse Warming. *Journal of Climate*, *30*(10), 3907–3925. https://doi.org/10.1175/JCLI-D-15-0789.1

Gelaro, R., McCarty, W., Suárez, M. J., Todling, R., Molod, A., Takacs, L., et al. (2017). The Modern-Era Retrospective Analysis for Research and Applications, Version 2 (MERRA-2). *Journal of Climate*, *30*(14), 5419–5454. https://doi.org/https://doi.org/10.1175/JCLI-D-16-0758.1

Grassi, B., Redaelli, G., Canziani, P. O., & Visconti, G. (2012). Effects of the PDO phase on the tropical belt width. *Journal of Climate*, *25*(9), 3282–3290. https://doi.org/10.1175/JCLI-D-11-00244.1

Graven, H. D., Keeling, R. F., Piper, S. C., Patra, P. K., Stephens, B. B., Wofsy, S. C., et al. (2013). Enhanced seasonal exchange of CO_2 by northern ecosystems since 1960. *Science*, *341*(6150), 1085–1089. https://doi.org/https://doi.org/10.1126/science.1239207

Gray, J. M., Frolking, S., Kort, E. A., Ray, D. K., Kucharik, C. J., Ramankutty, N., & Friedl, M. A. (2014). Direct human influence on atmospheric CO_2 seasonality from increased cropland productivity. *Nature*, *515*, 398–401. https://doi.org/10.1038/nature13957

Grise, K. M., Davis, S. M., Simpson, I. R., Waugh, D. W., Fu, Q., Allen, R. J., et al. (2019). Recent tropical expansion: Natural variability or forced response? *Journal of Climate*, *32*(5), 1551–1571. https://doi.org/10.1175/JCLI-D-18-0444.1

Gu, L., Baldocchi, D. D., Wofsy, S. C., William Munger, J., Michalsky, J. J., Urbanski, S. P., & Boden, T. A. (2003). Response of a Deciduous Forest to the Mount Pinatubo Eruption: Enhanced Photosynthesis. *Science*, *299*(5615), 2035–2038. https://doi.org/10.1126/science.1078366

Harris, J. M., & Kahl, J. D. (1990). A descriptive atmospheric transport climatology for the Mauna Loa Observatory, using clustered trajectories. *Journal of Geophysical Research: Atmospheres*, *95*(D9), 13651–13667. https://doi.org/https://doi.org/10.1029/jd095id09p13651

Harris, J. M., Tans, P. P., Dlugokencky, E. J., Masarie, K. A., Lang, P. M., Whittlestone, S., & Steele, L. P. (1992). Variations in atmospheric methane at Mauna Loa Observatory related to long-range transport. *Journal of Geophysical Research: Atmospheres*, *97*(D5), 6003–6010. https://doi.org/https://doi.org/10.1029/92JD00158

Haverd, V., Smith, B., Canadell, J. G., Cuntz, M., Mikaloff-Fletcher, S., Farquhar, G., et al. (2020). Higher than expected CO_2 fertilization inferred from leaf to global observations. *Global Change Biology*, *26*(4), 2390–2402. https://doi.org/10.1111/gcb.14950

Heimann, M., & Körner, S. (2003). *The global atmospheric tracer model TM3: Model description and user's manual Release 3.8 a*. MPI-BGC.

Hess, P. G. (1996). Trajectories and related variations in the chemical composition of air for the Mauna Loa Observatory during 1991 and 1992. *Journal of Geophysical Research Atmospheres*, *101*(D9), 14543–14568. https://doi.org/10.1029/95JD03611

Higuchi, K., Murayama, S., & Taguchi, S. (2002). Quasi-decadal variation of the atmospheric CO_2 seasonal cycle due to atmospheric circulation changes: 1979-1998. *Geophysical Research Letters*, *29*(8), 10–13. https://doi.org/10.1029/2001gl013751

Huang, B., Thorne, P. W., Banzon, V. F., Boyer, T., Chepurin, G., Lawrimore, J. H., et al. (2017). Extended reconstructed Sea surface temperature, Version 5 (ERSSTv5): Upgrades, validations, and intercomparisons. *Journal of Climate*, *30*(20), 8179–8205. https://doi.org/10.1175/JCLI-D-16-0836.1

Ito, A., Inatomi, M., Huntzinger, D. N., Schwalm, C., Michalak, A. M., Cook, R., et al. (2016). Decadal trends in the seasonal-cycle amplitude of terrestrial CO_2 exchange resulting from the ensemble of terrestrial biosphere models. *Tellus B : Chemical and Physical Meteorology*, *68*(1), 28968. https://doi.org/10.3402/tellusb.v68.28968

Jiao, W., Wang, L., Smith, W. K., Chang, Q., Wang, H., & D'Odorico, P. (2021). Observed increasing water constraint on vegetation growth over the last three decades. *Nature Communications*, *12*. https://doi.org/10.1038/s41467-021-24016-9

Johanson, C. M., & Fu, Q. (2009). Hadley cell widening: Model simulations versus observations. *Journal of Climate*, *22*(10), 2713–2725. https://doi.org/10.1175/2008JCLI2620.1

Jones, C. D., & Cox, P. M. (2005). On the significance of atmospheric CO_2 growth rate anomalies in 2002-2003. *Geophysical Research Letters*, *32*, L14816. https://doi.org/10.1029/2005GL023027

Jones, M. W., Andrew, R. M., Peters, G. P., Janssens-Maenhout, G., De-Gol, A. J., Ciais, P., et al. (2021). Gridded fossil CO_2 emissions and related O_2 combustion consistent with national inventories 1959–2018. *Scientific Data*, *8*(1), 1–23. https://doi.org/10.1038/s41597-020-00779-6

Kalnay, E., Kanamitsu, M., Kistler, R., & Collins, W. (1996). The NCEP/NCAR 40-Year Reanalysis Project. *Bulletin of the American Meteorological Society*, *77*(3), 437–472. https://doi.org/10.1175/1520-0477(1996)077<0437:TNYRP>2.0.CO;2

Keeling, C. D. (1960). The concentration and isotopic abundances of carbon dioxide in the atmosphere. *Tellus*, *12*(2), 200–203. https://doi.org/https://doi.org/10.1111/j.2153-3490.1960.tb01300.x

Keeling, C. D., Chin, J. F. S., & Whorf, T. P. (1996). Increased activity of northern vegetation inferred from atmospheric CO_2 measurements. *Nature*, *382*, 146–149. https://doi.org/10.1038/382146a0

Keeling, C. D., Piper, S. C., Bacastow, R. B., Wahlen, M., Whorf, T. P., Heimann, M., & Meijer, H. A. (2001). *Exchanges of atmospheric CO_2 and $^{13}CO_2$ with the terrestrial biosphere and oceans from 1978 to 2000. I. Global aspects, SIO Reference Series, No. 01-06, Scripps Institution of Oceanography, San Diego, 88 pages*.

Kobayashi, S., Ota, Y., Harada, Y., Ebita, A., Moriya, M., Onoda, H., et al. (2015). The JRA-55 reanalysis: General specifications and basic characteristics. *Journal of the Meteorological Society of Japan*, *93*(1), 5–48. https://doi.org/10.2151/jmsj.2015-001

Legler, D. M. (1983). Empirical orthogonal function analysis of wind vectors over the tropical Pacific region. *Bulletin of the American Meteorological Society*, *64*(3), 234–241. https://doi.org/10.1175/1520-0477(1983)064<0234:EOFAOW>2.0.CO;2

Lian, X., Piao, S., Li, L. Z. X., Li, Y., Huntingford, C., Ciais, P., et al. (2020). Summer soil drying exacerbated by earlier spring greening of northern vegetation. *Science Advances*, *6*(1). https://doi.org/10.1126/sciadv.aax0255

Lin, X., Rogers, B. M., Sweeney, C., Chevallier, F., Arshinov, M., & Dlugokencky, E. (2020). Siberian and temperate ecosystems shape Northern Hemisphere atmospheric CO_2 seasonal amplification. *Proceedings of the National Academy of Sciences*, *117*(35), 21079–21087. https://doi.org/10.1073/pnas.1914135117

Lintner, B. R., Buermann, W., Koven, C. D., & Fung, I. Y. (2006). Seasonal circulation and Mauna Loa CO_2 variability. *Journal of Geophysical Research Atmospheres*, *111*(13), D13104. https://doi.org/10.1029/2005JD006535

Liu, J., Wennberg, P. O., Parazoo, N. C., Yin, Y., & Frankenberg, C. (2020). Observational Constraints on the Response of High-Latitude Northern Forests to Warming. *AGU Advances*, *1*(4), e2020AV000228. https://doi.org/10.1029/2020av000228

Lu, J., Vecchi, G. A., & Reichler, T. (2007). Expansion of the Hadley cell under global warming. *Geophysical Research Letters*, *34*, L06805. https://doi.org/10.1029/2006GL028443

Lu, J., Deser, C., & Reichler, T. (2009). Cause of the widening of the tropical belt since 1958. *Geophysical Research Abstracts*, *36*, L03803. https://doi.org/10.1029/2008GL036076

Mantua, N. J., Hare, S. R., Zhang, Y., Wallace, J. M., & Francis, R. C. (1997). A Pacific Interdecadal Climate Oscillation with Impacts on Salmon Production. *Bulletin of the American Meteorological Society*, *78*(6), 1069–1079. https://doi.org/10.1175/1520-0477(1997)078<1069:APICOW>2.0.CO;2

Miller, J. M. (1981). A five-year climatology of back trajectories from the Mauna Loa Observatory, Hawaii. *Atmospheric Environment (1967)*, *15*(9), 1553–1558. https://doi.org/10.1016/0004-6981(81)90138-4

Muller, R., Rohde, R., Jacobsen, R., Muller, E., & Wickham, C. (2013). A New Estimate of the Average Earth Surface Land Temperature Spanning 1753 to 2011. *Geoinformatics & Geostatistics: An Overview*, *1*(1), 1–7. https://doi.org/10.4172/2327-4581.1000101

Murayama, S., Higuchi, K., & Taguchi, S. (2007). Influence of atmospheric transport on the inter-annual variation of the CO_2 seasonal cycle downward zero-crossing. *Geophysical Research Letters*, *34*, L04811. https://doi.org/10.1029/2006GL028389

Nevison, C. D., Mahowald, N. M., Doney, S. C., Lima, I. D., van der Werf, G. R., Randerson, J. T., et al. (2008). Contribution of ocean, fossil fuel, land biosphere, and biomass burning carbon fluxes to seasonal and interannual variability in atmospheric CO_2. *Journal of Geophysical Research: Biogeosciences*, *113*(1), 1–21. https://doi.org/10.1029/2007JG000408

Newman, M., Alexander, M. A., Ault, T. R., Cobb, K. M., Deser, C., Di Lorenzo, E., et al. (2016). The Pacific decadal oscillation, revisited. *Journal of Climate*, *29*(12), 4399–4427. https://doi.org/10.1175/JCLI-D-15-0508.1

NOAA (National Oceanic and Atmospheric Administration). 2019. Cold and warm episodes by season. https://origin.cpc.ncep.noaa. gov/products/analysis_monitoring/ensostuff/ONI_v5.php [Dataset].

Patra, P. K., Maksyutov, S., Ishizawa, M., Nakazawa, T., Takahashi, T., & Ukita, J. (2005). Interannual and decadal changes in the sea-air CO_2 flux from atmospheric CO_2 inverse modeling. *Global Biogeochemical Cycles*, *19*, GB4913. https://doi.org/10.1029/2004GB002257

Patra, P. K., Takigawa, M., Watanabe, S., Chandra, N., Ishijima, K., & Yamashita, Y. (2018). Improved chemical tracer simulation by MIROC4.0-based atmospheric chemistry-transport model (MIROC4-ACTM). *Scientific Online Letters on the Atmosphere*, *14*, 91–96. https://doi.org/10.2151/SOLA.2018-016

Peñuelas, J., Ciais, P., Canadell, J. G., Janssens, I. A., Fernández-Martínez, M., Carnicer, J., et al. (2017). Shifting from a fertilization-dominated to a warming-dominated period. *Nature Ecology and Evolution*, *1*, 1438–1445. https://doi.org/10.1038/s41559-017-0274-8

Piao, S., Liu, Z., Wang, Y., Ciais, P., Yao, Y., Peng, S., et al. (2018). On the causes of trends in

the seasonal amplitude of atmospheric CO_2. *Global Change Biology*, *24*(2), 608–616. https://doi.org/10.1111/gcb.13909

Pinheiro, J., Bates, D., DebRoy, S., & Sarkar, D. (2021). nlme: Linear and Nonlinear Mixed Effects Models. R package version 3.1-152, https://CRAN.R-project.org/package=nlme.

Randerson, J. T., Matthew, T. V., Conway, J., Fung, I. Y., & Field, B. (1997). The contribution of terrestrial sources and sinks to trends in the seasonal cycle of atmospheric carbon dioxide. *Global Biogeochemical Cycles*, *11*(4), 535–560. https://doi.org/https://doi.org/10.1029/97GB02268

Randerson, J. T., Field, C. B., Fung, I. Y., & Tans, P. P. (1999). Increases in early season ecosystem uptake explain recent changes in the seasonal cycle of atmospheric CO_2 at high northern latitudes. *Geophysical Research Letters*, *26*(17), 2765–2768. https://doi.org/10.1029/1999GL900500

Rödenbeck, C., Houweling, S., Gloor, M., & Heimann, M. (2003). CO_2 flux history 1982–2001 inferred from atmospheric data using a global inversion of atmospheric transport. *Atmospheric Chemistry and Physics*, *3*, 1919–1964. https://doi.org/https://doi.org/10.5194/acp-3-1919-2003

Van Der Schrier, G., Barichivich, J., Briffa, K. R., & Jones, P. D. (2013). A scPDSI-based global data set of dry and wet spells for 1901-2009. *Journal of Geophysical Research: Atmospheres*, *118*(10), 4025–4048. https://doi.org/10.1002/jgrd.50355

Schuldt, K. N., Mund, J., Luijkx, I. T., Aalto, T., Abshire, J. B., Aikin, K., et al. (2021). *Multi-laboratory compilation of atmospheric carbon dioxide data for the period 1957-2019; obspack_co2_1_GLOBALVIEWplus_v6.1_2021-03-01; NOAA Global Monitoring Laboratory. http://doi.org/10.25925/20201204* [Dataset].

Schwalm, C. R., Williams, C. A., Schaefer, K., Baldocchi, D., Black, T. A., Goldstein, A. H., et al. (2012). Reduction in carbon uptake during turn of the century drought in western North America. *Nature Geoscience*, *5*, 551–556. https://doi.org/10.1038/ngeo1529

Staten, P. W., Lu, J., Grise, K. M., Davis, S. M., & Birner, T. (2018). Re-examining tropical expansion. *Nature Climate Change*, *8*, 768–775. https://doi.org/10.1038/s41558-018-0246-2

Staten, P. W., Grise, K. M., Davis, S. M., Karnauskas, K., & Davis, N. (2019). Regional Widening of Tropical Overturning: Forced Change, Natural Variability, and Recent Trends. *Journal of Geophysical Research: Atmospheres*, *124*(12), 6104–6119. https://doi.org/10.1029/2018JD030100

Stein, A. F., Draxler, R. R., Rolph, G. D., Stunder, B. J. B., Cohen, M. D., & Ngan, F. (2015). Noaa's hysplit atmospheric transport and dispersion modeling system. *Bulletin of the American Meteorological Society*, *96*(12), 2059–2077. https://doi.org/10.1175/BAMS-D-14-00110.1

Taguchi, S., Murayama, S., & Higuchi, K. (2003). Sensitivity of inter-annual variation of CO_2 seasonal cycle at Mauna Loa to atmospheric transport. *Tellus B: Chemical and Physical Meteorology*, *55*(2), 547–554. https://doi.org/10.3402/tellusb.v55i2.16702

Takahashi, T., Sutherland, S. C., Wanninkhof, R., Sweeney, C., Feely, R. A., Chipman, D. W., et al. (2009). Climatological mean and decadal change in surface ocean pCO_2, and net sea-air CO_2 flux over the global oceans. *Deep-Sea Research Part II: Topical Studies in Oceanography*, *56*(8–10), 554–577. https://doi.org/10.1016/j.dsr2.2008.12.009

Tao, L., Hu, Y., & Liu, J. (2016). Anthropogenic forcing on the Hadley circulation in CMIP5 simulations. *Climate Dynamics*, *46*, 3337–3350. https://doi.org/10.1007/s00382-015-2772-1

Thomas, R. T., Prentice, I. C., Graven, H., Ciais, P., Fisher, J. B., Hayes, D. J., et al. (2016).

Increased light-use efficiency in northern terrestrial ecosystems indicated by CO_2 and greening observations. *Geophysical Research Letters*, *43*(21), 11339–11349. https://doi.org/10.1002/2016GL070710

Thoning, K. W., Tans, P. P., & Komhyr, W. D. (1989). Atmospheric carbon dioxide at Mauna Loa Observatory 2. Analysis of the NOAA GMCC data, 1974-1985. *Journal of Geophysical Research*, *94*(D6), 8549–8565. https://doi.org/10.1029/JD094iD06p08549

Wang, K., Wang, Y., Wang, X., He, Y., Li, X., Keeling, R. F., et al. (2020). Causes of slowing-down seasonal CO_2 amplitude at Mauna Loa. *Global Change Biology*, *26*(8), 4462–4477. https://doi.org/10.1111/gcb.15162

Wang, T., Liu, D., Piao, S., Wang, Y., Wang, X., Guo, H., et al. (2018). Emerging negative impact of warming on summer carbon uptake in northern ecosystems. *Nature Communications*, *9*(1), 1–7. https://doi.org/10.1038/s41467-018-07813-7

Wenzel, S., Cox, P. M., Eyring, V., & Friedlingstein, P. (2016). Projected land photosynthesis constrained by changes in the seasonal cycle of atmospheric CO_2. *Nature*, *538*, 499–501. https://doi.org/10.1038/nature19772

Zeng, N., Zhao, F., Collatz, G. J., Kalnay, E., Salawitch, R. J., West, T. O., & Guanter, L. (2014). Agricultural Green Revolution as a driver of increasing atmospheric CO_2 seasonal amplitude. *Nature*, *515*, 394–397. https://doi.org/10.1038/nature13893

Zhang, Y., Wallace, J. M., & Battisti, D. S. (1997). ENSO-like interdecadal variability: 1900-93. *Journal of Climate*, *10*(5), 1004–1020. https://doi.org/10.1175/1520-0442(1997)010<1004:eliv>2.0.co;2

Zhang, Y., Parazoo, N. C., Williams, A. P., Zhou, S., & Gentine, P. (2020). Large and projected strengthening moisture limitation on end-of-season photosynthesis. *Proceedings of the*

National Academy of Sciences, *117*(17), 9216–9222. https://doi.org/10.1073/pnas.1914436117

Zhao, F., Zeng, N., Asrar, G., Friedlingstein, P., Ito, A., Jain, A., et al. (2016). Role of CO_2, climate and land use in regulating the seasonal amplitude increase of carbon fluxes in terrestrial ecosystems: A multimodel analysis. *Biogeosciences*, *13*(17), 5121–5137. https://doi.org/10.5194/bg-13-5121-2016

Chapter 5 Concluding Remark

Over the past few decades, our quest to understand Earth's climate has led to a surge in data acquisition. This growth stems from a sophisticated network of monitoring systems that cover various layers of our atmosphere. Taking CO_2 observations as an example, we gather data from Earth's surface using stations, ships, and profiling floats. We also collect airborne observations from the free troposphere. More recently, satellites offer global insights from the atmosphere's uppermost layer. These platforms collectively offer an in-depth perspective on our climate and the global carbon cycle. Airborne data, in particular, provides a wide spatial view, capturing large-scale atmospheric features and offering vertical profiles less influenced by uncertainties in the atmospheric boundary layer.

This thesis focuses on the use of airborne data to promote our understanding of the global carbon cycle and atmospheric circulation. Making the best use of airborne data, however, is limited by its coverage and sensitivity to synoptic-scale disturbances. Here I pioneer the development of several toolboxes to leverage the use of airborne data, which builds upon a transformed isentropic coordinate system, $M_{\theta e}$, that is developed in Chapter 1 of my thesis. This coordinate, similar to the equivalent potential temperature (θ_e), is the preferential mixing surface of the atmosphere. Using $M_{\theta e}$ to study tracer distribution in the atmosphere allows me to leverage the way the atmosphere moves and focus sharply on the information content of CO_2 observations and corresponding surface fluxes, rather than the synoptic transport uncertainty.

Chapter 1 discuss the characteristic of the coordinate, which is of fundamental meteorology interest, and also illustrate two important applications of the coordinate for carbon cycle applications. One is to organize airborne observations to study the spatial and temporal pattern, for example, gradients over latitude, and seasonal cycles at different latitudes. The other is to calculate

tracer inventory in the troposphere. These two basic applications are the method foundation for other broader applications.

In Chapters 2 and 3, I apply this coordinate to calculate hemispheric-scale air-sea O_2 flux, and the Southern Ocean (SO) air-sea CO_2 flux over three latitude bands using the $M_{\theta e}$-aligned box model. The air-sea O_2 flux shows clear hemispheric asymmetry, suggesting key differences in the physical and biogeochemical processes that module the mixed layer dissolved oxygen changes. One major finding is the existence of subsurface oxygen maximum zones in the Northern Hemisphere, which prevents biological-driven O_2 outgassing. The SO CO_2 flux resolved in my thesis shows clear meridional shifts, with a biological-driven cycle that suggests strong summer-time CO_2 uptake in the high latitudes to a thermal-driven cycle that suggests strong winter-time CO_2 uptake in the mid-latitudes. We also find a weak winter-time outgassing in the high-latitude, which is driven mainly by ventilation processes that bring CO_2-rich water from the deep ocean to the surface ocean. This transition and winter-time outgassing features are seen in surface ocean pCO_2 measurements, but it is the first time we have resolved this from airborne data.

Air-sea O_2 and CO_2 flux estimates on regional to global scales are available also from other methods, such as from surface ocean pCO_2 and dissolved oxygen measurements, from inverse models that optimize surface station and ship data, and from Earth system models. This thesis also uses airborne-based estimates as a direct test on these models, identifying key limitations in these models, and tools that are used to create these models. These limitations include the insufficient coverage of surface ocean dissolved oxygen and pCO_2 measurements, uncertainty in gas-exchange velocity, and underrepresentation of stratification and biogeochemistry in general circulation models and ocean biogeochemistry models.

A noteworthy discovery in Chapter 3 is the ability to use $M_{\theta e}$ to evaluate the biases in atmospheric transport models (ATMs), which is crucial for determining the fluxes in inverse models. The $M_{\theta e}$-aligned box model suggests that the complex 3-D atmospheric circulation over the mid- to high-latitude SO could be simplified to 1-D, recognizing that the cross-isentrope diabatic transport is the most critical transport pathway. The timescale for this transport pathway is referred to as the diabatic mixing rate, which is similar to a diffusion coefficient. I propose two methods to derive this mixing rate, one is to parameterize the ATMs used in inverse models, and the other is based on the moist static energy budget (MSE) of meteorology reanalyses. I find that, in the high-latitude Southern Hemisphere, ATMs-based mixing rates are biased to suggest too rapid mixing in the austral summer, while MSE-based mixing rates are more realistic. This finding is confirmed by the fact that model-simulated CO_2 gradients across $M_{\theta e}$ are biased smaller than observed CO_2 gradients. Chapter 3 also establishes that the diabatic mixing rate derived from the MSE budget of reanalyses could help to further constrain ATMs. One path forward is to integrate MSE within atmospheric transport models (ATMs) as a passive tracer, similar to how CO_2 is currently represented. Comparing the simulated and observed (i.e., from reanalysis) MSE spatial distribution could help to identify key limitations in ATMs.

The applications of $M_{\theta e}$ coordinate have broader applications than originally anticipated. $M_{\theta e}$ is useful in the design phase of future airborne campaigns to ensure strategic coverage. Traditional airborne campaigns aimed at collecting air samples have often emphasized an extensive array of vertical profiles. I find that comprehensive coverage across various isentropes, rather than extensive coverage in latitude and pressure, is the main requirement for applications like resolving large-scale tracer gradients, and regional to hemispheric surface flux. Thus, future airborne campaigns with similar coverage as HIPPO, ORCAS, and ATom will have more

redundancy. This atmospheric coordinate not only ensures a strategic evolution in data acquisition and interpretation but is also a potential avenue for more cost-effective campaigns.

The $M_{\theta e}$ box model can be applied to calculate the surface fluxes for various tracers and spatial domains. For instance, one can use this model to estimate CO_2 fluxes in the Northern Hemisphere to understand the balance between tropical land CO_2 source and boreal forest uptake. One could also use this model to determine O_2 fluxes within the Southern Ocean, which has broader implications for understanding the SO carbon cycle. The model has implications for studying atmospheric chemistry, more specifically, quantifying the CH_4 chemical loss rate in the Southern Hemisphere. I note that CH_4 undergoes significant chemical loss in the atmosphere, while the exchange with the ocean is negligible. By employing this box model, we can pivot from traditional air-sea flux calculations to ascertain the atmospheric loss rate of CH_4, offering insights into a critical facet of its lifecycle. Collectively, these diverse applications underscore the versatility of the model, positioning it as a valuable tool for atmospheric and tracer studies.

This thesis introduces innovative methods essential for understanding atmospheric circulation, carbon cycles, and ocean biogeochemistry. Subsequent research can leverage the tools presented in this thesis to further enhance the utilization of airborne data and deepen our understanding of the global climate system.